Mechanical and Constitutive Modelling of the Photomechanical behavior of supramolecular organic Thin Films

Thesis supervised by Moussa NAIT ABDELAZIZ

Committee members

Referees	Rafael ESTEVEZ	Professor at Université de Grenoble	
	Stéphane LEJEUNES	Researcher at CNRS Marseille	
Examiners	Lucien LAIARINANDRASANA	Professor at Mines Paris Tech	Committee President
	Stéphane ALOISE	Associate Professor at Université de Lille	
	Sophie BARRAU	Professor at Université de Lille	
Supervisor	Moussa NAIT ABDELAZIZ	Professor at Université de Lille	

Mechanical and Constitutive Modelling of the Photomechanical behavior of supramolecular organic Thin Films

UNIVERSITÉ DE LILLE

École doctorale **ED SCIENCE DE L'INGÉNIÉRIE ET DES SYSTÈMES (ENGYS)**

Laboratoire **Unité Mécanique Lille (UML)**

Thèse présentée par **Rebeca CEDEÑO MADERA**

Soutenue le **4 mai 2023**

Pour obtenir le grade de docteur délivré par Université de Lille

Discipline **Génie Mécanique**

Spécialité **Mécanique des solides, des matériaux, des structures et des surfaces**

Modélisation mécanique et constitutive du comportement photomécanique de couches minces organiques supramoléculaires

Thèse dirigée par Moussa NAIT ABDELAZIZ

Composition du jury

Rapporteurs	Rafael ESTEVEZ	professeur à l'Université de Grenoble	
	Stéphane LEJEUNES	Ingenieur de recherche au CNRS Marseille	
Examinateurs	Lucien LAIARINANDRASANA	professeur au Mines Paris Tech	président du jury
	Stéphane ALOISE	MCF à l'Université de Lille	
	Sophie BARRAU	professeur à l'Université de Lille	
Directeur de thèse	Moussa NAIT ABDELAZIZ	professeur à l'Université de Lille	

This thesis has been prepared at

Unité Mécanique Lille (UML)

BATIMENT ESPRIT
59655 Villeneuve d'Ascq Cedex

Web Site   `https://uml.univ-lille.fr/`

A mis padres, Isabel y Adán

Gracias infinitas

Mechanical and Constitutive Modelling of the Photomechanical behavior of supramolecular organic Thin Films

Abstract

Recently, a new type of photoactive thin films has been developed by combining functionalized dithienylethene (DTE) and functionalized poly(ethylene-co-butylene) (PEB). These films exhibit photomechanical behavior due to the photo-switching property of the DTE molecule, while the elastomeric matrix (PEB) gives rubber-like properties and reversible deformation to the films. To investigate this phenomenon, we designed a movement tracking setup that combined a microscopic camera with visible (VIS) and ultaviolet (UV) light-emitting diodes (LEDs) to activate the molecular switch. We recorded multiple cycles of UV-VIS irradiation and analyzed the resulting video to confirm that light exposure caused photomechanical deformation in the thin films. Our primary objective was to couple the DTE photo-switching properties with the light-induced deformation of the thin films using a photo-kinetics model of DTE and the nonlinear mechanical models for rubber-like materials. We implemented both models in the finite element analysis (FEA) software Marc Mentat using user external subroutines. Through FEA simulations, we demonstrated the dependence of photomechanical activation on parameters such as light intensity and the photochemical and mechanical properties of the thin films. Finally, we validated the proposed mechanical model by comparing simulation results with experimental data.

Keywords: photomechanical effect, supramolecular chemistry, thin films, dyarylethene, mechanical modeling, mechanical characterization, finite element analysis

Modélisation mécanique et constitutive du comportement photomécanique de couches minces organiques supramoléculaires

Résumé

Récemment, un nouveau type de *thin films* photoactifs a été développé en combinant du diaryléthène (DTE) fonctionnalisé et du poly(éthylène-co-butylène) (PEB) fonctionnalisé. Ces films présentent un comportement photomécanique en raison de la propriété de commutation photochimique de la molécule DTE, tandis que la matrice élastomérique (PEB) confère aux films des propriétés similaires au caoutchouc et une déformation réversible. Pour étudier ce phénomène, nous avons conçu une installation de suivi de mouvement combinant une caméra microscopique et des diodes électroluminescentes (LED) émettant de la lumière visible (VIS) et ultraviolette (UV) pour activer la commutation moléculaire. Nous avons enregistré plusieurs cycles d'irradiation UV-VIS et analysé la vidéo obtenue pour confirmer que l'exposition à la lumière causait une déformation photomécanique des *thin films*. Notre objectif principal était de coupler les propriétés de commutation photochimique de DTE avec la déformation induite par la lumière des *thin films* en utilisant un modèle de photo-cinétique de DTE et des modèles mécaniques non linéaires pour les matériaux similaires au caoutchouc. Nous avons implémenté les deux modèles dans le logiciel d'analyse d'éléments finis (FEA) Marc Mentat en utilisant des sous-routines externes de l'utilisateur. Grâce aux simulations FEA, nous avons démontré la dépendance de l'activation photomécanique à des paramètres tels que l'intensité lumineuse et les propriétés photochimiques et mécaniques des *thin films*. Enfin, nous avons validé le modèle mécanique proposé en comparant les résultats de simulation avec les données expérimentales.

Mots clés : effet photomécanique, chimie supramoléculaire, couches minces, dyaryléthène, modélisation mécanique, caractérisation mécanique, analyse par éléments finis

Acknowledgements

I would like to express my deepest gratitude to the following individuals and institutions who have played a significant role in the completion of this PhD thesis.

First and foremost, I am immensely grateful to my supervisor, Moussa Nait-Abdelaziz, for their guidance, support, and invaluable expertise throughout this journey. Also to Stéphane Aloïse, whom if I had not met in Mexico City I would not have known about the great opportunity to participate in this project. Their unwavering commitment to excellence, patience, and encouragement have been instrumental in shaping my research and academic growth. I am truly fortunate to have had the opportunity to work under their mentorship.

I would like to extend my sincere appreciation to the members of my thesis committee, for their insightful feedback and constructive criticism. Their expertise and scholarly input have greatly enriched my research and strengthened the quality of this thesis.

I am deeply thankful to UML for providing me with the resources, infrastructure, and intellectual environment necessary for conducting my research. The collaborative atmosphere among the faculty and fellow researchers has fostered a stimulating academic experience, enabling me to explore new horizons in my field. Additionally, I would like to express my heartfelt appreciation to LASIRE and UMET for their warm reception and for providing me with the opportunity to conduct research in their exceptional facilities.

To my friends and colleagues, both in France and Mexico, thank you for your friendship, camaraderie, and moral support. Your presence has brought joy and laughter to my life, reminding me of the importance of balance during this demanding journey.

I would like to express my gratitude to CONACYT for the financial support that made this research possible. Their investment in my education has been instrumental in shaping my academic and personal growth.

Lastly, but certainly not least, I want to thank my family for their unconditional love, unwavering belief in my abilities, and constant encouragement. To my parents, my

brother, and extended family, thank you for always being there for me, even across the distance. Your unwavering support has been the cornerstone of my perseverance and success. Thank you for believing in me and accompanying me on this transformative journey.

Contents

The possibility of using light as an energy resource opens up opportunities for research work to develop photomechanical materials, offering promising technological advance. Because of their capacity to react to light stimulus, these materials allow the construction of lighter devices by reducing cables and other components. However, the study of photomechanical materials is rather complex because of the interplay between photo-chemistry, polymer chemistry, and physics. The discovery of the photomechanical effect has paved the way for the development of smart materials that enable the fabrication of new technology in robotics [1, 2], optics [3, 4], electronics [5, 6], biotechnology [7] and mechanics [8, 9].

One of the most used photoactive molecule was the azobenzene, since the seventies it has been widely studied and many technological applications have been developed since then, particularly liquid-crystalline networks (LCNs) materials [10–13]. The photo-transformation process in azobenzenes happens when under UV irradiation, the azobenzene isomerizes from a *trans* to a *cis* form (figure 1 a), which thermally relaxes back to the *trans* form, the reverse transformation occurs also under VIS irradiation (fig.1). This type of transformation is denoted as *photoswitch*.

A *photoswitch* is a molecular system that undergoes reversible changes in its properties, structure or functions upon light exposure, commonly by an isomerization (photoisomer-ization) or a electronic excitation (photocycloreversion) process. In the last two decades, diarylethene (DAE) (photoswitch molecule) derivatives have been studied, demonstrating excellent photochemical and thermal properties that favors the development of photo-actuators [15–19].

Few years ago, Takeshita et al. [20, 21] synthesized a new system combining a di-arylethene derivative (DTE), which is a photo-active molecule, with a thermoplastic elastomer applying a non-covalent bonding through a supramolecular approach (fig.3). The non-covalent bonding employed was a hydrogen-based unit called ureidopyrim-idinone (UPy), an efficient system previously used for supramolecular polymers [22, 23]. To obtain the photoactuator, first, in a chloroform solution UPy functionalized DTE
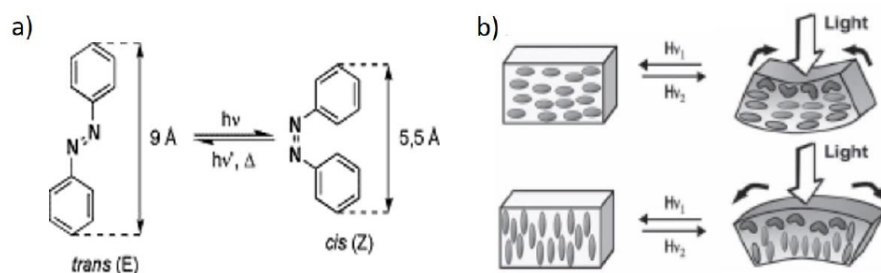
Figure 1: a) Cis-trans isomerization photochromism of azobenzene. b) Photomechanical effect in LCEs: the homogenous alignment of LCs produces bending towards the actinic light, whereas the isotropic alignment of LCs causes bending away from the light source [14]
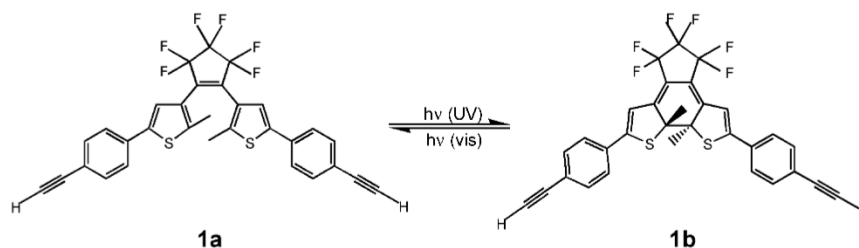
Figure 2: Diarylethene derivative photoswitch. Open-ring (1a) and closed-ring (1b) isomers [19].

and PEB (elastomer) are mixed. Under irradiation this solution shows photochromism (color change), initially it presents as colorless, which corresponds to its open form configuration (OF), under UV (330 ± 20 nm wavelength) irradiation it transforms to color blue, corresponding the closed form configuration (CF), the photochromism is reversible under VIS light (> 460 nm).

Takeshita's team elaborated thin films by spin coating process using the DTE-UPy-PEB solution. Upon visible irradiation, the initially bent blue film (CF) is instantaneously flattened and as long as light penetrates into the material (inducing a CF-OF gradient) [25]. Upon UV irradiation, the transparent film (OF), only moderate flattening was reported (fig.4).

Motivated by Takeshita's work, Louati et al. [24] developed photomechanical thin films using supramolecular chemistry to incorporate UPy functionalized DTE with semi-crystalline poly(ethylene-co-butylene) (PEB). As a result, the photoreversible properties of DTE coupled with the dynamic properties of supramolecular PEB, produce a promising photomechanical thin film.

DTE, in crystal form, has been extensively studied and their photochemical and thermal
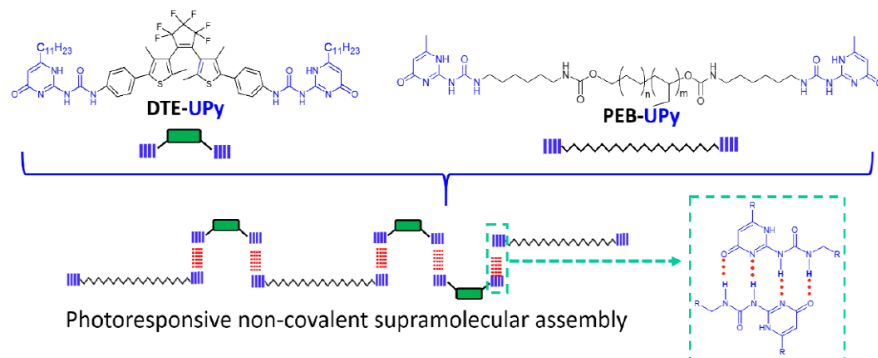
Figure 3: DTE-UPy/PEB-UPy supramolecular approach. DTE-UPy and PEB-UPy molecules and issued photoresponsive non-covalent self-assembly via quadruple hydrogen bonds [24].
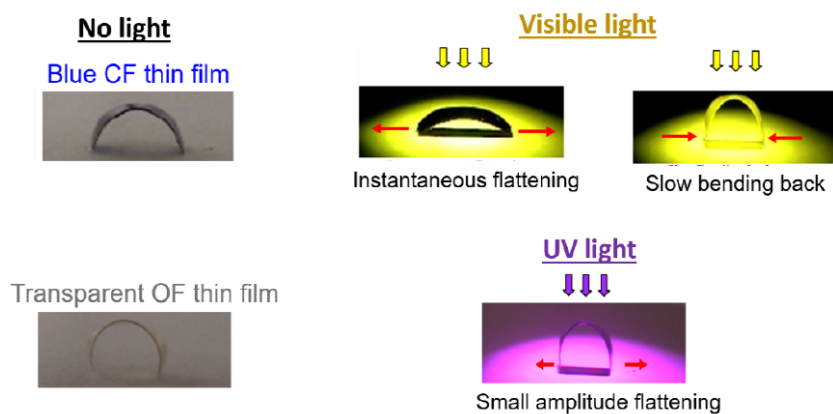
Figure 4: Photomechanical effects of thin film (film size: 1.5 cm$x$0.3 cm$x$80 µm) elaborated with spin coating under visible (blue film) and UV (transparent film) lights

properties make it ideal for smart materials applications [26–30]. However, the mechanical analysis on this material is limited and it has not been yet explored, specially in the form of elastomer-based supramolecular thin film.

To fully comprehend the potential applications of photomechanical materials, it is necessary to develop mechanical models that describe the macroscopic mechanical response, considering the photophysical and photochemical mechanisms. The foregoing is the main motivation for this thesis project.

We will base our study on previous work, in which other photomechanical materials made of similar photoactive molecules were studied [31–38], to conduct a complete mechanical study and propose a constitutive model to understand the photomechanical properties of the DTE-UPy-PEB thin films, with the aim of predicting their light-induced deformation from initial photochemical parameters such as, time light exposure, irradiation intensity, photoactive molecular concentration, etc.

The first chapter of this thesis will cover the photomechanical effect observed in the last decades in different types of photoresponsive materials. We will describe the mechanisms followed to obtain different macroscopical light-induced deformations such as expansion, contraction, bending, twisting, and even explosive effects that lead to fracture that have been observed in such materials. We will compare the different type of photoactive molecules used to produce the aforementioned materials. Finally, we will examine the most relevant research in respect to the mechanical analysis and modeling of photomechanical materials.

Next, the second chapter reviews the main mechanical models used to describe the behavior of elastomers that present viscoelastic properties, as well as methods of mechanical characterization. We will emphasize hyperelastic models, which researchers have used in photoresponsive materials with nonlinear mechanical properties and have successfully described the behavior of complex materials.

In the third chapter, we explain the elaboration methods to produce the supramolecular photoactive thin films, along with an analysis of their photochemical characteristics. Moreover, the first light-induced bending experimental observation is reported.

Chapter four contains the mechanical testing performed on the supramolecular thin films. The objective is to characterize both the UPy-PEB thin film and the photoactive DTE-UPy-PEB thin film through Dynamic Mechanical Analysis (DMA), stress relaxation, axial tensile test and creep test. We tested two types of functionalized PEB and established their main differences. Furthermore, we performed mechanical tests (creep and stress relaxation) under photoirradiation to understand the mechanical changes the material undergoes during the photochemical transition.

In the fifth chapter, the mechanical analysis concludes with a series of numerical and finite element (FE) simulations conducted to understand the photomechanical effect of the DTE-UPy-PEB thin films. First, the Pariani model [39] is numerically calculated to understand the light penetration depth in the material in function of its thickness,

DTE content and light intensity. By understanding this, we could correlate it with the light-induced curvature observed in the experimental study, applying a linear beam theory.

A purely hyperelastic model is proposed to simulate the light-induced bending of the thin films, we implement this model and the DTE photokinetics using user subroutines in the finite element analysis (FEA) MARC MENTAT. To calibrate the thin films' viscoelastic behavior, we performed an algorithm in MATLAB using the Bergstrom-Boyce model. The obtained viscoelastic parameters are applied directly in the MARC software. In this way we propose a complete hyper-viscoelastic model that is validated by comparing simulation and experimental results.

Photomechanical Materials overview: Light response mechanisms and mechanical modeling

Research work on photomechanical materials begun in the seventies. Lagowski and Gatos [40] reported one of the first photomechanical phenomena: the bending in cadmium sulfide (CdS) semi-conductor wafers occurring when irradiated with white light. Concluding that the photomechanical effect is a consequence of a light-induced surface change in the electric field of the wafer and, they demonstrated that the amplitude of such bending is more associated with the light irradiation than with the piezoelectric properties of CdS.

In the same decade, research work showed that polymer-based photochromic systems exhibited as well light-induced mechanical effects. At the beginning, these polymers were doped with azoaromatics to enhance pigmentation. Later research proved that combined photochromic dyes and polymeric matrix create materials that can have both reversible mechanical motion and change in color (photochromism). Agolini and Gay [10] worked on these kinds of polymers, observing that photo and thermal contraction arise alongside photochromism, concluding that the *trans-cis* isomerism of azocompounds is associated with the contractile behavior. Similar behavior occurs on spirobenzopyrans cross-linked with ethyl acrylate networks [41], where the contraction and elongation cycles are linked with the ring-opening of the spiropyran compound

under ultraviolet light.

1.1 Activation mechanisms

The main activation mechanisms of the photoresponsive materials are:

1.1.1 Photo-Induced Network Rearrangement (PNR) by radical induced bond exchange

Light exposure causes the chemical detachment of photoinitiator molecules, which are the active end group of the polymer chains, forming free radicals (fig.1.1a) that reattach with other slit-up chains. The macroscopically consequence of this light-induced network arrangement is stress relaxation and plastic deformation [34].

1.1.2 Photo-tunable molecular crosslink

Here the photoactive molecules (chromophores) are covalently attached to the polymer backbone. When irradiated, the chromophores dimerize, chemically bonding together and providing an additional crosslinking (fig. 1.1b) [31].

1.1.3 Photoswitch

Photoswitch effect is the change of the molecular structure into another isomeric form when photo-excited. This process is called photoisomerization for azobenzene (fig.1.1d) and photoelectrocyclization for diarylethene (fig.1.1c).

1.2 Types of photomechanical effects

As light is absorbed during photoirradiation, the material undergoes a molecular structure change at microscopic level, which leads to a series of transformations that results in a macroscopic mechanical response.

We can classify photomechanical materials response to light stimuli in four main types:

1.2.1 Expansion-Contraction

The concept of materials expanding and contracting due to temperature changes is a widely recognized phenomenon in physics. However, studies conducted over the past twenty years have revealed that certain materials, particularly diarylethene (DTE)

(a) Photo-induced Network Rearrangement (PNR)

(b) Photo-tunable Molecular Crosslinks (PMC)

(c) DTE photoswitch

(d) Azobenzene photoswitch
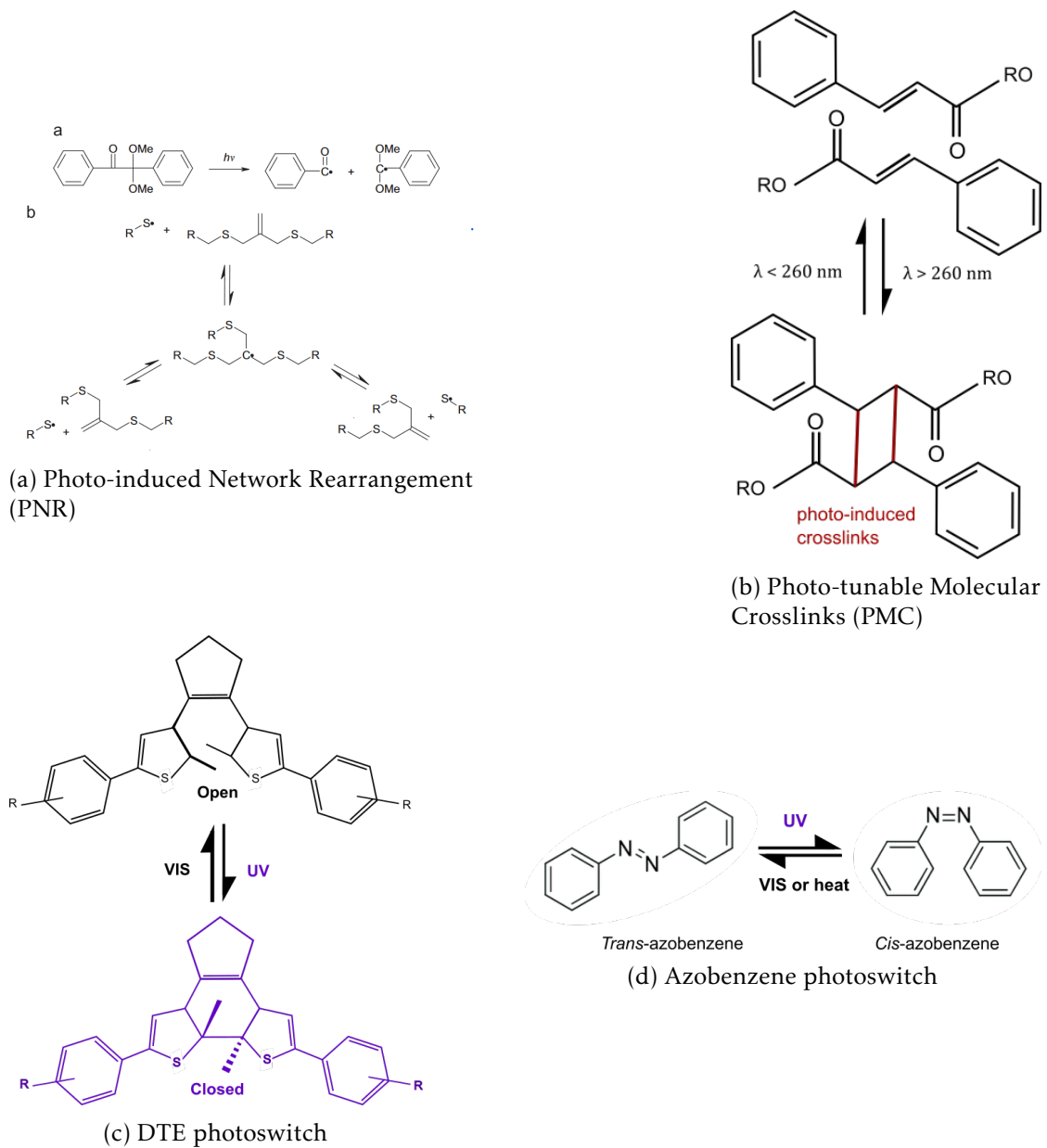
Figure 1.1: Activation mechanisms of photomechanical responsive materials

crystals [42] and azobenzene-based liquid crystal polymer (LCP), exhibit similar deformations under exposure to light. Macroscopically, this deformation is shown as contraction when irradiated with ultraviolet light (UV) and reversibly expanding back to the original shape when irradiated with visible light (VIS) (fig. 1.2b). If seen microscopically, these deformations result from a change in the morphology and structure of the material (fig. 1.2a). It has been reported a change of crystal lattice parameters with light [43], resulting in deformation of specific planes which are observable with Atomic Force Microscope (AFM) analysis.

1.2.2 Bending

Bending is a very common response in beam-like photomechanical materials. The bending reaction occurs as follows: on the irradiated surface, the photoactive units undergo a photoswitching process which creates photo-products. As light is absorbed through the material thickness, the conversion occurs asymmetrically, causing a transformation gradient that produces bending (figure 1.3). Recent studies describe the photo-induced bending behavior of mechanical materials as a dependency on many factors such as, thickness [27], irradiation power [45], light polarization [46] and molecular structure [47].

1.2.3 Twisting

Some photomechanical materials, especially in ribbon-like geometries [49, 50], have shown twisting under light irradiation [51] (fig.1.4 c.1) . This phenomenon is induced by shear strain in the diagonal direction relative to the sample's long axis (fig. 1.4 c).The twisting depends on the molecular structure orientation regarding the material's long axis direction, although the twisting direction can be controlled by adjusting the light incident angle [52].

1.2.4 Jumping and breaking

The two previously described photomechanical responses, bending and twisting, mainly occur when the light stimulus induces a continuous relax deformation. Contrary, when the light irradiation induces a spontaneous fast stress relaxation, the material suffers fracture or jumping [53]. These phenomena have been observed mostly in microcrystals(fig.1.4 d.1) [16, 54] and also in azobenzene based polymers (fig.1.4 d.2) [38].

(a) Morphology change observed in DTE crystals with AFM images. Initial state (D), after UV irradiation (E) and after VIS irradiation (F). [43]
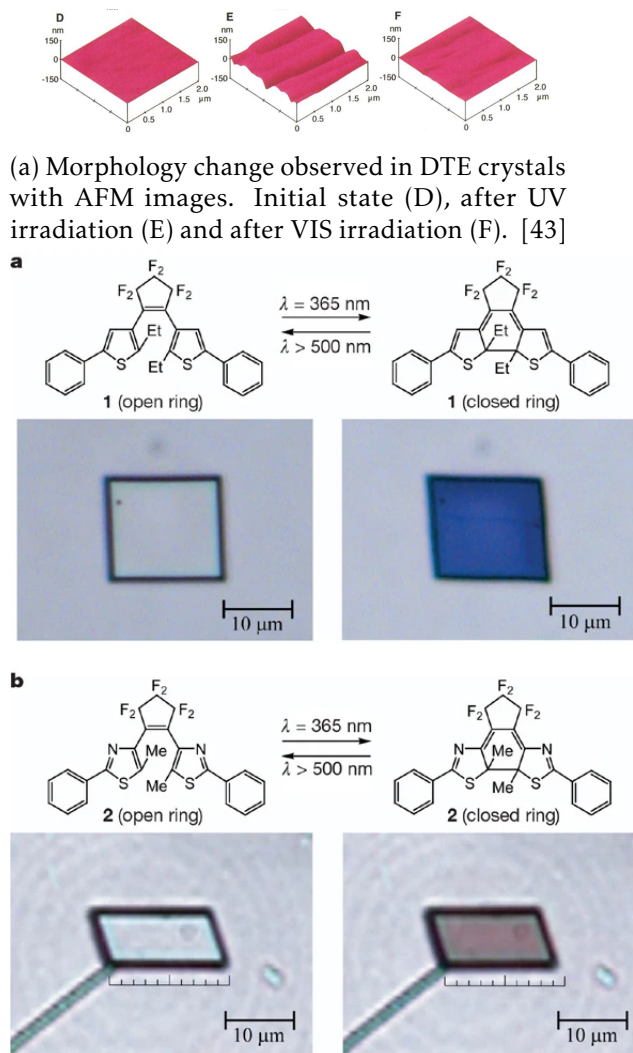
(b) Two DTE crystals reversibily changed their shape under light irradiation. In **a** the crystal with initial corner angles 88° and 92° changed to 82° and 98° and in **b** crystal contracted and expanded up to 7% [44]

Figure 1.2: Expansion and contraction of photomechanical materials at micro (a) and macro scale (b)
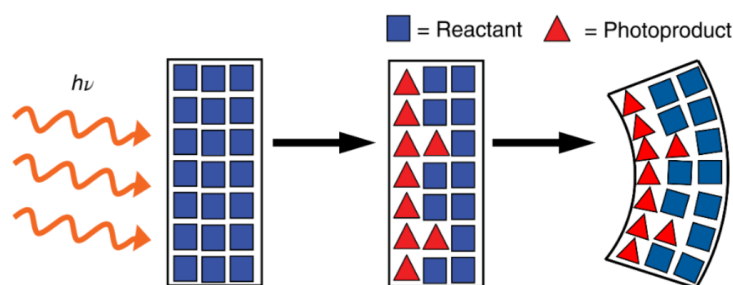
Figure 1.3: Schematic illustration of photo-induced bending [48]
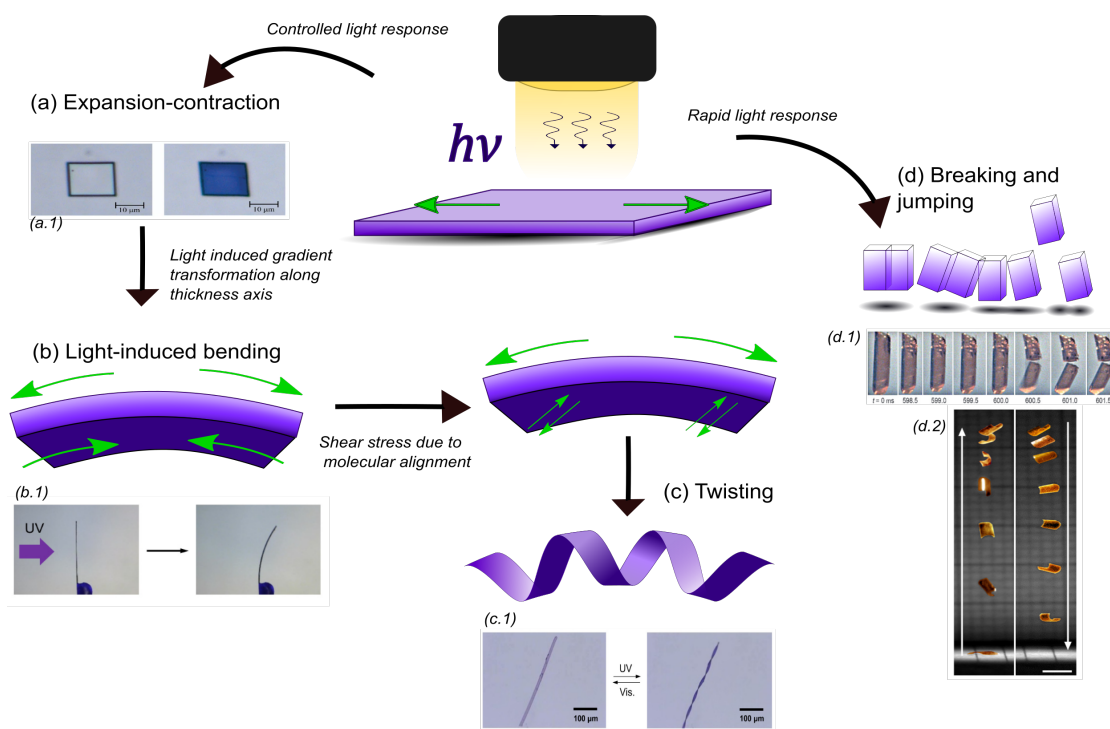
Figure 1.4: Types of photomechanical response.(a) The material molecular structure transforms as a result of light exposure inducing a reversibly expansion-contraction, as the light penetrates into the material, a gradient transformation is produced along the thickness axis inducing bending (b). Shear stress induced by the molecular orientation causes twisting of the material (c). Rapid light excitation produces an explosive response manifested as an abrupt fracture or jumping (d)

1.3 Photomechanical materials based on molecular photoswitches

The field of molecular photoswitches is promising and continuously growing thanks to its chemical versatility and photochromic reversibility. The most known molecular photoswitches are the azobenzene, the spiropyran and diarylethene (fig. 1.5). These organic molecules have photochromic properties and recent studies demonstrate that materials doped with these photoresponsive molecules present photomechanical responses. [29, 55–57].

1.3.1 Azobenzene based materials

The photo-transformation process in azobenzenes happens when under UV irradiation, the azobenzene isomerizes from a *trans* to a *cis* form (figure 1.5 (A)), which thermally relaxes back to the *trans* form, the reverse transformation occurs also under VIS irradiation [59].

Azobenzenes derivatives have been combined in cross-linked matrices to enhance materials' photochromic and photomechanical properties. One of the most notable applications of azobenzene is the doping of liquid crystal elastomer (LCE). Finkelmann's [60] work demonstrate the large reversible deformation of azo-polymers induced by UV light.

The tuneable molecular architecture of LCNs prior to polymerization allows for programmed actuation, such as bending, twisting or rolling. A recent study [61] described the possibility of re-programming an azobenzene-based LCN prepared on a thermoplastic substrate of poly(ethyleneterephthalate) (PET) that can be deformed when heated above its glass transition temperature. Different modes of actuation under UV light can therefore be achieved with a single material (fig. 1.5 (A)).

Among the various uses of azo-polymers and azo-LCNs are: optical waveguide and shutters [11], optical memories, photo-active artificial muscles [12, 14, 62], photo triggered carriers and membranes [63–66], etc.

1.3.2 Spiropyran based materials

Spiropyran is an organic molecule than upon irradiation can reversibly transform from a closed spiropyran form into an open merocyanine form (fig 1.5 (B)). Their photochromic properties have been known since the mid twenties and, recently, spiropyran has been added to macromolecular chains to create new materials capable of reacting to light and produce movement [67]. An example of spiropyran-based material photomechanical
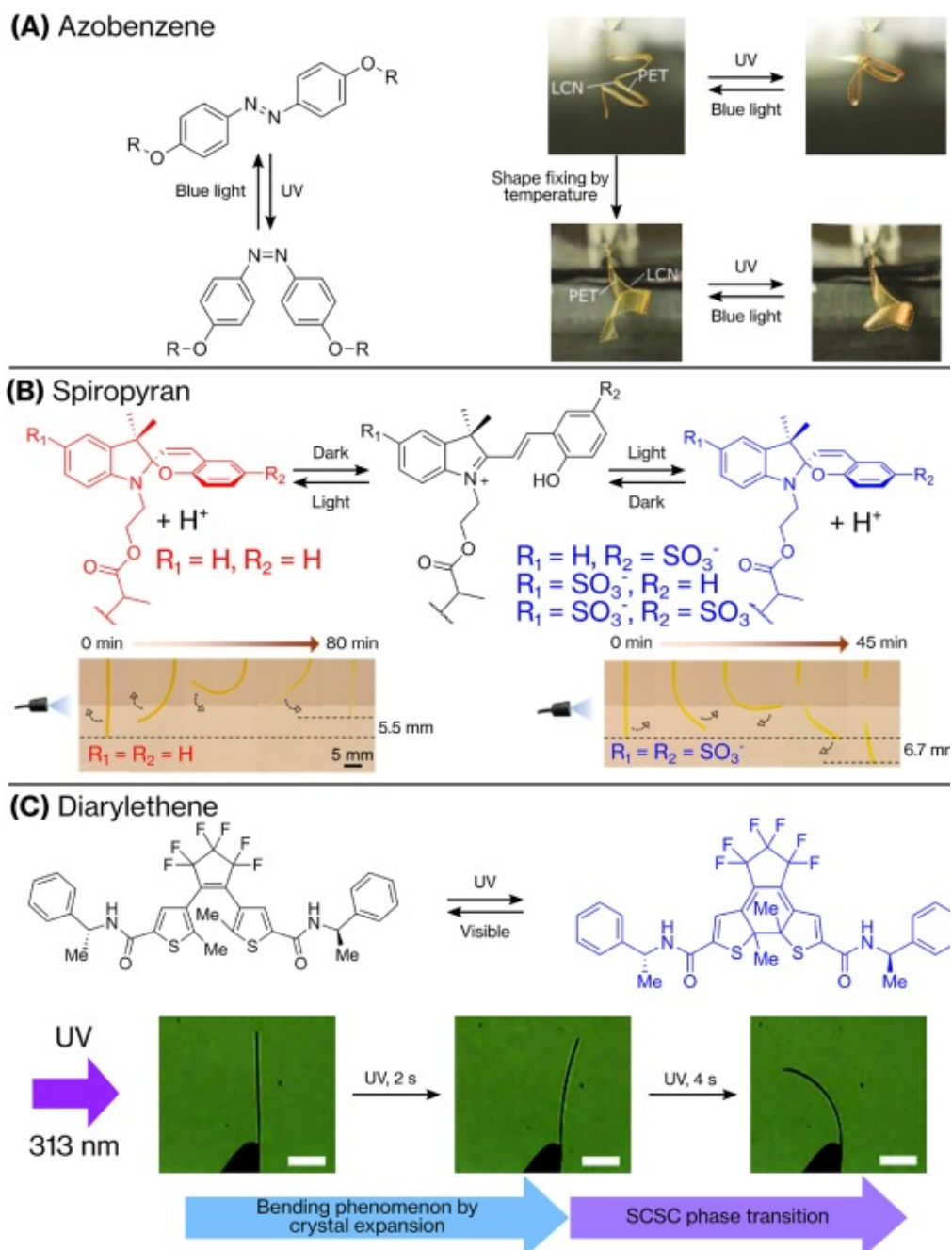
Figure 1.5: Representative examples of actuators based on photoswitches. (A) Reprogrammable azobenzene LCN. (B) Spiropyran-based gels. (C) Diarylethene-based crystal. (source [58]).

bending is shown in figure 1.5 (B): when merocyanine has no sulfonate group, ring closure under UV light decreases the net charge of the molecule, leading to a contraction towards the light source. However, when merocyanine has sulfonate groups, ring closure under UV light increases the net charge of the molecule, leading to an expansion of material and, therefore, a bending motion away from the light source. In both cases, for prolonged irradiation times, unbending occurs as the deformation gradient disappears.

Applications of spiropyran based materials, include: photochromic lenses, semiconductors, optical memory in quantum computers [68] and biomaterials intended for drug delivery systems [69].

1.3.3 Diarylethene (DTE) based materials

Diarylethene derivatives, particularly dithienylethene, have shown in several studies excellent thermal, optical and mechanical properties [15, 29]. The reversible photoisomerization occurs when irradiated with UV light, the DTE in open form (OF) transforms into a closed form (CF) isomer and, under VIS light, the CF photoisomerizes back to OF (figure 1.5(C)). Contrary to azobenzene, the DTE photoproduct is thermally stable, meaning that if it is not subjected to irradiation, the isomer remains unchanged. This is true for certain diarylethene derivatives, because this stability is related to the type of aryl group of the closed ring [18].

Researchers have extensively studied the photomechanical effect of DTE crystals, noting that the effect depends on several factors, such as sample thickness [27], light power [45], light wavelength [28], or light polarization [46]. An example of light-induced bending of DTE crystals is displayed in figure 1.5(C). The DTE crystal is irradiated from the left side. Under UV light, the crystal first bends away from the light source because of the change in geometry of the photoswitch molecule, which leads to an expansion of the crystal. For longer irradiation times, however, the greater population of photocyclized molecules triggers a crystallinity change, leading to a bending motion towards the light [30].

To expand the applications of DTE photoswitches, in the last two decades, researchers have developed new DTE-based materials, combining it with supramolecular polymers [20]. Supramolecular polymers are a new class of material that, besides allowing simpler chemical synthesis, possesses great thermal properties [22]. DTE supramolecular polymers have been analyzed at a molecular level [17, 70, 71] and in their liquid state [72]. These studies have motivated research work to explore the possibilities of DTE polymers in a solid state, especially in thin films [73].

1.4   Photomechanical Modeling: coupling light and mechanics

To understand the photomechanical effect, first is necessary to describe mathematically how light activation induces mechanical deformation. Photomechanical materials are activated by light differently depending on its nature. Photoactive molecules own different photochemical kinetics that can be explained in terms of mathematical expressions. Once identified, the photokinetics is coupled with the mechanical model that best defines the type of deformation.

1.4.1   Light penetration: Beer-Lambert Law

Light propagation through a chemically homogenous medium without internal sources or scattering is described by the Beer-Lambert law, which states that the absorbance (A) of light varies linearly with both the sample length and the concentration of photoactive molecules. The Beer-Lambert law is expressed as:

$$A = \epsilon l c \tag{1.1}$$

where l is the path length of incident light, c is the concentration of light-absorbing molecules and ϵ is the molar absorptivity.

Absorbance A is defined as:

$$A = -\ln(I/I_0) \tag{1.2}$$

where I_0 is the intensity of incident light and I is the light intensity going through the sample.

Combining equations 1.2 and 1.1:

$$\ln(I/I_0) = -\epsilon l c \tag{1.3}$$

The three dimensional version of the Beer-Lambert Law, known as the Radiative Transfer equation is [74]:

$$\Omega(y,t) \cdot \nabla I(y,\Omega,t) = -\epsilon(y,t)I(y,\Omega,t) \tag{1.4}$$

Where Ω is the light direction and $\epsilon(y,t)$, defined as $\epsilon = \alpha c$, is the extinction field which characterizes the spatial depletion of the light intensity field and, it is related with the photochemistry of the photoactive molecule.

If the characteristics of the absorption remain constant during the exposure, and the

irradiation flux with intensity I_0 is normal to the flat exposed surface, then the light attenuation in x direction is:

$$I(x,t) = I_0 \exp(-\epsilon x) \tag{1.5}$$

1.4.2 Photochemical kinetics of Azo-polymers

Since the discovery of the photomechanical effect, there have been several studies that model the phenomena. The most studied materials are the azo-polymers [32, 35, 75–79]. When irradiated with UV, photons react with photoactive molecules as they traverse the material thickness in the y direction, changing from *trans* to *cis* form. Part of the *cis* isomers change back to *trans* isomers due to thermal effect.

The *cis* population is a function of space and time $\mathcal{P}(y,t)$. Assuming the quantum yield and absorption are not dependent of the degree of transformation and the UV light is unpolarized, the photoinduced *cis* transformation rate can be define as:

$$\frac{\partial \mathcal{P}(y,t)}{\partial t} = k_{ph}(1 - \mathcal{P}(y,t))\nabla \cdot I(y,t) - k_{th}^{-1}\mathcal{P}(y,t) \tag{1.6}$$

where $\mathcal{P}$ is the *cis* fraction of molecules transformed by light, $I(y,t)$ is the local light intensity, k_{ph} is the absorption constant and k_{th} is a constant linked to reverse thermal transformation, defined as: $k_{th} = T_0 \exp \Delta/k_B T$, with T_0, Δ positive constants, and k_B the Boltzmann constant.

The solution of the equation 1.6, adding 1.5, is:

$$\mathcal{P} = \mathcal{P}_0(y)[1 - \exp(-t[k_{th} + k_{ph}\exp(-\epsilon y)])] \tag{1.7}$$

$$\mathcal{P}_0(y) = \frac{k_{ph}\exp(-\epsilon y)}{k_{th} + k_{ph}\exp(-\epsilon y)} \tag{1.8}$$

where $1/\epsilon$ is the characteristic penetration depth and $\mathcal{P}_0(y)$ is the stationary profile of the degree of transformation attainable within a characteristic time k_{th}^{-1} [53].

Effect of the reverse thermal reaction

Depending on the difference between the phototransformation and thermo-reverse reaction rates, the evolution of the concentration profile $\mathcal{P}(y,t)$ differs at the early stage and the late stage of the process. If the rate of the reverse thermal reaction is significantly lower than the rate of the direct phototransformation, complete transformation is nearly achieved on the surface of the crystal within time on the order of k_{th}^{-1}. When the thermal

reverse reaction is faster, at high temperatures, the growing exponential transformation $k_{ph}\exp(-\epsilon x)$ is conserved, but it is slowed down exponentially with time as:

$$\mathcal{P}(y,t) \approx \frac{k_{ph}}{k_{th}}\exp(-\epsilon y)[1 - \exp(-k_{th}t)] \tag{1.9}$$

In this case, the maximum degree of transformation can only reach a value equal to the ratio $\frac{k_{ph}}{k_{th}}$.

Light-induced stress-strain relation for azo-LCEs

The nematic-isotropic phase transition temperature T_{ni} can be lowered by the photoisomerization process that changes the configuration from *trans* to *cis*. The degree of reduction can be estimated by a proportional relation with $\mathcal{P}$, $T_{ni} = T_{ni}^0 - \beta\mathcal{P}$. β is a positive constant and T_{ni}^0 is the nematic–isotropic phase transition temperature without illumination. The stress-free deformation in corresponding to the isotropic phase can be calculated as $\lambda_{i \to n} = 1 + \alpha(T_{ni} - T)^\xi$, when $T < T_{ni}$. α and ξ are positive constants. While when $T \geq T_{ni}$, $\lambda_{i \to n} \equiv 1$.

The uniaxial stress-strain is [80]:

$$\sigma_{xx} = \mu\left[\left(\frac{\lambda}{\lambda_m}\right)^2 - \frac{\lambda_m}{\lambda}\right] \tag{1.10}$$

where μ is the shear modulus dependent on the temperature, *lambda* is the stretch in x direction and λ_m is the stress-free deformation. Being the unirradiated configuration the reference then:

$$\lambda_m(I) = \frac{\lambda_{i \to n}(T_{ni}(I), T)}{T_{ni}^0, T} \tag{1.11}$$

In the case of azobenzene-based materials, the thermal effect influences the photomechanical behavior because the *cis* photo-product is metastable, hence the light-induced stress-strain relation depends on the light intensity and the temperature.

1.4.3   Photokinetics of DTE

The DTE is a photo-active molecule that undergoes a change in its structure between two configurations: the closed ring form (CF) and the open ring form (OF). The CF, when irradiated with visible light (500-600 nm) changes to the OF configuration and

the backward reactions occur when the OF is irradiated with UV (300-400 nm) (fig. 1.6). Contrary to azobenzene, DTE transformation has no thermal back reaction and when the irradiation stops, the transformed molecules stay in the given configuration.
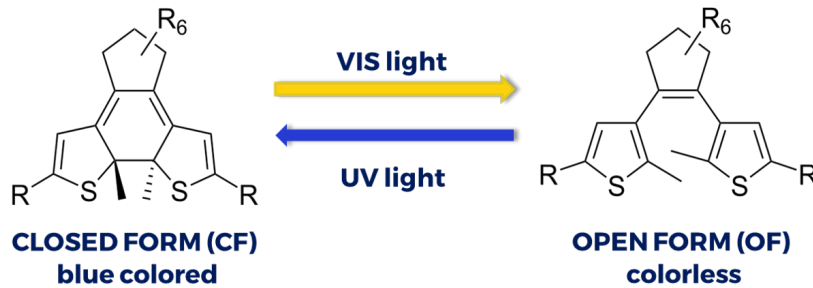
Figure 1.6: Photoswitch mechanism in DTE molecule

Pariani et al. [39] reported a kinetic model to describe the phototransformation of DTE species in solid state. The model is then applied to measure photochemical properties of DTE-polymer thin films like quantum yield.

When the thin film is irradiated, the molecular fractions of both configurations (χ_{OF} and χ_{CF}) are defined as:

$$\chi_{OF}(x,t) = N_{OF}(x,t)/N$$

$$\chi_{CF}(x,t) = N_{CF}(x,t)/N$$

where N is the number of total active molecules, N_{OF} and N_{CF} are the number of OF and CF form molecules, respectively. And, $\chi_{OF} + \chi_{CF} = 1$

The rate of conversion of the OF molecules follows the first-order kinetic rate proportional to the population of activated molecules:

$$\frac{d\chi_{OF}(y,t)}{dt} = -I(y,t) \cdot \epsilon_{OF} \cdot \Phi_{(OF-CF)} \cdot \chi_{OF}(y,t) \tag{1.12}$$

where ϵ_{OF}, with units (m^2/molecules), is the absorption cross section of species of the OF configuration and $\Phi_{(OF-CF)}$ is the quantum yield of the photoreaction, which can be defined as the efficiency of the molecule transformation from OF to CF:

$$\Phi_{(OF-CF)} = \frac{\text{photons absorbed}}{\text{molecules transformed}} = \frac{\sigma_{OF}(\lambda)}{\epsilon_{OF}(\lambda)} \tag{1.13}$$

here, $\sigma_{OF}(\lambda)$ is the interaction cross section for molecules in OF configuration that

absorb a photon and promotes the CF transformation and λ is the wavelength. The same definitions apply to $\epsilon_{CF}, \sigma_{CF}(\lambda), \Phi_{(CF-OF)}$ for the backward photoreaction.

The light penetration follows the Beer-Lambert law. The photon flux $I = I(y, t)$, given in photons/m$^2 \cdot$ s, is assumed uniform and equals $I(0, t) = I_0$ at the irradiated surface (fig. 1.7).
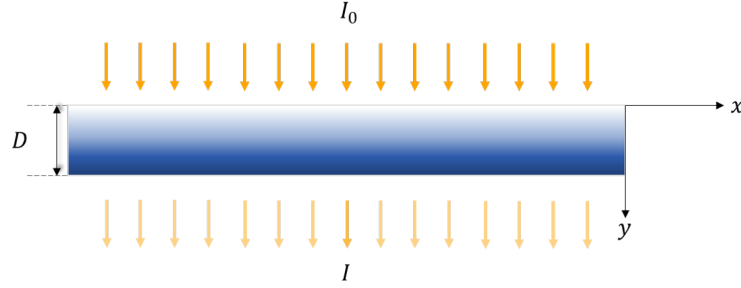
Figure 1.7: Photon flux across sample thickness D

The photon flux at any y position across thickness is the integral of the absorbance of the sample from the irradiated surface up to the point y through the thickness.

$$I(y, t) = I_0 \cdot \exp\left[-\int_0^y A(y', t)\, dy'\right] \tag{1.14}$$

Where A is the total absorbance in the sample, which is equal to the sum of the absorbance of each element in the thin film:

$$\begin{aligned}
A &= A_{CF} + A_{OF} + A_{matrix} \\
&= \epsilon_{CF}\chi_{CF}(y', t)C + \epsilon_{OF}[1 - \chi_{CF}(y', t)]C + \alpha_{matrix}
\end{aligned} \tag{1.15}$$

The concentration of active molecules C (molecules/m^3) can be determined by:

$$C = \frac{g\%\rho N_A}{M_{ph}}$$

where $g\%$ is the weight percentage of active molecules, ρ is the thin film's density and M_{ph} is the active molecules' molar mass in g/mol.

C is distributed uniformly throughout the thickness and at $t = 0$ the population fraction of CF molecules is $\chi_{CF}(z', 0) = 1$.
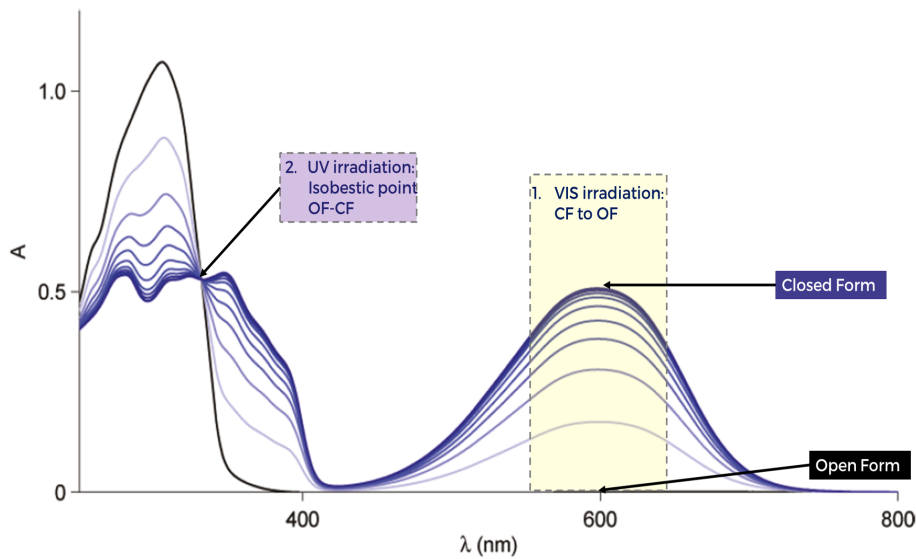
Figure 1.8: Example of DTE absorbance spectra [39]: (1) Under VIS irradiation only the CF configuration absorbs light and (2) under UV irradiation both configurations have the same absorption.

The explicit solution of equation 1.12 can be performed at two particular points [39] in the absorbance DTE spectra (fig. 1.8):

(1) In the VIS range (around 600 nm) the CF configuration of the DTE molecule is the only one contributing to the total absorption hence, the OF and the polymer matrix absorption can be neglected and,

(2) At the isobestic point (around 300 nm wavelength); under UV irradiation, the OF and CF absorption are equal, in this point, the polymer matrix absorption is non-zero. The total absorption is the sum of the absorbance of the CF portion and the polymer matrix.

For the case when the OF to CF transformation is triggered at wavelengths that do not correspond to that of the isobestic point and the two chromophore forms are absorbing light simultaneously and at different absorption coefficients, the solution of 1.12 is approximated by a parametrized statistical photoisomerization model [81].

CF-OF transformation (VIS irradiation)

During the VIS irradiation the CF population decreases. Each species of CF turns into OF and, at all times, the absorption of the OF molecules and the polymer matrix equals zero. The light penetration (eq. 1.14) along the sample thickness becomes:

$$I(y,t) = I_0 \cdot \exp\left[-\int_0^y \epsilon_{CF}\chi_{CF}(y',t)C\,dy'\right] \qquad (1.16)$$

Let $\epsilon_{CF} \cdot C = \alpha_{CF}$ be the absorption coefficient of the CF configuration, similarly, $\epsilon_{OF} \cdot C = \alpha_{OF}$ the absorption coefficient of the OF. The CF transformation rate becomes:

$$\frac{d\chi_{CF}(y,t)}{dt} = -I(y,t) \cdot \frac{\alpha_{CF}}{C} \cdot \Phi_{(CF-OF)} \cdot \chi_{CF}(x,t) \qquad (1.17)$$

The CF fraction is derived analytically from equation 1.17 in [82]:

$$\chi_{CF}(y,t) = \frac{1}{1 + e^{-\alpha_{CF}y} \cdot (e^{k_{vis}t} - 1)} \qquad (1.18)$$

Where $k_{vis} = I_0 \cdot \frac{\alpha_{CF}}{C} \cdot \Phi_{CF-OF}$ is CF to OF conversion rate.

OF-CF transformation (UV irradiation)

The other case occurs at the isobestic point (usually at wavelengths between 300 to 400 nm) where $\alpha_{CF} = \alpha_{OF} = \alpha_{UV}$, at which the photoactive molecules go from the open form to the closed form. At this state both of the forms absorb light with the same absorbance. The transformation is finite, getting up to 73% [81], a complete transformation is attainable if both sides of the film are irradiated. The Beer-Lambert law equation for CF is:

$$I(y,t) = I(y) = I_0 \cdot \exp\left[-\int_0^y (\alpha_{UV} + \alpha_{matrix})\,dy'\right]$$
$$= I_0 \cdot \exp\left[-(\alpha_{UV} + \alpha_{matrix})y\right] \qquad (1.19)$$

At the isobestic point the photon flux through the thickness becomes independent of time thus, equation 1.12 becomes:

$$\frac{d\chi_{OF}(y,t)}{dt} = I_0 \cdot \exp\left[(\alpha_{UV} + \alpha_{matrix})y\right] \cdot \frac{\alpha_{UV}}{C} \cdot \Phi_{(OF-CF)} \cdot \chi_{OF}(y,t)$$
$$= \exp\left[-(\alpha_{UV} + \alpha_{matrix})y\right] \cdot k_{uv} \cdot \chi_{OF}(y,t) \qquad (1.20)$$

Where $k_{uv} = I_0 \cdot \frac{\alpha_{UV}}{C} \cdot \Phi_{(OF-CF)}$. Then equation 1.20 can be solved by separation of variables:

$$\frac{d\chi_{OF}(y,t)}{\chi_{OF}(y,t)} = -f(y)dt \tag{1.21}$$

Solving equation 1.21 the fraction of OF molecules during UV irradiation is obtained:

$$\chi_{OF}(y,t) = \exp\left[-e^{-(\alpha_{UV}+\alpha_{matrix})y} \cdot k_{uv}\right] \tag{1.22}$$

1.4.4 Timoshenko's beam model: an aproach to light-induced bending

The Timoshenko's model describe the bending of a bi-metal beam submitted to uniform heating. If the metals constituting the beam have different thermal expansion coefficients, α_1 and α_2 respectively, the heating from an initial temperature T_0 to T will produce bending.

Assuming that the expansion coefficients remain constant during the heating process and the width is much smaller that the length, the curvature of the strip is obtained by [83]:

$$\frac{1}{R} = \frac{6(\alpha_2 - \alpha_1)(T-T_0)(1+m)^2}{h(3(1+m)^2 + (1+mn)(m^2 + \frac{1}{mn}))} \tag{1.23}$$

where $m = \alpha_1/\alpha_2$, $n = E_1/E_2$ and h is the beam thickness.
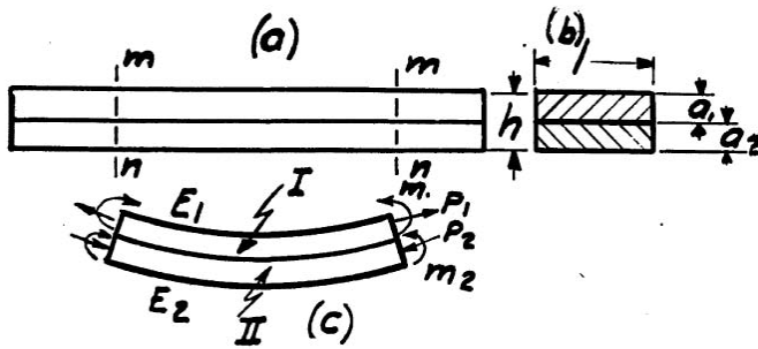
Figure 1.9: Deflection of a bi-metal strip while uniformly heated: the beam is composed by two different metal types with different thermal expansion coefficients (α_1, α_2) and different Young moduli (E_1, E_2), when heated, the expansion in II is larger than I which induces bending [83].

Equation 1.23 can describe the light-induced bending caused by the transformation gradient along the thickness direction. For DTE light-induced bending, Kitagawa
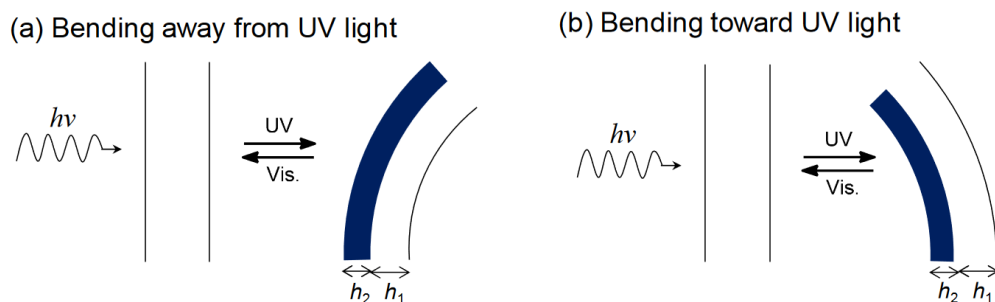
Figure 1.10: Illustration of Timoshenko's bimetal model in the case of (**a**) bending away and (**b**) towards UV light.

[84] explains the curvature in terms of closed-form chromophore concentration in the sample. Similar to figure 1.9, in figure 1.10 we have a DTE sample bending under UV light irradiation, it either bends towards or away from the light source depending on the expansion coefficient α and the thickness h_2, determined by the closed-form concentration. The curvature based on Timoshenko's simplified bi-metal model is:

$$\frac{1}{R} = \frac{\alpha_2 - \alpha_1}{h_2} \frac{6mn(1+m)}{1 + 4mn + 6m^2n + 4m^3n + m^4n^2} \tag{1.24}$$

Similar to 1.23 $m = h_1/h_2$ and $n = E_1/E_2$ (Young Moduli ratio), R is the curvature radius, h_2 and h_1 are the layer thickness and, α_1 and α_2 are the actuation strains. Actuation strain is the coefficient of expansion or contraction of the first layer under UV irradiation. In the non-photoreacted layer, the value of actuation strain α_1 is always zero because the layer cannot expand or contract.

When the sample bends away from UV light, the value of α_2 is the coefficient of expansion. In contrast, α_2 is the coefficient of contraction when the crystal bends toward UV light. Moreover, the assumption that the Young's modulus E_1 is the same as E_2 is introduced because only a few percentage of diarylethene molecules in the crystal are converted from the open-ring isomer to the closed-ring isomer in the initial stage of the bending. As a result, the Timoshenko's equation becomes:

$$\frac{1}{R} = \frac{\alpha_2}{h_2} \frac{6m(1+m)}{1 + 4m + 6m^2 + 4m^3 + m^4} \tag{1.25}$$

In this model, h_2 plays an important role to dictate the extent of the bending reaction: when h_2 is very small relative to the crystal thickness, the crystal cannot bend to a signif-

icant extent. However, the crystal can bend to a large extent when h_2 is approximately half of the crystal thickness.

The value of h_2 depends on the absorption and the penetration length of the light source, when irradiated with 365 nm light, photoisomerization of diarylethene molecules occurs only at the crystal surface because of the high absorbance at this wavelength. This means that, h_2 is very small relative to the crystal thickness and the conversion of the photoreacted layer increases quickly. Therefore, bending toward the incident light occurs immediately (fig. 1.11b).
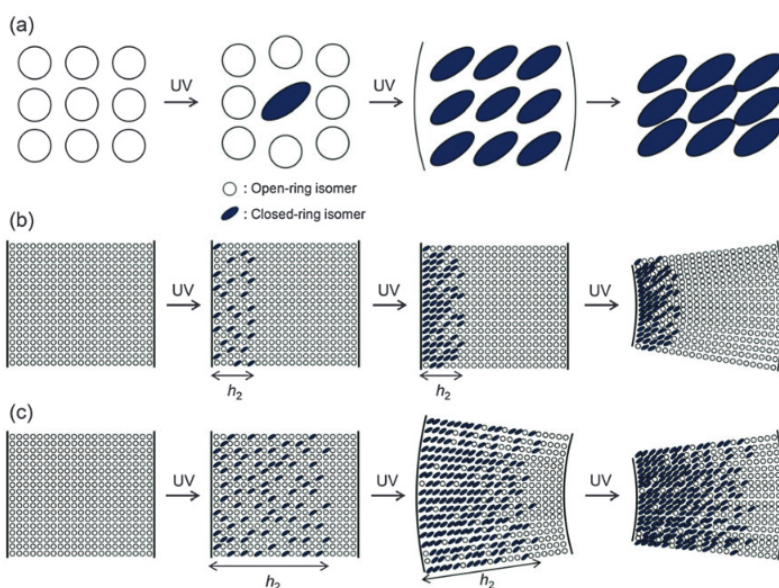
Figure 1.11: Schematic illustration of photo-induced bending on DTE materials. (**a**) Photoisomerization of DTE from open-form to closed-form, (**b**) bending when high absorption is present and, (**c**) bending model when low absorption and deep light penetration

Upon irradiation with visible light, photocycloreversion from the closed-ring isomer to the open-ring isomer occurs simultaneously in the photoreacted layer because h_2 is very small. Therefore, the bent crystal returns to the original straight shape through the same trajectory of bending. In contrast, when irradiated with 380 nm light, photoisomerization of diarylethene molecules can occur deeply within the crystal because diarylethene has a low absorption at 380 nm compared with that at 365 nm. This means that h_2 is close to the crystal thickness and conversion of the photoreacted layer proceeds slowly. Therefore, initial bending away from the light source can be observed clearly

and subsequent bending toward the incident light occurs slowly (fig. 1.11c) [28].

1.4.5   Linear beam model approach for beam-like azobenzene-based materials

Another methodology to describe the light-induced bending of photomechanical beam-like materials couples the linear beam theory and the photoactive unit photochemistry. In figure 1.12 a cantilever bends by light stimulus. The photo-induced strain (ε_{ph}) is assumed to be proportional to the chromophore population n_c converted by light absorption [85]:

$$\varepsilon_{ph} = -\mathcal{A}n_c(x) \tag{1.26}$$

with $\mathcal{A}$ as a proportionality constant.

And the effective strain is:

$$\varepsilon(x) = \frac{x}{R} + K - \varepsilon_{ph}(x) \tag{1.27}$$

Where R is the radius of curvature and K is a material constant determined for a given thickness w and illumination intensity.
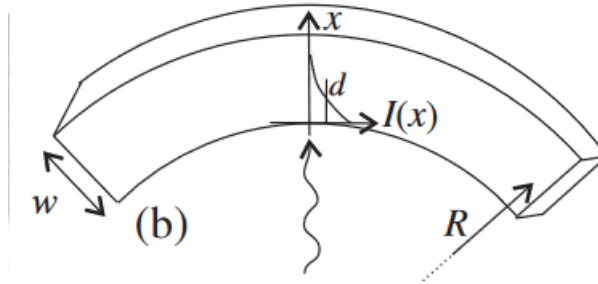
Figure 1.12: Photo-radiation penetration with linear absorption length d giving light-induced bend [85]

The stress at x direction in the beam equals the modulus times the strain: $\sigma_x = E\epsilon(x)$. To obtain the forces and torque we integrate the stress and the moment through the thickness w. Without external forces, the mechanical equilibrium is then, expressed as:

$$\int_0^w \left[\frac{x}{R} + K - \epsilon_p\right]dx = 0 \tag{1.28}$$

$$\int_0^w \left[\frac{x}{R} + K - \epsilon_p\right]xdx = 0 \tag{1.29}$$

From equations 1.29 and, substituting 1.26, the curvature radius is obtained in terms of the chromophore population:

$$\frac{w}{R} = \frac{12\mathcal{A}}{w^2} \int_0^w \left(\frac{w}{2} - x\right) n_c(x) dx \qquad (1.30)$$

Equation 1.30 can be solved for azo-polymers in a photo-stationary profile to obtain an equation analogous to 1.23 [86].

1.4.6 Simulation and Modelling of light-induced deformation

To explain the macroscopic effect of the photomechanical process, it is necessary to connect the photochemistry and the mechanical deformation. Recently, there have been several proposed models to link the photochemistry of photoswitches and solid polymer mechanics to build a constitutive model of the photomechanical effect, mainly for PMC materials and azobenzene doped LCEs. In this section we will explore some of those proposed models.

PMC Materials

A proposed constitutive model for PNR and PMC materials (figures 1.1a and 1.1b) by Long [31], describes the phototransformation profile as a function of space and time $C(y,t)$. As mentioned in section 1.1, light irradiation promotes a new cross-linked network in these kind of materials. The photomechanically altered network is assumed to be stress free in the configuration in which it is formed and it references an intermediate configuration dependent in the photoirradiation time. In figure 1.13, the body is deformed from its initial configuration through the motion characterized by the deformation gradient ($\mathbf{F}$) and the left Cauchy–Green deformation tensor ($\mathbf{B}$):

$$F_1 = \frac{\partial \mathbf{y}}{\partial \mathbf{x}} \qquad (1.31)$$

$$\mathbf{B_1} = \mathbf{F}_1 \mathbf{F}_1^T \qquad (1.32)$$

where $\mathbf{F}^T{}_1$ is the transpose of the deformation gradient.

When the light is switched off and the mechanical constraints are released, the body deforms again from the intermediate to the current configuration as described by the deformation gradient:

$$F_2 = \frac{\partial \mathbf{z}}{\partial \mathbf{y}} \tag{1.33}$$

$$\mathbf{B}_2 = \mathbf{F}_2 \mathbf{F}_2^T \tag{1.34}$$

Due to the parallel nature of the network decomposition, the total stress $\mathbf{T}_{total}$ at a material point is the sum of the stresses in each network:

$$\mathbf{T}_{total} = f_{original} \mathbf{T}_1 + f_{new} \mathbf{T}_2 \tag{1.35}$$

The volume fractions of the original $f_{original}$ and reformed networks f_{new} are expressed in terms of the phototransformation function $C(y, t)$:

$$\frac{d f_{original}}{dt} = -k_1 C(y, t) f_{original}^p$$

$$f_{original} + f_{new} = 1$$

$$f_{original}(t = 0) = 1, f_{new}(t = 0) = 0$$

And to represent the Cauchy stress, they used the hyperelastic Arruda-Boyce model:

$$\mathbf{T}_i = \frac{\mu_r}{3} \frac{\sqrt{N}}{\lambda_{chain}^{(i)}} \mathscr{L}^{-1} \left[\lambda_{chain}^{(i)} / \sqrt{N} \right] \mathbf{B}_i - p\mathbf{I} \tag{1.36}$$

with $\mathscr{L}^{-1}[\beta] = \coth[\beta] - \frac{1}{\beta}$, the inverse Langevin function. μ_r is the initial shear modulus, and N is the locking stretch of the chain. The stretch of each chain in the network relates to the first invariant of $\mathbf{B}_i$ through $\lambda_{chain}^{(i)} = \sqrt{I_1^{(i)}/3}$.

The rule of mixtures (eq.1.35) was implemented in Finite Element Analysis (FEA) software. In particular, the general framework is solved incrementally in time with the following sequence of steps per increment: the photo-chemical field equations are implemented in COMSOL MULTIPHYSICS, then passed to ABAQUS, which solves for the photomechanical coupling and the mechanical response via a user material subroutine. The current geometry (mesh) is exported from ABAQUS to COMSOL, and the cycle repeats with the next time increment. Experimental and simulated
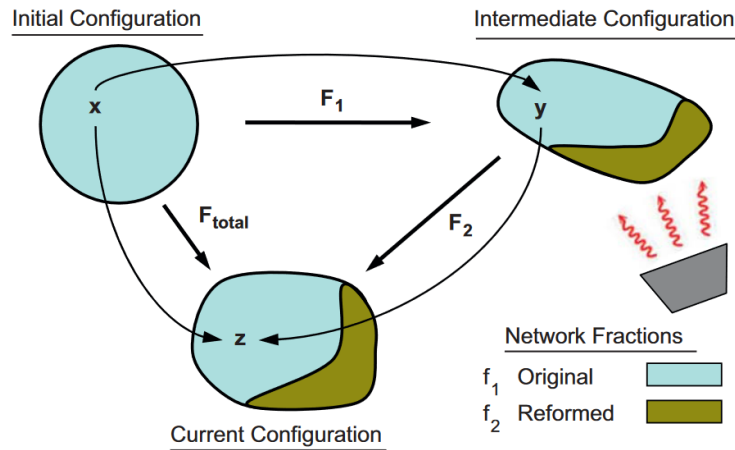
Figure 1.13: Deformation decomposition. In the experimental protocols described, the sample, originally at **x**, is deformed to and held at an intermediate configuration, **y**. In this intermediate configuration, it is irradiated. After mechanical constraints are released, the sample deforms to the current configuration, **z**. [31]

stress-relaxation tests were compared thus, validating the proposed model. In Hamel's work [33], thy solved this framework by using an Abaqus user element (UEL), the weak forms of the radiative transfer and balance of linear momentum were discretized and approximated using linear two- and three-dimensional isoparametric elements, and the overall system solved implicitly with a Newton method (fig. 1.14).

Ma [34], following Long's model and, based on the observation that stress relaxation due to light irradiation is a time-dependent process, similar to that in viscoelastic solids with an irrecoverable deformation after light irradiation, implemented a photo-viscous element. v^{ph} in figure 1.15.

The creep law equation of the photo-viscous element is a function of the light-induced crosslinking. This model was implemented in FEA software, validating that the model accurately captures the response of PNR photomechanical materials under a wide range of coupled photo-mechanical loading conditions, such as light induced stress relaxation, creep in tension and bending (fig. 1.16).

Azobenzene doped Materials

Regarding azobenzene-doped LCP, Corbett and Warner [75, 85–89] did an extensive work to build a model that describes the bending behavior of LCPs considering the
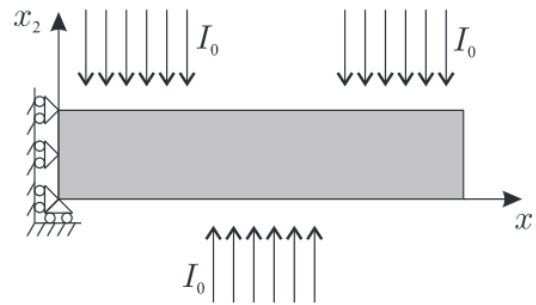
(a) Geometrical and photo-mechanical boundary conditions.
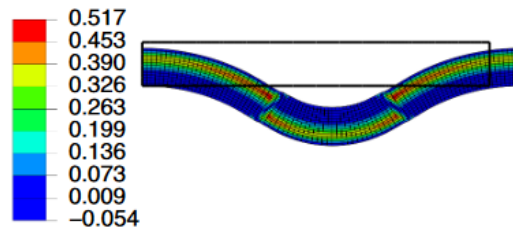
(b) after 400 s of irradiation at 200 nm wavelength during the cleavage reaction.

Figure 1.14: Contours of the volume fractions f. Results from the Abaqus FEA using UEL proposed by Hamel [33].
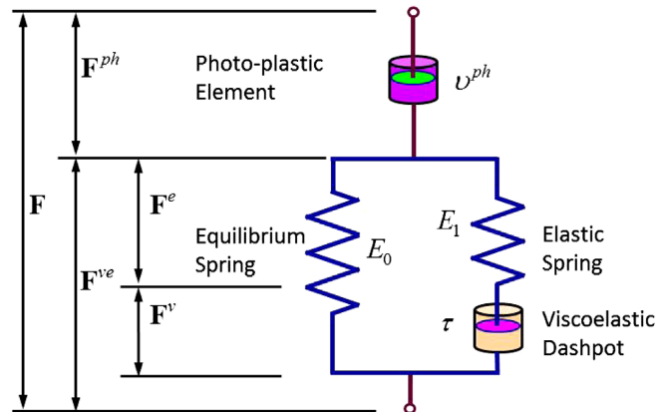
Figure 1.15: Rheological scheme of a PNR material, representing the photoactive response as a viscous element v^{ph} [34]
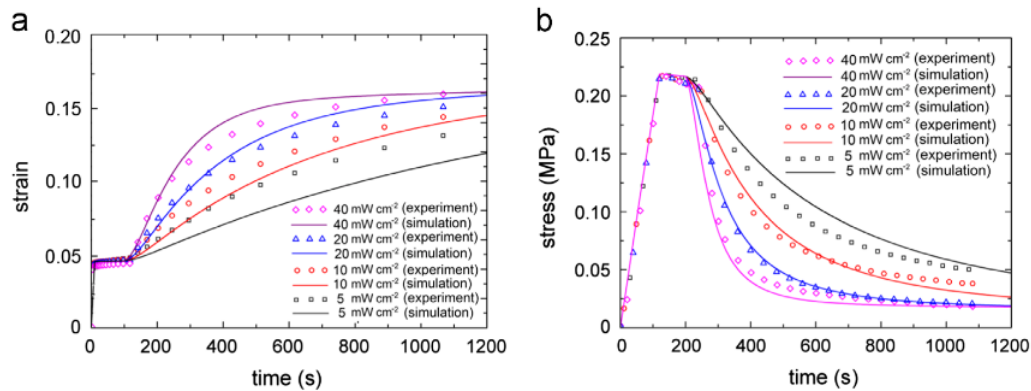
Figure 1.16: Comparison of experimental results and model simulations for (a) creep and (b) light irradiation induced stress relaxation [34].

anisotropic behavior that arises from the nematic order of LCPs when cooled [90]. The models were based on the Timoshenko bi-metal beam model (section 1.4.4).

Dunn [32], developed stress-strain relations considering the photostrains generated when the light is absorbed by the material and the *cis-trans* process occurs. The strains in the material depend on the orientation of the azo-polymer and on the light polarization. The constitutive model is analytically solved by the Finite Element (FE) numerical method predicting a saddle-like bending on azo-LCPs plates (fig. 1.17), similar results were observed on experimental work.

Oates et al. have done also a broad study on the modelling of azo-polymers [35–37].
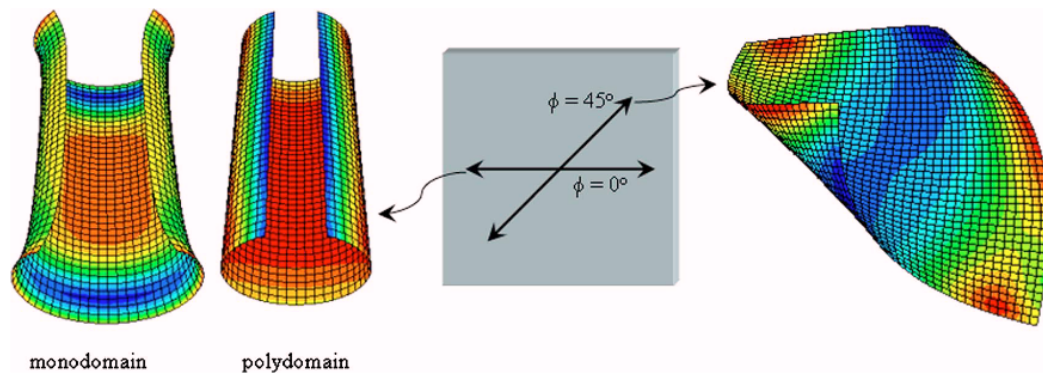
Figure 1.17: Saddle-like bending on azo-LCPs plates with different polarization directions ϕ

Here, a modeling framework is introduced beginning with the governing equations for a liquid crystal glassy polymer network which includes: mechanical equilibrium, viscoelasticity and a liquid crystal director force balance [91]. The constitutive model is solved in MATLAB and then compared to blocked stress experiments (creep tests) (fig. 1.18a). The experiment consisted on tensing the LCP sample and induced stress by light irradiations cycles (fig. 1.18b).

The jumping effect of azo-LCN monoliths is analyzed and implemented in the FEA software Abaqus by modeling the material as a two layer composite shell. Each layer has the same stiffness according to the stacking direction, but the photo-strain is different. Finally, the model for the jumping simulation of the azo-LCN monolith consists of a reference plane and an azo-LCN monolith comprising two composites separated by a certain height from the reference plane (fig. 1.19) [38].

In their work Halabi et. al. [92] explore the performance of molecular crystals in conversion light to work. In their experiments they calculated the force exerted by an azobenzene crystal when bending and they determined the maximum displacement and effective Young modulus using the Stoney equation. Using the Ansys static structural model, the partially isomerized single crystal was then modeled as a *trans–cis* bilayer micro-cantilever and the photogenerated *cis* layer as a homogeneous thin film of varying thickness. The photoinduced strain was replicated through thermal strain induced by a temperature change in the thin-film layer only. By varying the strain and the thickness of the thin film representing the isomerized cis layer affects the total displacement of the modeled crystal (fig. 1.20).

(a)

(b)

(c)
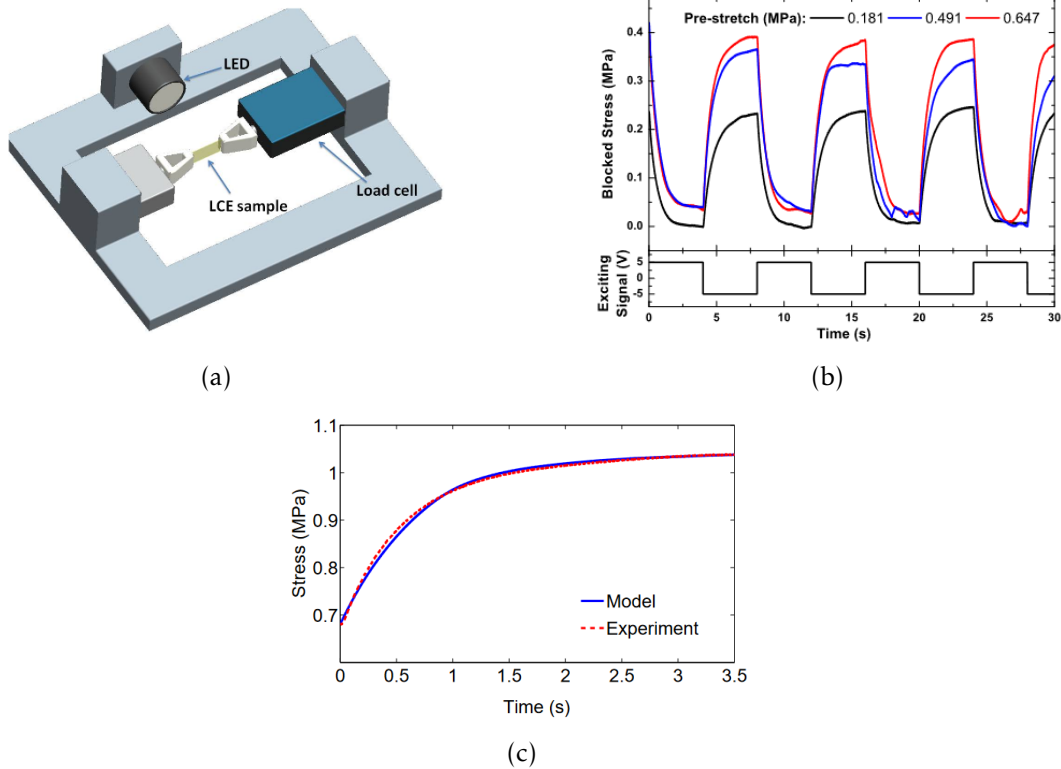
Figure 1.18: Results from the constitutive model proposed by Oates [91]: (a) A schematic of the experimental setup used to measure blocked stresses of the liquid crystal networked that are stimulated by light. (b) Light induced blocked stresses vs. time for different pre-loads. LED on when signal is -5 V and off when the signal is 5 V. (c) Comparison of the time-dependent blocked stress under continuous LED exposure to the photomechanical liquid crystal network model.
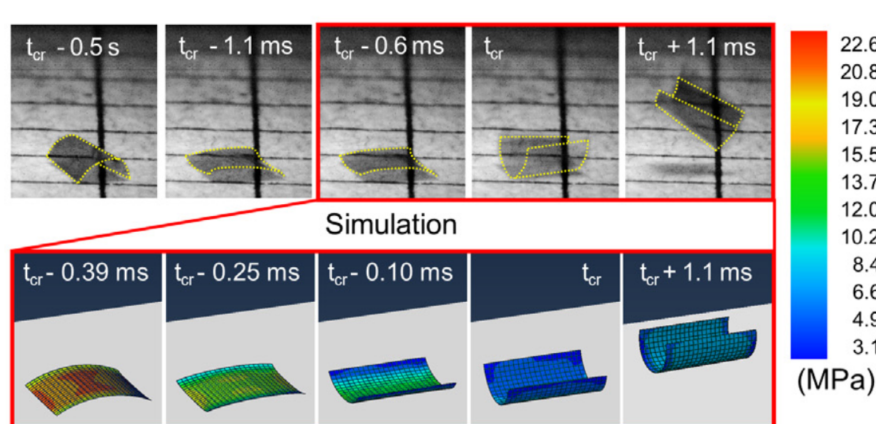
Figure 1.19: Comparison of experimental jumping results (top) with FEM simulation (bottom) via snap-through; film dimension: 2 mm x 2 mm [38].
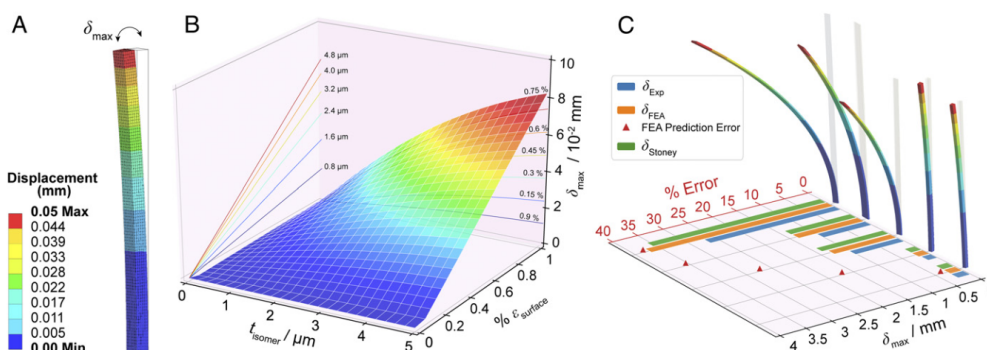
Figure 1.20: Finite element analysis (FEA) of the bending of a single azobenzene crystal. (A) Ansys-simulated and meshed model crystal color-coded by displacement from the initial position. (B) A 3D surface plot of the change in maximum displacement with respect to the depth of the isomerization and the surface strain of the model crystal. (C) The accuracy of the numerically solved model in predicting the maximum displacement of five different azobenzene single crystals. [92]

1.5 Conclusion

In this first chapter, we revisited the photomechanical materials research work done over the last decades, which has made significant progress to fully exploit the abundant natural resource that light provide us. Researchers have used azobenzenes in several technological applications, especially in the smart materials field, to design chemical sensors [3], light-responsive biomaterials [93], data storage [94], photochromic coatings, to cite some examples. Consequently, in the literature there is a vast information about both photochemical and photomechanical constitutive models for azo-polymers (section 1.4.6).

On the other hand, diarylethenes are promising photoactive molecules that are thermally stable, unlike azobenzenes. DTE crystals can deform under light irradiation, mainly expanding, contracting, twisting, and bending, leading to the development of new DTE-based materials with numerous technological applications similar to azo-materials.

Although their developement begun in the early 2000s, there is relatively little work reported concernig the photomechanical modeling of DTE-based materials. In the next chapters we will analyze the photomechanical behavior of DTE-based thin films experimentally and analytically, including the mechanical characterization. By exploring in detail the phototokinetic model that accurately predicts the OF and CF population dynamics (section 1.4.3) and based in previous photomechanical coupling proposed models, a first photomechanical modeling for DTE-based thin films is proposed.

Mechanical models and characterization methods

2.1 Mechanics of solid polymers

Polymers are materials that are formed by large molecules (macromolecules) composed of units linked by covalent bonds, called monomers. These monomers form large chain-like structures. The different macromolecules (polymeric chains) can be arranged into a network structure by crosslinks or entanglements, and they interact by weak van der Waals forces. The weak bonding between these chains gives interesting mechanical properties to polymer materials, which will be detailed in this section.

2.1.1 Linear viscoelasticity and rheological models for viscoelastic materials

Linear viscoelastic theory describes the relation between stress, strain and time, with mathematical simplicity. Most of the mathematical expressions are in shear or tensile form, where the deformation is small enough to ensure that the Young's modulus and the stress-strain rate ratio are independent from the strain.

A viscoelastic material can be modelled by a combination of springs and dashpots link together in parallel or/and in series. The spring represents the elastic part and it follows the Hooke's Law $\sigma_s = E\varepsilon_s$ (fig. 2.1). The dashpot is the representation of the viscous behavior, whose response is strain-rate proportional $\sigma_v/\dot{\varepsilon}_v = \eta$ (fig. 2.2):
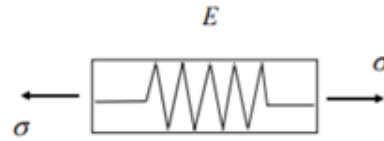
Figure 2.1: Elastic part represented by a spring
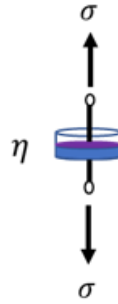
Figure 2.2: Viscous part represented by a dashpot

Maxwell Model

This model is commonly used to represent the behavior of a viscoelastic fluid. It consists of two elements, a dashpot and a spring in series (Fig.2.3). The constitutive relation is built as follows:
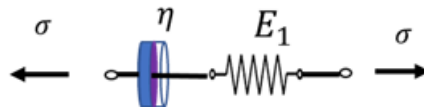
Figure 2.3: Maxwell rheological model

Both mechanical elements strain response occurs at different rates, this leads to the total strain being the combination of the dashpot strain and the spring strain:

$$\varepsilon_{total} = \varepsilon_v + \varepsilon_s$$

Differentiating the equation:

$$\dot{\varepsilon}_{total} = \dot{\varepsilon}_v + \dot{\varepsilon}_s \tag{2.1}$$

$$\dot{\varepsilon} = \frac{\sigma_v}{\eta} + \frac{\dot{\sigma}_s}{E} \tag{2.2}$$

For equilibrium, the total stress is equal to the sum of the dashpot and in the spring stresses:

$$\sigma = \sigma_v = \sigma_s$$

substituting in 2.2:

$$\dot{\varepsilon} = \frac{\sigma}{\eta} + \frac{\dot{\sigma}}{E}$$

$$\dot{\sigma} + \frac{E}{\eta}\sigma = E\dot{\varepsilon} \tag{2.3}$$

Kevin-Voigt Model

In this other two-element model the dashpot and the spring are in parallel (fig. 2.4). The strain experienced by the spring is the same as that experienced by the dash-pot. This time, the constitutive equation results in:

$$\sigma = \sigma_v + \sigma_s$$

$$\sigma = \eta\dot{\varepsilon} + E\varepsilon \tag{2.4}$$
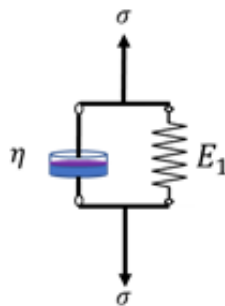
Figure 2.4: Kevin-Voigt rheological model

Standard Linear Solid (SLS) Models

When combined, the Maxwell and Kevin-Voigt models are the simplest and most efficient models to represent viscoelastic behavior. To represent a Standard Linear Solid (SLS), three elements are used: two springs and one dashpot (fig. 2.5 a and b). To represent viscous materials more elements could be added (fig. 2.5 c and d). Their respectively constitutive equations are displayed in figure 2.6.
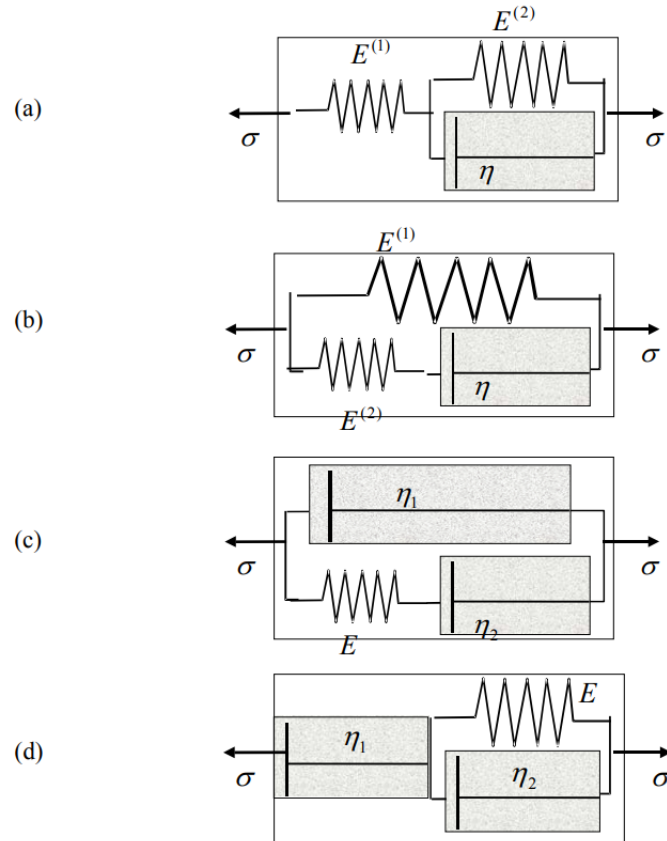
Figure 2.5: Three-elements model: (a) Standard Solid I, (b) Standard Solid II, (c) Standard fluid I, (d) Standard Fluid II [95]

$$\text{(a)} \qquad \sigma + \frac{\eta}{E_1 + E_2}\dot{\sigma} = \frac{E_1 E_2}{E_1 + E_2}\varepsilon + \frac{\eta E_1}{E_1 + E_2}\dot{\varepsilon}$$

$$\text{(b)} \qquad \sigma + \frac{\eta}{E_2}\dot{\sigma} = E_1\varepsilon + \frac{\eta(E_1 + E_2)}{E_2}\dot{\varepsilon}$$

$$\text{(c)} \qquad \sigma + \frac{\eta_2}{E}\dot{\sigma} = (\eta_1 + \eta_2)\dot{\varepsilon} + \frac{\eta_1\eta_2}{E}\ddot{\varepsilon}$$

$$\text{(d)} \qquad \sigma + \frac{\eta_1 + \eta_2}{E}\dot{\sigma} = \eta_1\dot{\varepsilon} + \frac{\eta_1\eta_2}{E}\ddot{\varepsilon}$$

Figure 2.6: Constitutive equations of SLS Models

2.1.2 Mechanical characterization of polymers

There are different experimental techniques to characterize the mechanical behavior of polymers. The most commonly performed is the uniaxial tension or compression

test, using grips for tension tests, and plates for compression tests. This kind of test consists of applying a uniaxial force to the specimen at a controlled and constant speed. An extensometer or strain gauge measures the specimen deformation. The result is the stress-strain curve, which gives some information about the material, although it does not consider the time-dependent behavior and neither the effect of multi-axiality.

To examine the history-dependent behavior, the specimen must undergo another type of mechanical testing like stress relaxation, creep, dynamic mechanical analysis (DMA), or fatigue tests.

Uniaxial tension and compression

The stress-strain test is probably the most widely used technique for the determination of mechanical properties. From the stress-strain (σ-ε) behavior in figure 2.7, four important material qualities can be derived [96]:

- The Young's modulus(E). Characterizes the resistance of the material to low strain deformation ($< 1\%$). It is the value of the slope of the elastic or linear region of the curve.

- The yield strength (σ_y). Is the limit of the elastic behavior, the point at which the plastic deformation begins.

- The tensile strength (σ_b). The maximum stress value.

- The ultimate elongation (ε_b). It is the maximum strain that a material can withstand before rupture.

Moreover, the stress-strain curve could indicate which type of polymer the specimen is in terms of elasticity and brittleness. Figure 2.8 displays different plots of polymeric materials, ranging from tough-brittle, showing limited strain with applied stress, to rubbery materials with substantial elongation with applied stress.

Stress relaxation

Suppose a polymer specimen is strained to a fixed value and maintained for a period of time. The polymeric chains experience physical changes such as, realignment of the elastomer strands under strain, reconfiguration of chain entanglements and chain end movement. It also involves breakdown and rearrangement of bonds by virtue of secondary valence forces between the polymer and filler materials. Macroscopically, the material exhibits a stress decrease during this process, reaching an equilibrium stress
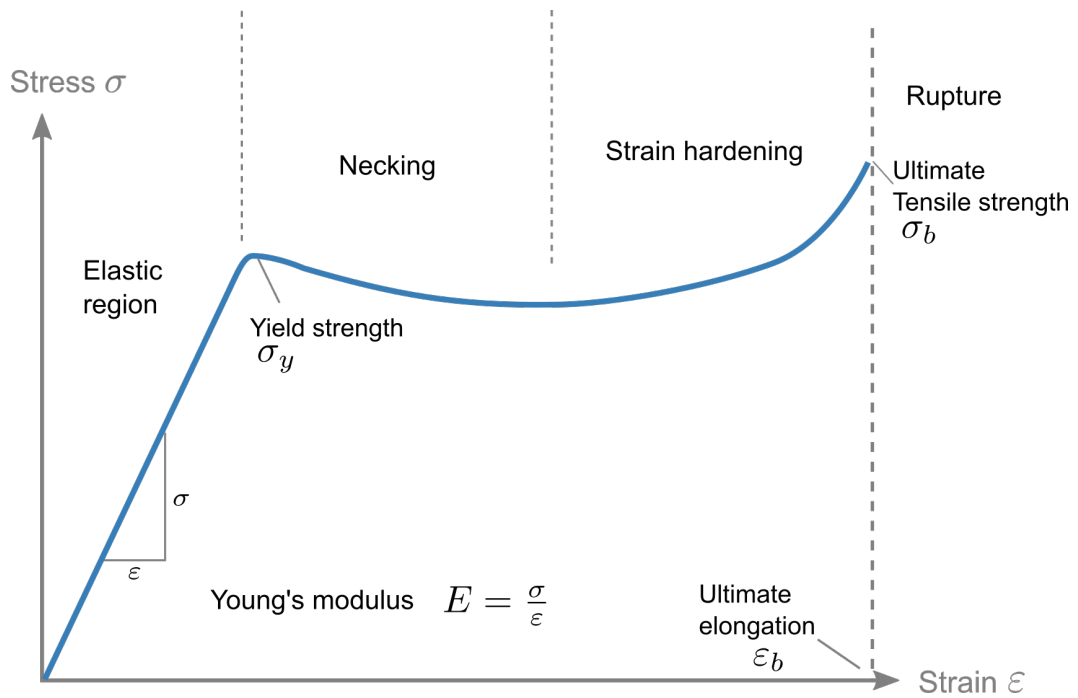
Figure 2.7: Typical strain-stress curve of a polymer
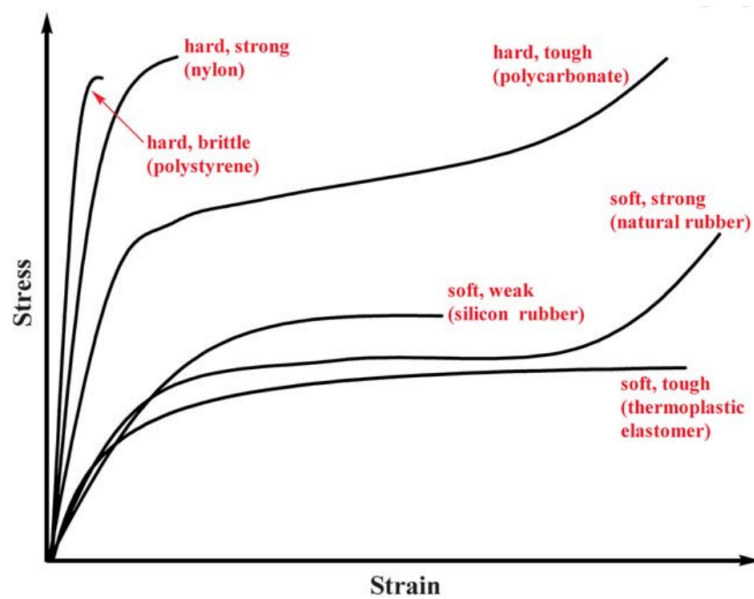
Figure 2.8: Stress-strain curves of various polymeric materials [97]

value. This gradual decrease of stress when the material is held at constant strain is

called *stress relaxation*.

If we suppose the strain input to be a Heaviside step function ($\mathcal{H}(t)$) of magnitude ε_0:

$$\varepsilon(t) = \varepsilon_0 \mathcal{H}(t)$$

the stress $\sigma(t)$ in a viscoelastic material will decrease until attaining a plateau and recover as the strain is suppressed.

The ratio:

$$E(t) = \frac{\sigma(t)}{\varepsilon_0} \tag{2.5}$$

is the relaxation modulus, which for linear materials, maintains its dependence on time and not on the strain level. The symbol E is used for uniaxial tension and compression.

If we apply this test to a classic elastic material, the stress response will not decrease over time and will be zero when the strain is suppressed. A viscous material under the same conditions will "flow", reaching a zero value of stress ultimately (fig. 2.9).
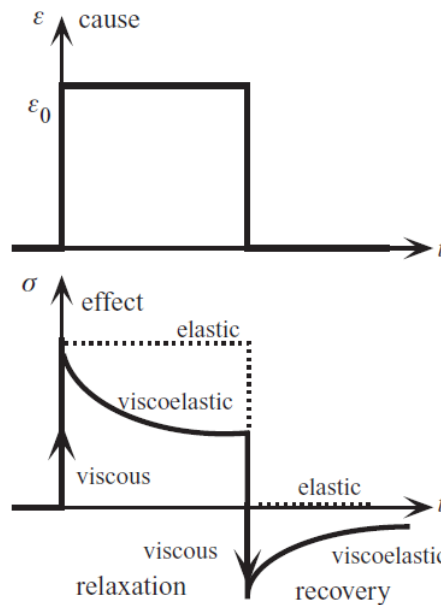
Figure 2.9: Stress relaxation and recovery when a strain [98]

Creep

If instead of a constant strain, the polymer specimen is subjected to a constant stress it will progressively deform. A common creep behavior displays four stages: primary, where the *creep* occurs next, secondary, proceeds at a nearly constant strain, and tertiary, the strain increases abruptly leading to a very probable fracture (fracture by creep).

Typical Creep Curves
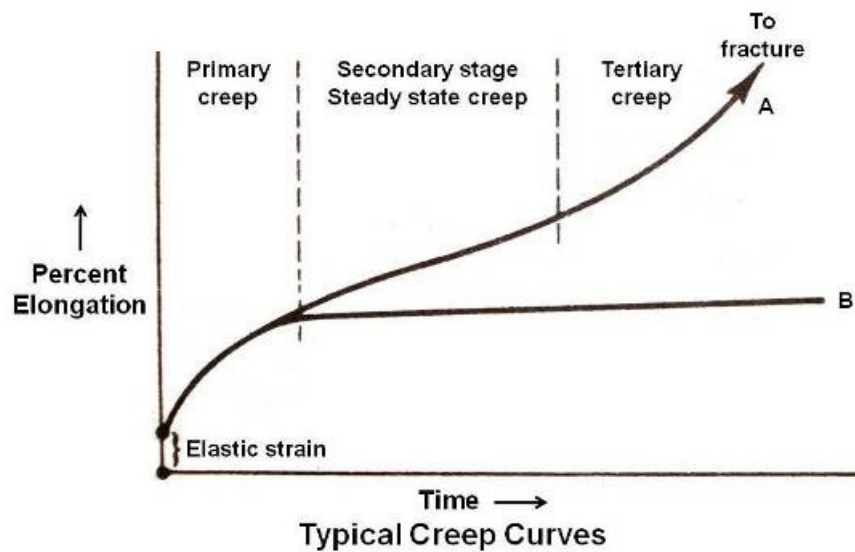
Figure 2.10: Creep curve stages: At high stresses the material arrives at a tertiary stage where the fracture occurs. In some cases, at low stresses, the secondary stage may extend for a relative long time [99]

Polymeric materials are often subjected to creep-recovery test, where the load is released at the secondary stage ant the specimen undergoes a recovery stage (fig.2.11). In this case the stress input is a Heaviside step function, similar to the stress relaxation test,

$$\sigma(t) = \sigma_0 \mathcal{H}(t)$$

and the ratio:

$$J(t) = \frac{\varepsilon(t)}{\sigma_0} \tag{2.6}$$

is the creep compliance.
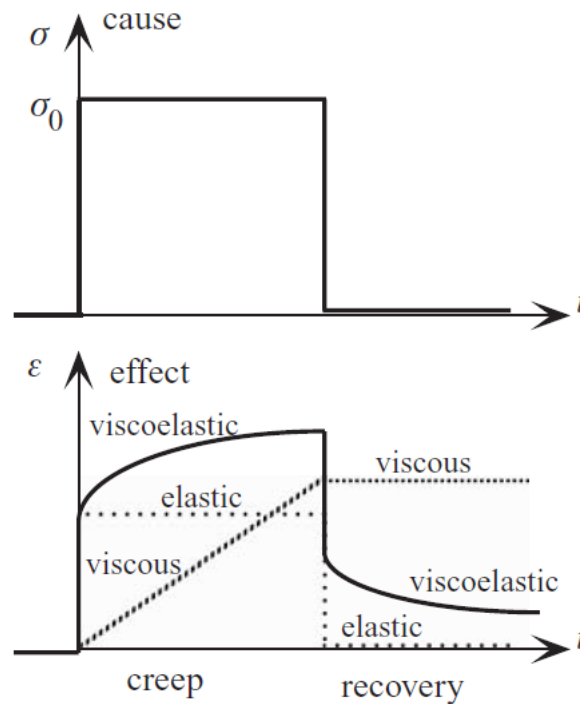
Figure 2.11: Creep-recovery tests

Dynamic Mechanical Analysis (DMA)

A practical way to visualize viscoelastic behavior is to subject a viscoelastic material to a cyclic force. The viscoelastic material's response signal will be out of phase regarding to the input signal and the gap or shift angle δ range value will be between $0°$ and $90°$. DMA is a useful technique for characterizing a viscoelastic material at small stress-strain ranges. It measures the stiffness and the viscous damping properties under cyclic loading, either at different temperatures or at different frequencies.

Considering a harmonic stress input in figure 2.12, with load that varies sinusoidally with time:

$$\sigma(t) = \sigma_0 \sin(\omega t)$$

The strain response could be expressed as:

$$\varepsilon(t) = \varepsilon_0 \sin(\omega t - \delta)$$

where, as discussed above, δ is the phase shift angle and is related with the time
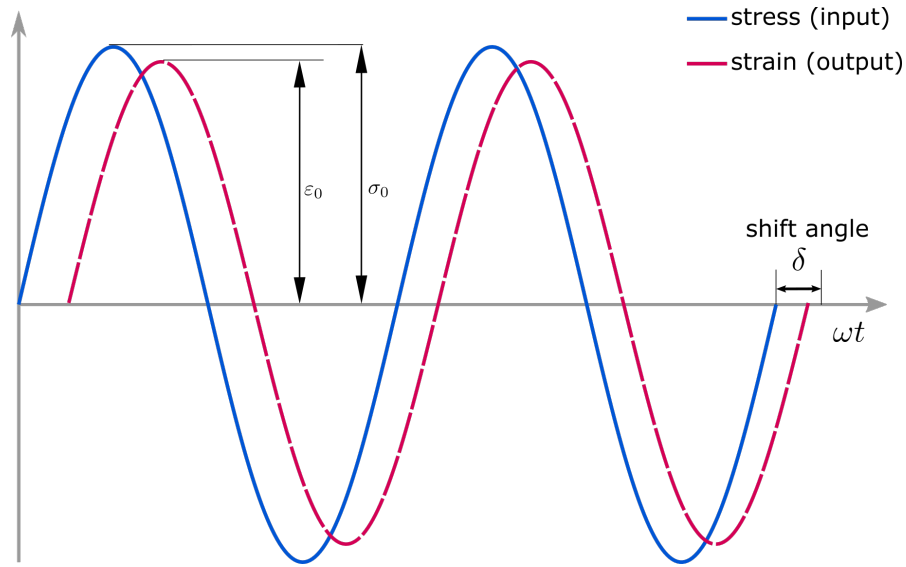
Figure 2.12: Cyclic loading response of a viscoelastic material

difference between the input and output signal by $\delta = \omega \Delta t$ and, ω is angular frequency $\omega = 2\pi f$. Due to this stress-strain phase gap, the dynamic stiffness is defined as a complex number:

$$E^* = E' + iE'' \tag{2.7}$$

where:

$$E' = \frac{\sigma_0}{\varepsilon_0} \cos(\delta) \tag{2.8}$$

$$E'' = \frac{\sigma_0}{\varepsilon_0} \sin(\delta) \tag{2.9}$$

E' is the storage or elastic modulus and, E'' is the loss or viscous modulus.

The shift phase angle δ is also called the damping factor and indicates how efficiently the material loses energy to molecular rearrangements and internal friction [100]. Defined as:

$$\delta = \frac{E''}{E'} \tag{2.10}$$

There are many practical information one can get from a DMA test, for example, it is possible to characterize the phase transition of polymers as indicated in figure 2.13, where the main curve is divided into six regions that corresponds to: (6) local motions, (5) bond bending and stretching, (4) movements in the side chain or adjacent atoms in

the main chain, (3) the region of the T_g, (2) coordinated movements in the amorphous portion of the chain, (1) and the melting region.
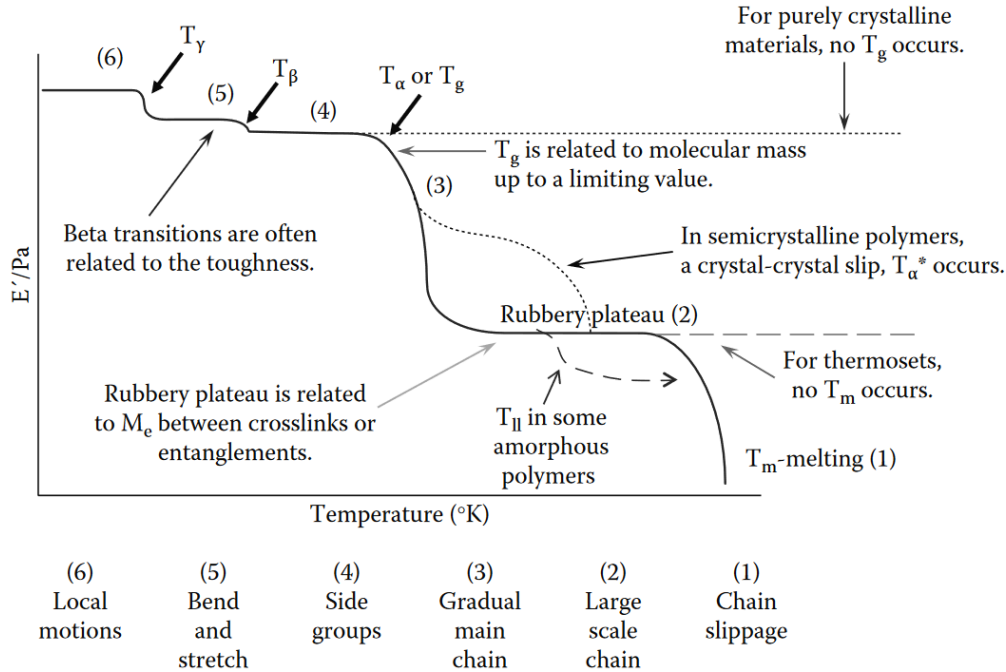
Figure 2.13: Idealized phase transition of polymers [100]

2.2 Hyperelasticity models

In the case of infinitesimal strain, the relation between stress and strain in the linear or elastic region is described by Hooke's law:

$$\sigma = E\varepsilon$$

In three dimensional generalized tensor form, considering both axial and shear strains:

$$\varepsilon_{ij} = \frac{1}{E}\sigma_{ij} - \frac{\nu}{E}\sigma_{kk}\delta_{ij} \tag{2.11}$$

Where E is the Young's modulus and ν is the Poisson's ratio.

When materials exhibit large elastic deformation (above 1% elongation), hyperelasticity is the best framework to describe their material behavior. For these materials the stress-
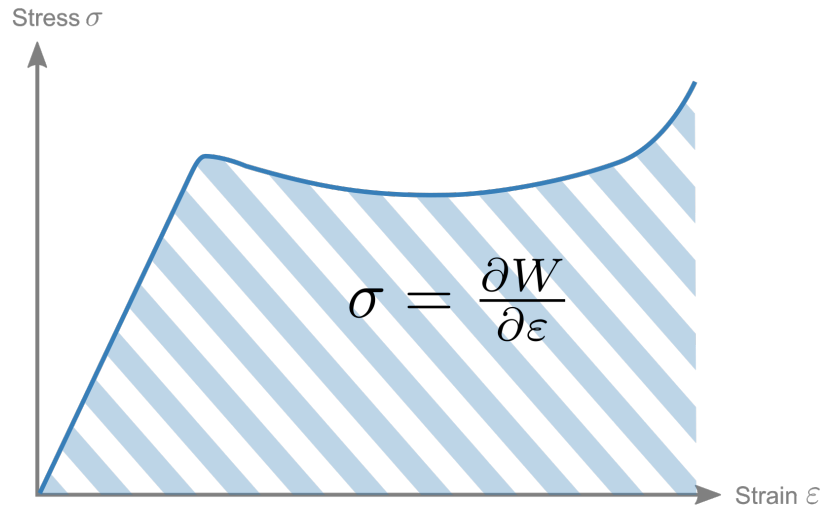
Figure 2.14: Strain energy in a stress-strain curve

strain relation is best described in terms of the strain energy density Ψ (eq. 2.13), which is the area under the stress-strain curve (fig. 2.14).

$$\sigma = \frac{\partial \Psi}{\partial \varepsilon} \tag{2.12}$$

$$\Psi = \int_x \frac{1}{2} \sigma : d\varepsilon \tag{2.13}$$

The strain energy is a function of the three invariants (I_1, I_2, I_3) of the Cauchy-Green deformation tensor $\mathbf{C} = \mathbf{F}^T \mathbf{F}$:

$$\mathbf{F} = \begin{bmatrix} \lambda_1 & 0 & 0 \\ 0 & \lambda_2 & 0 \\ 0 & 0 & \lambda_3 \end{bmatrix}$$

$$\Psi = f(I_1, I_2, I_3)$$
$$I_1 = \lambda_1^2 + \lambda_2^2 + \lambda_3^2$$
$$I_2 = \lambda_1^2 \lambda_2^2 + \lambda_2^2 \lambda_3^2 + \lambda_3^2 \lambda_1^2$$
$$I_3 = \lambda_1^2 \lambda_2^2 \lambda_3^2$$

where λ_1^2, λ_2^2, λ_3^2 are the principal stretches or extension ratios and, $\mathbf{F}$ is the deformation

gradient tensor.

2.2.1 Phenomenological models

The phenomenological models are formulated to best describe the experimental data of the observed mechanical behavior of polymers. The formulation considers the macroscopic nature of the material hence treating the problem from the continuum mechanics viewpoint. The phenomenological models presented here are Mooney-Rivlin, Ogden, and Gent.

Mooney-Rivlin Model

In 1956 Rivlin [101] specified the form of equation 2.13 with the power series:

$$\Psi = \sum_{i+j+k=1}^{\infty} C_{ijk} (I_1 - 3)^i (I_2 - 3)^j (I_3 - 1)^k \tag{2.14}$$

where C_{ijk} are material parameters.

For incompressible materials, $I_3 = 1$, and equation 2.14 becomes:

$$\Psi = \sum_{i+j+k=1}^{\infty} C_{ijk} (I_1 - 3)^i (I_2 - 3)^j \tag{2.15}$$

Taking only the first two terms of equation 2.15 yields to the Mooney-Rivlin equation [102]:

$$\Psi = C_{10} (I_1 - 3) + C_{01} (I_2 - 3) \tag{2.16}$$

Taking only the first term of this equation yields the neo-Hookean model:

$$\Psi = C_{10} (I_1 - 3) \tag{2.17}$$

The Mooney-Rivlin material description is typically used to characterize rubber-like materials undergoing large strains. The conventional Mooney-Rivlin material is defined by the strain-energy function 2.16.

Ogden model

The Ogden model [103] is frequently used to describe the behavior of biological tissue and incompressible solid polymers. The strain energy function 2.18 depends on the

principal stretches λ_1, λ_2 and, λ_3:

$$\Psi(\lambda_1, \lambda_2, \lambda_3) = \sum_{p=1}^{m} \frac{\mu_p}{\alpha_p} \left(\lambda_1^{\alpha_p} + \lambda_2^{\alpha_p} + \lambda_3^{\alpha_p} - 3 \right) \tag{2.18}$$

where m, α_p and μ_p are material constants and the shear modulus mu is defined as:

$$2\mu = \sum_{p=1}^{m} \mu_p \alpha_p \tag{2.19}$$

Assuming incompressibility:

$$\Psi(\lambda_1, \lambda_2) = \sum_{p=1}^{n} \frac{\mu_p}{\alpha_p} \left(\lambda_1^{\alpha_p} + \lambda_2^{\alpha_p} + \lambda_1^{-\alpha_p} \lambda_2^{-\alpha_p} - 3 \right) \tag{2.20}$$

Gent model

A phenomenological model of rubber elasticity that is based on the concept of limiting chain extensibility [104]. In this model, a simple mathematical form is used to describe the nonlinear constitutive model of rubber. Gent [105] proposed the use of a simple two-parameter phenomenological constitutive model for hyperelastic isotropic incompressible materials. The strain energy function most commonly used in finite element method:

$$\Psi = -G \frac{J_m}{2} \ln \left(1 - \frac{I_1 - 3}{J_m} \right) + \frac{K}{2} \left(\frac{1}{2} (J^2 - 1) + \ln J \right) \tag{2.21}$$

where J is the volume ratio (det $\mathbf{F}$) after and before deformation. For incompressible materials, $J = 1$. I_1 is the first invariant of Cauchy strain tensor. G is the initial shear modulus, J_m is the limiting value of term $I_1 - 3$ and, K is the bulk modulus.

2.2.2 Micro-mechanical models

Contrary to the phenomenological models, micro-mechanical models are formulated from a microstructural point of view. At micro scale, polymers are built of chains that are randomly oriented and joined into a network-like structure.

The development of these models require the assumption that the mechanical behavior of polymeric chains will follow probability functions, which can be *Gaussian* or *Non-Gaussian*. The first approach is the treatment of the statistical properties of the single
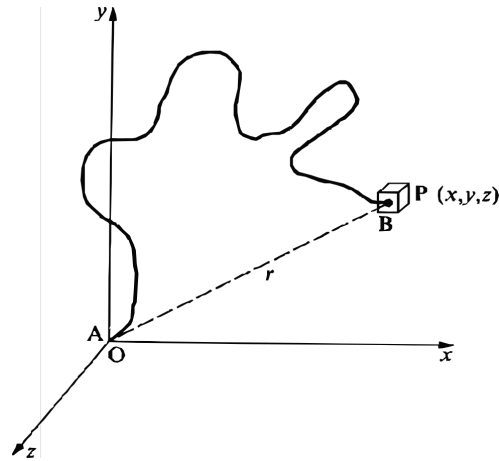
Figure 2.15: Geometrical representation of the idealized single-chain model [106]

long-chain molecule in terms of its geometry, and secondly, the application of this treatment to the problem of the network of long-chain molecules corresponding to a cross-linked rubber.

Single-chain model: *Gaussian* **statistics formulation**

Let us imagine an idealized model of a chain of n links of equal length l. This chain is randomly jointed and its end A is fixed at the origin of a Cartesian coordinate system, while the other end B can move freely (fig. 2.15). Not all positions of B are equally probable, there is an associated probability that the end B will be located within a small rectangular volume with dimensions $dxdydz$. The probability function is proposed by Kuhn, Guth and Mark [107], which is a probability density in the form of the Gaussian error function.

$$p(x, y, z)dx\, dy\, dz = \frac{b^3}{\pi^{3/2}} \exp\left(-b^2(x^2 + y^2 + z^2)\right)dx\, dy\, dz \qquad (2.22)$$

where,

$$b^2 = 3/2nl^2 \qquad (2.23)$$

This approximation derives from the assumption that the distance r between the ends of the chain is not comparable with the maximum length nl of the chain.

If now we consider the end B to be located in a spherical shell volume of radius r and

thickness dr, the probability $(P(r))$ is:

$$P(r)dr = (b^3/\pi^{\frac{3}{2}})\exp(-b^2r^2)4\pi r^2 dr \tag{2.24}$$

From equation 2.24 we obtain the mean squared value of r:

$$\overline{r^2} = \frac{\int_0^\infty rP(r)dr}{\int_0^\infty P(r)dr} = \frac{3}{2b^2} = nl^2 \tag{2.25}$$

Now, if we want to elongate the chain from a distance r to $r + dr$, the work required is equal to the change in the Helmholtz free energy:

$$\frac{d\Psi}{dr} = -\Theta\frac{ds}{dr} \tag{2.26}$$

Θ is the temperature and s is the entropy function that is derived according to the Boltzmann statistical thermodynamics.

The entropy will be proportional to the logarithm of the number of possible configurations in the system. In the single-chain idealized model all configurations have the same probability, hence:

$$s = k\{\ln p(x,y,z)d\tau\} \tag{2.27}$$

where τ is the volume element assumed to be constant and, k is the Boltzmann's constant.

Substituting equation 2.22 in 2.27 we obtain:

$$s = c - kb^2r^2 \tag{2.28}$$

where c is and arbitrary constant linked to the volume $d\tau$.

By differentiating 2.28 with respect to r we obtain:

$$d\Psi/dr = 2k\Theta b^2 r \tag{2.29}$$

Being $f = d\Psi/dr$ the tensile force acting along the direction r.

The extension is defined by the principal extension ratios λ_i, where $\lambda_1\lambda_2\lambda_3 = 1$ is satisfied.

Let us consider an individual chain (fig. 2.16) having an end-to-end distance represented
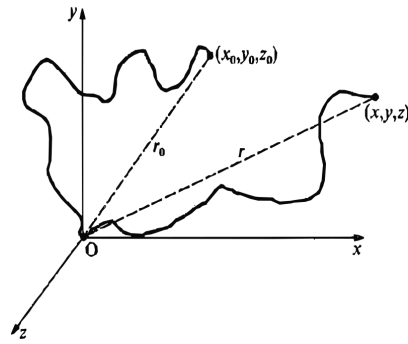
Figure 2.16: Deformation of chains [106]

by the vector $r_0 = (x_0, y_0, z_0)$ in the undeformed state, and $r = (x, y, z)$ the vector in the deformed configuration. The relation between original and deformed state is $x = \lambda_1 x_0, y = \lambda_2 y_0, z = \lambda_3 z_0$. Then, the entropy in the original state is given by:

$$s_0 = c - kb^2 r_0^2 = c - kb^2(x_0^2 + y_0^2 + z_0^2) \tag{2.30}$$

where b^2 is the constant in the Gaussian distribution function. Similarly, the entropy in the strained state is:

$$s = c - kb^2(\lambda_1^2 x_0^2 + \lambda_2^2 y_0^2 + \lambda_3^2 z_0^2)$$

The total entropy of deformation is $\Delta s = s - s_0$. Assuming all chains in the network have the same molecular weight, $i.e$ $b^2 = constant$. The total entropy for all the N chains contained in one unit volume in the network is:

$$\Delta S = \sum \Delta s = -kb^2 \left\{ (\lambda_1^2 - 1) \sum x_0^2 + (\lambda_2^2 - 1) \sum y_0^2 + (\lambda_3^2 - 1) \sum z_0^2 \right\} \tag{2.31}$$

Since the directions of the chain vectors r_0 in the undeformed state are entirely random, there will be no preference for the x, y, z directions, then, $\sum x_0^2 = \sum y_0^2 = \sum z_0^2 = \frac{1}{3} \sum r_0^2$. Where, $\sum r_0^2 = N \overline{r_0^2}$.

If the mean-square chain vector length in the unstrained state is the same as for a corresponding ser of free chains, then $\overline{r_0^2} = 3/2b^2$. Hence from equation 2.31:

$$\Delta S = -\frac{1}{3} Nk(\lambda_1^2 + \lambda_2^2 + \lambda_3^2 - 3) \tag{2.32}$$

The Helmholtz free energy or work of deformation is:

$$\Psi = \frac{1}{2}Nk\Theta(\lambda_1^2 + \lambda_2^2 + \lambda_3^2 - 3) \tag{2.33}$$

We define the rubbery modulus $G = Nk\Theta$, which is a physical parameter dependent on the structure of the material and related with the number of chains per unit volume, N. This material parameter is equivalent to the shear modulus and can be obtain from the stress-stain curve and from the DMA tests. Ogden model, revisited in subsection 2.2.1, was inspired from result (2.33), adding material parameters to be adjusted according to experimental results (eq. 2.18).

Non-Gaussian chain statistics

The *Gaussian* formulation previously describe predicts relatively well the behavior of elastomer at low strains, however at large strains the elastomer (particularly rubber-like materials) present high stresses, derived from the finite stretch of the polymer chains. This phenomenon is not predicted by this type of formulation, because the *Gaussian* approximation considers that the chain end-to-end distance r_{chain} (current chain length) is much less than the fully extended length.

The *non-Gaussian* treatment of the single chain takes into account the finite extensibility of the polymer chains. In this statistical mechanics approach the idealized chain is now a chain of N links, each of length l. Each link is a segment that undergoes rigid body motion in response to an imposed strain. Then, the initial chain length is:

$$r_0 = \sqrt{N}l \tag{2.34}$$

The fully extended chain is approximately $r_L = lN$, the chain limit extensibility (λ_{lock})is:

$$\lambda_{lock} = \frac{r_L}{r_0} = \sqrt{N} \tag{2.35}$$

Contrary to the *Gaussian* approach, where the probability of the final position of the end point of the entire chain is calculated, the problem in this case is to find the most probable angular distribution of rigid links about the chain vector length. Kuhn and Grün [108] solved this problem by proposing a probability density function that involves Langevin statistics. In this manner, the entropy of deformation is:

$$s = k\left[c - N\left(\frac{r_{chain}}{Nl}\beta + \ln\frac{\beta}{\sinh\beta}\right)\right] \tag{2.36}$$

where β is:

$$\beta = \mathscr{L}^{-1}[r_{chain}/Nl] \tag{2.37}$$

The Langevin function ($\mathscr{L}$) is used in terms of the fractional extension of the chain (r_{chain}/Nl) and is defined as:

$$\mathscr{L}[x] = \coth(x) - \frac{1}{x} \tag{2.38}$$

and the inverse Langevin function approximation:

$$\mathscr{L}^{-1}[x] = x\frac{3-x^2}{1-x^2} \tag{2.39}$$

The work of deformation is:

$$\Psi = nk\Theta N\left(\frac{r_{chain}}{Nl}\beta + \ln\frac{\beta}{\sinh\beta}\right) - \Theta c' \tag{2.40}$$

where n is the chain density, k Boltzmann's constant and, Θ is the temperature and, c' is a combination of constants. N and n are linked to each other by the polymer molecular weight.

This proposed formulation adds mathematical complexity to calculate the deformation in a general polymer network, therefore, different simplifications have been proposed, of which two will be described: the three and eight-chain models.

Three-chain model

The simplest of the *non-Gaussian* models is the three-chain model, each of the 3 chains is located along the axes of the undeformed cubic element (fig. 2.17). When the deformation is applied, the chains will deform at the same time as the cubic structure, with the stretch on each chain corresponding to the principal stretch value λ.

$$r_x = \lambda r_0$$
$$r_y = r_z = r_0\lambda^{-\frac{1}{2}}$$
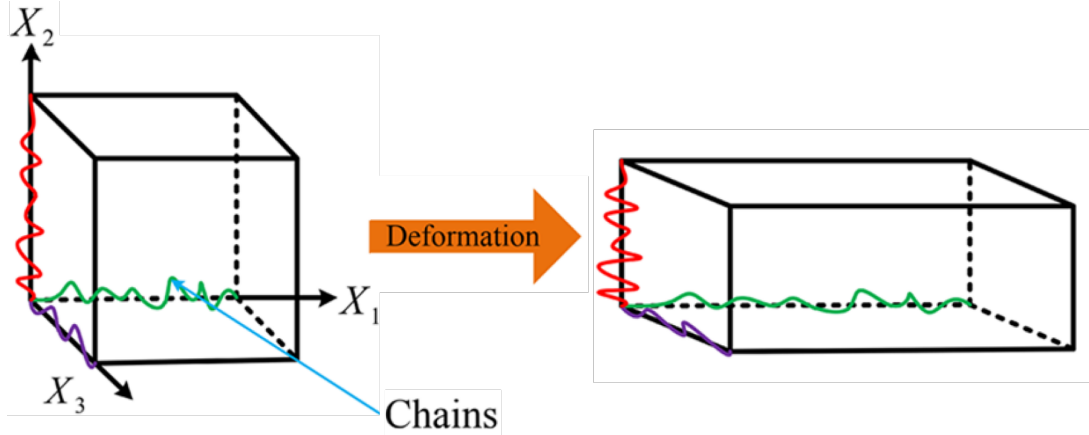
Figure 2.17: Schematic representation of the three-chain network structure in uniaxial deformation [109]

The work of deformation is from the *non-Gaussian* entropy (eq.2.36):

$$\Psi_{3-chain} = \frac{nk\Theta}{3}\sqrt{N}\sum_{i=1}^{3}\left[\lambda_i\beta_i + \sqrt{N}\ln\frac{\beta_i}{\sinh\beta_i}\right] \tag{2.41}$$

where λ_i is the principal stretch ratio in the ith axis and $\beta_i = \mathscr{L}^{-1}(\frac{\lambda_i}{\sqrt{N}})$.

The 3-chain model predicts accurately the uniaxial experimental data but fails to capture the biaxial and planar shear behavior [109].

Arruda-Boyce Model: eight-chain model

The models described herein up to this point are not sufficient to approximate the observed physical behavior of carbon-black-filled rubbers [110]. Arruda and Boyce proposed a constitutive model that, with mathematical simplicity accurately characterize the carbon-filled rubbers. The molecular network structure is represented by an eight-chain model which replaces classical three- and four-chain models [111].

The unstretched eight-chain model in figure 2.18a includes eight chains of length r_0 inside a cube of dimension a_0. From this geometry:

$$a_0 = \frac{2}{\sqrt{3}}r_0$$

In figure 2.18b the cube is stretched by $\lambda_1\hat{\imath}$, $\lambda_2\hat{\jmath}$, $\lambda_1\hat{k}$. A chain vector from the center of

the cube to a corner may be written for one chain as:

$$\mathbf{c}_1 = \frac{a_0}{2}\left(\lambda_1 \hat{\imath} + \lambda_2 \hat{\jmath} + \lambda_3 \hat{k}\right)$$

This chain has a vector length (r_{chain}):

$$r_{chain} = \frac{a_0}{2}\left(\lambda_1^2 + \lambda_2^2 + \lambda_3^2\right)^{1/2}$$

As well as all the remaining chains in the given network geometry. The vector length of the chains in terms of the statistical parameters and the principal stretches:

$$r_{chain} = \frac{1}{\sqrt{3}}\sqrt{N}l\left(\lambda_1^2 + \lambda_2^2 + \lambda_3^2\right)^{1/2} \tag{2.42}$$

The material is considered to be incompressible and the principal stresses can be determined from the work of deformation to within an arbitrary pressure p,

$$\sigma_i = \lambda_i \frac{d\Psi}{d\lambda_i} + p \tag{2.43}$$

with $i = 1, 2, 3$.

The stress-stretch relations are frequently written in terms of the difference in two principal stresses to eliminate the pressure term.

$$\sigma_1 - \sigma_2 = \lambda_1 \frac{d\Psi}{d\lambda_1} - \lambda_2 \frac{d\Psi}{d\lambda_2} \tag{2.44}$$

Substituting 2.42 in 2.40 and 2.44 yields to the stress-stretch relation:

$$\sigma_1 - \sigma_2 = \frac{nk\Theta}{3}N\mathscr{L}^{-1}\left[\lambda_{chain}/\sqrt{N}\right]\frac{\lambda_1^2 - \lambda_2^2}{\lambda_{chain}} \tag{2.45}$$

where the chain stretch $\lambda_{chain} = r_{chain}/r_0$, is the same in each chain and is given by:

$$\lambda_{chain} = \frac{1}{\sqrt{3}}(\lambda_1^2 + \lambda_2^2 + \lambda_3^2)^{1/2} \tag{2.46}$$

$$\lambda_{chain} = \frac{1}{\sqrt{3}}I_1^{1/2} \tag{2.47}$$

Integrating 2.45 and using the series expansion form for the inverse Langevin function,
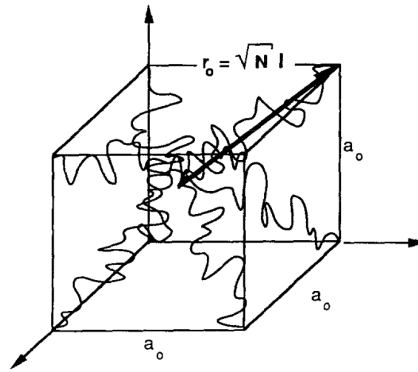
(a) Unstretched network for the proposed eight-chain model
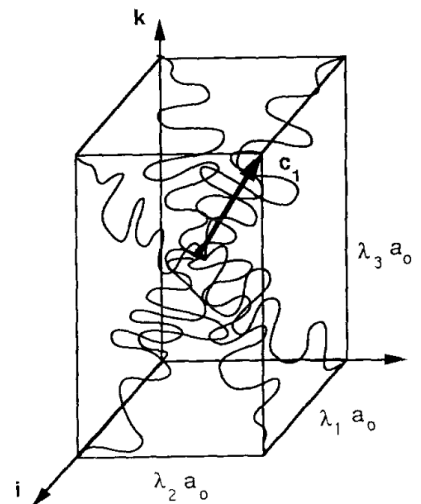
(b) The eight chain network in a stretched configuration

Figure 2.18: Three-dimensional eight-chain model [111]

the Arruda-Boyce strain energy function results in:

$$\Psi = G\left[\frac{1}{2}(I_1 - 3) + \frac{1}{20N}\left(I_1^2 - 9\right) + \frac{11}{1050N^2}\left(I_1^3 - 27\right) + \ldots\right] + \frac{K}{2}(J - 1)^2 \qquad (2.48)$$

where G is the rubbery modulus. J is the determinant of the deformation gradient and for an incompressible material $J = 1$ eliminating the second term of equation 2.48.

For finite element analysis, the typical form of the Arruda-Boyce model for an isotropic incompressible polymer is in series expansion up to five terms:

$$\Psi = G\left[\frac{1}{2}(I_1 - 3) + \frac{1}{20N}\left(I_1^2 - 9\right) + \frac{11}{1050N^2}\left(I_1^3 - 27\right)\right]$$
$$+ G\left[\frac{19}{7000N^3}\left(I_1^4 - 81\right) + \frac{519}{673750N^4}\left(I_1^5 - 243\right)\right] + \ldots \qquad (2.49)$$

There are other hyperelastic models that characterize the broad polymer behavior [112, 113], table 2.1 recapitulates the most used models:

Model	Strain energy function Ψ	Parameters
Mooney-Rivlin	$\Psi = C_{10}(I_1 - 3) + C_{01}(I_2 - 3)$	C_{10}, C_{01}
Neo-Hookean	$\Psi = C_{10}(I_1 - 3)$	C_{10}
Ogden	$\Psi = \sum_{p=1}^{m}\frac{\mu_p}{\alpha_p}\left(\lambda_1^{\alpha_p} + \lambda_2^{\alpha_p} + \lambda_3^{\alpha_p} - 3\right)$	μ_p, α_p, m
Arruda-Boyce	$\Psi = G\left[\frac{1}{2}(I_1 - 3) + \frac{1}{20N}\left(I_1^2 - 9\right) + \ldots\right] + \frac{K}{2}(J - 1)^2$	G, N
Gent	$\Psi = -G\frac{J_m}{2}\ln\left(1 - \frac{I_1 - 3}{J_m}\right) + \frac{K}{2}\left(\frac{1}{2}(J^2 - 1) + \ln J\right)$	G, J_m
Yeoh	$\Psi = \sum_{i=1}^{3} C_{i0}(I_1 - 3)^i + \sum_{k=1}^{3}\frac{K}{2}(J - 1)^{2k}$	C_{i0}

Table 2.1: Hyperelastic models summary

2.2.3 Large strain viscoplasticity: Boyce-Bergström Model

The Bergström-Boyce model [115] describes accurately the rate-dependant behavior of elastomers. It is based on the eight-chain network Arruda-Boyce model for hyperelastic elastomers.

Based on the standard linear solid (SLS) rheological model in figure 2.20, the viscoelastic behavior can be divided in the elastic (time-independent) and the viscous part (time-dependent).

Let us call the elastic part A and the viscous part B. The network A can be represented by an hyperelastic relation which acts as the equilibrium component with a stiff modulus
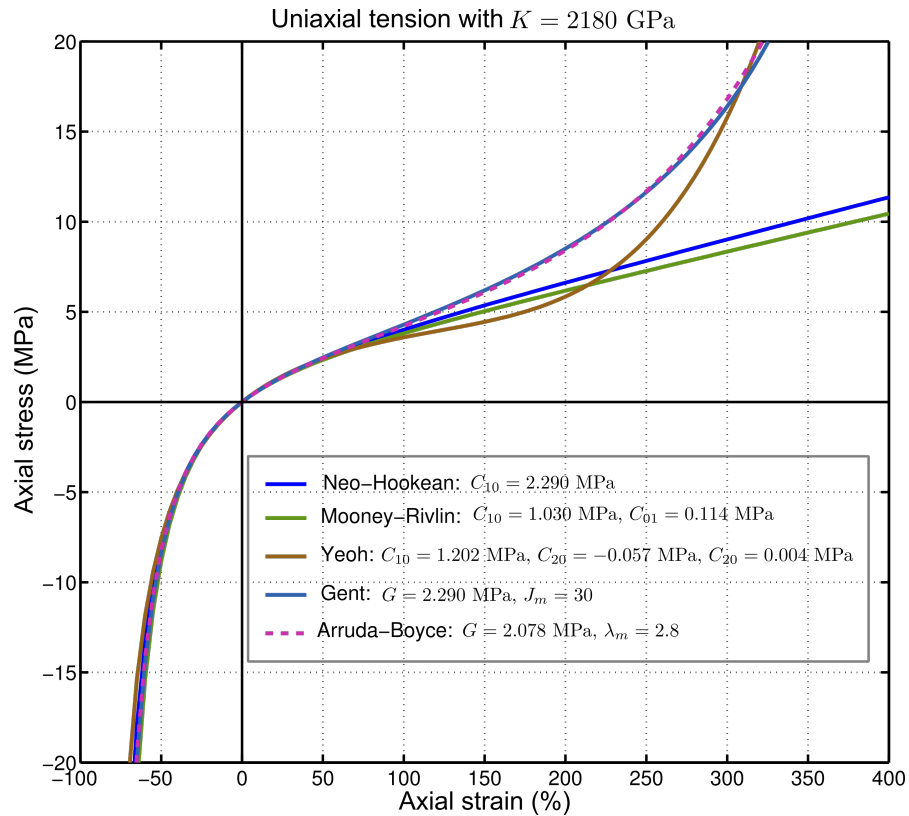
Figure 2.19: Stress-strain curves under uniaxial test of different hyperelastic models [114]
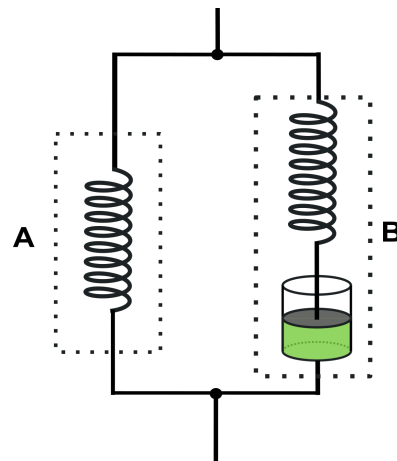
Figure 2.20: Elastic (A: time-independent) and viscous (B: time-dependent) representation of the Standard Linear Solid (SLS) rheological model.
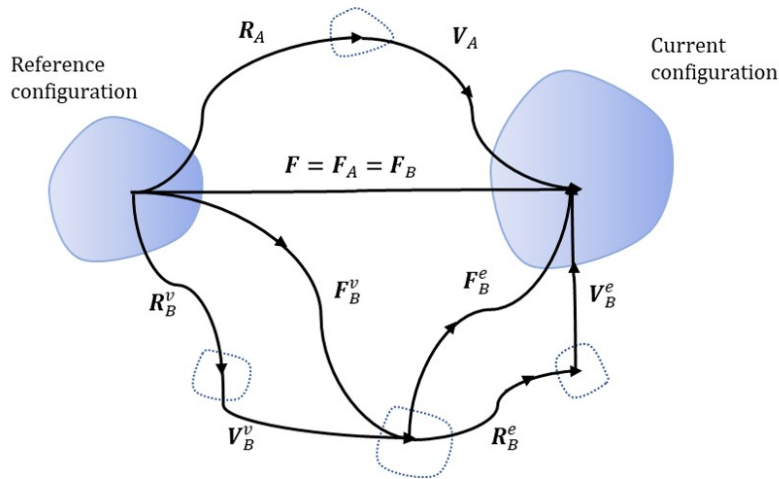
Figure 2.21: Decomposition of the deformation gradient

E_e and, the network B is a Maxwell element that includes a viscous time-dependent element with a relaxation time τ_σ and an elastic time-independent element with a stiff modulus E_1.

The total deformation $\mathbf{F} = grad(\mathbf{x}) = \nabla \mathbf{x}\mathbf{x}$ acts on both networks A and B i.e. $\mathbf{F} = \mathbf{F}_A = \mathbf{F}_B$.

Due to nearly incompressibility of elastomers, the deformation gradient can be decomposed into distortional and dilatational parts: $\bar{\mathbf{F}} = J^{-1/3}\mathbf{F}$, where, $J = det(\mathbf{F})$ is the volume change. The viscous effects are assumed to be purely dilatational.

The deformation gradient of the network B can be decomposed into elastic ($\mathbf{F}_B^e$) and viscous or inelastic ($\mathbf{F}_B^v$) parts (eq. 2.50).

$$\mathbf{F}_B = \mathbf{F}_B^e \mathbf{F}_B^v \tag{2.50}$$

Each one can be decomposed respectively into stretch and rotation components:

$$\mathbf{F}_B^e = \mathbf{V}_B^e \mathbf{R}_B^e \tag{2.51}$$

$$\mathbf{F}_B^v = \mathbf{V}_B^v \mathbf{R}_B^v \tag{2.52}$$

Kinematics of the hyperelastic elements at network A

The stress in network A can be obtained from the Arruda-Boyce model of rubber elasticity [111]:

$$\mathbf{T}_A = \frac{G^{(A)}}{J\bar{\lambda}^*} \frac{\mathscr{L}^{-1}(\bar{\lambda}^*/\sqrt{N_A})}{\mathscr{L}^{-1}(1/\sqrt{N_A})} dev(\mathbf{B}^*) + \kappa_B[J-1]\mathbf{I} \tag{2.53}$$

where $G^{(A)} = \frac{nkT}{3}$ is proportional to the initial hardening modulus of the network orientation portion of the strain hardening curve (rubbery modulus).

$N^{(A)}$ is the crosslink density and $\sqrt{N^{(A)}}$ the limiting network stretch λ_{lock}, the isochoric left Cauchy-Green deformation gradient tensor $\mathbf{B}^*$ is:

$\mathbf{B}^* = \bar{\mathbf{F}}\bar{\mathbf{F}}^T$,

$J = det(\mathbf{B}^*)$ and,

κ_B is the bulk modulus,

the elastic stretch $\bar{\lambda}^*$ is:

$$\bar{\lambda}^* = \frac{1}{\sqrt{3}}\left[(\lambda_1^{(A)})^2 + (\lambda_2^{(A)})^2 + (\lambda_3^{(A)})^2\right]^{\frac{1}{2}} = [trace(\mathbf{B}^*)/3]^{1/2} \tag{2.54}$$

$\mathscr{L}^{-1}(u) = \frac{u(3-u^2)}{(1-u^2)}$ is the Cohen rounded Padé approximation of the inverse Langevin function [116].

Correspondingly, the total stress of the hyperelastic (loading configuration) element in network B can be calculated similarly to equation 2.53:

$$\mathbf{T}_B = \frac{G^{(B)}}{J_B^e \bar{\lambda}_B^{e*}} \frac{\mathscr{L}^{-1}(\bar{\lambda}_B^{e*}/\sqrt{N_B})}{\mathscr{L}^{-1}(1/\sqrt{N_B})} dev(\mathbf{B}_B^{e*}) + \kappa_B[J_B^e - 1]\mathbf{I} \tag{2.55}$$

where $J_B^e = det(\mathbf{F}_B^e)$, $\mathbf{B}_B^{e*} = \bar{\mathbf{F}}_B^e \bar{\mathbf{F}}_B^{e T}$ and, $\bar{\lambda}_B^{e*} = [trace(\mathbf{B}_B^{e*})/3]^{1/2}$

The total stress in the system becomes $\mathbf{T}_{total} = \mathbf{T}_A + \mathbf{T}_B$.

Kinematics of time-dependent network B

The total velocity gradient (strain-rate tensor) $\mathbf{L}_B = \dot{\mathbf{F}}_B \mathbf{F}_B^{-1}$, can be decomposed similarly as in equation 2.50 in elastic and viscous components:

$$\mathbf{L}_B = \mathbf{L}_B^e + \mathbf{F}_B^e \mathbf{L}_B^v (\mathbf{F}_B^e)^{-1} = \mathbf{L}_B^e + \tilde{\mathbf{L}}_B^v \tag{2.56}$$

where $\mathbf{L}_B^v = \dot{\mathbf{F}}_B^v \mathbf{F}_B^v = \mathbf{D}_B^v + \mathbf{W}_B^v$ and $\tilde{\mathbf{L}}_B^v = \tilde{\mathbf{D}}_B^v + \tilde{\mathbf{W}}_B^v$. $\mathbf{D}$ is the deformation rate tensor and $\mathbf{W}$ is the spin tensor.

For the viscous part $\tilde{\mathbf{W}}_B^v = 0$ meaning that all rotations occur during the viscoelastic and elastic unloading [34] (relaxed configuration).

The viscous deformation rate of the network B can be defined as

$$\tilde{\mathbf{D}}_B^v = \dot{\gamma}_B \mathbf{N_B} \tag{2.57}$$

where $\mathbf{N_B}$ is the direction of the driving stress state of the relaxed configuration.

Noting that $\mathbf{T}_B$ is computed in the loading configuration, the driving stress is then given by:

$$\mathbf{T}_B^* = \mathbf{T}_B$$
$$\mathbf{T}_B^{*'} = \mathbf{T}_B^* - \frac{1}{3}\text{trace}[\mathbf{T}_B^*]\mathbf{I} = dev[\mathbf{T}_B^*] \tag{2.58}$$

The driving stress state on the relaxed configuration convected to the current configuration is then given by equation 2.58 and its direction $\mathbf{N}_B$ is given by:

$$\mathbf{N}_B = \frac{\mathbf{T}_B^{*'}}{\sqrt{2}\tau_B} \tag{2.59}$$

The effective shear stress acting on branch B (τ_B) is defined as

$$\tau_B = \left[\frac{1}{2}\text{trace}(\mathbf{T}_B^{*'}\mathbf{T}_B^{*'})\right]^{\frac{1}{2}} \tag{2.60}$$

The flow rate or the creep rate $\dot{\gamma}_B$ will be defined later.

Creep rate function

To describe the effective creep rate of network B, it is assumed that the time-dependent behavior is caused by the reptation of inactive or free polymer chains, that as consequence of carrying less load, are capable of changing conformation during creep loading.

If the polymer is stretched at enough high rate, the free chains will stretch synchronously with the active chains. Hence, the free chains contribute also to the material resistance to stretch. If this stretch is held constant, the free chains, by Brownian motion, will reconfigurate to a stress-relaxed state.

The average displacement of the free chain can be described by the theory of reptational motion of chain molecules (Tube model [117]):

$$< u >= C_3 < u^2 >^{1/2} \equiv C_3 \sqrt{\phi(t)}$$

Then, the effective length of the chain in creep is:

$$l(t) = l_0 + C_3 \sqrt{\phi(t)} \tag{2.61}$$

The function $\phi(t)$ describes the motion of a free chain:

$$\phi(t) = \begin{cases} t^{1/2} & t \leq \tau_e \\ t^{1/4} & \tau_e \leq \ t \leq \tau_R \\ t^{1/2} & \tau_R \leq \ t \leq \tau_d \\ t & \tau_d \leq \ t \end{cases} \tag{2.62}$$

Where τ_e is the time at which the first constraint is felt, τ_R is the Rouse time relaxation and, τ_d denotes the tube disengagement time. According to [115] equations 2.61 and 2.62 can be simplified to obtain the inelastic network stretch:

$$\lambda_i^B(t) = \frac{l(t)}{l_0} = 1 + C_2 t^{C_3} \tag{2.63}$$

where $C_2 > 0$ and $C_3 \in [0.125, 0.5]$.

Taking the derivative of 2.63 gives:

$$\dot{\lambda}_i^B(t) = C_3 C_2 t^{C_3 - 1} \tag{2.64}$$

Combining equations 2.63 and 2.64 we obtain:

$$\dot{\lambda}_i^B(t) = C_4 [\lambda_i^B - 1]^{C_\tau} \tag{2.65}$$

where $C_4 > 0$ and $C_\tau \in [-1, 0]$.

Note that equation 2.65 is for a fixed stress level, the dependance with stress can be considered to take a power law relation:

$$\dot{\gamma}_B = \dot{\gamma}_0 [\lambda_i^B - 1]^{C_\tau} \left(\frac{\tau_B}{\hat{\tau}_B}\right)^m \tag{2.66}$$

Where τ_B is introduced in equation 2.60, $\hat{\tau}_B$ is a material property and, $m > 0$ and $\eta = \frac{\dot{\gamma}_0}{\hat{\tau}_B^m} > 0$. From reptational dynamics considerations $C_\tau \approx -1$ and, the creep rate function becomes:

$$\dot{\gamma}_B = \eta \left(\frac{1}{\lambda_i^B - 1 + \xi}\right) \tau_B^m \tag{2.67}$$

where $\xi \approx 0.01$ is a parameter that eliminates the singularity nature of the $\lambda_i^B - 1$ expression. λ_i^B is correlated to the principal macroscopic stretch state by the eight-chain assumption [114].

$$\lambda_i^B = \left(\frac{1}{3} \text{trace}(\mathbf{F}_B^v \mathbf{F}_B^{vT})\right)^{1/2} \tag{2.68}$$

2.3 Conclusion

This chapter has explored the main mechanical theories of solid polymers, shedding light on their fundamental principles and significance in understanding the mechanical behavior of these materials.

We began by delving into the concept of viscoelasticity, which encompasses the combined characteristics of elasticity and viscosity exhibited by polymers. The Maxwell and Kelvin-Voigt models provide the time-dependent response of polymers to applied forces, highlighting the role of internal mechanisms such as relaxation and creep.

Moreover, the concept of hyperelasticity was examined by establishing its foundation, which considers the strain-energy density function as a key element in describing the material's response to deformation. The chapter discussed various hyperelastic models, including the widely used Neo-Hookean, Mooney-Rivlin, and Ogden models, each offering different degrees of accuracy and complexity in capturing the nonlinear behavior of polymers. Additionally, we provided insights into the principles of micro-mechanical

models from the single-chain to the eight-chain model, also known as the Arruda-Boyce model. These micro-mechanical models offer a more detailed understanding of the molecular-level interactions and their influence on the overall mechanical properties of polymers.

Furthermore, we examined the Bergström-Boyce model, which incorporates the influence of strain rate and temperature on the mechanical response of polymers. This model addresses the viscoelastic nature of polymers and offers a more comprehensive representation of their time-dependent behaviors.

In conclusion, the integration of hyperelastic models and the Bergstrom-Boyce model provides a robust framework for developing a mechanical model for photomechanical polymers. This comprehensive approach will contribute to a deeper understanding of their mechanical behavior and facilitate the design of innovative applications.

DTE-UPy-PEB thin films sample elaboration and photo-induced bending analysis

Thin films are materials whose thickness vary from the scale of nanometers to micrometers. The basis of its fabrication is the transfer of a material, commonly metals or polymers, from a solution onto a solid substrate from which it will be detached once the solvent evaporates to form the thin film. The transfer is known as deposition. There are different techniques that are used, depending on the type of application and material.

This chapter contains an introductory description of the elaboration methods of thin films, including the elaboration process of DTE-UPy-PEB photomechanical films performed by our collaborators [24, 118]. Additionally, the photokinetics of the closed form and open form transformation of the thin films are experimentally analyzed via spectroscopy. Finally, we report the first photo-induced bending under VIS-UV irradiation.

3.1 Photomechanical thin films: elaboration methods

Advances in thin film deposition techniques during the 20th century made possible technological development in applications such as, magnetic recording media, electronic semiconductor devices, LEDs, optical coatings, hard coatings on cutting tools and,

energy generation (thin-film solar cells) and storage (thin-film batteries) [119]. Recently, researchers have developed thin films with photo-reactive materials for applications that require remotely controlled actuation and surface modulation [120].

In this project, we developed thin films composed of a photo-reactive molecule and a elastomer. Using supramolecular chemistry, both compounds form a photomechanical material.

3.1.1 Deposition techniques

These techniques are branched in two categories: physical deposition methods (PDM) and chemical deposition methods (CDM).

Physical Deposition Methods

In vacuum conditions, PDMs use mechanical, electrical or thermodynamical force to move particles from a high to a low-energy environment. The thin film is formed as the material particles are deposited on the substrate's surface.

Some examples are:

- Thermal evaporator

- Electron beam evaporator

- Sputtering

- Laser ablation

Chemical Deposition Methods

CDM involve a chemical reaction where the product self-assemblies and coats the substrate's surface, producing a thin film on it. Unlike the PDMs, CDMs reaction is not produced at vacuum conditions and it can be done at high or room temperatures [121]. Some examples:

- Chemical solution or bath Deposition

- Langmuir-Blodgett-Shaefer (LBS)

- Chemical vapor Deposition

- Spin coating

- Dip coating

- Drop casting

The thin films studied in this thesis were produced using the techniques drop casting, spin coating and LBS.

Drop casting   Drop casting is the simplest way for deposition of material into a substrate. It comprises casting a drop of solution directly on the substrate's surface and, as the solvent evaporates, the solid thin film will form. The thin film thickness result non-uniform and cracks may appear because of different evaporation rates along the surface. However, some techniques have been applied to control thickness uniformity, for example, multiple-drop casting [122] or a substrate vibration-assisted drop casting [123].

Spin coating   In the spin coating method, a drop of material is cast on a solid substrate. Here, the substrate is spinning at a constant angular velocity. Because of centrifugal forces acting on, the material spreads from the center to the substrate's borders.

With this method it is possible to get better thickness uniformity by dividing the process in two steps. First, using a moderate spinning rate to form a relatively thick and uniform liquid layer. Next, once the uniform layer is formed, the spinning rate may be increased (spin-up phase) to decrease thickness and drive an air convection above the liquid film.

Langmuir-Blodgett-Shaefer   Langmuir-Blodgett (vertical) and Langmuir-Shaefer (horizontal) films are formed when monolayers of amphiphilic molecules at the liquid-gas interface (Langmuir films) are transferred onto a solid substrate. These molecules, having a hydrophobic tail and a hydrophilic head, are spontaneously oriented at a liquid/gas interface.

This technique provides advantages over other methods aforementioned, as it allows a better molecule alignment at each monolayer, resulting in a well molecular structured material [124].

3.1.2   Supramolecular chemistry

Recently, supramolecular chemistry has given a new way to create photomechanical smart materials (like self-healing polymers). The principle of supramolecular chemistry is that, by non-covalent interactions, molecules spontaneously organize into complex
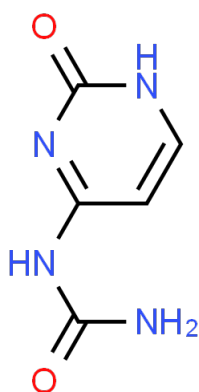
Figure 3.1: UPy structure [126]

structures. They are directed to their proper locations by attractions and repulsions induced by their electrical charges, magnetic properties and complementary shapes. These mechanisms allow molecules to organize into plates, spheres, rods and other useful structures.

Supramolecular materials, linked with polymer chains by non-covalent bonds, have the potential to provide dynamic functions that are not given by covalently cross-linked polymers [125]. Supramolecular polymers are thermally responsive and exhibit low melt viscosities. The non-covalent bonding gives to the structure the self-healing abilities, elasticity, shape memory and easy recycling process. This dynamic nature of non-covalent interactions has given rise to the creation of new materials with interesting properties for applications within different fields of technology.

Hydrogen functionalized bonding in polymers

Recent work has showed that by adding secondary highly directional bonding to the polymer network improves its mechanical properties [23]. This additional linking is given by a functional group composed by several hydrogen bonds, adding strength to this interaction and at the same time, enabling the polymer network a controlled and reversible disassembly upon external stimulus (fig. 3.2).

The quadruple hydrogen bonding functional group UPy (fig. 3.1) is employed in the chain extension of polysiloxanes, poly(ethylene/butylenes), polyethers, polyesters, and polycarbonates [22].
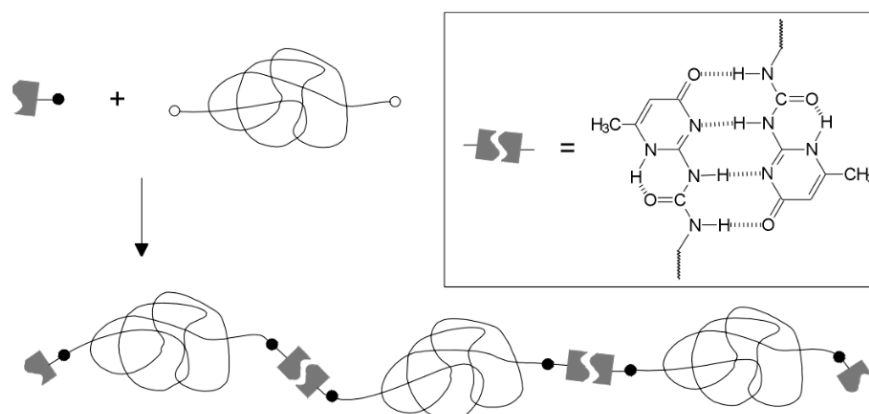
Figure 3.2: Schematic representation of functionalized polymers with UPy's units bonded at the end of the polymer chain [22]

Mechanical properties of functionalized PEB

PEB is a thermoplastic elastomer whose polymer chains are strongly interacting in certain segments that alternate with weakly interacting segments producing materials with a soft-block/hard-block morphology. With the aggregation of UPy groups to the hard block segment, the strong hydrogen interactions give useful mechanical properties [127].

In previous work, supramolecular UPy-PEB-UPy thin films were elaborated by drop casting and subsequent compression moulding at high temperature and tested using Dynamic Mechanical Thermal Analysis (DMTA) (fig. 3.3). The storage modulus at -70 °C is 1744 ± 160 MPa, at 25 °C is 7 ± 2 MPa and the melting/failing temperature is around 60 to 80 °C [128].

Photoswitches with UPy bonding

Photoswitches integrated to supramolecular polymers add a light-induced reversible switching [129, 130]. Following the Takeshita's team work [20, 21] in our laboratories, we have initiated an intense campaign to elaborate novel photactuators combining PBE-UPy and DTE-UPy. The process of fabrication will be described in the next sections.
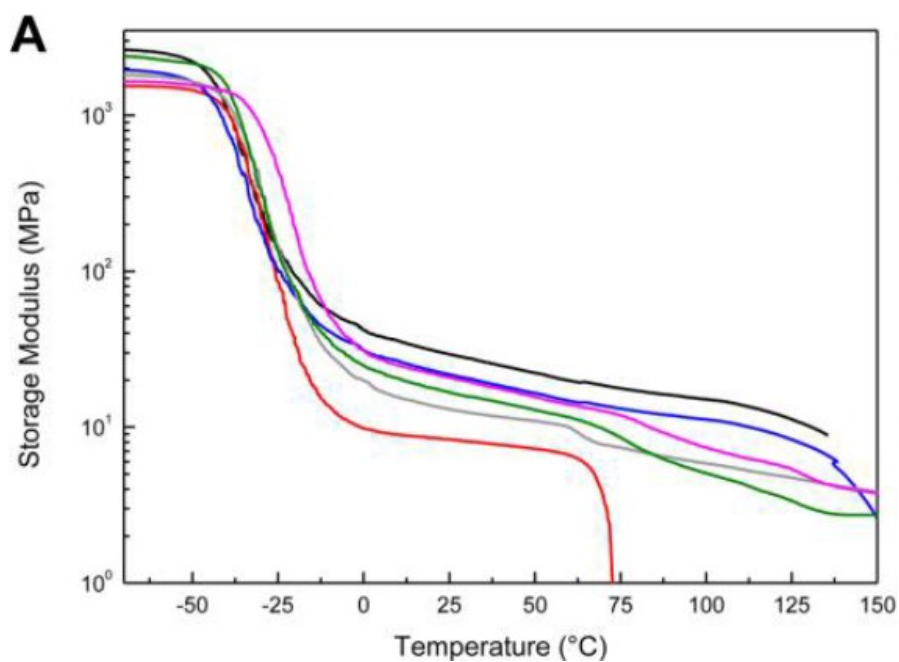
Figure 3.3: Representative DMTA traces of films of the neat metallosupramolecular polymer [Fe(MebipPEB-Mebip)](ClO4)2 (black), the neat UPy-PEB-UPy (red), and the following blends [Fe(Mebip-PEB-Mebip)](ClO4)21.0(UPy-PEB-UPy)1.0 (blue), [Fe(Mebip-PEB-Mebip)](ClO4)21.0(UPy-PEB-UPy)0.7 (gray), [Fe(Mebip-PEB-Mebip)](ClO4)21.0(UPy-PEB-UPy)0.5 (green), and [Fe(Mebip-PEB-Mebip)](ClO4)21.0(UPy-PEB-UPy)0.3 (pink). [128]

3.2   DTE-UPy-PEB photomechanical thin films elaboration by spin coating

To elaborate the photochemical thin films, both DTE and elastomer PEB were function-alized with the quadruple hydrogen bonding UPy unit. The functionalized DTE used was developed by Takeshita and the functionalization process of PEB was adapted and optimized based on protocols followed by Louati [24]. Both DTE-UPy and PEB-UPy were diluted in chloroform (CHCl3) at a constant magnetic stirring and temperature of 80 °C.

During the stirring process, the solution is irradiated with UV light to generate DTE in closed form. Once the DTE-UPy-PEB solution was ready and cooled down, the films were elaborated using the spin coater APT SPIN 150. The substrates materials varied between quartz, sapphire and silicon paper (fig. 3.4).
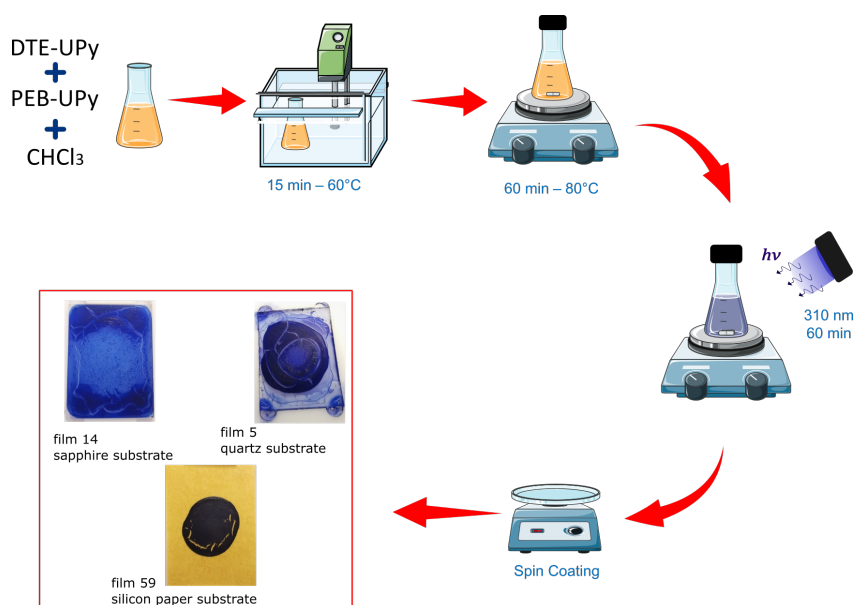
Figure 3.4: Thin film elaboration by spin coating process

Once ready, the thin films were detached from the substrate. We selected those with more apparent homogeneity to cut a rectangular portion out to be analyzed under the spectrometer and observed under photoirradiation.

3.3   DTE-UPy-PEB photomechanical thin films elaboration by thermoforming

Another method used to fabricate the DTE-UPy-PEB photomechanical thin films involved two methods: drop casting and thermoforming. First, a solution of functionalized DTE and PEB in chloroform was prepared and stirred, following the same process described in the previous section.

Three different solutions were prepared to fabricate DTE-UPy-PEB photomechanical thin films in OF and CF configuration and, functionalized PEB thin films.

After 60 minutes stirring, it was left to reach room temperature and then the solution was deposited on silicon paper using a 10 microliter syringe (fig. 3.5). After the drop casting, the dried drops were deposited into rectangular and dog-bone shape molds to proceed to thermoforming in a hydraulic press at a temperature of 80 °C and 60 bar of pressure. With this process we obtained thin films samples of 70 to 80 μm thickness (measured manually utilizing a micrometer) which were used to perform mechanical testing (reported in the next chapter).

3.4   Photomechanical response analysis

After the elaboration of DTE-UPy-PEB thin films by spin coating, a rectangle segment cut from the thin film was analyzed under photoirradiation. The specimen fixed with precision tweezers in a vertical position, underwent VIS-UV photoirradiation cycles and was recorded to study the mechanical movement during the photoisomerization process by means of video processing tools.

The thin film was irradiated with VIS and UV irradiation for three to four hours, with a period of no irradiation in between. This process was repeated up to three times. The films deformed under both VIS and UV light, the extent of such deformation is associated with different parameters, being the most important the gradient of deformation along the film's thickness. This gradient is formed only at relatively low light intensities. This means that at high light intensities, the transformation occurred rapidly, leaving no time for the transformation gradient to form and no photomechanical effect could be observed.

To observe the aforesaid phenomena, first we used a halogen UV-Visible lamp, which was replaced later for two LEDs to control the photoirradiation time with a LabView
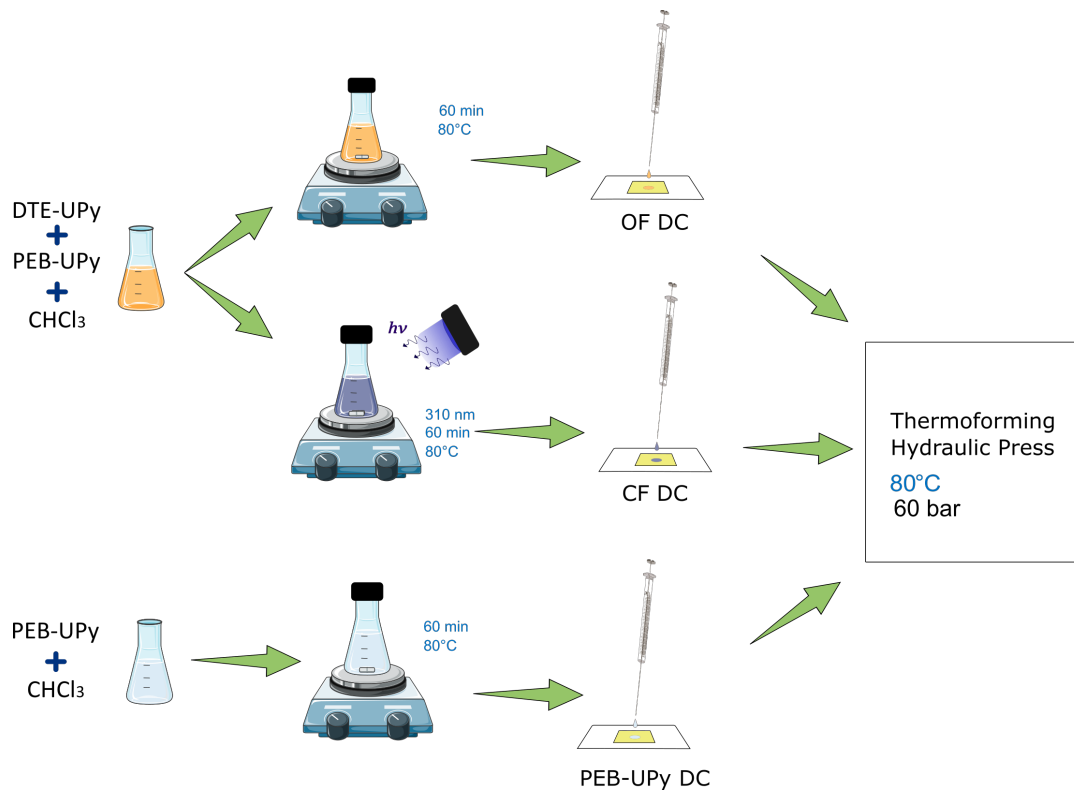
Figure 3.5: Thin film elaboration by thermoforming. .

timer script. A Nikon camera was used at all times to record the movement as a time lapse video (one frame each 2 seconds). The recorded videos were processed in MATLAB, to measure the bending amplitude. In this section all the details of the experimental procedure and results will be documented.

3.4.1 Materials and Experimental setup

The first experimental setup (fig. 3.6)used to analyze the thin films movement was based on previous work [24]. To irradiate the sample at 570 nm and 390 nm a Hamamatsu LC8 UV-Visible lamp was used and, with a Nikon D5600 Nikon camera complemented with a 44 mm macro lens, knowing that the augmented zoom allows a better video analysis. Videos of the sample movement during photoirradiation were obtained in a time lapse mode, shooting a photo each two seconds.

In the second experimental setup (fig. 3.7), the lamp was interchanged by two MIGH-TEX collimated LED lamps with wavelengths of 590 nm and 310 nm for VIS and UV irradiation, respectively. Both LEDs were fixed in a multi-wavelength combiner. In this
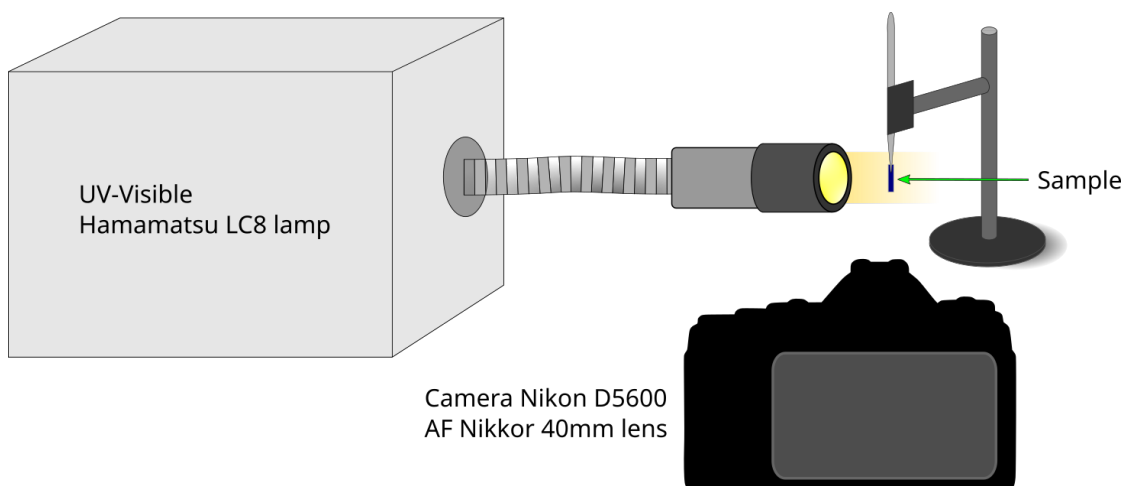
Figure 3.6: Experimental setup 1
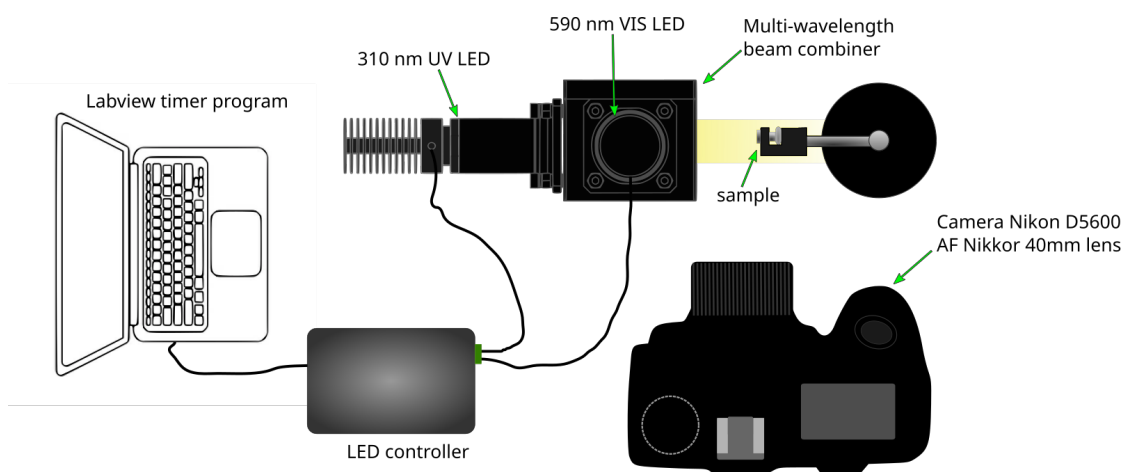
Figure 3.7: Experimental setup 2

way, the sample irradiation comes from the same side in both UV and VIS phase. This type of lamps enabled us to control the time and output power via a LabView script. The same Nikon camera was used.

3.4.2   Video analysis: processing and tracking algorithm

For the video processing, we developed a script in MATLAB based on computer vision algorithms, which are useful for video data extraction such as image recognition, object detection, activity recognition, 3D approximation, motion estimation and video tracking.

Because of the change of illumination, the videos were prepared before the analysis
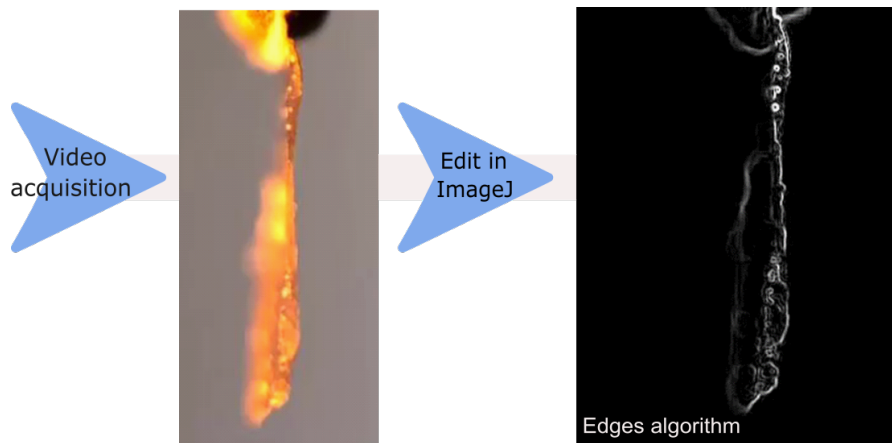
Figure 3.8: Example of pre-processing videos with the Edges algorithm

using the image processor software ImageJ. The videos were edited to extract only the silhouette or the edges of the object 3.8. In this way, the sample motion would be distinctly analyzed.

MATLAB provides Computer Vision add on that includes different functions dedicated to video analysis. Among these functions is the Point Tracker object that tracks a set of points using the feature-tracking Kanade-Lucas-Tomasi algorithm (KLT) [131]. There are four different point tracker methods of the KLT algorithm:

- **Number of pyramid levels**: The point tracker implementation of the KLT algorithm uses image pyramids. The tracker generates an image pyramid, where each level is reduced in resolution by a factor of two compared to the previous level. Each pyramid level is formed by down-sampling the previous level by a factor of two in width and height. The point tracker tracks each point at the lowest resolution level and continues tracking until convergence (fig. 3.9). The object propagates the result to the next level as the initial guess of the point locations. In this way, the tracking is refined with each level, up to the original image.

- **Forward-backward error threshold**: the tracker tracks each point from the previous to the current frame. It then tracks the same points back to the previous frame. The object calculates the bidirectional error. This value is the distance in pixels from the original location of the points to the final location after the backward tracking (fig. 3.10). The corresponding points are considered invalid when the error is greater than the value set for this property.
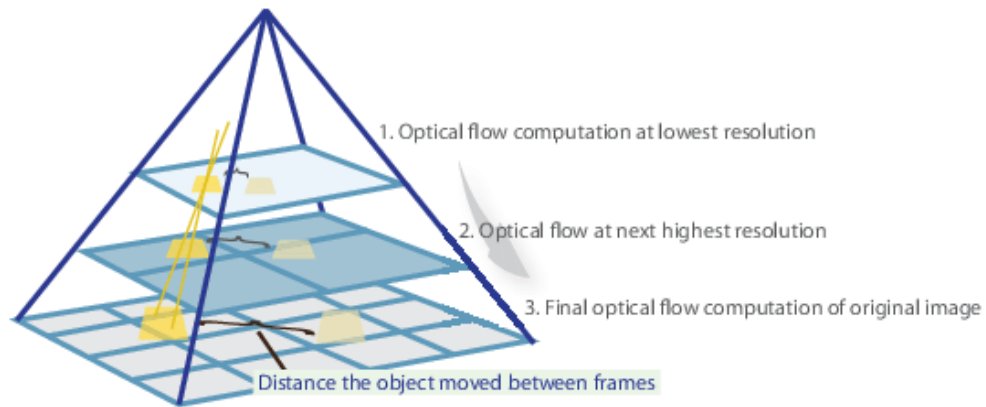
Figure 3.9: Pyramid levels algorithm implementation
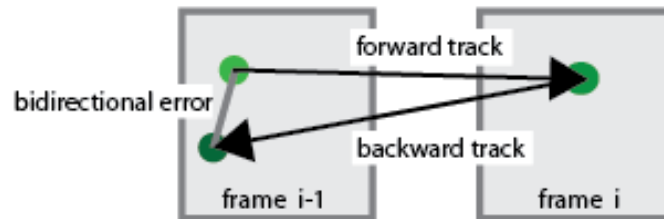
Figure 3.10: Maximum bidirectional error computation

- **Size of neighborhood**: the point tracking is computed around a defined neighborhood size.

- **Maximum number of search iterations**: The KLT algorithm performs an iterative search for the new location of each point until convergence.

The script reads the video information. From the first frame, the user manually selects the points to be tracked. To increase the accuracy, the points selected had to be on the edges of the sample. Each point is followed frame by frame using a point tracker function that compares the information obtained in the previous frame with the current frame. Forward-backward error threshold was the algorithm implemented. If the point is valid, each position of each point is saved in a matrix, having at the end all the history of the sample movement (fig. 3.11). At the end of the program, the displacement is calculated in the horizontal and vertical direction for each of the selected points (fig. 3.12) .
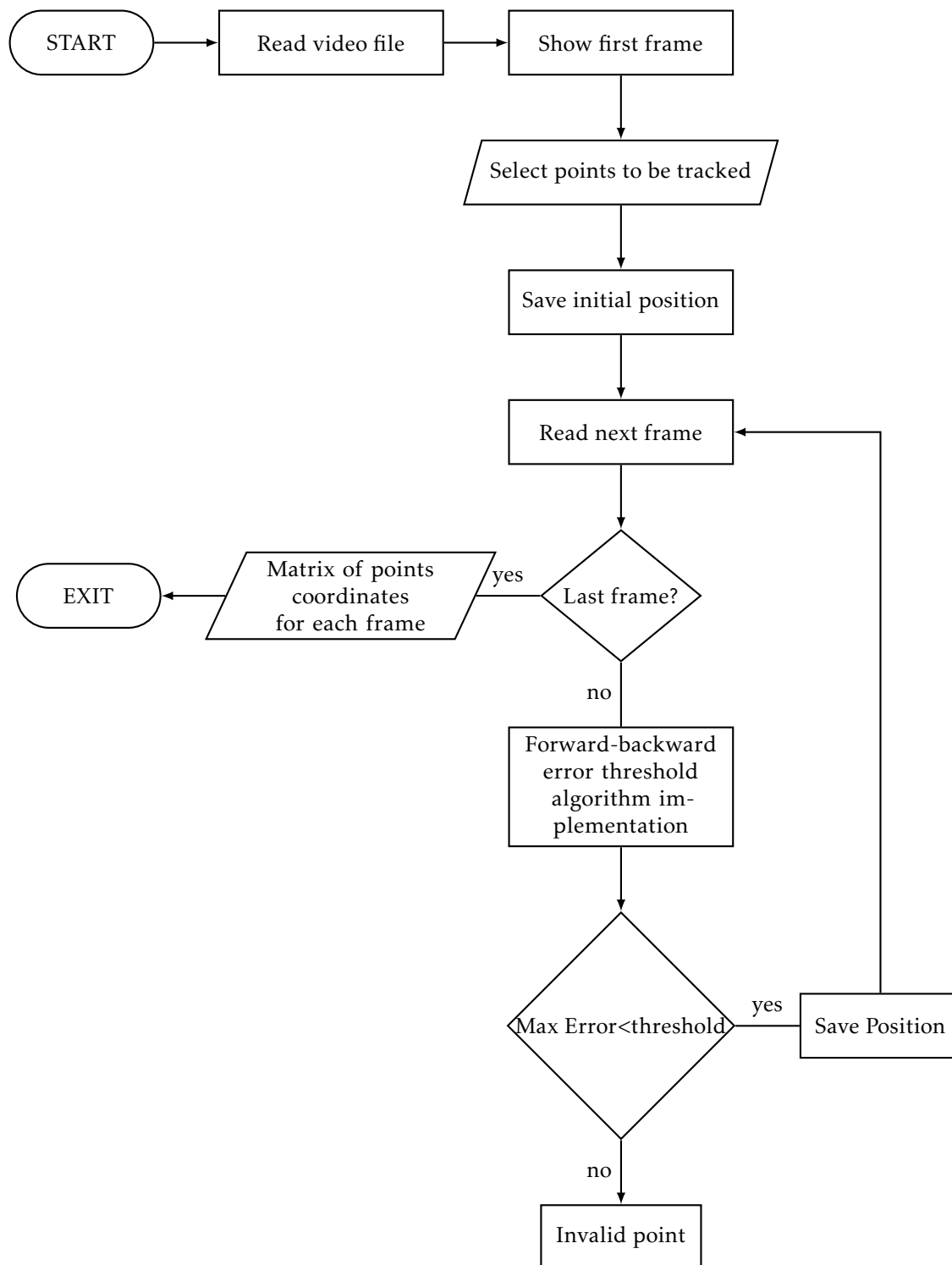
Figure 3.11: Flowchart of the tracking point MATLAB script
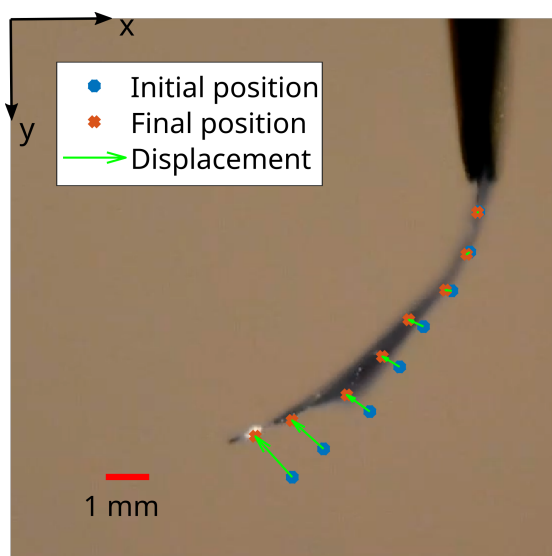
Figure 3.12: Displacement measurement through video tracking in MATLAB

3.4.3   Light-induced bending of DTE-UPy-PEB thin films

With the experimental set-up 1, we observed the thin films' first photomechanical response. For this, the Hamamatsu lamp was set at 10% intensity for VIS irradiation and 5% intensity for UV irradiation (around 1.1 mW/m^2). The samples were cut out from thin films elaborated by spin-coating of around $10 - 20$ µm thickness, the sample's dimensions were 1 mm wide and 5 mm long. The bending of the first studied sample occurred during both 50 minutes of VIS and UV irradiation, with a maximum displacement of 0.85 and 0.51 mm respectively.

The displacement during UV irradiation was smaller since the film's VIS deformation left it almost parallel to the beam light. It is important to mention that the films did not present color change during the period of photoirradiation, thus the time given was not quite optimal.

The experimental setup 2 facilitated us the photoirradiation time programming, being able to obtain the videos for complete VIS-UV irradiation cycles at longer periods, extended up to 5 hours VIS and 3 hours UV irradiation, time in which the sample presented photochromism.

However, the beam combiner reduced the UV intensity so we put the LEDs in different positions with reference to the sample. To keep the perpendicularity of the light beam to the sample surface, the LEDs were positioned facing each other with the sample in the
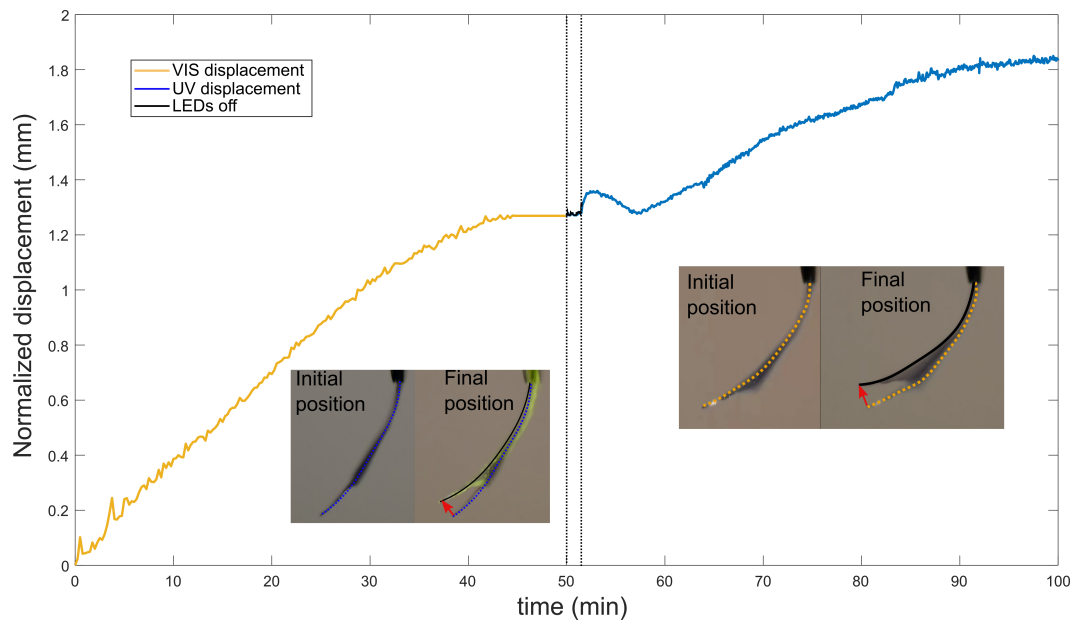
Figure 3.13: Displacement calculation of thin films under VIS-UV irradiation using set up 1.

middle (fig.3.14). The samples studied in these two configurations were also extracted from spin-coating films.
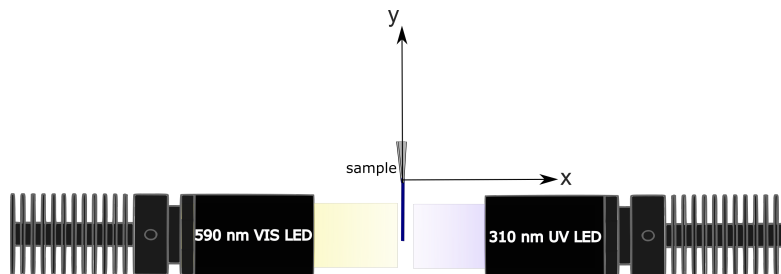
Figure 3.14: LEDs arrangement without the beam combiner

This LEDs arrangement allowed us to see in detail the bending direction of the film in relation to the beam light direction. The analyzed sample underwent one cycle of photoirradiation, 4.5 hours of VIS light and 3 hours of UV light, both at 0.1 mW.

Our analyzed specimen exhibited a bending direction pattern: during the 4.5 hours of visible irradiation it bent towards the light and during the UV irradiation bent in the away from the light source changing direction in the middle of the irradiation period (fig. 3.15). In this case the displacement in the y can be neglected because the
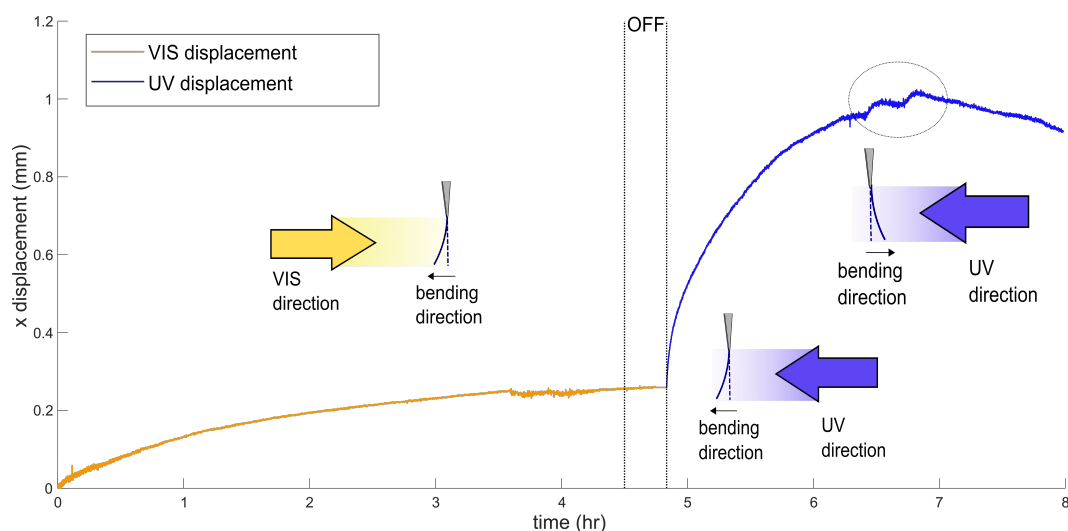
Figure 3.15: Bending direction according to the light source direction.Under VIS irradiation the sample bends towards the light and under UV irradiation bends away from the light changing direction after 2 h of light exposure (circled)

displacement in x direction is more significant.

The direction switch happened when the sample turned visible blue. This is a phenomenon that could be explained based on the results of Kitagawa [28]. Initially, as the specimen is irradiated with UV light, the OF to CF conversion occurs randomly. This means that the transformation may occur at different thickness depths (as the UV light can penetrate the material further than VIS light) inducing repulsion between OF and CF isomers and, resulting in an expansion of the photo-reacted layer. As the CF population grows, the said repulsion decreases and CF isomers create interaction between each other, producing contraction of the material. Hence, changing the bending direction.

3.5   Photokinetics of DTE-UPy-PEB thin films

To analyze the photokinetic behavior of the thin films, various UV-VIS absorbance tests were performed using a CARY1 spectrometer and an *in situ* transmittance measuring was implemented as well (fig. 3.16). The samples were tested at different photoirradiation times to observe the difference in UV-VIS spectra as the photoisomer population changes.

We use for the *in situ* transmittance measurement in figure 3.16 one Helium-Neon
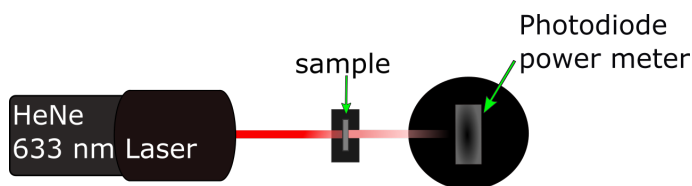
Figure 3.16: Transmittance measurement method

(HeNe) laser, supplemented with two neutral density filters of 6 and 1 to reduce the light power and avoid interactions with the thin film sample, and a photodiode powermeter. The results were later compared with those of the CARY1 at 633 nm to validate the measurement *in situ*.

Absorbance measurements at different photoirradiation times

We carried out the UV-VIS absorbance spectra of the thin films using the CARY1. In the first measurement, the sample contained only CF isomers. Then, the sample underwent visible (VIS) irradiation for 1 minute, obtaining a second measurement in the CARY1 afterwards. This process continued, gradually increasing the exposure time to 3, 10 and 20 minutes. As the OF isomers population increases with VIS exposure, the absorbance in the VIS range decreases (fig. 3.17a). Similarly, the inverse process was completed under UV irradiation. In this case the absorbance increases as the UV exposure time increases(fig. 3.17b).

The same procedure was performed using the experimental set-up in figure 3.16. In this case the transmittance is measured *in situ*. Absorbance (A) and transmittance (T) are related by the equation:

$$T = \exp(-A) \tag{3.1}$$

And the absorbance is simply calculated as:

$$A = \log \frac{P_0}{P_t} \tag{3.2}$$

Where P_0 is the power of the light source and P_t is the transmitted power measured by the power-meter.

The calibration between the CARY1 and the laser is displayed in figures 3.18a and 3.18b. The measured points are showed in figures 3.17a and 3.17b (red dashed line) where

(a) VIS irradiation
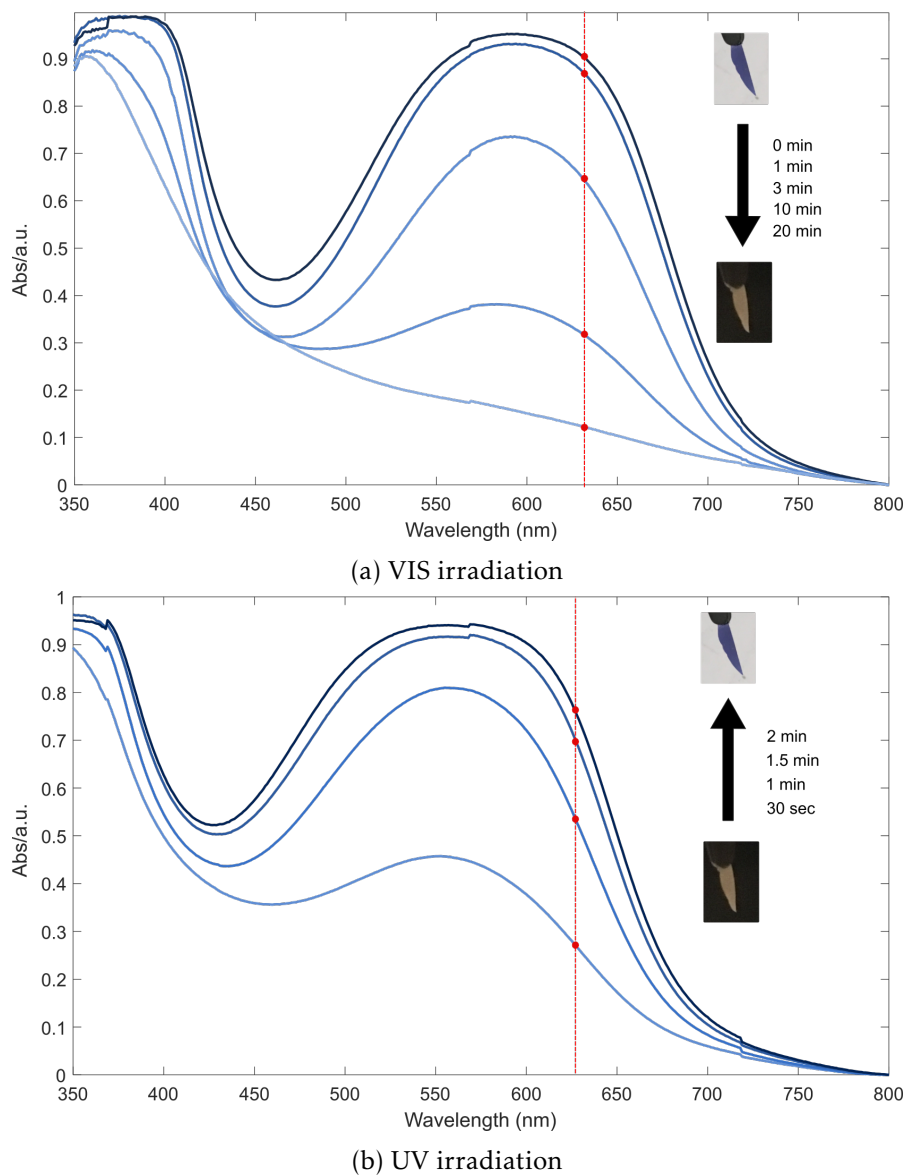
(b) UV irradiation

Figure 3.17: Absorbance spectral change of a DTE-UPy-PEB thin film after VIS and UV irradiation at 590 nm and 310 nm, respectively. The red dashed line represents where the absorbance measures corresponds to 633 nm, the laser wavelength used for *in situ* absorbance measurement.
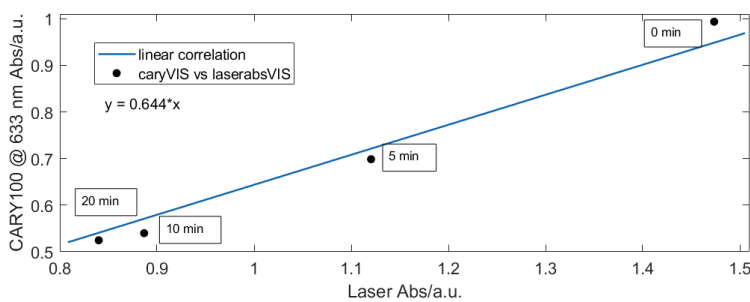
(a) VIS irradiation
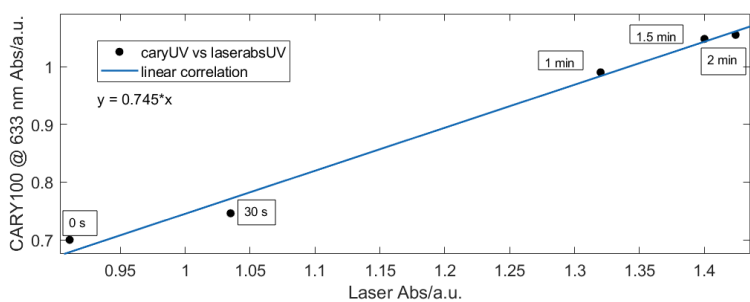
(b) UV irradiation

Figure 3.18: Linear correlation between the absorbance measurements *in situ* and in the CARY1 for 633 nm wavlength

the 633 nm line intersect. The linear correlation determines to what extent the *in situ* measurements vary from that of the CARY1.

Absorbance measurements at different DTE concentrations

Different solutions at different DTE concentrations were prepared to measure the absorbance spectra in the CARY1 spectrometer.

The concentration varied depending on a desired molar ratio from 0.4:3, 0.8:3, 1:3 and 1.2:3.

The same effect observed in the previous experiment is observed when the DTE concentration in the thin films changes. As the DTE concentration decreases, the absorption of DTE molecules in the visible spectrum drops (fig.3.19).
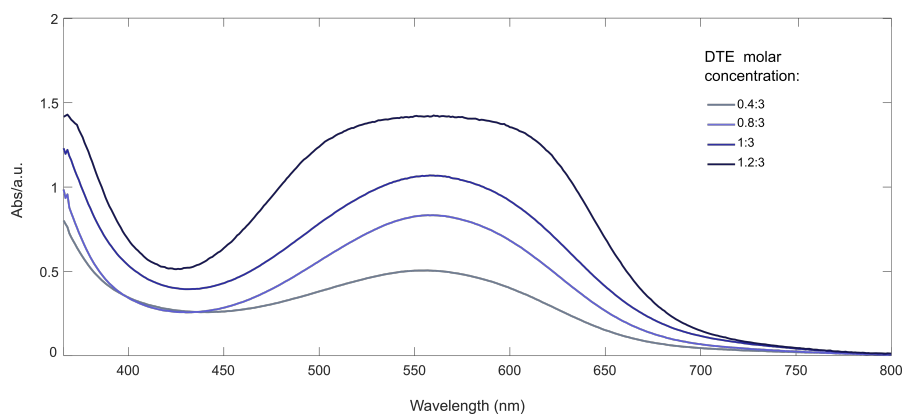
Figure 3.19: Absorbance spectra at different DTE concentrations

3.5.1   Photokinetics during light-induced bending under VIS-UV irradiation

The DTE-UPy-PEB thin films, initially blue, change into colorless form when irradiated with VIS light at 590 nm. The color transition is associated with the CF to OF isomerization process of the sample.

The color transition was analyzed using the image processor ImageJ with an open source plug-in that calculates the pixel intensity (or gray value). It assigns to each pixel from a selected region of interest (ROI) a value from 0 to 255 (being 0 black and 255 white). The software treats the video as a stack of pictures, enabling the frame-by-frame analysis.

An example of this color transition is shown in figure 3.20 where the ROI is selected on a section where the sample presents no position change and the photochromism is visible. The pixel intensity grows exponentially during the VIS exposure and an exponential decay occurs in UV irradiation. The data from the VIS and UV stages can be fitted into a first order kinetics equation where the time or kinetic factor k provides information about the velocity of phototransformation.

The first order kinetics reaction is:

$$A \xrightarrow{\text{k}} B$$
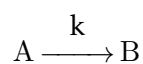
And the equation that describes the transformation during VIS irradiation from A to B in terms of the pixel value $p(t)$ as a function of time:

$$p_{vis}(t) = 1 - \exp(-k_{vis}t) \tag{3.3}$$
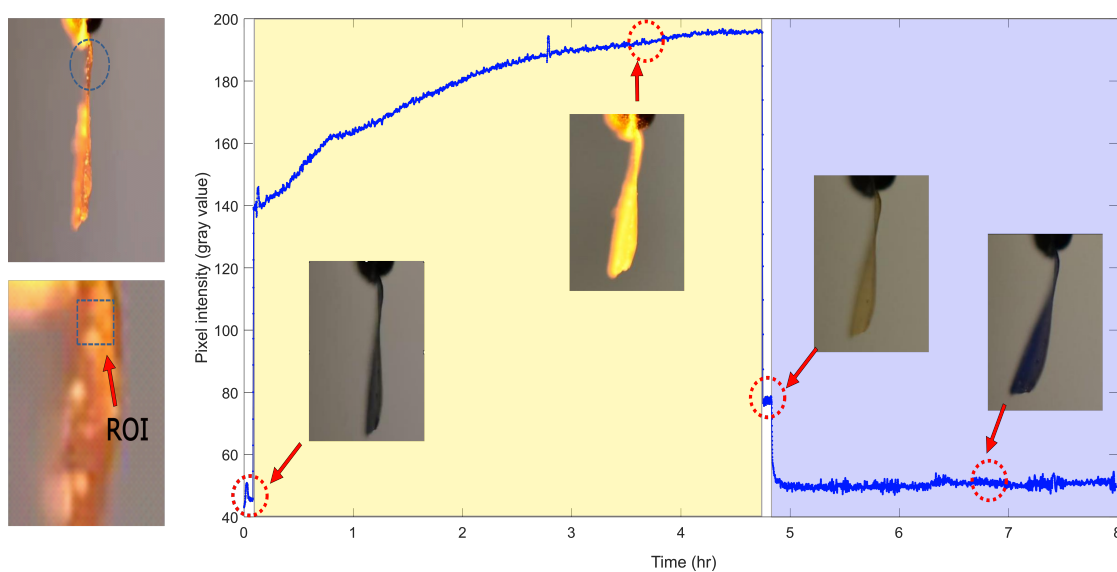
Figure 3.20: Video analysis of DTE-UPy-PEB thin film photochromism by computing the gray value of the ROI (left) at each frame

During UV irradiation the pixel intensity decay is described by:

$$p_{uv}(t) = 1 + \exp(-k_{uv}t) \tag{3.4}$$

The experimental data fit was done implementing the built-in fitting application in MATLAB resulting: $k_{vis} = 1.66$ and $k_{uv} = 0.0186$, both in x10^{-4}s^{-1}. The photoswitching from CF to OF is faster than that of the OF to CF, i.e., $k_{uv} \ll k_{vis}$.
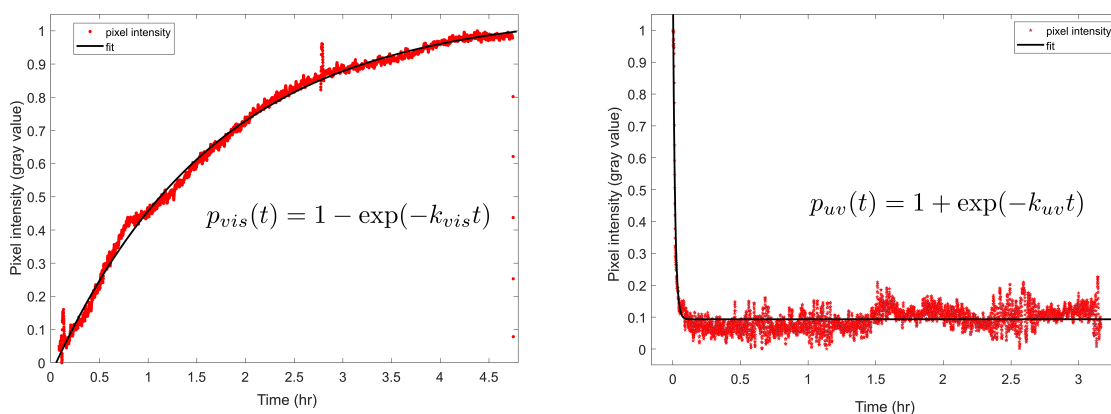
Figure 3.21: Curve fit first order kinetics model for VIS (left) and UV (right) irradiation

3.5.2   Transmittance measurements under irradiation cycles

To measure the transmittance during the photoirradiation cycles, the films elaborated by the spin coating method were also tested under the experimental setup shown in figure 3.22. For this test, we used the same LED power lamps in a multi-wavelength beam combiner, a 635 nm compact laser with USB connector and a photodiode power meter. The 635 nm laser beam was pointed to the upper part of the sample, to avoid errors in the measurement affected by the sample bending. The photodiode power meter, assembled with a 635 nm filter, was placed behind the sample so that the photodiode detects the transmitted power of the laser beam.

(a)

(b)
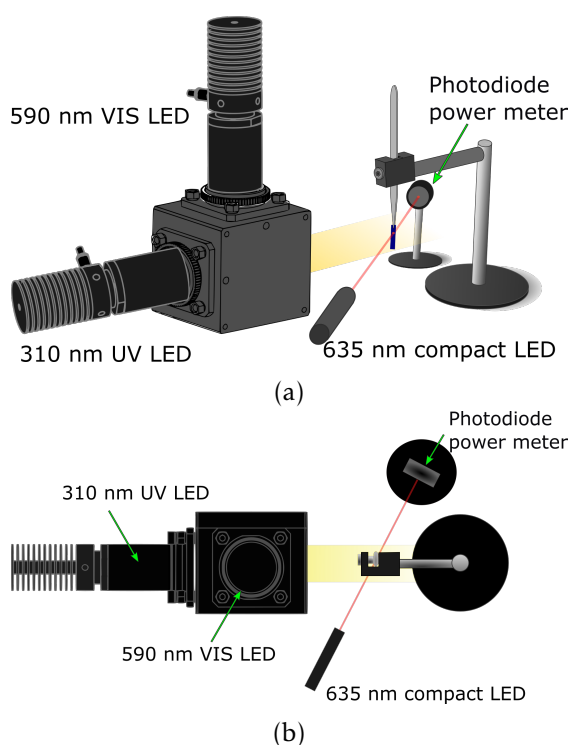
Figure 3.22: Transmittance measurement experimental setup

The sample was irradiated during 5 hours with VIS and UV light with a 15 min LEDs off step between photoirradiations. The LEDs intensity remained the same as in the previous experiments where we observed the photo-induced bending. In figure 3.23, the VIS light transmittance is an increasing function of time. Inversely, the transmittance under UV irradiation is decreasing in time.

From the results of the different tests performed in this current section, we deduce that
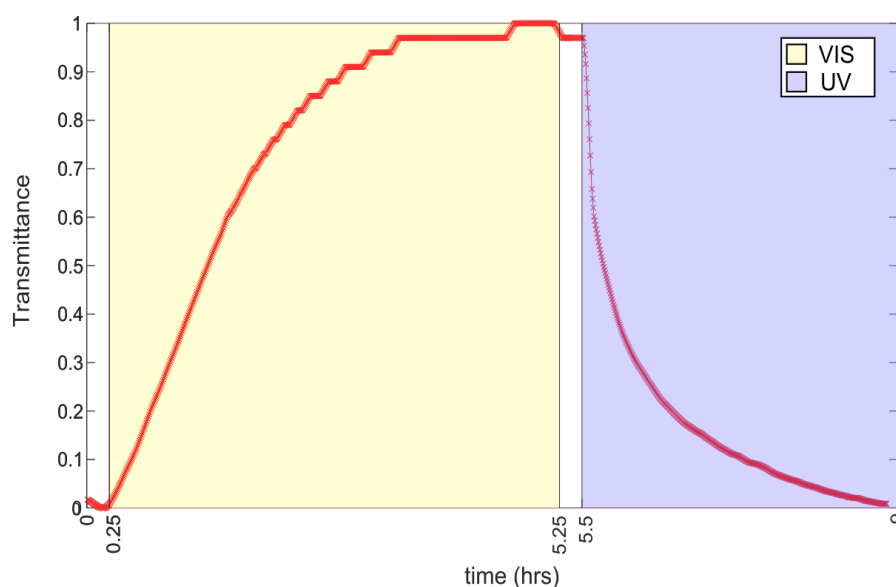
Figure 3.23: Transmittance measurement under VIS-UV photoirradiation cycles

the transmittance, as well as the absorbance, are function of the photoisomer population. Being that, the transmittance is directly proportional to the increase of OF population in time and, inversely proportional to the increase of CF population.

3.6   Relation between photokinetics and photomechanical effect

In chapter 1, we revisited the first observed photomechanical effects in DTEs. One of the common characteristics is that the photochromism occurs in parallel with the photomechanical deformation. From the photo-induced bending analysis of DTE-UPy-PEB thin films compiled in this chapter is noticeable that the bending is linked with the DTE photokinetics.

By observing the videos, we can verify that the thin film changes color. Using the method described in the section 3.5.1, we demonstrated that the color transition time varies between VIS and UV irradiation. The photomechanical effect during VIS and UV varies as well depending on the type of light irradiation (figure 3.15).

As exhibited in the figures 3.17a, 3.17b and 3.19, the photochromism of the thin films is related to the OF and CF transformation. It is, at the same time, associated with the absorbance/transmittance of the sample. Hence, the photo-induced deformation is
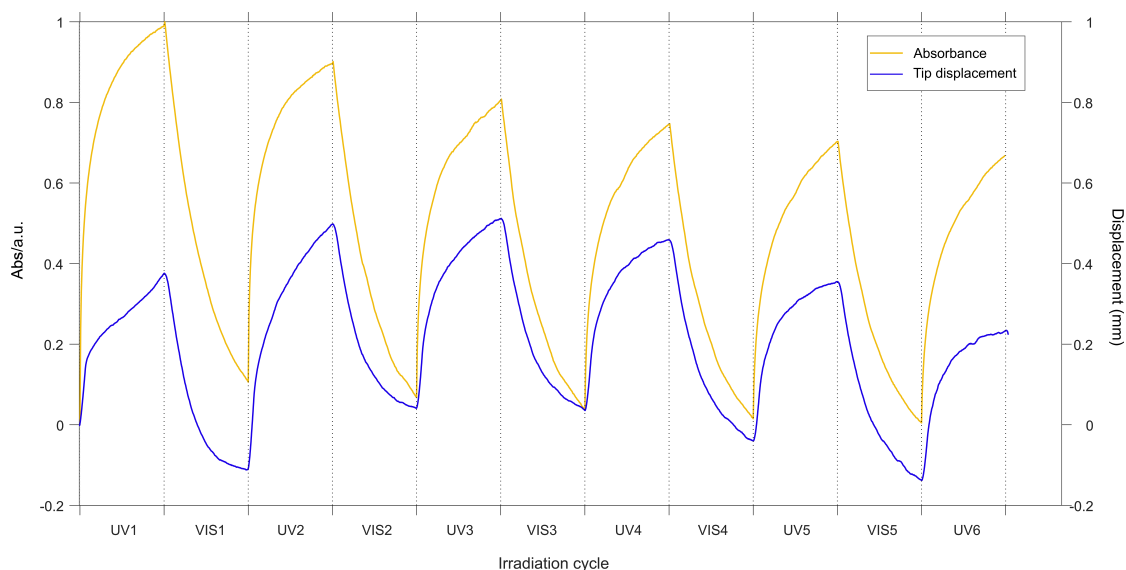
Figure 3.24: Absorbance *in situ* compared with the sample's tip displacement. Evidently, the photo-induced bending is related with the DTE photochemical transformation

related to the photokinetics of the DTE.

In the figure 3.24, the absorbance (measured *in situ*) and tip displacement are compared during 5 photoirradiation cycles. The displacement measurements were performed using a different experimental setup with a microscopic camera, which enables a more detailed view of the sample. Both, absorbance/transmittance and photo-induced bending were captured in parallel. This image aid us to associate more clearly the photomechanical effect with the photochemical transformation.

In the next chapters, we will explore more thoroughly this theory to build up a mechanical model that represents this phenomenon.

Mechanical characterization of DTE-UPy-PEB thin films

Photo responsive materials react macroscopically to light stimuli in different ways: bending, expansion, contraction, twisting, jumping, etc. To link the photo response with the mechanical behavior, recent work has been conducted to test mechanically photo-responsive polymer samples under photoirradiation. Light-induced changes in the photomechanical materials behavior depend mostly on the light intensity and on the volume fraction of transformation altering the time-dependent behavior [34, 132–134].

It is known that temperature variations affect the mechanical behavior of most materials. Light irradiation of active materials can influence their mechanical behavior similarly. Koseki [135] measured the light-induced relaxation of amorphous selenium films, where the photo-induced bond interchange creates an expansion of the material and, therefore, a light-dependant stress relaxation.

For this thesis, we studied the macroscopic mechanical response under photoirradiation of supramolecular DTE-UPy-PEB thin films. The samples were produced by a combination of two methods: drop casting (section 3.2) and thermoforming (section 3.3), using a hydraulic press at 80°C and 60 bar with molds made of yellow silicon paper. Drops of the DTE-UPy-PEB solution were deposited on silicon paper. Once dried, they were carefully removed and used to fill the molds to use in the hydraulic press. Obtaining at

(a) TA instruments RSA3 Dynamic Me-
chanical Analysis (DMA)

(b) Instron Electropuls E3000

Figure 4.1: Instrumentation utilized for the mechanical characterization of DTE-UPy-PEB and PEB-UPy thin films. RSA3 DMA provided by the laboratory UMET (Unité Matériaux et Transformations).

the end rectangular samples of 10x6x0.07 mm.

The mechanical tests carried out were: :

- Mechanical characterization of functionalized PEB

- Dynamic Mechanical Analysis (DMA): Frequency Sweep

- Stress relaxation tests

- Axial tensile test

- Creep tests

For these tests we used a TA instruments RSA3 Dynamic Mechanical Analysis (DMA) machine (fig. 4.1a)and an Instron Electropuls E3000 (fig. 4.1b), with a 10 N load cell for the creep test.

4.1   Mechanical characterization of PEB-UPy thin films

In previous work [24], an extensive chemical and thermal characterization for the functionalized PEB-UPy thin films was performed. In summary, the PEB-UPy thin films

are semi-crystalline polymers with 23% of crystallinity, these crystal fragments melt at 50 °C and completely disappear at 70 °C.

Previously in this thesis (section 3.1.2), it was explained how the functionalization of polymers with hydrogen bonding UPy improves some of the polymer mechanical characteristics, especially the ability to reassembly itself upon external stimulus. This is observed as a greater Young modulus by comparing the functionalized versus the non-functionalized PEB in a Dynamic Mechanical Thermo-Analysis (DMTA). Additionally, the functionalized PEB showed more resistance to degradation by comparing with non-functionalized PEB in a thermogravimetric analysis (TGA).

Two kinds of functionalized PEB have been prepared by our collaborators:

i. an optimum compound fully functionalized with UPy moieties, i.e. 100% functionalized (fig. 4.2 (a)) and,

ii. an analogous compound with around 50% functionalization in which the network is build up with a mixture of polymer chains which may have UPy at both ends, at only one or none (fig. 4.2 (b)).
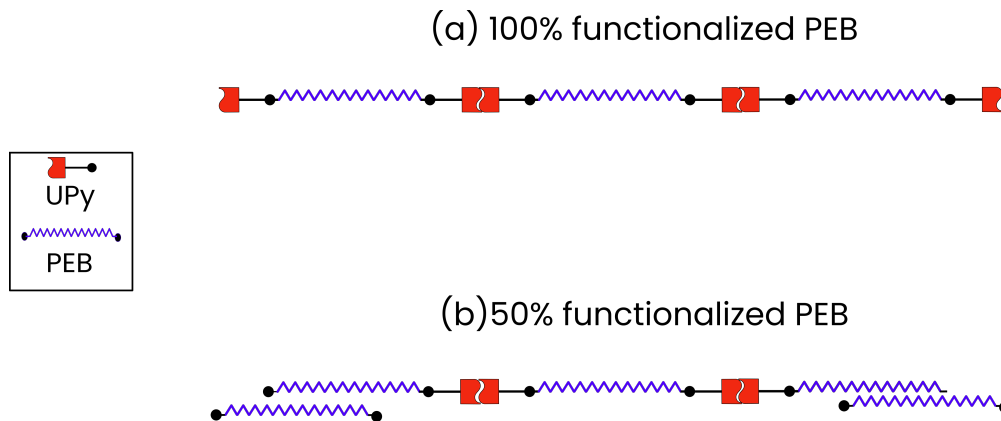
Figure 4.2: Scheme of PEB-UPy functionalization

4.1.1 UPy Functionalization influence on mechanical behavior

Stress relaxation and tensile tests were performed to assess the mechanical behavior of the B_{100} and B_{50} thin films. For the stress relaxation tests, samples of 10x5x0.07 mm were tested at 0.6% deformation during 1 hr (fig. 4.3).

To identify the distinction between the both, we did a fit using the Weibull equation (eq.
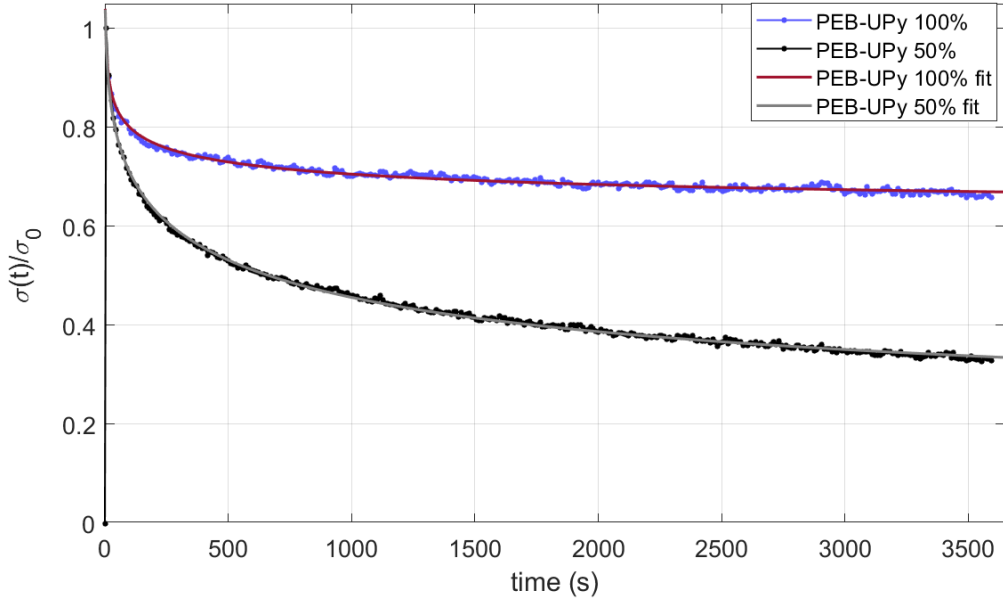
Figure 4.3: Stress relaxation curves for UPy functionalized PEB thin film at 100% (blue) and 50% (black).

PEB-UPy	τ_σ(s)	k_2	β
100% func.	3.24	0.6	0.15
50% func.	331.5	0.21	0.30

Table 4.1: Weibull parameters for stress relaxation of 100% and 50% functionalized PEB-UPy

4.1) for stress relaxation [136].

$$\frac{\sigma(t)}{\sigma_0} = \exp(-\frac{t}{\tau_\sigma})^\beta + k_2 \qquad (4.1)$$

where τ_σ is the stress relaxation characteristic time, k_2 the final decrease of the stress fraction and β is the shape parameter.

From the stress relaxation tests results (table 4.1), we could note that the fully functionalized elastomer has a lower characteristic time, meaning that it reaches the plateau or final stress fraction k_2 in less time than the half-functionalized PEB. In general, the UPy functionalization gives the elastomer flow resistance.

The PEB-UPy thin film samples underwent also tensile test using the DMA RSA3, with a constant strain rate of $1x10^{-4}s^{-1}$ during 100 seconds to remain in the linear region.

PEB-UPy	EMpa
100% func.	21.8
50% func.	21.1

Table 4.2: PEB-UPy Young Moduli

The samples functionalized at 50 and 100% demonstrated similar tensile behavior, as we can appreciate in figure 4.4.
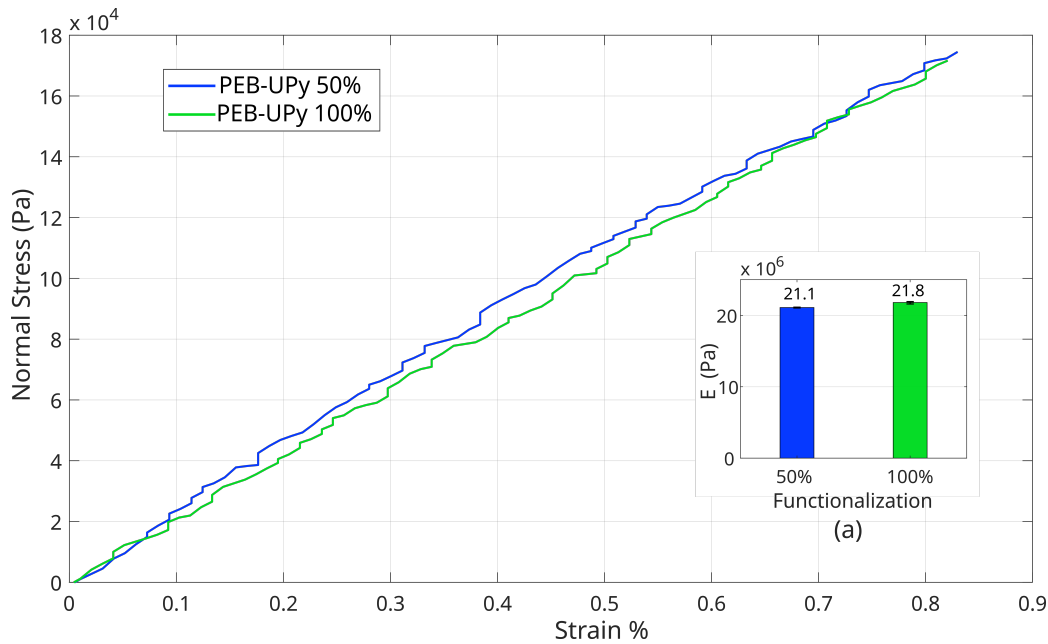
Figure 4.4: Stress-strain curve for the PEB-UPy functionalized thin films at 50 and 100%. (a) Calculated Young Moduli

Calculating the Young modulus for both of the functionalized thin films, we obtained that E_{100} and E_{50} differ by 0.7 Mpa, which is nearly negligible (table 4.2).

The type of functionalization influences only the time-dependent behavior, while the rigidity remains unaffected.

4.2 Dynamic Mechanical Analysis (DMA): Frequency Sweep

First, Dynamic Frequency Sweep (DFS) tests were carried out to have an initial understanding of the type of polymer behavior the DTE-UPy-PEB thin films have and it helped us to get the strain percentage necessary to attain the expected stress-relaxation

results.

DFS tests went from 0.1 to 100 Hz (0.6 to 600 rad/s). The PEB-UPy and the DTE-UPy-PEB thin films underwent DFS tests at 0.4% strain. The strain value was determined by performing a quick Dynamic strain sweep, identifying the Linear viscoelastic region (LVER) (fig 4.5).
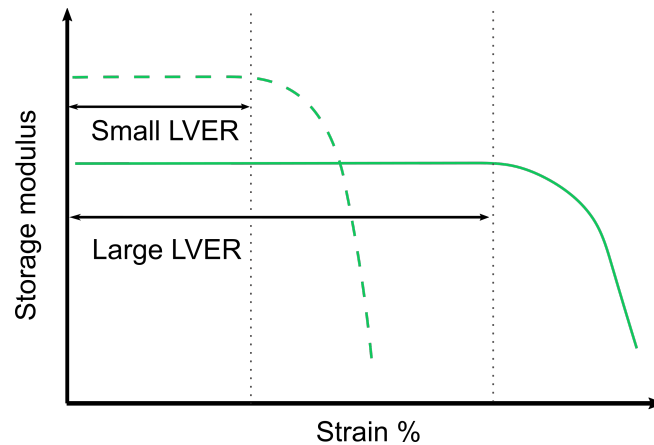
Figure 4.5: Identifying the linear viscoelastic region (LVER) in a dynamic strain sweep [137]

In both cases, pure elastomer and elastomer with DTE, the loss factor ($tan\delta$) remained between 0° and 0.1° in the 0.6 to 100 rad/s range. The Loss ($E^{''}$) and the Storage modulus ($E^{'}$) are linear with respect to the frequency in this range. In the region above 100 rad/s, the samples enter a fluctuating area (figures 4.6 and 4.7).

DFS tests are useful to identify viscoelastic properties of the sample in function of a timescale. In our case, the storage modulus dominates, which tells us that the material structure is more elastic than viscous. Also, the addition of DTE increases both the storage and loss modulus ($E^{'}, E^{''}$) up to 5 times.

Moreover, it has a time-dependent viscous factor and it can be represented by the SLS model (section 2.1.1)[137].
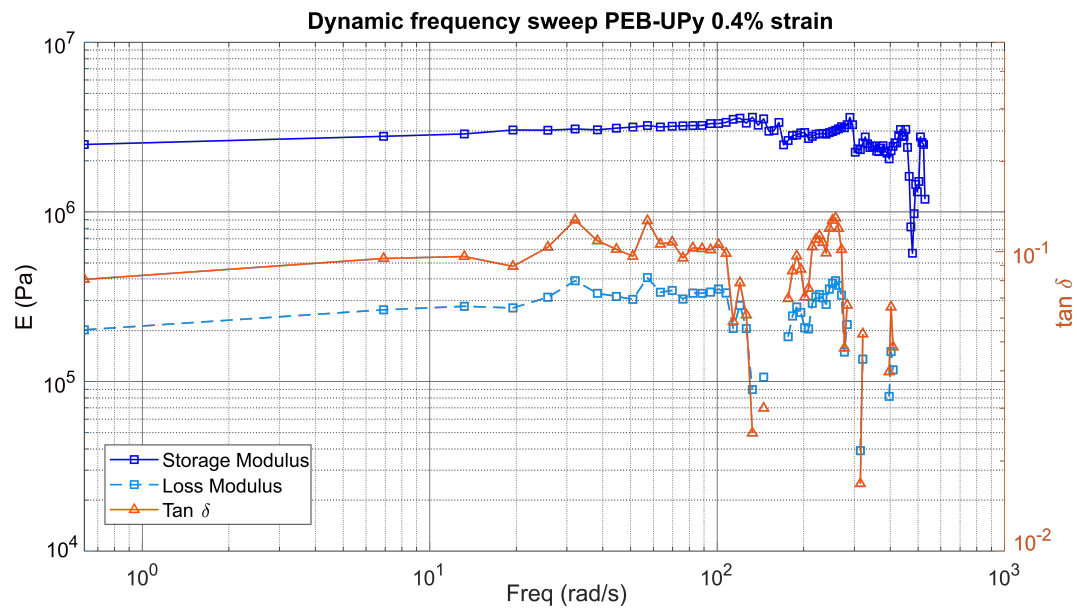
Figure 4.6: DFS of PEB-UPy thin film at 0.4%
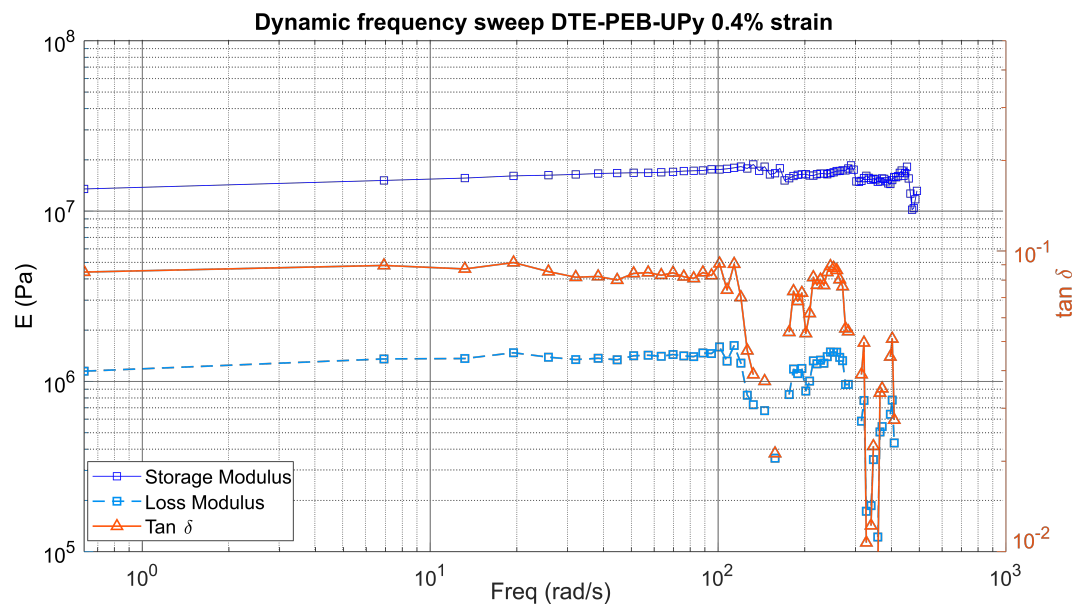
Figure 4.7: DFS of DTE-PEB-UPy thin film at 0.4%
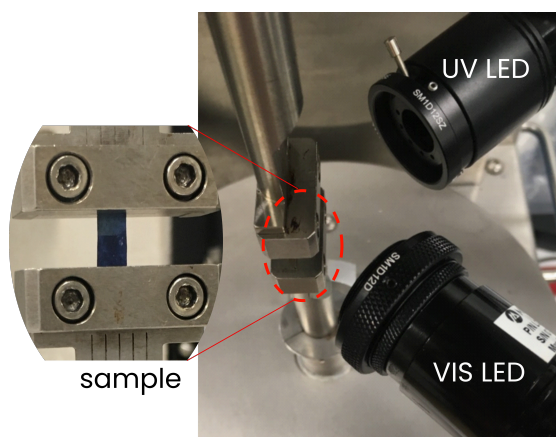
Figure 4.8: Experimental setup for the stress relaxation tests under VIS-UV photoirradiation cycles in the DMA RSA3

4.3   Stress relaxation tests under VIS-UV photoirradiation cycles

Using the RSA3 DMA, we subjected DTE-UPy-PEB rectangular specimens to stress-relaxation tests at a constant 0.6% deformation. The specimens' length varied from 15 to 20 mm, the width from 5 to 6 mm and, the thickness from 70 to 80 microns. The thin films varied in DTE:PEB molar ratios: 1:1, 1:3 and 1:8.

When the sample attained a relaxation plateau, it was irradiated with visible light during 2 to 3 hrs next, a period of no irradiation and then 2 to 3 hours of UV irradiation. We followed the same photoirradiation cycles of the photo-induced bending experimental observations. Also, the same MIGHTEX LEDs at the same intensity were used.

The DTE-UPy-PEB thin films exhibited an instantaneous stress decrease at the moment the light exposure began. This stress loss varied depending mainly on the type of light and intensity. For the thin at 1:3 molar ratio, after the first 30 minutes, it reached the stress plateau. Immediately, the VIS irradiation began, and the stress dropped from 0.84 to 0.8. During the VIS irradiation, the material continued the stress relaxation. After the irradiation ceased, the material recover from 0.74 to 0.75. Similarly, during the next VIS photo-irradiation, the thin film experienced an instantaneous stress drop, observing a recovery at the final of the irradiation period.

Concerning the stress relaxation during UV irradiation, the value of the stress loss is lower than those observed during VIS irradiation, although the after photo-irradiation
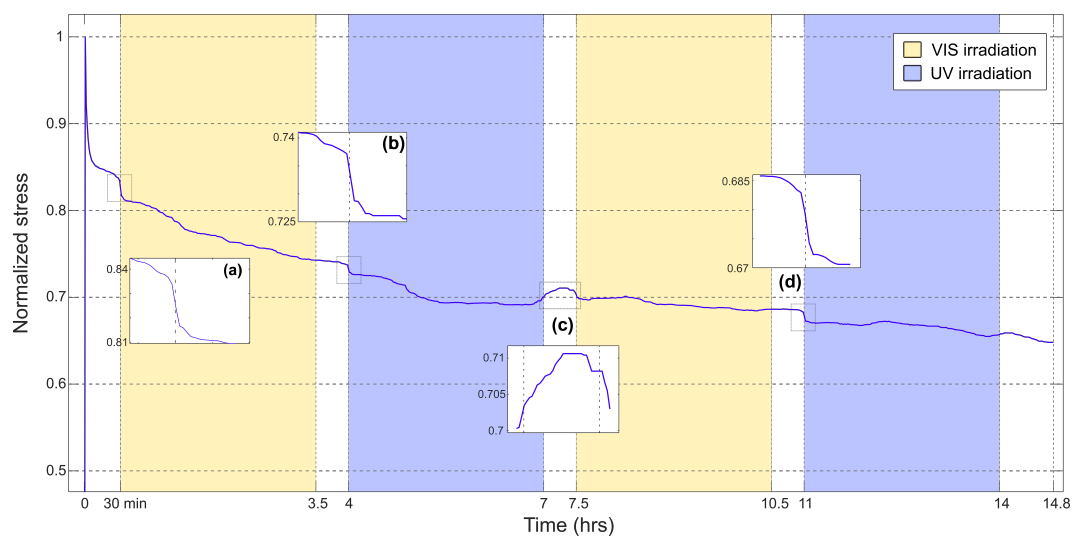
Figure 4.9: DTE-UPy-PEB 1:3 molar ratio thin film stress relaxation. (a), (b) and (d) show the light-induced stress decrease at the instant the irradiation starts. After the UV irradiation there is stress recovery (c).
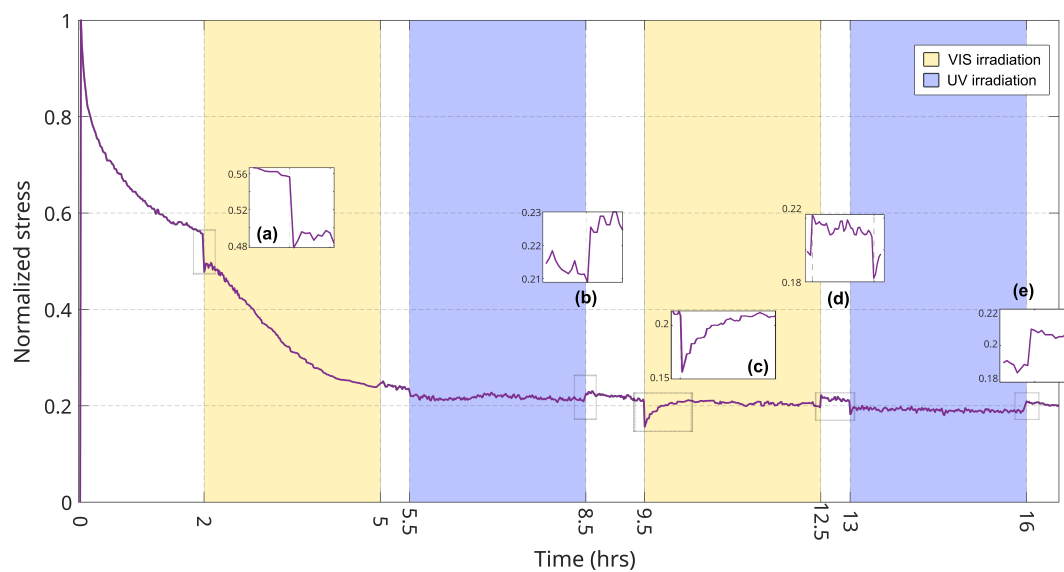
Figure 4.10: DTE-UPy-PEB 1:1 molar ratio thin film stress relaxation. (a) and (c) show the light-induced stress decrease at the instant the VIS irradiation starts. After the UV irradiation there is stress recovery (b) and (e). (d) At the end of the second VIS irradiation the sample recovers and relaxes as the second UV irradiation starts.
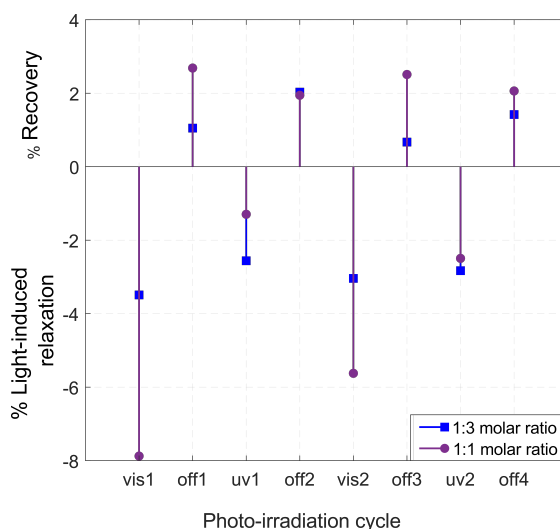
Figure 4.11: Light-induced relaxation and post-irradiation stress recovery comparison between films 1:1 (violet) and 1:3 (blue) molar ratios.

recovery is more noticeable.

The thin film at 1:1 molar ratio showed similar patterns to the one previously described. It took 2 hours to reach the plateau and after, the VIS irradiation started. The VIS light-induced stress decrease was bigger than that of the previous sample, going from 0.56 to 0.48 for the first irradiation. In the second VIS irradiation, there is an instantaneous stress drop following a gradual stress recovery reaching the value of 0.2 ((c) in figure 4.10), where the sample is completely relaxed. The after photo-irradiation recovery is observed, after the UV irradiations and also after the second VIS light exposure.

In the same manner, two thin films with molar ratios 1:1 and 1:8 were tested under photoirradiation cycles. This time, the cycles started with UV light.

Both films experienced stress loss induced by photoirradiation. A noteworthy characteristic is that the after light irradiation recovery occurred steadily for half an hour following an equally steady stress drop (fig. 4.12).

The sample at 1:8 molar ratio had an attenuated light-induced stress decrease, showing that the DTE content is too low to induce a stress relaxation. However, it underwent a post-light stress recovery analogously to the 1:1 sample.

To summarize, all tested samples experienced a light-induced stress relaxation. In most of the cases, the one induced by VIS light was greater than the one induced by

(a) Light-induced stress relaxation

(b) Post-light exposure recovery
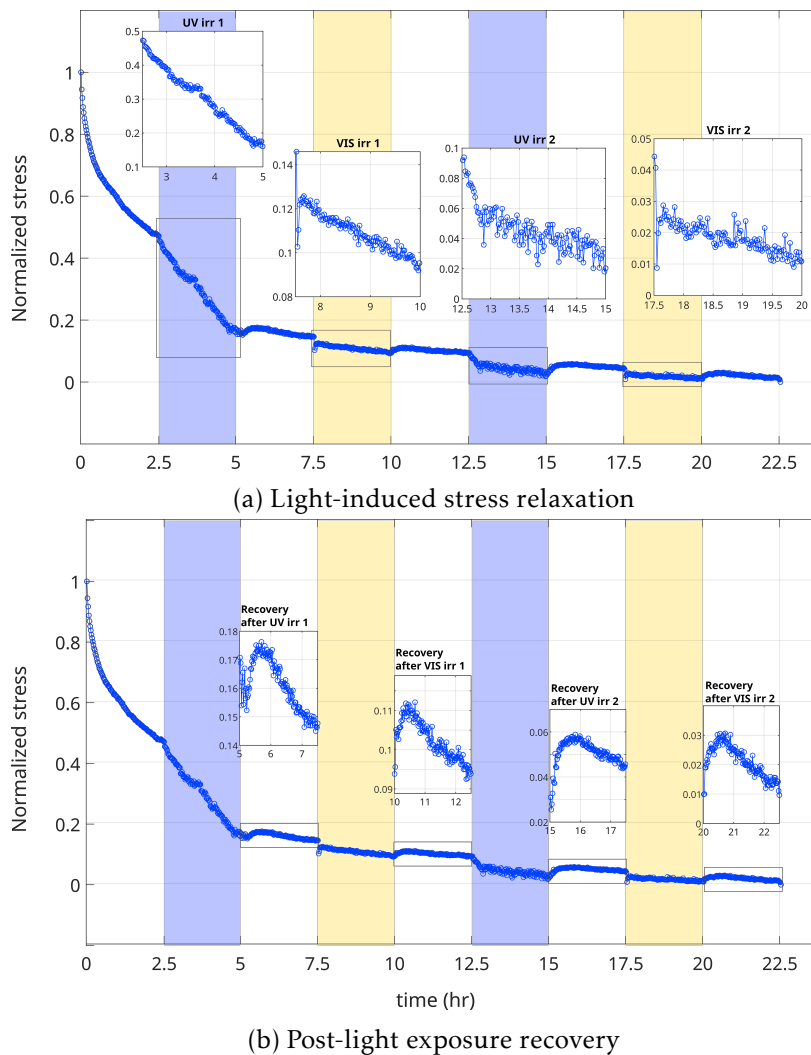
Figure 4.12: DTE-UPy-PEB 1:1 molar ratio thin film stress relaxation. Starting the photoirradiation cycles with UV light for 2.5 hours, VIS irradiation and LEDs-off period for 2.5 hours, equally. (a) shows a closeup detail of the stress relaxation during light exposure and (b) displays the detail of the stress recovery when the light turned off.

the UV light (figures 4.11 and 4.14). Furthermore, all samples experienced post-light stress recovery, being more observable in the tests where the photoirradiation cycles started with UV light (fig. 4.12b). Going back to the initial hypothesis, there is a small mechanical reversibility induced by the light exposure that occurs afterwards. Overtime the thin films continued their mechanical stress relaxation, which overlaps the light-induced stress recovery.
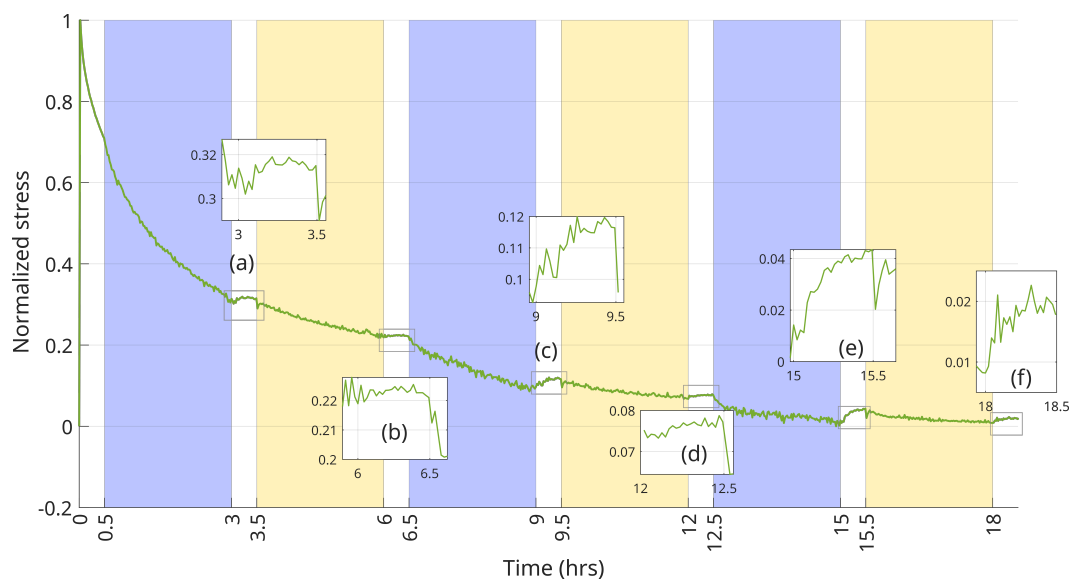
Figure 4.13: DTE-UPy-PEB 1:8 molar ratio thin film stress relaxation. Starting the photoirradiation cycles with UV light for 2.5 hours, VIS irradiation for 2.5 hours as well and LEDs-off 30 min period. The image shows a closeup detail of the stress recovery when the light turned off.
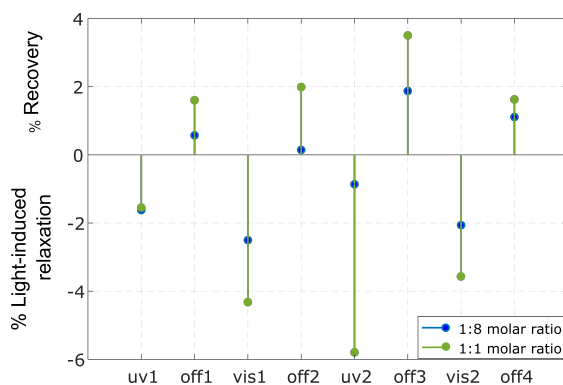
Figure 4.14: Light-induced relaxation and post-irradiation stress recovery comparison between films 1:8 (blue) and 1:1 (green) molar ratio.

4.4 Axial tensile: phototransformation effect on stiffness

The aim of the axial tensile experiments was to approximate the Young modulus value E of the thin films in both closed and open form configurations and to have a first approach to the phototransformation effect on the material's rigidity. We tested the DTE-UPy-PEB thin films in both RSA3 and Instron Electropulse to analyze the time-independent

behavior.

4.4.1 DMA axial tensile test

First, we used the RSA3 to analyze thin film rectangular strips of 10x5x0.07 mm. Although the device's focus is to perform DMA testing, it can perform traction tests in a controlled force/strain rate mode [138]. We carried out the tests with a constant strain rate of $1x10^{-4}s^{-1}$ during 100 seconds to remain in the linear region, thus avoiding fracture.

To obtain the Young modulus in closed form E_{CF}, the sample received 5 hrs of UV irradiation before being tested. After this, the sample remained under 5 hours of VIS irradiation before being tested again to get the Young modulus in open form E_{OF}. It applies to mention that the same sample was used after UV and VIS irradiation to perform the tests.
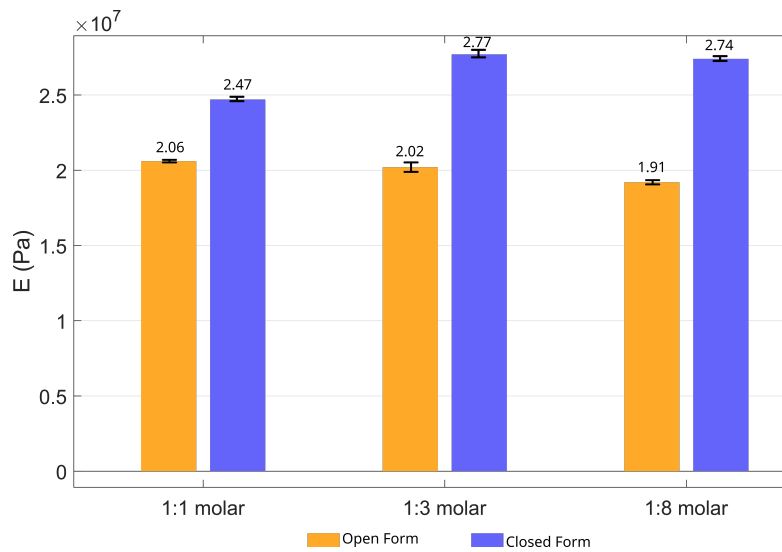
Figure 4.15: E_{CF} and E_{OF} of DTE-UPy-PEB thin films at different molar ratios

The samples had different DTE-PEB molar ratios: 1:1, 1:3 and 1:8. By looking at figure 4.15 we note that E_{CF} is bigger than E_{OF} for all three samples. DTE quantity appears not to influence the thin films stiffness, although more tests are necessary to conclude so. It is clear, however, that the phototransformation changes the material's stress-strain curve (fig. 4.16).

(a) Sample at 1:1 molar ratio.

(b) Sample at 1:3 molar ratio.

(c) Sample at 1:8 molar ratio.
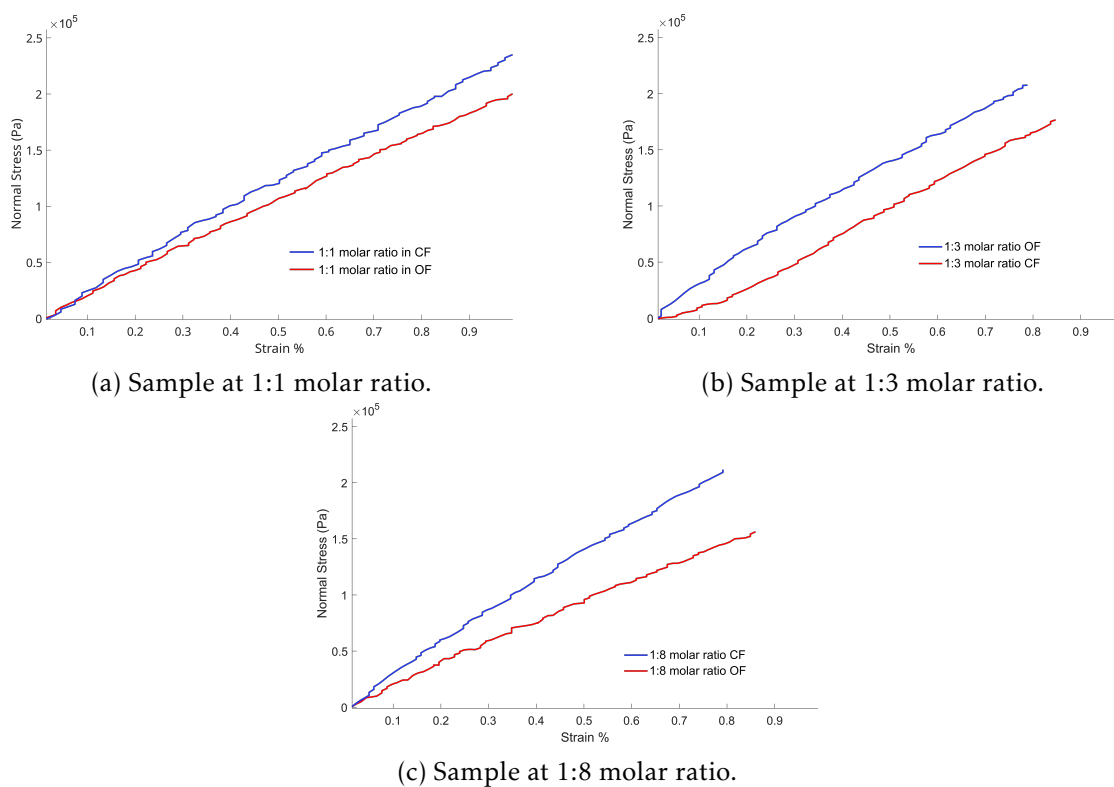
Figure 4.16: Stress-strain curves of DTE-UPy-PEB thin films at different molar ratios after UV (blue line) and VIS (red line) irradiation

4.4.2   Instron Axial tensile test

The samples used for the axial tensile tests in the Instron Electropulse had dog bone shape with dimensions displayed in figure 4.17 and 70 µm thickness. They were also fabricated by thermoforming in the hydraulic press. Here, all samples had a DTE-PEB molar ratio of 1:3 and 50% functionalized PEB.

New non-irradiated samples were tested in both CF and OF, also PEB-UPy thin films samples. The figure 4.17 displays the average curve for each configuration (CF, OF and elastomer). The last point of each curve is the fracture stress, being the elastomer thin films the most stretchable, reaching up to 4.3% of elongation. CF thin films appear to be the brittlest of them all, breaking at 1.75% elongation. OF thin films failed at 4% elongation, similar to the elastomer thin films. All of them exhibit a non-linear stress-strain response.
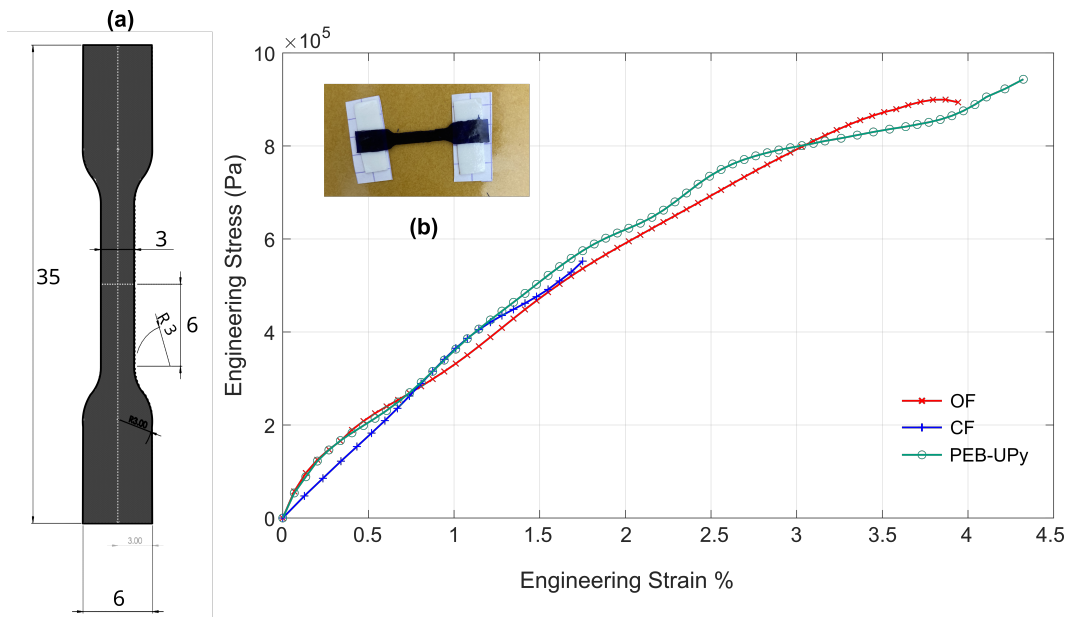
Figure 4.17: Dog bone shape thin film dimensions in mm(a). Average stress-strain curves for thin films in CF, OF and elastomer PEB-UPy (right) at displacement rate of $7x10^{-3}$ mms^{-1}.(b) Thermoformed thin film specimen

4.5 Creep tests during DTE phototransformation

For the creep tests, instead of carrying them out during cycles of photoirradiation, we followed the method showed in figure 4.18. The purpose was to obtain the creep behavior of the non-irradiated and the irradiated thin films to compare the light-induced effect on the thin films in OF and CF configurations. The creep test was carried out using the Instron Electropuls and the samples dimensions are the same as shown in figure 4.17.

As well, we use the same MIGHTEX LEDs at the same intensity as in the previous tests (fig. 4.19).

The nominal stresses applied remained between 0.1 and 0.2 MPa attained in 30 s. In figure 4.20 are displayed the creep behavior of the non-irradiated DTE-UPy-PEB thin film in CF and OF, their behavior is similar at short times ($t < 1000$ s) and at longer times the terminal deformation differs, being 0.62% for CF and 0.54% for OF configuration.

Samples in CF were irradiated with VIS light from $t = 0$ to obtain the creep behavior during the CF to OF transition. Comparing the latter with the non-irradiated CF creep
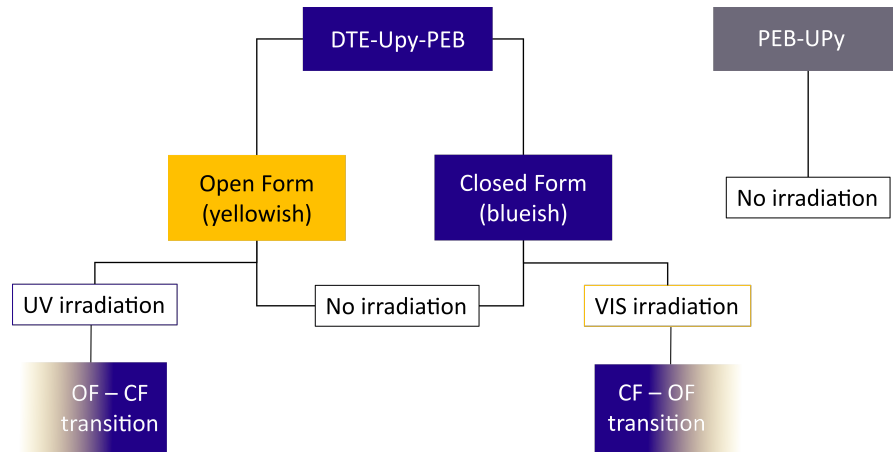
Figure 4.18: Methodology to obtain creep behavior of the irradiated and non-irradiated OF and CF thin films.
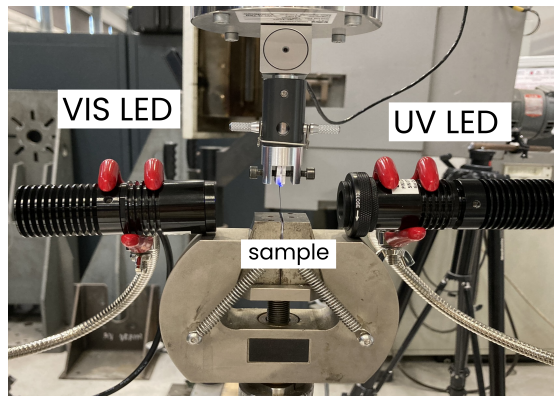
Figure 4.19: LEDs positioning in the creep tests under photoirradiation

curve, we can observe that the deformation increases during the phototransformation (fig 4.21).

In the same way, the OF samples underwent UV irradiation from the beginning of the test, thus obtaining the creep curve of the OF to CF phototransformation. Resulting as well, in an increasing light-induced deformation (fig 4.22). Subtracting the irradiated minus the non-irradiated creep curves, we can obtain the VIS and UV light-induced deformation as a function of time.

The creep tests allowed us to confirm that there is a mechanical effect when the thin films are exposed to photoirradiation. The increasing creep deformation is analogous to the relaxed behavior observed in the stress relaxation tests. Hence, the phototransformation
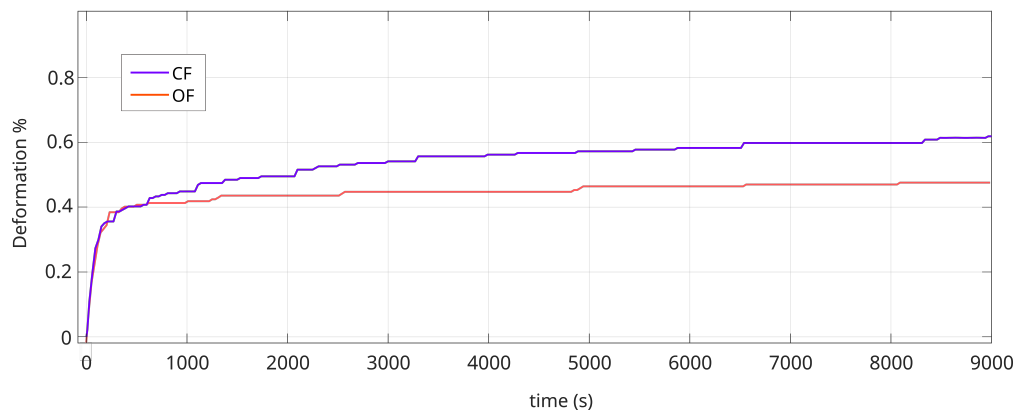
Figure 4.20: Creep behavior of the non-irradiated OF (orange) and CF (violet) thin film
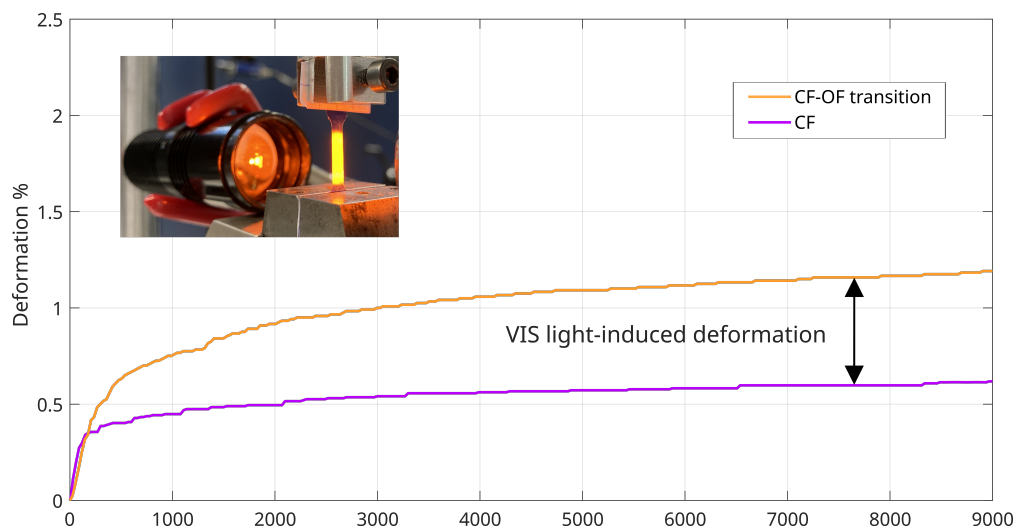
Figure 4.21: Creep curves comparison demonstrating the VIS light-induced deformation

induces a mechanical deformation, which expands the material.

4.6 Conclusions: Light-induced Mechanical Behavior

In this chapter, we described the results obtained for the mechanical testing of DTE-UPy-PEB thin films, as well as PEB-UPy thin films. One of the most relevant result is that the thin films with photo reactive DTE molecules undergo light-induced mechanical behavior, what we could verify in the stress relaxation and creep tests.

This is an effect that has been reported in previous work where polymer thin films with dispersed carbon nanotube (CNT) exhibited a light-induced stress variation when
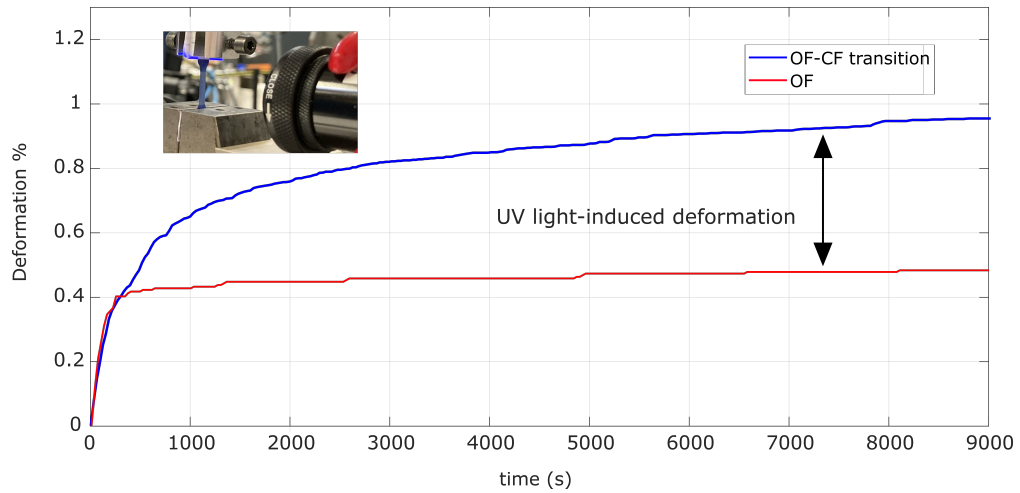
Figure 4.22: Creep curves comparison demonstrating the UV light-induced deformation
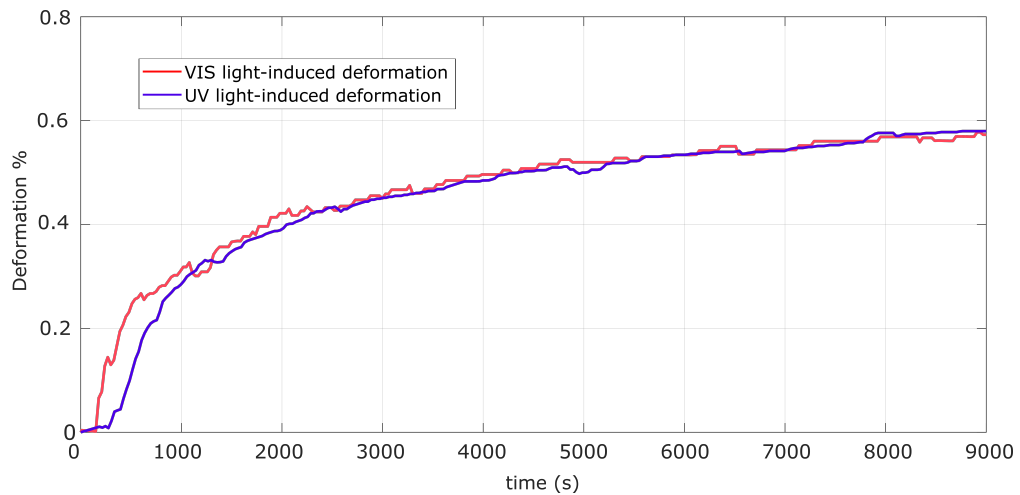
Figure 4.23: ViS and UV light-induced deformation in function of time.

exposed to light. Here, the light irradiation induces the melting of crystalline domains. After removing the light irradiation, recrystallization of these domains occurs and connects to the relaxed polymer chains again, increasing the stress value [139].

In the stress relaxation tests under photoirradiation reported in this work, the isomerization of photo-active molecules induces a network rearrangement, which is displayed as a stress decrease. Long [140] reported this mechanism for photo-induced network rearrangement (PNR) and photo-tuneable molecular cross-links (PMC) materials, that could be extrapolated for the DTE-UPy-PEB thin films. The applied deformation of the material lowers the conformational entropy of the network by partially aligning polymer

chains. Then, light triggers photo-chemical reactions that transform the geometry of the active molecules, which are bonded with the polymer chains. The photo-transformation reforms the network to a higher state of conformational entropy, thus relieving the macroscopic state of stress.

In a low stress creep test without photoirradiation, when the material reaches the specified nominal stress, the deformation rate gradually decreases until the material deformation stabilizes at a constant value. When the sample is under light exposure, at short times the creep behavior equals that of the non-irradiated sample. As the phototransformation occurs, the material's creep deformation and characteristic time increases, getting to a steady value when the photo-transformation is completed.

The aforementioned results reveal that the photo-reactive films undergo expansion when photo-irradiated. This is a consequence of the sum of the polymer chain's elongation and the DTE's change of molecular geometry. Regarding the observed recovery after light exposure, it may be the tendency of the polymer to return to its unstretched state.

To conclude this chapter, the rigidity depends on the configuration of the DTE molecule, being more brittle the thin films in CF. While the elastomer and OF thin films share analogous elongation and rupture stress.

Mechanical modelling and simulation of the DTE-UPy-PEB thin films photomechanical effect

Mechanical characterization and numerical simulations, like Finite Element methods, are essential tools for introducing photoresponsive materials into technological applications, such as smart materials development. It allows to know the quantitative behaviour of any photoresponsive material under different irradiation conditions without having to resort to experimental analysis.

Regarding DTEs photomechanical effect, numerical methods have been proposed to comprehend the absorption performance in optical lithography [141], the photomechanical effect from the molecular scale [81] and the effect on surface plasmon resonance by changing the index refraction of gold gratings [142], to mention some examples. However, the DTE based thin films developed and studied in this work have not been mechanically analyzed because of its relative novelty.

In this chapter, we determined the photophysical constants for the DTE-UPy-PEB thin films using the absorbance experimental data obtained in section 3.5.

Using MATLAB, we carried out numerical simulations of the Pariani model to gain insight into the DTE phototransformation dynamics in relation to factors such as geometric parameters, light intensity, and DTE content. In our initial photomechanical

simulation, we combined this photokinetic model with the linear beam theory to observe the light-induced curvature of the thin films.

Moreover, based on the Arruda-Boyce and Bergstrom-Boyce model we propose a hyperelastic and a visco-hyperelastic mechanical model to predict the photomechanical behavior of DTE-UPy-PEB thin films. We conducted material calibration utilizing the experimental data collected from mechanical tests in the preceding chapter. This establishes the input data for the finite element model (FEM) - both photochemical and mechanical parameters.

By employing user subroutines to implement said models, we conducted finite element numerical simulations software MARC to assess the thin films' photoresponse performance given certain initial parameters, such as light intensity, geometric dimensions and DTE content. Finally, the photo-visco-hyperelastic model is validated by comparing FEA and experimental results.

5.1   Photokinetics analysis of DTE based thin films

In the first chapter, we reviewed the photokinetics behavior of the DTE photoactive molecule. Pariani et. al. [39] proposed a model that successfully describes the CF and OF population dynamics in DTE-based polymer thin films when irradiated with VIS and UV light (equations 5.1 and 5.2). These equations depend on several parameters and we will discuss in this section the computing of each one, as well as, their influence on the photokinetics behavior of the DTE-UPy-PEB thin films.

$$\chi_{CF}(y,t) = \frac{1}{1 + e^{-\alpha_{CF}y} \cdot (e^{k_{vis}t} - 1)} \tag{5.1}$$

$$\chi_{OF}(y,t) = \exp\left[-e^{-(\alpha_{UV} + \alpha_{matrix})y} \cdot k_{uv}t\right] \tag{5.2}$$

5.1.1   Photokinetics parameters

The photophysical parameters k_{vis} and k_{uv} define the reaction velocity (transformation rate) and depend on the initial light source intensity I_0 given in (photons/m^{2}s), the absorption cross section $\epsilon(\lambda)$ in (m^2/molecules) and the quantum yield $\Phi(\lambda)_{CF-OF}$ of

the phototransformation from configuration CF to OF.

$$k = I_0 \epsilon(\lambda) \Phi(\lambda)_{A-B} \tag{5.3}$$

First we have to convert the LED power source P_{vis} and P_{uv} (W) into (photons/m^{2}s), to do so, we calculate the energy E_{vis} and E_{uv} given by the VIS and UV light at 590 and 310 nm respectively.

$$E_{light} = h\nu = \frac{hc}{\lambda} \tag{5.4}$$

where h is the Planck's constant, c is the speed of light and λ is the wavelength.

The light intensity in (W/m^2) is $I_{light} = P_{light}/$area LED, then in (photons/m^{2}s):

$$I_0 = \frac{I_{light}}{E_{light}} \tag{5.5}$$

The quantum yield, as mentioned previously, is a constant of the material that indicates the efficiency of the active molecules to use the light energy to transform their molecular configuration. This was successfully measured experimentally by Pariani. Although their results apply for polyurethane films, the type of DTE used is like ours, the quantum yield values could give us an approximation.

From the first-order kinetics reaction, calculated in section 3.5.1, the transformation during UV irradiation has a larger transformation rate k, meaning that the transformation is faster, thus a larger quantum yield during OF to CF transformation. Previous experimental results confirm this (section photokinetics)

From the literature, the values for DTE quantum yield in solution and in solid state are displayed in tables 5.1 and 5.2. The Φ_{OF-CF} is always larger than Φ_{CF-OF} in both, solution and solid state, cases.

λ (nm)	Φ_{OF-CF} %
313	71 ± 3
404	1.6 ± 0.1
λ (nm)	Φ_{CF-OF} %
549	0.64 ± 0.03
589	0.32 ± 0.02

Table 5.1: Quantum yield values for DTE in acetonitrile solution ($\sim 3x10^{-5}$ molL^{-1}) at different wavelengths [19]

λ (nm)	Φ_{CF-OF} %
514	1.2 ± 0.1
532	0.9 ± 0.1
632	0.5 ± 0.1

Table 5.2: Quantum yield values for 50% DTE based thin films at different wavelengths [39]

Measuring the quantum yield for the DTE-UPy-PEB films following a similar method to Pariani [39] is outside the scope of this project. However, the transformation rate k can be obtained from the absorbance in situ experimental results (fig. 3.24). The absorbance in function of time during VIS irradiation (ring opening) is derived from integrating between 0 and the whole thickness w:

$$\int_0^w (A(y',t))\,dy = \int_0^w (\epsilon(\lambda)\chi_{CF}(y',t))\,dy \tag{5.6}$$

resulting:

$$A_{VIS}(t) = \ln\left[1 + De^{-kt}\right] \tag{5.7}$$

Where $D = e^{\epsilon(\lambda)Cw} - 1$, C is the concentration of photoactive molecules and will be defined later. Then, equation 5.7 is used to fit the experimental data (fig. 5.1a). In this manner, we obtain the rate of transformation from CF to OF, k_{VIS}.

The solution to the absorbance during UV irradiation (ring closing) could originate more mathematical complexity because both CF and OF active molecules are absorbing photons for the phototransformation. One simplification is to fit the experimental absorbance data into a time-dependent exponential form to obtain the transformation rate from OF to CF, k_{UV}. Following this solution, k_{VIS} can be similarly obtained (fig. 5.1b).

To assure the convergence between the experimental data and the fit model during UV irradiation, the transmittance (T_{UV}) is as well fitted with the exponential model (fig. 5.2). In tables 5.3 and 5.4 the computed values for the transformation rates during VIS and UV irradiation are displayed, which will be used for the subsequent numerical and finite element simulations.
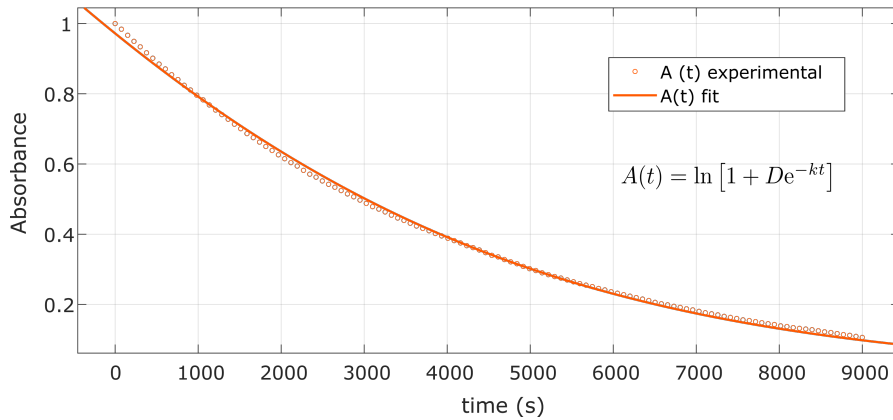
(a) Absorbance experimental data fit corresponding the ring opening phase using Pariani model
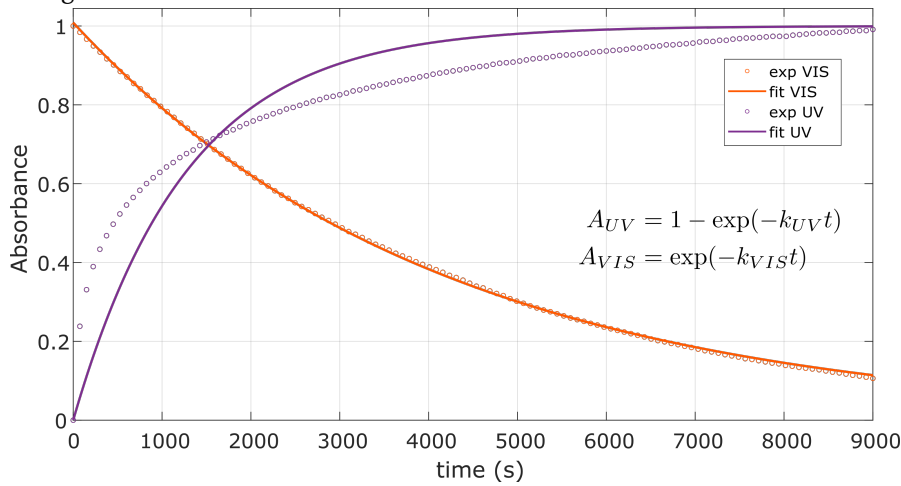
(b) Absorbance experimental data fit for UV and VIS irradiation using exponential equations

Figure 5.1: Experimental data fit methods for VIS and UV time-dependent absorbance.

	k_{VIS}	R^2
Pariani model	3.07	0.999
Exponential	2.42	0.999

Table 5.3: Transformation rate values in x10^{-4}s^{-1} from absorbance experimental data fits

5.1.2 Absorption Coefficients

The absorption cross section $\epsilon(\lambda)$ is a material parameter that measures the interaction between active molecules in OF configuration and photons to promote the transition to
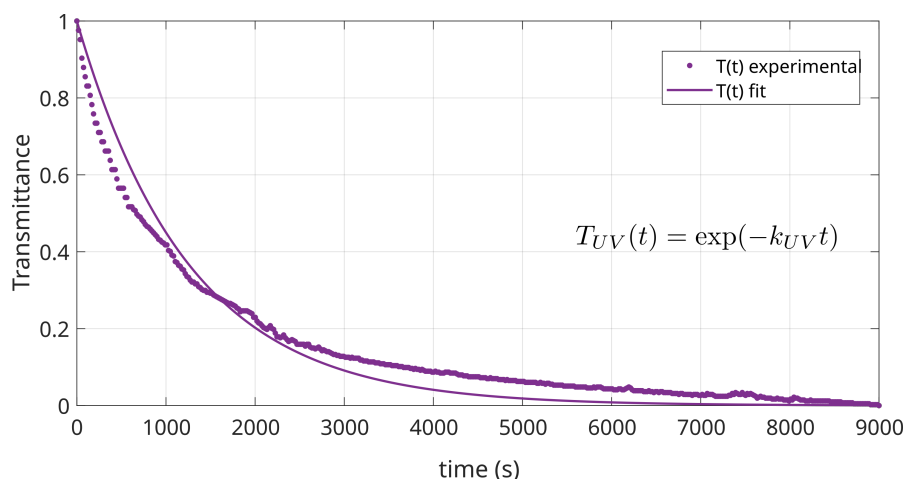
Figure 5.2: Transmittance experimental data fit for UV irradiation using exponential equation

	k_{UV}	R^2
Exponential	7.80	0.952

Table 5.4: Transformation rate values in x10^{-4}s^{-1} from transmittance experimental data fit

the CF state, and vice versa. It depends on the wavelength λ and its relation with the absoption coefficient $\alpha(\lambda)$ is:

$$\epsilon(\lambda) = \frac{\alpha(\lambda)}{C} \tag{5.8}$$

where C (molecules/m^3) is the concentration of active molecules and can be determined by:

$$C = \frac{g\%\rho N_A}{M_{ph}} \tag{5.9}$$

where $g\%$ is the weight percentage of active molecules, ρ is the thin film's density and M_{ph} is the active molecules' molar mass in g/mol.

From the absorption spectra of the DTE molecule in figure 5.3 we can obtain the molar absorption coefficient. The significant points in the DTE spectra are the maximum peak at 313 nm, the isobestic point at 329 nm and the broad band with maximum at 600 nm, that corresponds to DTE in CF configuration.

The Pariani model explained in section 1.4.3 for the UV irradiation is only valid for the isobestic point. For this reason we will use the value $\epsilon = 36000$ Lmol^{-1}cm^{-1} and for the
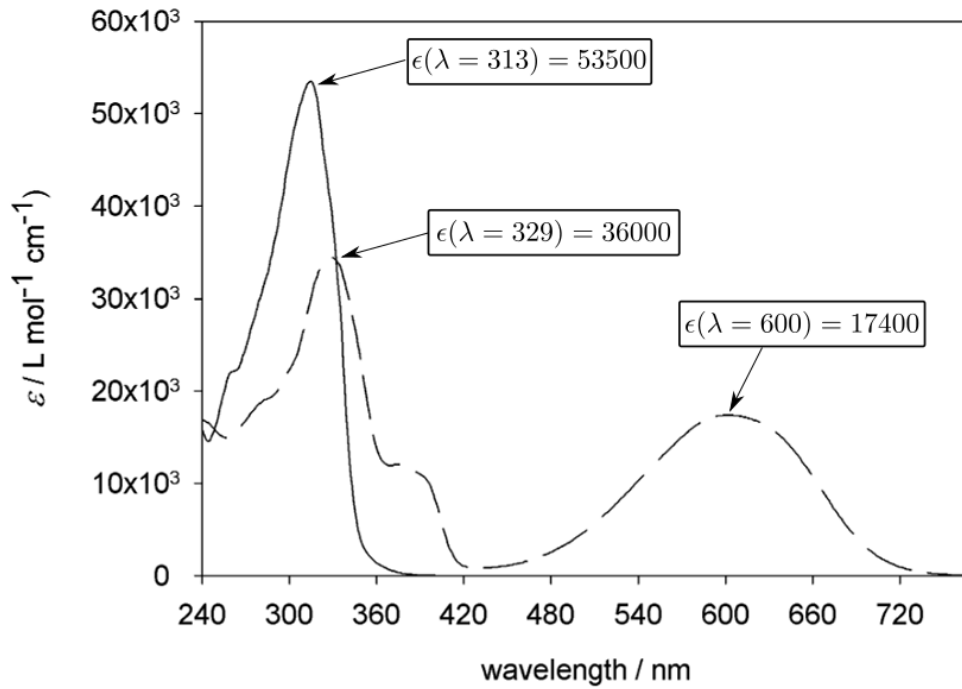
Figure 5.3: Absorption spectra of the OF (line) and CF (dash) isomers of DTE in acetonitrile [19]

VIS irradiation: $\epsilon = 17400$ Lmol^{-1}cm^{-1}. Having the corresponding molar absorption coefficients and using formula 5.9, the absorption coefficient for the thin film in OF during UV irradiation (α_{uv}) and in CF during VIS irradiation (α_{vis}) are computed, considering a 1 to 3 molar DTE-PEB ratio (12% DTE mass ratio).

	ϵ x10^{3}m^{2}mol^{-1}	α x10^{6}m^{-1}
VIS irradiation	1.74	0.304
UV irradiation	3.60	0.649

Table 5.5: Absorption coefficients for DTE-UPy-PEB thin films during VIS and UV irradiation

5.2 Numerical simulation of the DTE photokinetics

Using MATLAB we conducted a numerical simulation of the Pariani model (equations 5.1 and 5.2) applying the photochemical parameters calculated in tables 5.3, 5.4 and 5.5. Changing the variables thickness, light intensity and DTE content, we analyzed the pen-

etration of light into the material, which indicates the value of the DTE transformation gradient.

5.2.1   Light penetration thickness dependance

Figure 5.4 exhibits the transformation gradient for various thin film thickness w. The phototransformation in thicker thin films (> 70 µm) is complete in less than half the width for the CF to OF conversion (fig. 5.4a) after 3 hours. For the OF to CF conversion, after the same amount of time, the phototransformation is complete only at 10% deep in the thickness (fig. 5.4b).

As the thickness decreases, the CF to OF phototransformation is finished in two hours (fig. 5.4e). The inverse transformation is completed in around half the width after three hours of photoirradiation (fig. 5.4f).

The UV light penetration is less profound because both isomers absorb photons, obstructing the back layers to receive the UV energy. To attain the complete CF phototransformation along the thickness, the other side of the thin film will have to receive UV light. Consequently, this will create a stagnant phototransformation gradient.

On the contrary, during the VIS irradiation, only the CF isomers absorb photons. As the irradiated surface is transformed, it lets the light pass through allowing the back layers to perform the phototransformation, therefore, the phototransformation gradient will increase to a maximum point and decrease to zero. Evidently, the transformation is performed faster if the thickness is thinner.

5.2.2   Light penetration DTE concentration dependance

The same numerical simulation was performed, this time changing the DTE content in a 20 µm thick thin film. Figure 5.5 shows the light penetration depth for 5%, 12% and 25%.

At low contents of DTE, both VIS and UV light will penetrate deeper (figures 5.5a and 5.5b). At longer times under VIS irradiation, the thin film will complete the OF phototransformation. However, for the UV light, the depth will be steady at less than the half of the thickness, not attaining the complete CF transformation.

As DTE content increases, the VIS light will pass through the material slower, after three hours it will reach barely half of the material's thickness (figures 5.5c and 5.5e).

(a) 70 µm width thin film CF phototransformation

(b) 70 µm width thin film OF phototransformation

(c) 30 µm width thin film CF phototransformation

(d) 30 µm width thin film OF phototransformation

(e) 10 µm width thin film CF phototransformation

(f) 10 µm width thin film CF phototransformation
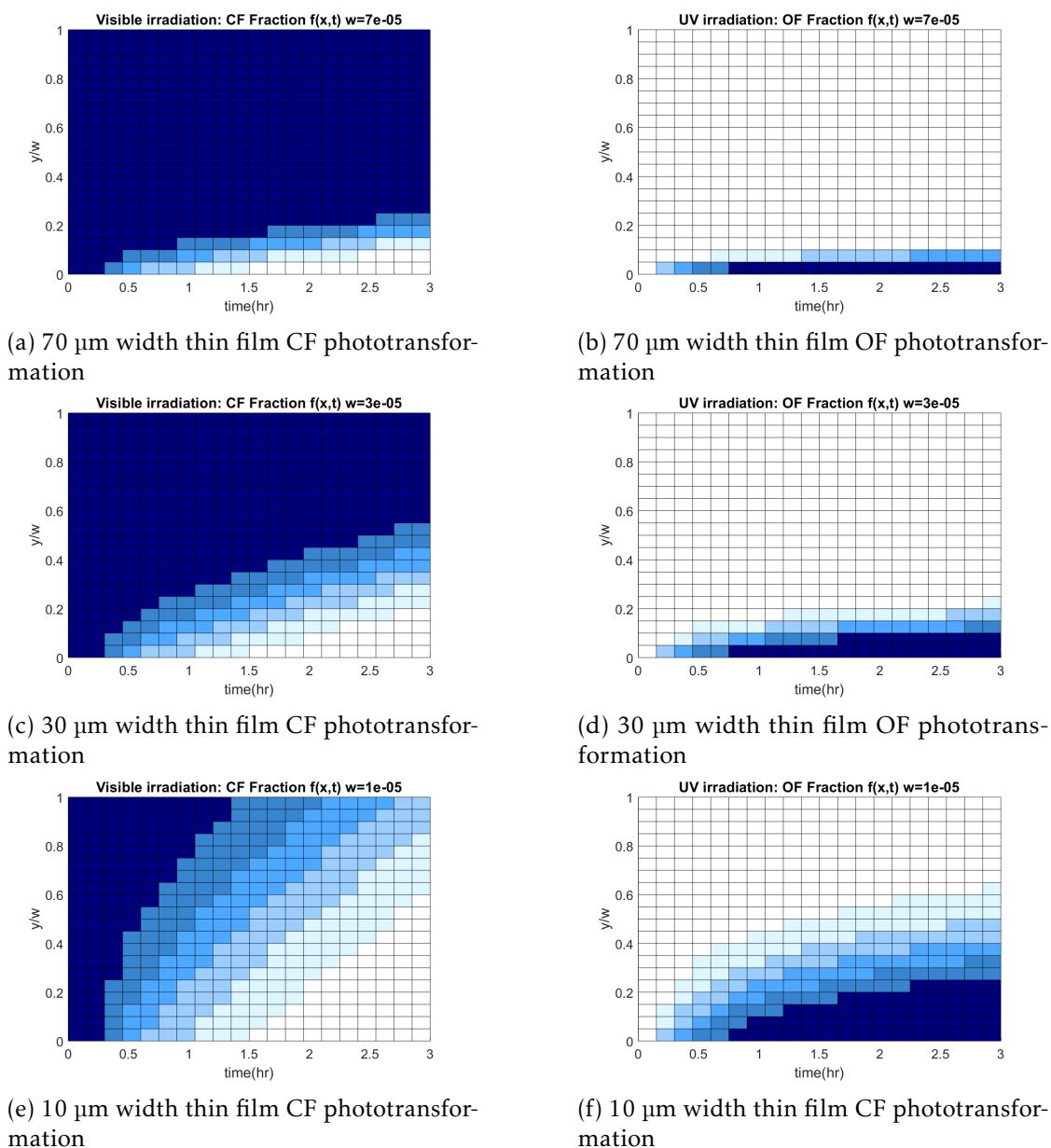
Figure 5.4: Thin film phototransformation for different thickness. The bluest color corresponds to CF isomers and white to OF isomers. As the thickness thins the light penetration is deeper at shorter times.

And as for the UV light extent, the high content of DTE will allow only a superficial CF transformation (figures 5.5d and 5.5f).

(a) 8% DTE mass ratio CF phototransformation

(b) 8% DTE mass ratio OF phototransformation

(c) 12% DTE mass ratio CF phototransformation

(d) 12% DTE mass ratio OF phototransformation

(e) 25% DTE mass ratio CF phototransformation

(f) 25% DTE mass ratio OF phototransformation
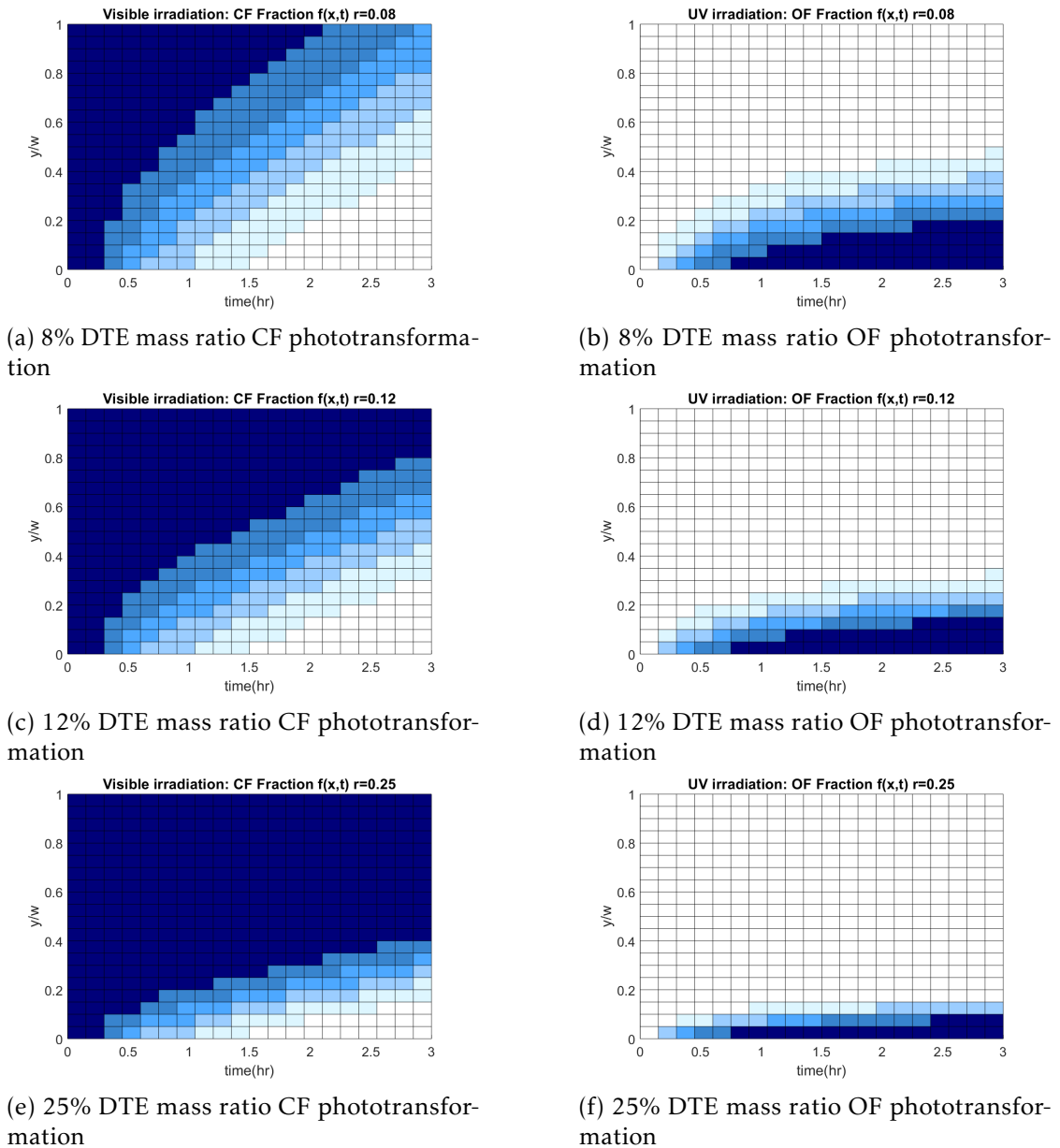
Figure 5.5: Thin film phototransformation for different DTE mass ratio. As the DTE concentration increases the light penetration decreases, the same effect as enlarging the thickness. The bluest color corresponds to CF isomers and white to OF isomers.

5.2.3 Light penetration light intensity dependance

Similarly, we carried out the numerical simulation for a 30 µm thick thin film with 12% DTE mass content, varying the value of the kinetic rate of phototransformation k, which

depends on the light intensity I_0. The figure 5.6 displays the results of the VIS and UV light penetration at $0.5k$, $1.5k$ and $3k$.

When the light intensity is reduced the time to complete the OF phototransformation will increase (fig. 5.6a), after 3 hours the OF fraction reaches 60% of the thickness. While the CF fraction during UV irradiation at half intensity, reaches almost 20% of the width (fig. 5.6b).

Increasing the light intensity will decrease the time for complete OF phototransformation (figures 5.6c and 5.6e). This does not apply for the CF transformation, the UV light penetration arrive at a stagnant value (figures 5.6d and 5.6f), meaning that for a certain DTE content and thin film's thickness corresponds a plateau value of the phototransformation gradient.

Figure 5.7 displays plainly the trends of the light penetration extent for VIS and UV irradiation depending on the thin film's thickness w, DTE content r_{DTE} and light intensity I_0. Complete OF phototransformation is attainable under VIS irradiation for thinner films, at low DTE content ($< 20\%$) and relatively high light intensity.

On the other hand, the complete CF transformation during UV irradiation, is only obtainable for thinner thickness ($< 10 \, \mu m$). As the thickness increases the transformation gradient $\nabla \chi(y, t) = $ constant when $t \to \infty$.

5.3 Photo-induced bending: numerical simulation

Experimental observations reported previously in this thesis, suggests that the DTE-UPy-PEB thin films undergo a photo-induced bending during VIS and UV irradiation. In previous work ([35, 53, 80, 85, 86, 143, 144]), the light-induced bending is caused by a photostrain, which results from the transformation gradient along the thickness. Thus the total strain (ε_T) for an elastic thin film is:

$$\varepsilon_T(y, t) = \varepsilon_e(y, t) + \varepsilon_{ph}(y, t) \tag{5.10}$$

where ε_e is the elastic strain due to mechanical loading and ε_{ph} is the photo-induced strain.

As we concluded in the previous chapter, the photo-irradiation causes a global expansion of the photo-responsive material. In the case of a one-extreme constrained cantilever beam (figure 5.8), the expansion is inhomogeneous through the thickness, be-

(a) Half light intensity CF phototransformation

(b) Half light intensity CF phototransformation

(c) 150% light intensity increase CF phototransformation

(d) 150% light intensity increase OF phototransformation

(e) 300% light intensity increase CF phototransformation

(f) 300% light intensity increase OF phototransformation
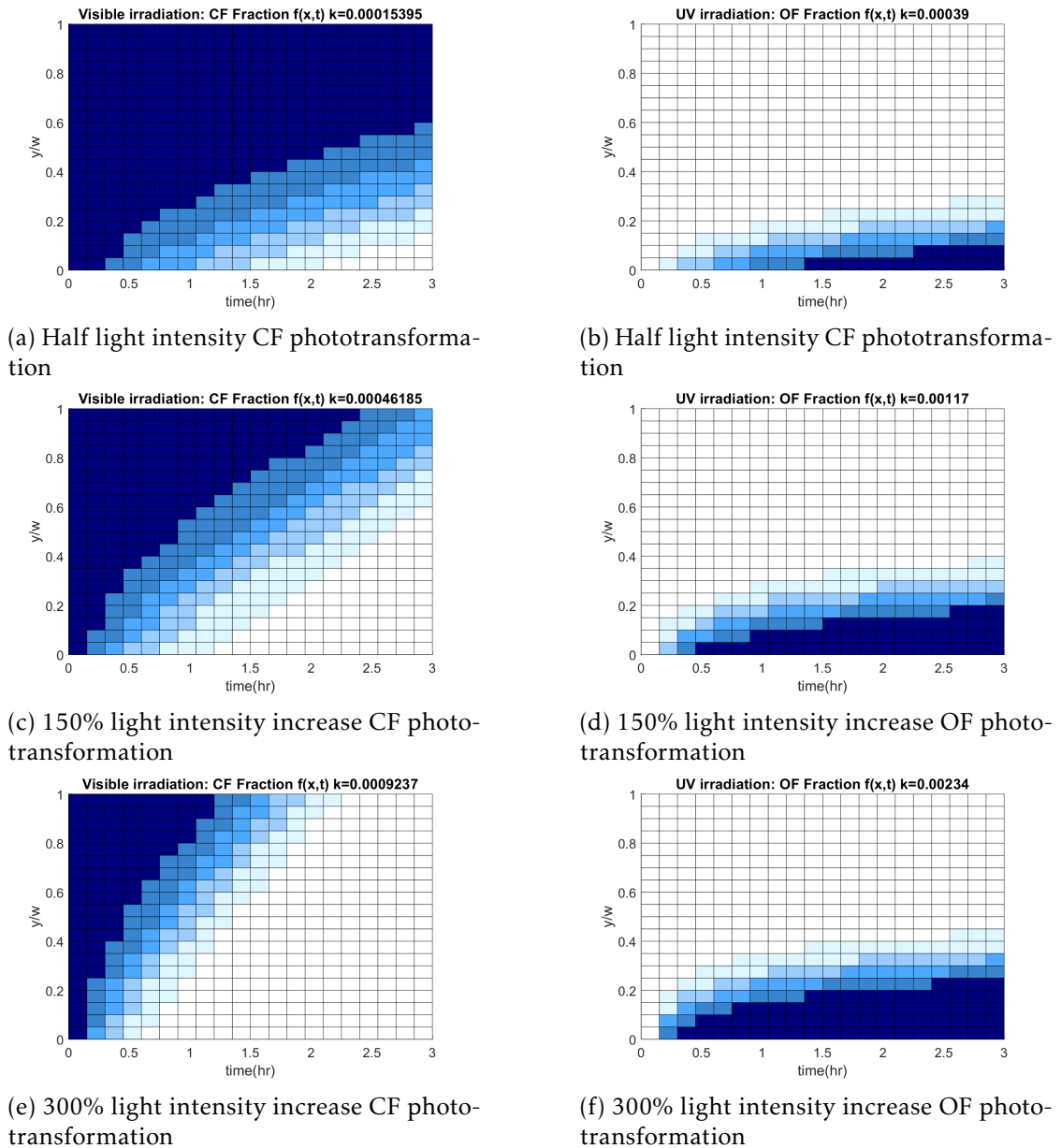
Figure 5.6: Thin film phototransformation dependance on the light intensity I_0. The light intensity influences the VIS light penetration, while for the UV light the penetration length will reach a steady value. The bluest color corresponds to CF isomers and white to OF isomers.

ing greater in the irradiated surface where the phototransformation occurs first. Hence,
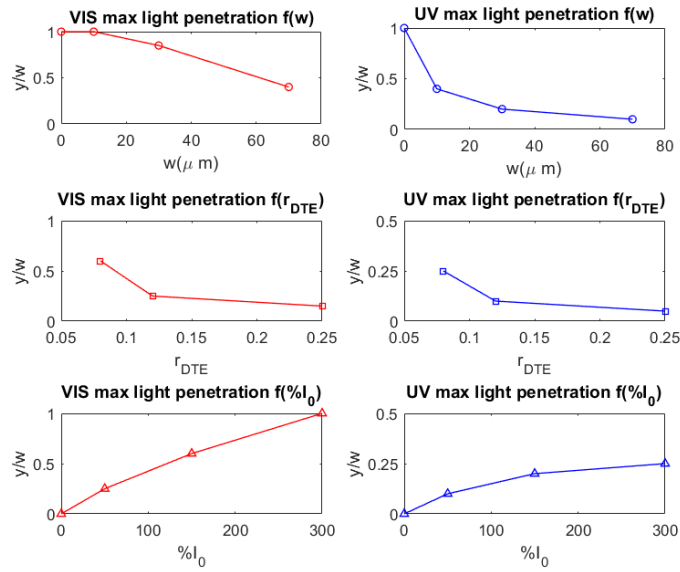
Figure 5.7: Maximum light penetration after 3 hours irradiation depending on the thin film's thickness w, DTE content r_{DTE} and light intensity ($\%I_0$).

the photostrain is a function of the fraction of transformed molecules χ:

$$\varepsilon_{ph} = f(\chi(y, t))$$

where χ is the phototransformed fraction.

If we assume that the dependence of ε_{ph} on the transformation fraction χ is a linear function of the form:

$$\varepsilon_{ph} = \varepsilon_{ph\infty} \chi(y, t) \tag{5.11}$$

where $\varepsilon_{ph\infty}$ corresponds to the strain along the thickness at a complete conversion. Then, according to the beam theory, the curvature κ of a rectangular cross-section thin film with non-uniform distribution of the phototransformation across its thickness is described as [145]:

$$\kappa = \frac{1}{R} = \frac{12}{bw^3} \varepsilon_{ph\infty} \int_0^w \left(\frac{w}{2} - y \right) \chi(x, t) \mathrm{d}y \tag{5.12}$$

where b and w are the thin film's width and thickness, respectively.
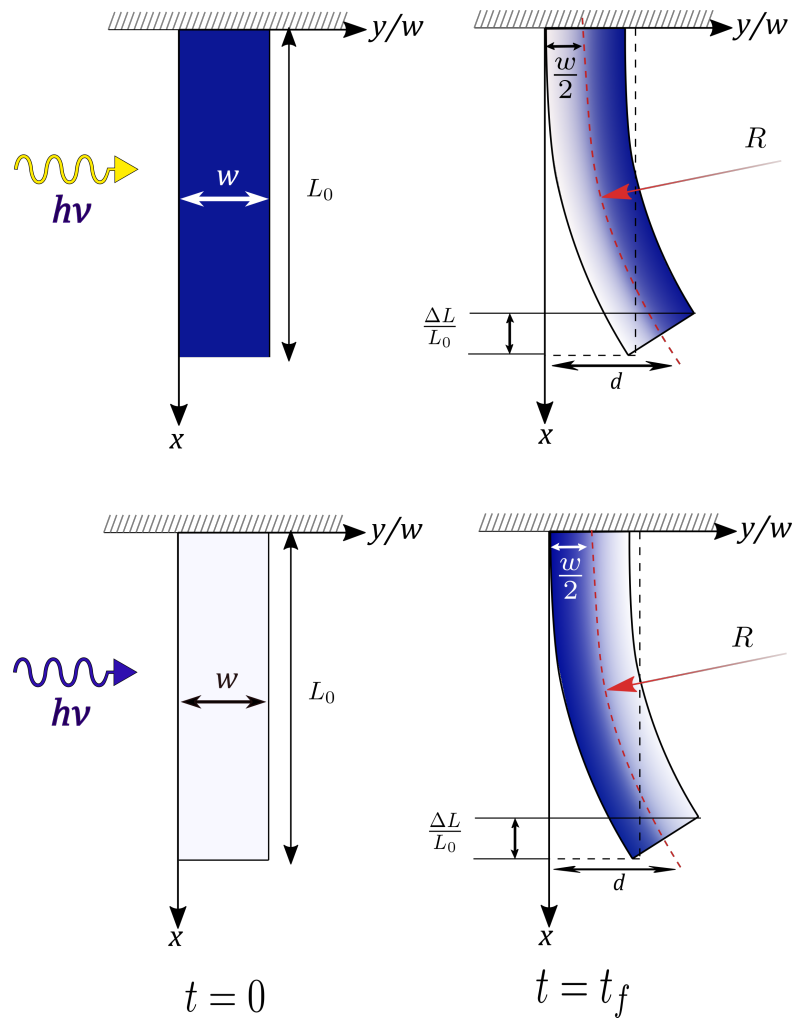
Figure 5.8: Light penetration scheme. R is the curvature radius function of the transformed fraction gradient $\nabla \chi(y, t)$

The bending rate is defined by:

$$\frac{\mathrm{d}}{\mathrm{d}t}(\kappa) = -\frac{12}{bw^3}\varepsilon_{ph\infty}\int_0^w \left(\frac{w}{2} - y\right)\frac{\mathrm{d}\chi(y,t)}{\mathrm{d}t}\mathrm{d}y \qquad (5.13)$$

The relative change in the thin film's length is defined by the average strain across its thickness:

$$\frac{\Delta L}{L_0} = \frac{\varepsilon_{ph\infty}}{w}\int_0^w (\chi(y,t))\,\mathrm{d}y \qquad (5.14)$$

Equations 5.12 and 5.14 are solved in MATLAB obtaining the change of curvature and
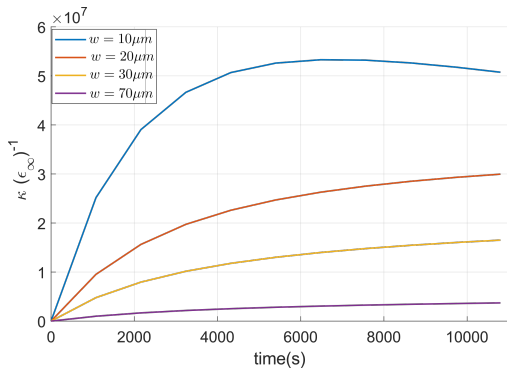
(a) UV irradiation κ OF to CF transformation.
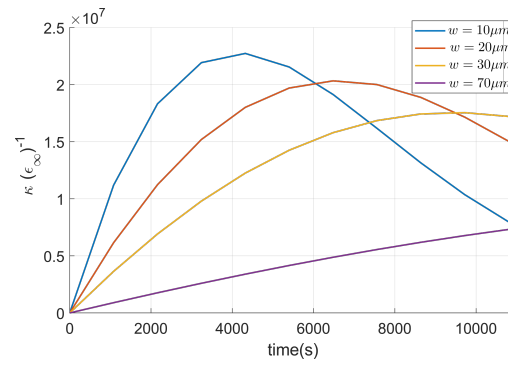
(b) VIS irradiation κ CF to OF transformation.
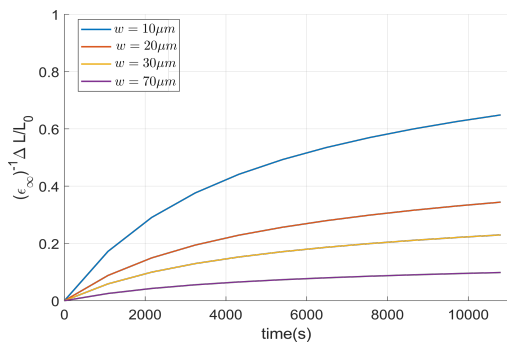
(c) UV irradiation $\frac{\Delta L}{L_0}$ OF to CF transformation.
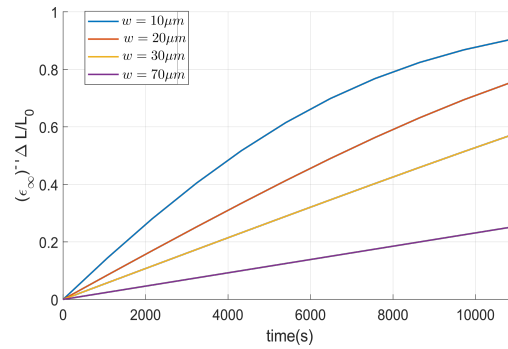
(d) VIS irradiation $\frac{\Delta L}{L_0}$ CF to OF transformation.

Figure 5.9: Curvature (κ) and length change ($\Delta L/L_0$) in time during phototransformation.

length in time for different thin film's thickness, for the CF to OF (VIS) and for the OF to CF (UV) transformation (fig. 5.9).

The thin film's expansion arrives at a plateau during both irradiations. The extent of the expansion depends on the value of $\varepsilon_{ph\infty}$. The expansion during UV irradiation (fig. 5.9c) does not reach the final value of $\varepsilon_{ph\infty}$ because the UV light penetration does not reach the posterior layers behind the irradiated surface, contrary to the VIS irradiation expansion (fig. 5.9d) where, at a time, the thin film will reach the final transformation and hence, the $\varepsilon_{ph\infty}$ value.

Given that the curvature is proportional to the inhomogeneous phototransformation along the thickness,

$$\kappa \approx -\varepsilon_{ph\infty} \frac{\partial \chi(y,t)}{\partial y} \tag{5.15}$$

the curvature during the VIS irradiation attains a maximum point (figs. 5.9b), meaning that the phototransformation gradient initially increases and subsequently decreases to a stationary state when the transformation is complete. This stationary state is zero for the VIS irradiation and will be attained faster for thinner films, while for the UV irradiation (figs. 5.9a), the stationary state differs from zero because for the OF to CF transformation $\partial\chi(y,t)/\partial y \neq 0$, meaning that the transformation is not complete as $t \rightarrow \infty$.

The deflection d at the free end of the thin film from the constant curvature κ induced by the photo-strain is [146]:

$$d = \kappa \frac{L_0^2}{2} \tag{5.16}$$

for $L_0 << R$.

As an example, to scale the deflection results to mm we fix the constant $\varepsilon_{ph\infty} \approx 1x10^{-3}$. The deflection results are displayed in figure 5.10.

(a) UV irradiation deflection d OF to CF transformation.

(b) VIS irradiation deflection d CF to OF transformation.
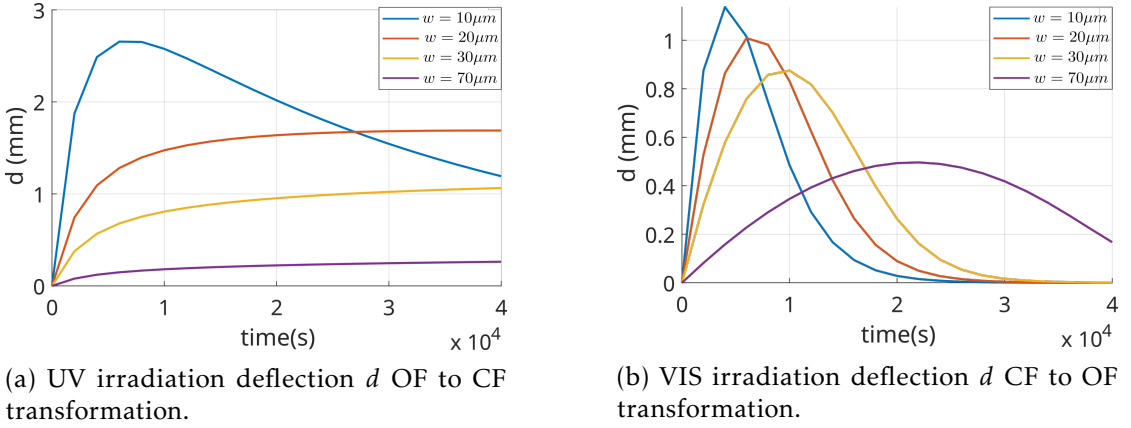
Figure 5.10: Thin film's tip deflection (d) change in time during phototransformation.

5.4 Photo-induced bending: FE simulation in MARC

5.4.1 Photostrain

Even though the previous approach based upon the beam theory is quite easy to implement and can give the main trends of the deformation process, the assumption of linear elasticity can alter the results since the material can exhibit non-linear behavior. Therefore, to simulate the light-induced bending of the DTE-UPy-PEB thin films, we used the user subroutine ANEXP for MARC MENTAT. This subroutine is used to specify anisotropic thermal strain increments in the orientation defined by the user [147]. The

user must enter the incremental thermal strain vector $\Delta\varepsilon_{ij}^{th}$, which for a material with a thermal expansion coefficient α_{ij}^{th} is:

$$\Delta\varepsilon_{ij}^{th} = \alpha_{ij}^{th}\Delta T \tag{5.17}$$

where $\Delta T = T_i - T_{i-1}$ is the temperature change.

Considering that the photo-reactive thin film undergoes a light induced expansion, we could make the analogy of equation 5.17 using the light intensity instead of the temperature. Then, the incremental photo-strain will be:

$$\Delta\varepsilon_{ij}^{ph} = c_{ij}^{ph}\Delta I(y,t) \tag{5.18}$$

where c_{ij}^{ph} is the photo-expansion coefficient that indicates the rate of expansion in the ij direction by photons absorbed by area unit and, $\Delta I(y,t)$ is the light intensity decay through the material's thickness, defined as:

$$\Delta I(y,t) = I_0\Delta\left(\exp\left(-\int_0^y A(y',t)\mathrm{d}y'\right)\right) \tag{5.19}$$

where I_0 is the light intensity on the irradiated surface and A is the absorbance:

$$A(y',t) = \alpha_A\chi_A(y',t) + \alpha_B\chi_B(y',t) + \alpha_{PEB} \tag{5.20}$$

the subscripts A and B indicate OF isomers and CF isomers respectively. α is the absorption coefficient, χ is the isomers fraction and, α_{PEB} is the elastomer matrix absorption coefficient.

According to the Pariani model [39] during the VIS irradiation $\alpha_A = \alpha_{PEB} = 0$, being the light intensity decay:

$$I(y,t) = I_0\exp\left(-\int_0^y \alpha_B\chi_B(y',t)\right) \tag{5.21}$$

Solving the integral leads to:

$$I(y,t) = I_0\chi_B(y,t) \tag{5.22}$$

Then the incremental photo-strain during VIS irradiation is:

$$\Delta\varepsilon_{ij}^{vis} = a_{ij}^{vis}\Delta\chi_B(y,t) \tag{5.23}$$

where $a_{ij}^{vis} = c_{ij}^{ph} I_0^{vis}$.

In the same way we derive the equation for the incremental photo-strain during UV irradiation:

$$\Delta\varepsilon_{ij}^{uv} = a_{ij}^{uv}\Delta\chi_A(y,t) \tag{5.24}$$

where $a_{ij}^{uv} = c_{ij}^{ph} I_0^{uv}$.

$\Delta\chi(y,t)_{A,B}$ is the change of the photoisomer fraction given a certain time increment Δt, which is:

$$\frac{\Delta\chi(y,t)_{A,B}}{\Delta t} \approx \frac{\partial}{\partial t}\chi(y,t)_{A,B} \tag{5.25}$$

Provided that the time increment is significantly small to capture the χ evolution, then:

$$\Delta\varepsilon_{ij}^{ph} = a_{ij}^{ph}\frac{\partial}{\partial t}\chi(y,t)_{A,B}\Delta t \tag{5.26}$$

The photostrain will be computed at each increment (inc) as:

$$\varepsilon_{ij(inc)}^{ph} = \Delta\varepsilon_{ij(inc)}^{ph} + \varepsilon_{ij(inc-1)}^{ph} \tag{5.27}$$

5.4.2   Kinematics

As a first approximation, the material was modeled as a three-branch network. Each network represents the polymer matrix, the DTE in CF and the DTE in OF, respectively (fig. 5.11). The three are represented as hyperelastic springs that follow the Arruda-Boyce eight chain model, which defines the strain energy density as:

$$\Psi = \frac{nkt}{3}\sqrt{N}\left(\beta\sqrt{\frac{I_1}{3}} + \sqrt{N}\ln\frac{\beta}{\sinh\beta} - \frac{\beta_0}{3}\ln J_M\right) + \frac{K}{2}(J_M - 1)^2 \tag{5.28}$$

where n is the average number of chains per unit volume, k is the Boltzman constant, t is the temperature, $\sqrt{N} = \lambda_{lock}$ is the network stretch limit and K is the bulk modulus, which will be assumed as $K \approx 500nkt$ in this manner the material could be assumed as incompressible ($J_M = 1$). Leading to:

$$\Psi = \frac{nkt}{3}\sqrt{N}\left(\beta\sqrt{\frac{I_1}{3}} + \sqrt{N}\ln\frac{\beta}{\sinh\beta}\right) \tag{5.29}$$

The terms β and β_0 correspond to the inverse Langevin function (equations 2.38 and 2.39).
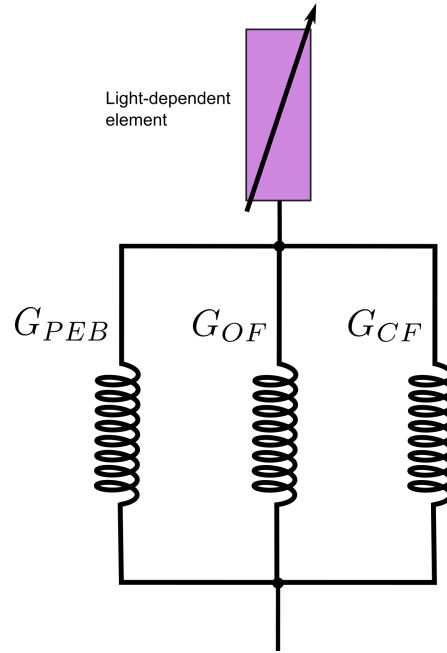
Figure 5.11: Representation of proposed hyperelastic photomechanical model

For the finite element analysis, equation 5.29 is approximated in the five terms form:

$$\Psi = G\left[\frac{1}{2}(I_1 - 3) + \frac{1}{20N}(I_1^2 - 9) + \frac{11}{1050N^2}(I_1^3 - 27) + \ldots\right]$$
$$G\left[\ldots + \frac{19}{7000N^3}(I_1^4 - 81) + \frac{519}{673750N^4}(I_1^5 - 243)\right] \quad (5.30)$$

G is the rubbery modulus and, $G = nkt/3$. The total strain energy density is the sum of the individual energies of each branch multiplied by the volume fraction f:

$$\Psi_T = f_{matrix}\Psi_{matrix} + f_{\text{DTE}}\left(\chi_{OF}(y,t)\Psi_{OF} + \chi_{CF}(y,t)\Psi_{CF}\right) \quad (5.31)$$

For a 1 to 3 DTE-PEB molar ratio, the volumetric fraction of the polymer matrix is $f_{matrix} = 0.88$ and $f_{\text{DTE}} = 0.12$. From the uniaxial tensile results and using the experimental data fit calculation software MCalibration, the values of the rubbery modulus G and λ_{lock} for the polymer PEB and the thin film in their respective OF and CF configurations are obtained (table 5.6).

	G (MPa)	λ_{lock}
PEB	10.1	100
OF	9.35	100
CF	11.56	100

Table 5.6: Eight-chain model calibration results for the PEB pure, DTE-UPy-PEB in OF and CF thin films

λ_{lock} remains unchanged, because by not having large stretches in the experimental data (maximum stretch is around 3.5%) it is not necessary to calibrate this value.

The rule of mixtures (equation 5.31) is implemented via the user subroutine UELAS-TOMER, which allows definition of the user's own hyperelastic models by defining the strain energy density function either in terms of the invariants (I_i) or the principal stretches($\hat{\lambda}_i$). Being the eight chain an invariant-based model, the function is defined in terms of the first invariant I_1, assuming incompressibility (deviatoric part only): $\Psi = \Psi_{dev}(I_1)$.

5.4.3   Finite Element Model (FEM) geometry and mesh

The thin film is represented by a rectangular beam with a w/L ratio of 1/1000. The Finite Element model is performed as a planar 2D with assumed strain. The type of element used is a four-node quadrilateral in plane strain. The beam is partitioned in five parts (fig. 5.12), each one represents a fraction of the thickness y/w. In this manner, each part will expand at different rates, depending on the photoisomer (CF or OF) fraction thus, inducing the beam bending.

This is an analogous effect of the Timoshenko's bimetallic beam [27, 83] where the bimetallic beam deflects because of the different thermal expansion coefficients of the two metals. In the FEM, the beam is virtually made of different parts whose light expansion coefficients vary in function of time and thickness fraction 5.26.

5.4.4   Finite Element Analysis (FEA) Results

The finite element simulations were conducted to calculate the maximum photome-chanical response, which, regarding the thin film, is measured as the maximum tip displacement in the vertical direction, parallel to the light irradiation direction.

The displacement is a function of the OF phototransformation gradient, which leads the thin film to bend in y positive direction during the VIS irradiation then, $d_{vis} = f(+\nabla\chi_{OF})$
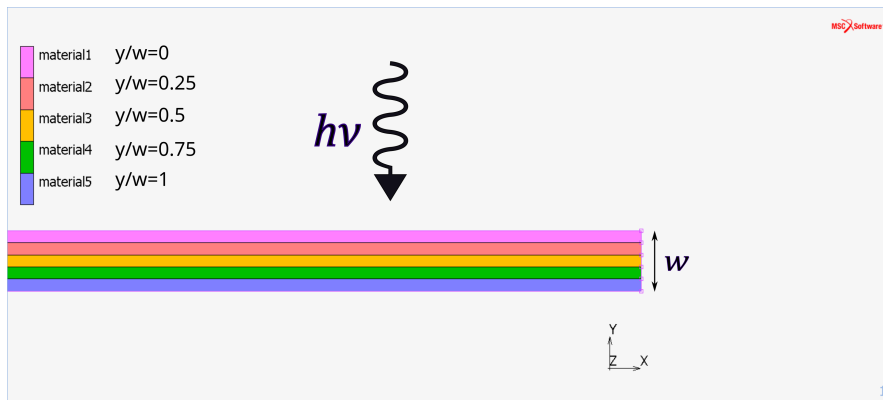
Figure 5.12: FEM geometry partition tip close-up. Each partition represent a fraction of the thin film's thickness and they all have the same material type. The light irradiation comes from the upper side of the window, indicating that at $y/w = 0$ the light intensity $I(0, t) = I_0$.
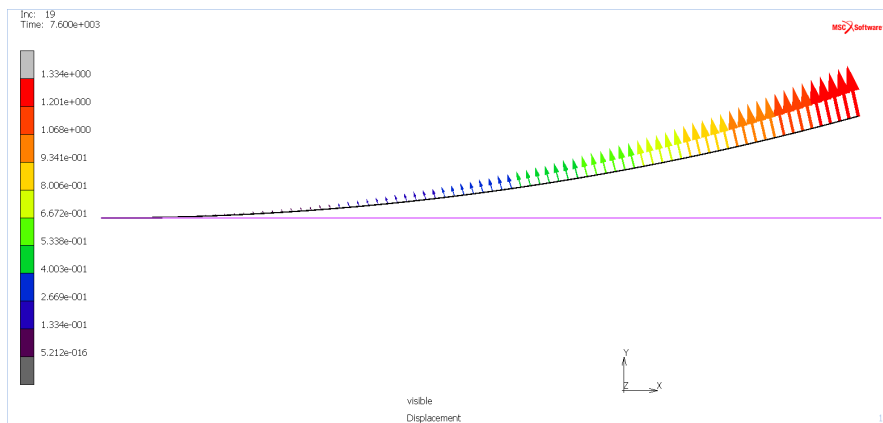
Figure 5.13: FEM displacement profile results during VIS irradiation.

(fig. 5.13). The inverse occurs during UV irradiation, where the bending direction is in the y negative axis, being $d_{uv} = f(-\nabla \chi_{OF})$ (fig. 5.14).

Maximum displacement: FEA vs. Numerical simulation

First the FEA simulations were performed varying the thin film's thickness. This was already computed in numerical simulations, although these did not account the material's hyperelastic properties. The difference in both results is shown in figures 5.15-5.17.

The main difference is that there is a change in stiffness during both photo-irradiations. During VIS irradiation, the DTE isomers change from a more constrained configuration
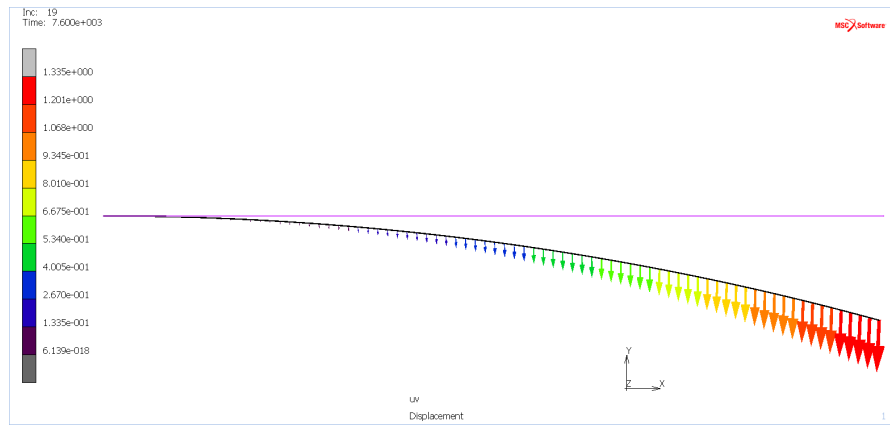
Figure 5.14: FEM displacement profile results during UV irradiation.

(CF) to a configuration where the molecule can rotate more easily (OF), meaning that the stiffness decreases with time. The opposite occurs during UV irradiation, where the material gets stiffer and prevents the unrestricted movement of molecules.
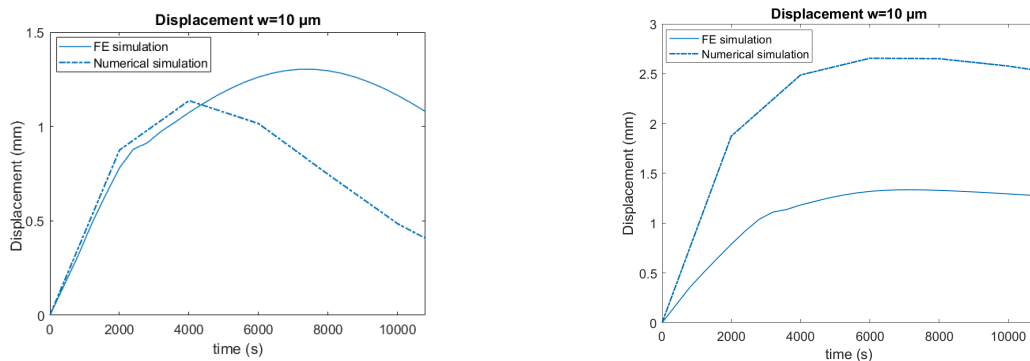
(a) VIS irradiation tip displacement CF to OF transformation

(b) UV irradiation tip displacement OF to CF transformation.

Figure 5.15: Thin film's tip displacement change in time during phototransformation 10 µm thick thin film. FE vs. Numerical simulation.

For a 10 µm thick thin film, during the VIS irradiation, the maximum tip displacement in the FEA simulation is $d_{vis}^{FEA} = 1.3$ mm and $d_{vis}^{NS} = 1.1$ mm in the numerical simulation. For the former, the maximum value is reached slower than the latter (fig. 5.15a). During the UV irradiation, the stiffness increase effect is observable (fig. 5.15b), the maximum tip displacement in the numerical simulation is greater than the FEA simulation $d_{uv}^{NS} > d_{uv}^{FEA}$, reaching these values at the same time.
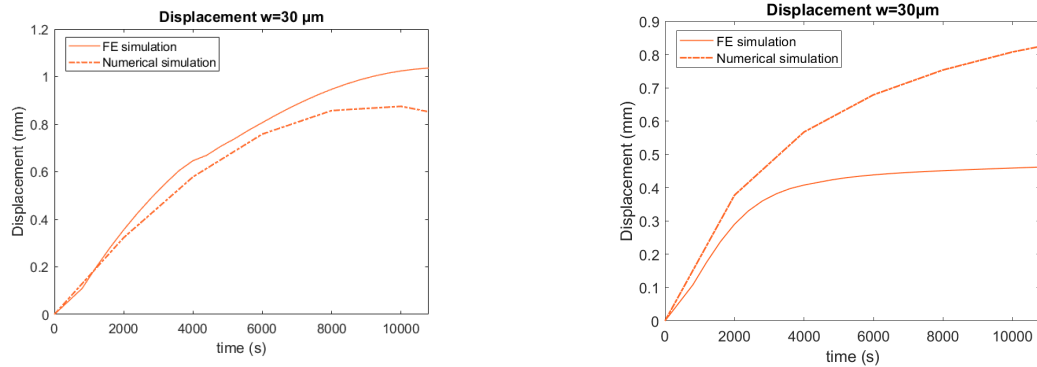
(a) VIS irradiation tip displacement CF to OF transformation

(b) UV irradiation tip displacement OF to CF transformation.

Figure 5.16: Thin film's tip displacement change in time during phototransformation 30 µm thick thin film. FE vs. Numerical simulation.

The simulations for the thin film of 30 µm thickness follow a similar trend, during the VIS irradiation the $d_{vis}^{FEA} > d_{vis}^{NS}$ (fig. 5.16a) and inversely, during the UV irradiation $d_{uv}^{FEA} < d_{uv}^{NS}$ (fig. 5.16b).
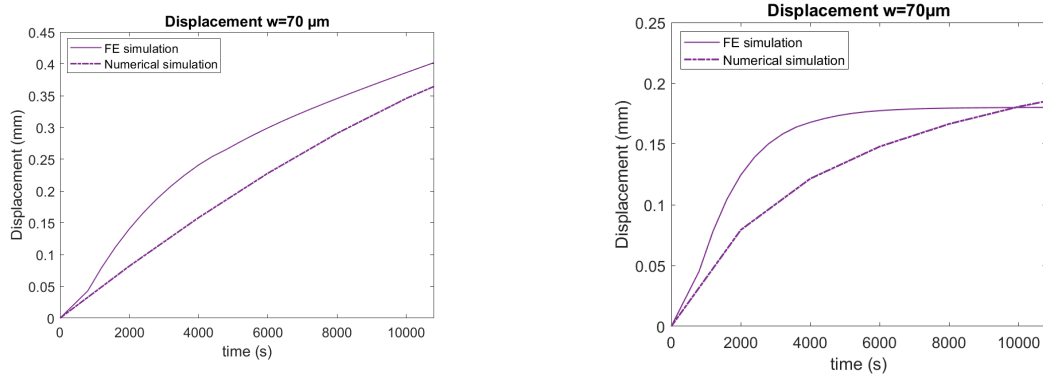
(a) VIS irradiation tip displacement CF to OF transformation

(b) UV irradiation tip displacement OF to CF transformation.

Figure 5.17: Thin film's tip displacement change in time during phototransformation 70 µm thick thin film. FE vs. Numerical simulation.

Finally, comparing the results for the 70 µm thick thin film, the maximum point of the VIS tip displacement occurs after ~ 3 hrs in both simulations and $d_{vis}^{FEA} \approx d_{vis}^{NS}$. During the UV irradiation, the maximum tip displacement in the FEA simulation is reached in < 2 hrs and, $d_{uv}^{FEA} < d_{uv}^{NS}$.

In brief, the rigidity change due to the non-linear behavior during VIS irradiation makes

the thin film's tip displacement reach a maximum point in less time and have a larger movement. While for UV radiation, the tip displacement reaches a steady value in less time, also having its displacement a smaller amplitude.

Maximum displacement: parameters variation

In the FEA simulations, we analyze the maximum tip displacement in function of the thickness w and light intensity I_0 and the DTE content r_{DTE}. As it was performed for the light penetration depth.

First, we study the movement amplitude as a function of the specimen width (fig. 5.18). Regarding the VIS irradiation displacement (fig. 5.18a), we observe that there is a bending reversion effect caused by the phototransformation gradient variation in time. This effect is predicted in the numerical simulations. When the gradient has a maximum value, the displacement is maximum and then it decreases as the phototransformation is complete along the thickness, reversing the movement.

For thinner specimens, the phototransformation is faster likewise, the maximum tip displacement is greater. Conversely, As the thickness increases, the time required to reach the maximum value increases, while the maximum tip displacement decreases.

On the other hand, the UV light presents more difficulty to penetrate the material due to the high UV light absorbance of both OF and CF isomers, this causes a steady phototransformation gradient, hence the displacement plateau. Despite this, the bending reversion effect is obtainable for thinner films and, eventually returning to a blocked movement state (fig. 5.18b).

(a) VIS irradiation tip displacement   (b) UV irradiation tip displacement
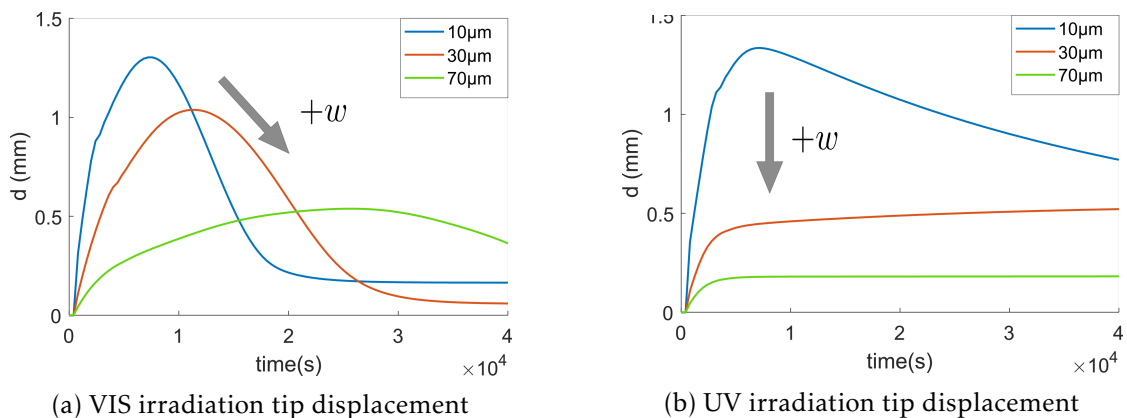
Figure 5.18: Thin film's tip displacement during VIS and UV at different specimen thickness w

The same FEA simulation is conducted varying the light intensity keeping the thickness $w = 10\,\mu m$ and DTE content $r_{DTE} = 0.12$ constant. We observed changes in the maximum tip displacement, as well as the time required to attain it. Increasing the irradiation intensity translates into decreasing the maximum displacement, however, it reaches it faster. The equal effect is present during VIS and UV irradiation FEA simulations. The reversion effect is present likewise, a consequence of a thin thickness (fig. 5.19).

(a) VIS irradiation tip displacement   (b) UV irradiation tip displacement
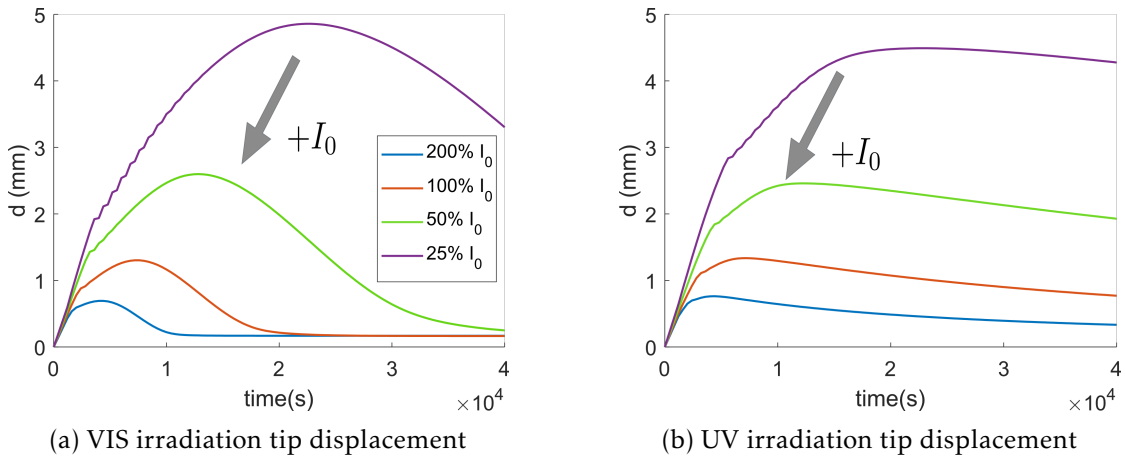
Figure 5.19: Thin film's tip displacement during VIS and UV at different light intensity $\%I_0$

(a) VIS irradiation tip displacement   (b) UV irradiation tip displacement
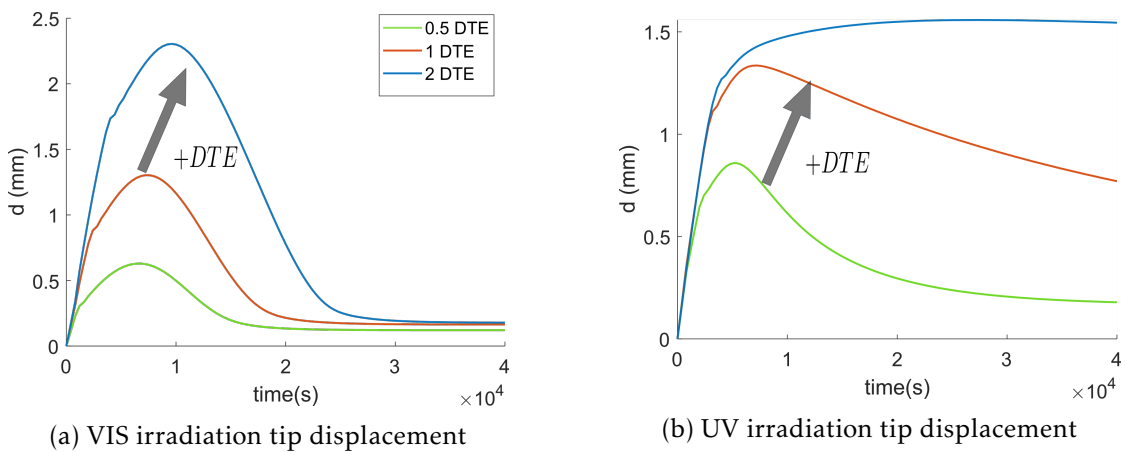
Figure 5.20: Thin film's tip displacement during VIS and UV at different DTE content r_{DTE}

Last, the simulations were performed by changing the DTE content and maintaining $w = 10\,\mu m$ and $I_0 = 100\%$. A high DTE content means a higher thin film movement

at relatively same velocities during VIS irradiation (fig. 5.20a). For the UV irradiation, the higher DTE content as well means a greater maximum tip displacement, yet we encounter a stagnant value as the DTE content increases (fig. 5.20b). Which results from the DTE high UV light absorbance that prevents light from passing through the material and a constant phototransformation gradient $\nabla \chi(y, t)$.

Altogether, figure 5.21 displays the tip maximum displacement trends in function of thickness, light intensity and DTE content, it is important to mention that this does not account for the velocity to reach said maximum point. Regarding the thin film's photoreaction in function of its width, we find a linear decrease for the VIS irradiation and an exponential decrease for the UV irradiation (fig. 5.21a). The trends are similar when changing the light intensity during both irradiations (fig. 5.21b).
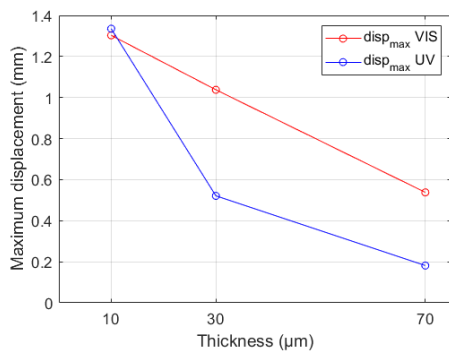
(a) Thin film's maximum tip displacement in function of thickness w.
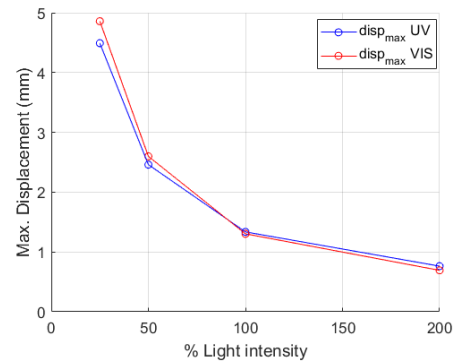
(b) Thin film's maximum tip displacement in function of light intensity I_0.
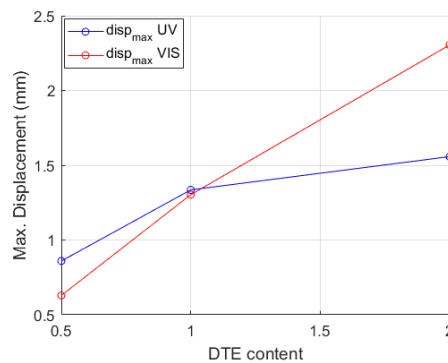
(c) Thin film's maximum tip displacement in function of DTE content.

Figure 5.21: Thin film's maximum tip displacement simulation results in function of thickness, light intensity and DTE content.

5.5   Viscoelastic effect: Parameters calculation

To accurately capture the photo-induced deformation, it is important to consider the non-linear behavior effect. Including the viscous effects in the mechanical analysis is necessary since the material experiences stress relaxation and creep. The Bergstrom-Boyce formulation of non-linear viscoelasticity is recommended to characterize the viscoelastic behavior of DTE-UPy-PEB thin films. This model has been successful in predicting the time-dependent behavior of elastomers by considering the relaxation of a single entangled chain within a polymer matrix. Therefore, it can describe the large strains and nonlinear stress-strain relationships observed in DTE-UPy-PEB thin films, as shown in the mechanical tests previously discussed (chapter 4).

In the Bergstrom-Boyce model, the inelasticity theory is founded on the multiplicative decomposition of the deformation gradient in elastic $\mathbf{F}^e$ and inelastic $\mathbf{F}^i$:

$$\bar{\mathbf{F}}_B := J^{-1/3}\mathbf{F}_B \tag{5.32}$$

$$\bar{\mathbf{F}}_B := \mathbf{F}_B^e \mathbf{F}_B^i \tag{5.33}$$

where $\bar{\mathbf{F}}$ is the isochoric part of the deformation gradient, as it is assumed the viscous effect is purely isochoric given the incompressible behavior of elastomers.

The complexity of the nonlinear evolution creep law (eq. 5.34) requires the implementation of an algorithm to perform numerical simulations of the model [148].

$$\dot{\gamma} = \eta \left(\lambda_{chain}^i - 0.99 \right)^c \tau_B^m \tag{5.34}$$

where $\dot{\gamma}$ is the creep strain rate, η is the evolution law multiplier (MPa$^{\mathrm{m}}$s^{-1}), c is the evolution law power constant controlling the kinetics of the chain relaxation and m is the stress sensitivity constant that regulates the energy activated during inelastic flow. And as a reminder:

$$\tau_B = \left[\frac{1}{2} \mathrm{trace}(\mathbf{T}_B^{'} \mathbf{T}_B^{'}) \right]^{\frac{1}{2}}$$

$$\lambda_{chain}^i = \left(\frac{1}{3} \mathrm{trace}(\mathbf{F}_B^i \mathbf{F}_B^{iT}) \right)^{1/2}$$

In order to incorporate the viscoelastic parameters (η,c and m) from the Bergstrom-Boyce model into the light-induced bending finite element simulation in MARC, it is necessary

to first determine the PEB parameters. This can be achieved through the use of a MATLAB script that calculates the stress for the time-independent and time-dependent branches (fig. 5.22) in function of time.
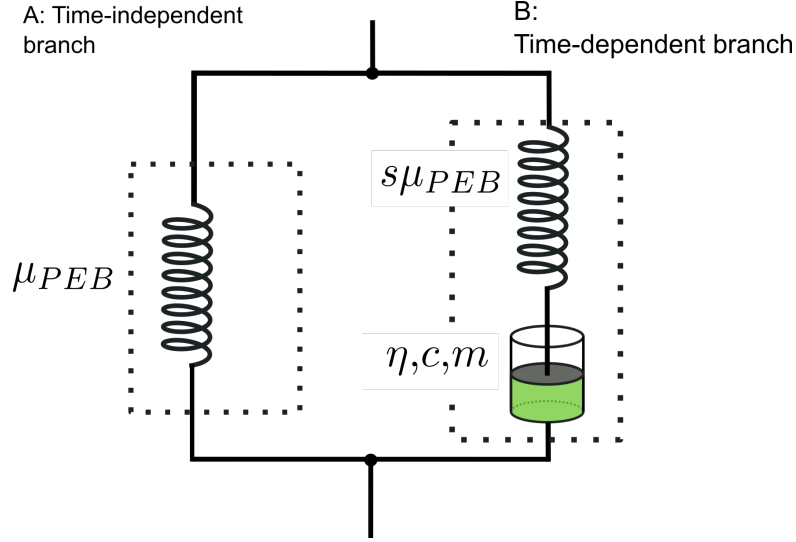
Figure 5.22: Rheological representation of PEB elastomer.

To calibrate both 50 and 100 % functionalized PEB (PEB_{50} and PEB_{100})we used the stress relaxation tests experimental data (section 4.1). To obtain the deformation gradient $\mathbf{F}$ corresponding to the axial deformation during a stress relaxation test, a FEA is performed where a dog-bone specimen (fig. 5.23) is stretched to 0.6% in 5 seconds and held during 1h (replicating the PEB stress relaxations tests).

Once the deformation gradient $\mathbf{F}$ is obtained from the FEA simulation, we proceed to initialize the loop for the n number of increments in the simulation (fig. 5.24). For the first increment $\mathbf{F} = \mathbf{I}$. Then, we calculate the isochoric part $\bar{\mathbf{F}}$ and the left Cauchy-Green tensor $\mathbf{B}^* = \bar{\mathbf{F}}\bar{\mathbf{F}}^T$ and $\mathbf{B}_B^{e*} = \bar{\mathbf{F}}_B^{e*}(\bar{\mathbf{F}}_B^{e*})^T$, for the branch A and B respectively. The above definition induces a further split of the Cauchy stress:

$$\mathbf{T}_{total} = \mathbf{T}_A(\mathbf{B}^*) + \mathbf{T}_B(\mathbf{B}_B^{e*})$$
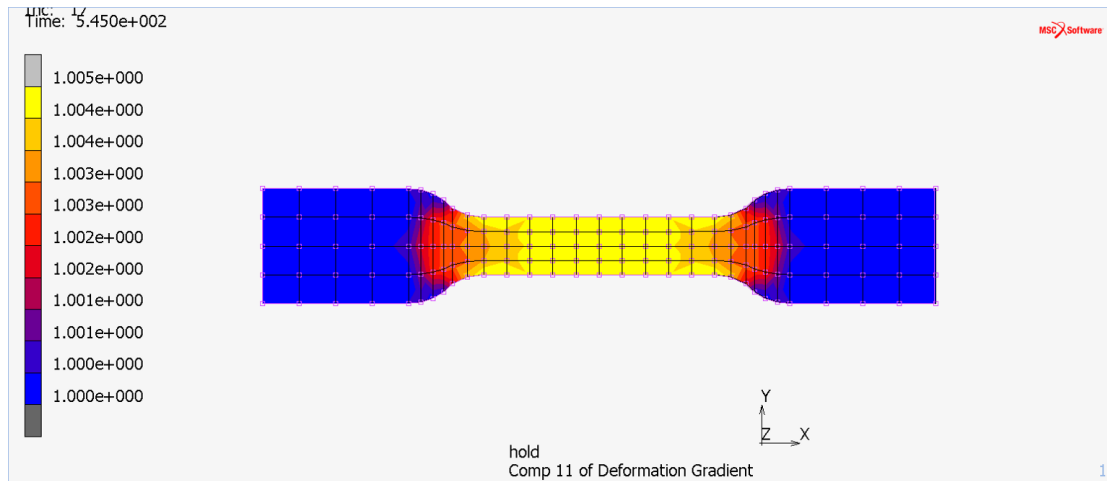
Figure 5.23: FEA results for the PEB stress relaxation tests.

where:

$$\mathbf{T}_B = \frac{s\mu^{(B)}}{J_B^e \bar{\lambda}_B^{e*}} \frac{\mathscr{L}^{-1}(\bar{\lambda}_B^{e*}/\lambda_{lock}^B)}{\mathscr{L}^{-1}(1/\lambda_{lock}^B)} dev(\mathbf{B}_B^{e*})$$

$$\mathbf{T}_A = \frac{\mu^{(A)}}{J\bar{\lambda}^*} \frac{\mathscr{L}^{-1}(\bar{\lambda}^*/\lambda_{lock}^A)}{\mathscr{L}^{-1}(1/\lambda_{lock}^A)} dev(\mathbf{B}^*)$$

The creep law is applied in the subsequent increments. To calculate the current elastic deformation of branch B, the following expression is utilized:

$$\bar{\mathbf{F}}_{B(inc)}^{e*} = \bar{\mathbf{F}}_{inc} \left(\bar{\mathbf{F}}_{B(inc)}^{i*} \right)^{-1} \tag{5.35}$$

where $\bar{\mathbf{F}}_{B(inc)}^{i*}$ is the inelastic deformation gradient tensor that was saved at the end of the last increment and can be accessed at the start of the current one. Additionally, the inelastic deformation gradient rate tensor,$\dot{\bar{\mathbf{F}}}_{B(inc+1)}^{i*}$, and the inelastic deformation gradient, $\bar{\mathbf{F}}_{B(inc+1)}^{i*}$ can be recalculated as:

$$\dot{\bar{\mathbf{F}}}_{B(inc+1)}^{i*} = \left(\bar{\mathbf{F}}_{B(inc)}^{e*} \right)^{-1} \mathbf{D}_{B(inc+1)}^{i} \bar{\mathbf{F}}_{B(inc)} \tag{5.36}$$

$$\bar{\mathbf{F}}_{B(inc+1)}^{i*} = \dot{\bar{\mathbf{F}}}_{B(inc+1)}^{i*} \Delta t + \bar{\mathbf{F}}_{B(inc)}^{i*} \tag{5.37}$$

where $\mathbf{D}_{B(inc+1)}^{i} = \dot{\gamma}(\mathbf{T}_{B(inc)}^{'}/(\sqrt{2}\tau_B))$ is the inelastic stretching rate tensor at the end of the current increment and Δt is the time increment size.
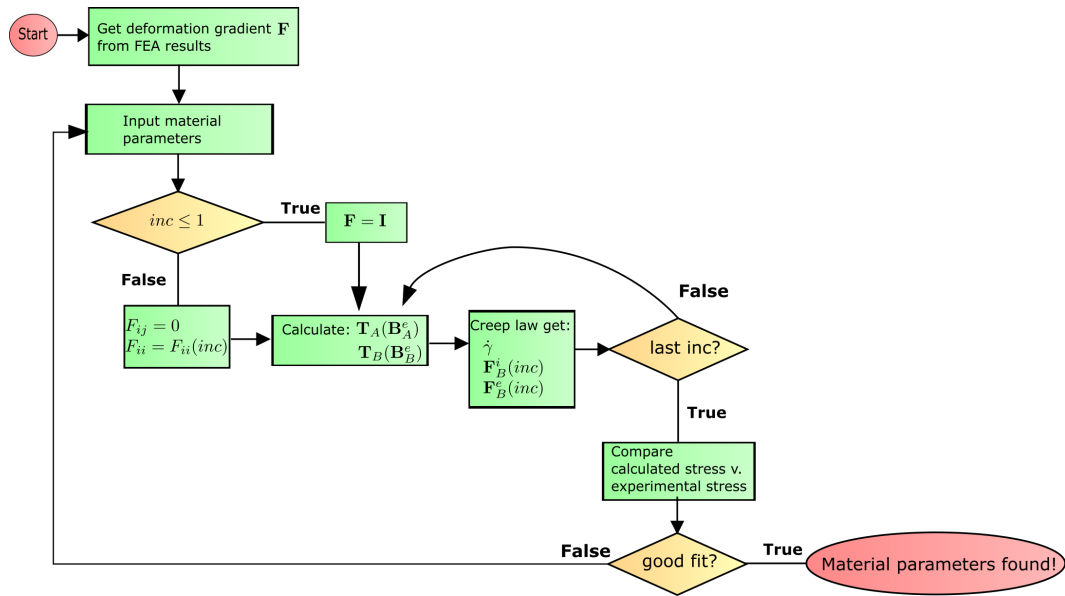
Figure 5.24: Flowchart Bergtrom-Boyce model parameters calculation algorithm

When the final increment is reached, the script plots the total stress in the axial direction T_{11} in function with time. This numerical result is compared with the experimental stress relaxation data, if both the correlation is satisfied, the viscoelastic model parameters are found (fig. 5.25).

Following the algorithm represented by the flowchart in figure 5.24, the parameters for the PEB_{50} and PEB_{100} are:

Parameter	PEB_{50}	PEB_{100}
s	3	0.5
η	$1x10^{-4}$	$5x10^{-4}$
c	-0.5	-0.6
m	2	1.5

Table 5.7: Viscoelastic parameters for PEB_{50} and PEB_{100}. η is in MPa^{m}s^{-1}

It is important to clarify that the parameter $\lambda_{lock} = 100$ remains unchanged, since it has no influence because the applied strain is very weak.

The stress relaxation test FEA simulation is carried out again with the parameters in table 5.7 applied. Results are shown in figure 5.25 for both functionalized elastomers.
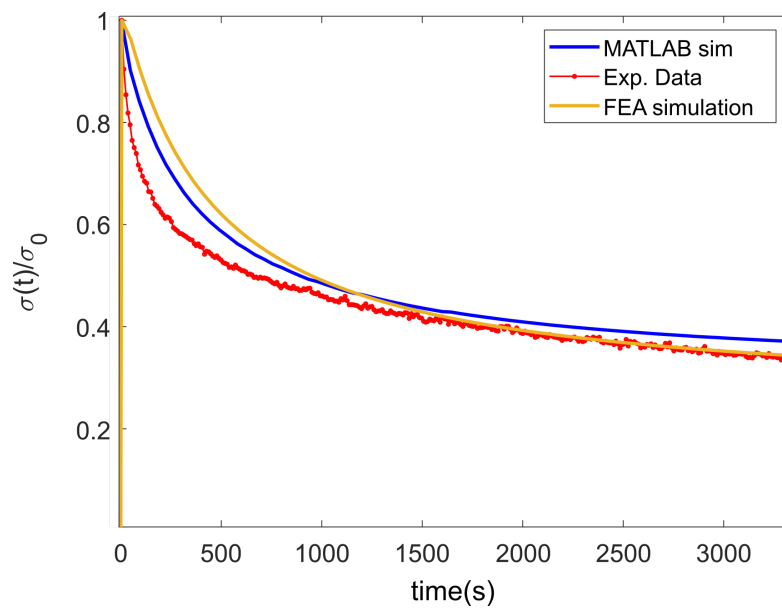
(a) 50% functionalized PEB calibration
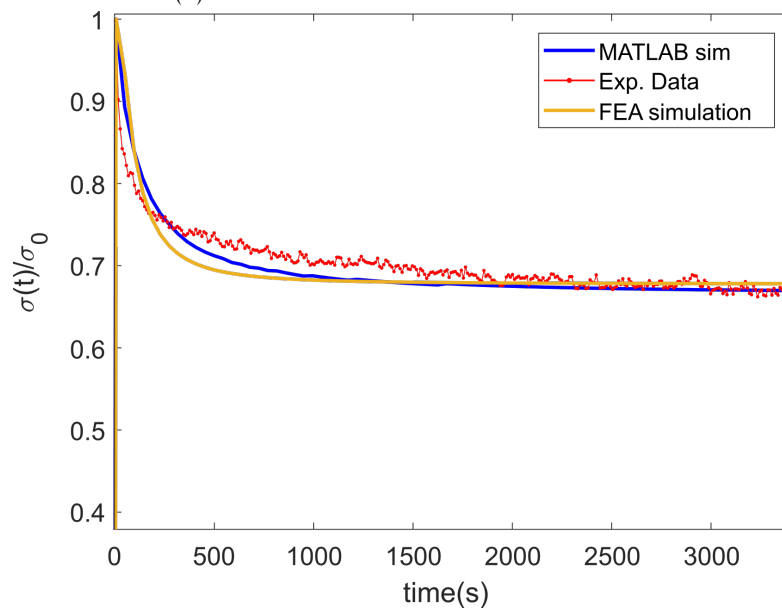
(b) 100% functionalized PEB calibration

Figure 5.25: Stress relaxation test for 50% (a) and 100% (b) functionalized PEB numerical, FEA simulation and experimental results.

5.6 Photo-visco-hyperelastic constitutive model and FE implementation

The constitutive model proposed considers the finite strain photo-visco-hyperelastic behavior of DTE-UPy-PEB thin films. The rheological representation is provided in figure 5.26. To consider the photo-mechanical behavior, we assume that the overall resistance to deformation consists of a component that is dependent on light acting in series with a mechanical network. This mechanical network is linked to stress-free photo-expansion and large strain visco-elastic behavior.

In this case, the time-independent branches are assumed to be three, representing the PEB (μ_{PEB}) and the DTE stiffness in OF (μ_{OF}) and CF (μ_{CF}). The time-dependent branch is similar to that of the elastomer model, meaning that the viscoelastic parameters are assumed to remain constant from the PEB and will depend on the type of functionalized elastomer used to create the photo-responsive thin film.
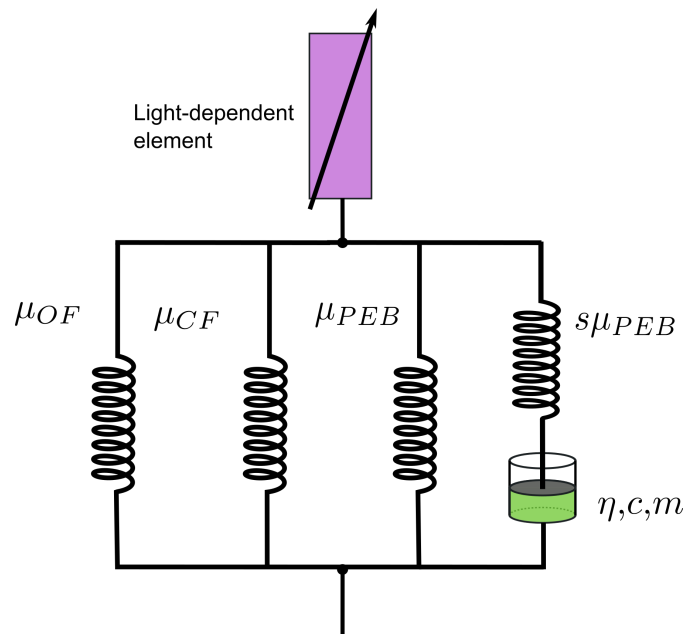
Figure 5.26: Rheological representation of PEB DTE-UPy-PEB thin films.

5.6.1 Kinematics

To incorporate the relation between the photo-expansion and the mechanical behavior of the continuum body the photo-mechanical response can be described as the prod-
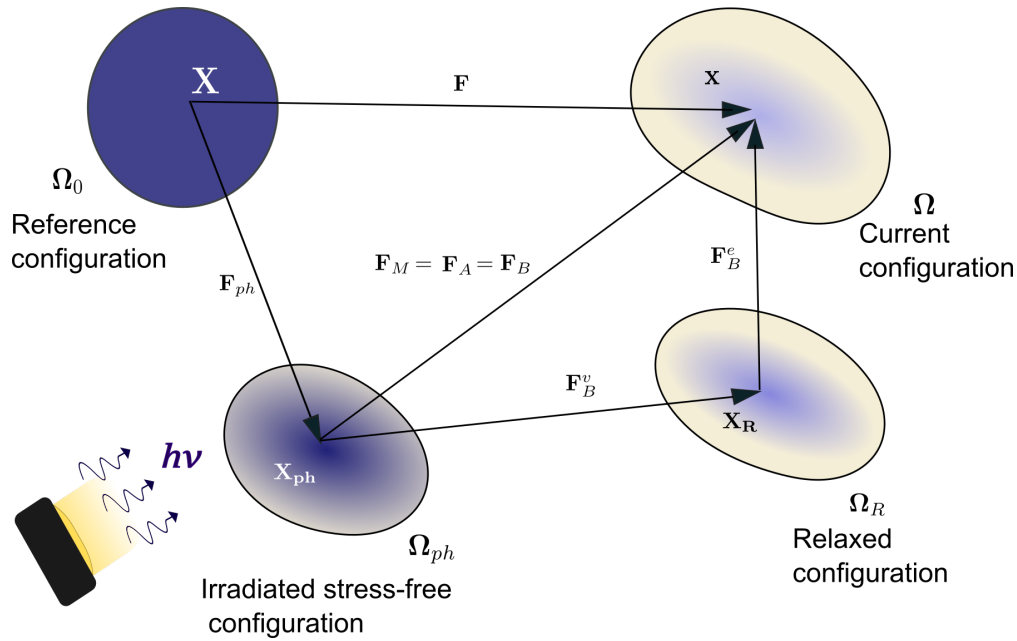
Figure 5.27: Deformation gradient decomposition

uct of two parts: a photo-physical component, represented by $\mathbf{F}_{ph}$, and a mechanical component, $\mathbf{F}_M$ (fig. 5.27). This idea is known as multiplicative decomposition of the deformation gradient and has been proposed by Ovalle-Rodas [149] for thermo-mechanical coupling.

$$\mathbf{F} = \mathbf{F}_{ph}\mathbf{F}_M \tag{5.38}$$

The three first resistance could be contained in the time-independent branch A in the PEB model (fig. 5.22). In this manner: $\mathbf{F}_M = \mathbf{F}_A = \mathbf{F}_B$.

The irradiated stress-free configuration Ω_{ph} is related to the photo-expansion of the continuum body, and is characterized by the photo deformation gradient tensor, derived from the photostrain tensor ε^{ph}, previously discussed. The relaxed configuration Ω_R is associated with the configuration obtained during a spontaneous virtual elastic unloading of the branch B. It is defined by the time-dependent deformation gradient tensor $\mathbf{F}_B = \mathbf{F}_B^e \mathbf{F}_B^i$. And is computed following the Bergstrom-Boyce formulation.

Likewise equation 5.31, the total Cauchy stress $\mathbf{T}$ is the sum of the Cauchy stresses of the relaxed-response of the time-independent branches and the time-dependent branch B:

$$\mathbf{T} = f_{matrix}\mathbf{T}_{PEB} + f_{\text{DTE}}\left(\chi_{OF}(y,t)\mathbf{T}_{OF} + \chi_{CF}(y,t)\mathbf{T}_{CF}\right) + \mathbf{T}_B \qquad (5.39)$$

5.6.2   Light-induced bending during VIS-UV cycle irradiation: FEA v. experimental results

Once more, the finite element simulation described in the section 5.4 was carried out, incorporating the viscoelastic parameters listed in table 5.7. To compare the simulation results with those obtained from experiments, it is necessary to calibrate the photo-expansion constant a^{ph}_{ij} for both VIS and UV irradiation, which is introduced in equations 5.23 and 5.24. Moreover, a^{ph}_{ij} will indicate the extent of the tip displacement.Its value is affected by not only photochemical factors such as light absorbance coefficient $\alpha_{(vis,uv)}$ or the DTE transformation rate $k_{(vis,uv)}$, but also by PEB properties.

During the experimental study, thin films with 50% functionalized PEB showed a small photomechanical effect, determined by the extent of the tip displacement (fig. 5.28a). While those with 100% functionalized PEB resulted in a higher tip displacement (fig. 5.28b). It's noteworthy that both types of films had the same DTE content and were evaluated under identical light intensities.

The photo-expansion coefficient could be defined as the linear expansion by photon absorbed. Assuming that during the UV irradiation occurs a material expansion and during VIS irradiation the material contracts in the opposite direction, the photo-expansion coefficients in the x axis a^{ph}_{11} for thin films with a 1:1 mol ratio are listed in table 5.8.

	DTE–UPy–PEB$_{50}$	DTE–UPy–PEB$_{100}$
VIS	$-6x10^{-4}$	$-4x10^{-3}$
UV	$8x10^{-4}$	$6x10^{-3}$

Table 5.8: Photo-expansion coefficient a^{ph}_{11} for DTE-UPy-PEB thin films with a 1:1 molar ratio

The comparison of the results from the FEA simulation and the experiments is shown in figure 5.28. In both, the photomechanical thin films go through a single photoirradiation cycle (1h VIS and 1h UV), demonstrating that the photomechanical effect seen in the experimental study is predicted by the model that has been proposed (fig. 5.26).

(a)

(b)
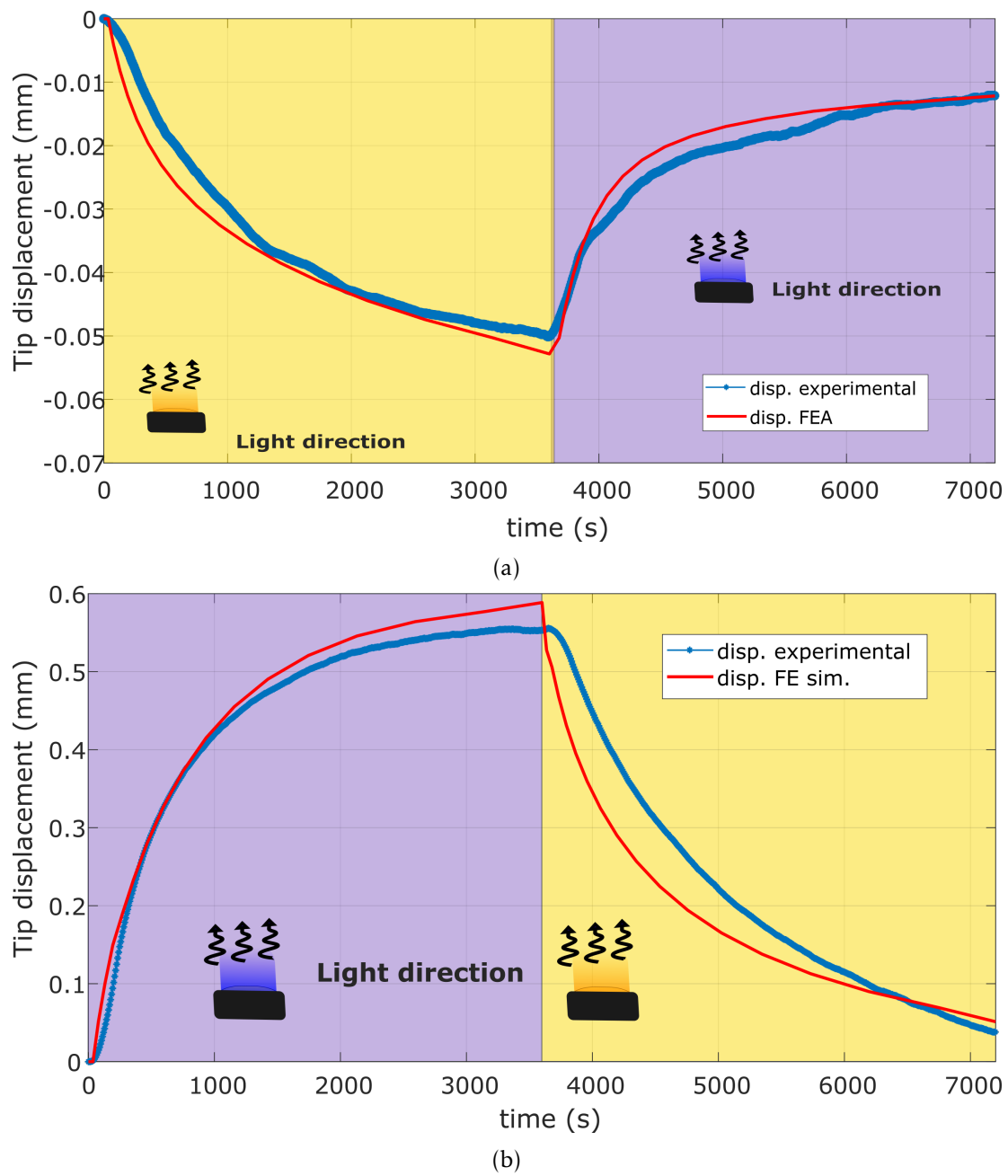
Figure 5.28: FEA simulation v. experimental results tip displacement comparison for DTE-UPy-PEB 1:1 molar ratio. With 50% (a) and 100% (b) functionalized PEB

5.6.3   Photoexpansion in function of DTE content

In the experimental study, DTE-UPy-PEB (100% functionalized) thin films with different DTE content were analyzed under photoirradiation and their maximum tip displacement was measured. These measurements suggest that the range of photo-expantion is dependent of the DTE mass fraction (fig. 5.29a).

The relation could be fitted using the a form of the Sifmoid function:

$$f(r_{DTE}) = a_{max}\left(\frac{1}{1 + De^{-kr_{DTE}}}\right) \tag{5.40}$$

where a_{max} is the maximum tip displacement at a saturated DTE concentration, r_{DTE} is the DTE mass fraction and, D and k are constants.

Using the same relation (eq. 5.40) the value for the photo-expansion coefficient a^{ph} can be determined with respect to the DTE mass fraction r_{DTE}. In table 5.9 the fitting results are given.

	Maximum tip displacement	Photo-expansion
a_{max}	0.55 (mm)	$6x10^{-3}$ (mm/mm)
D	242.1	77.74
k	48.83	34.43

Table 5.9: Photo-expansion coefficient a_{11}^{ph} for DTE-UPy-PEB thin films with a 1:1 molar ratio

Finally, FEA simulations were performed introducing the photoexpansion coefficients corresponding to a r_{DTE} and compared to the experimental data (fig. 5.30).

5.7   Conclusions: Constitutive model for photomechanical thin films

In this final chapter, we investigated the photochemical behavior of DTE-UPy-PEB thin films using the Pariani model, which led us to the computation of their absorbance coefficients in both UV and visible light, denoted as α_{uv} and α_{vis}, respectively, as well as their photo-transformation rates, denoted as k_{uv} and k_{vis}.

Moreover, we coupled the aforementioned photokinetic model with the mechanical properties of the elastomer PEB and its functionalization. We proposed a mechanical model represented by a network of springs, modeled by the Arruda-Boyce hyperelastic
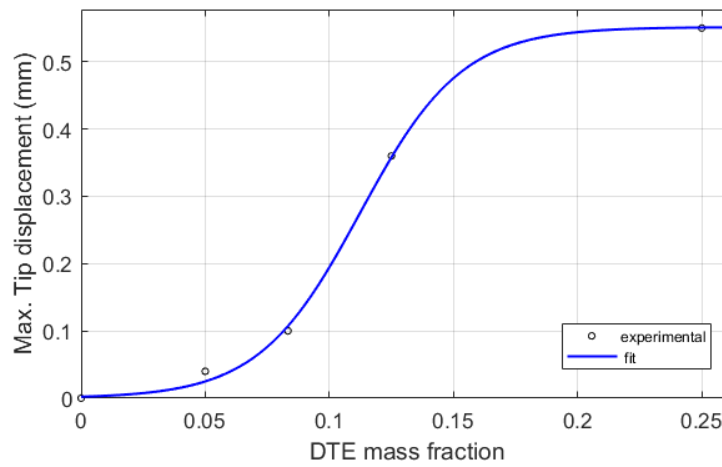
(a)
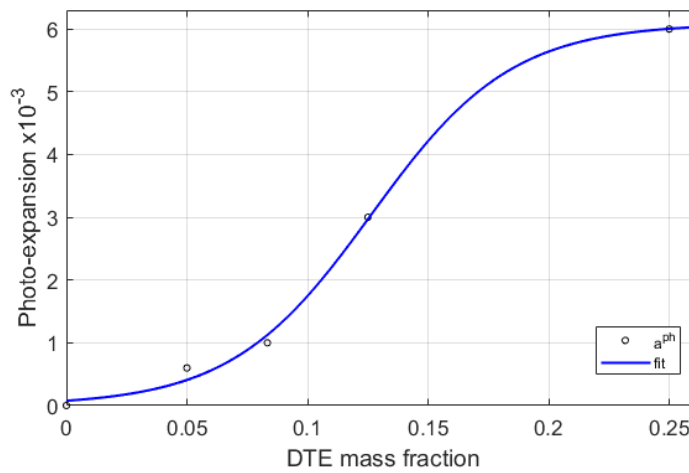
(b)

Figure 5.29: Photo expansion and maximum tip displacement in function of DTE mass fraction fitting results (blue line).

nonlinear strain density equation, which is connected to a light-dependent element. We implemented this rheological model using external user subroutines in the FEA software MARC, which allowed us to estimate the light-induced bending of the thin films, as well as the impact of various factors such as the thickness, light intensity, and DTE content.

To take into account the viscoelastic behavior, we utilized an algorithm based on the Bergstrom-Boyce model to calculate the viscoelastic parameters, which were then incorporated into the FEM. This approach provided more accurate results, which we
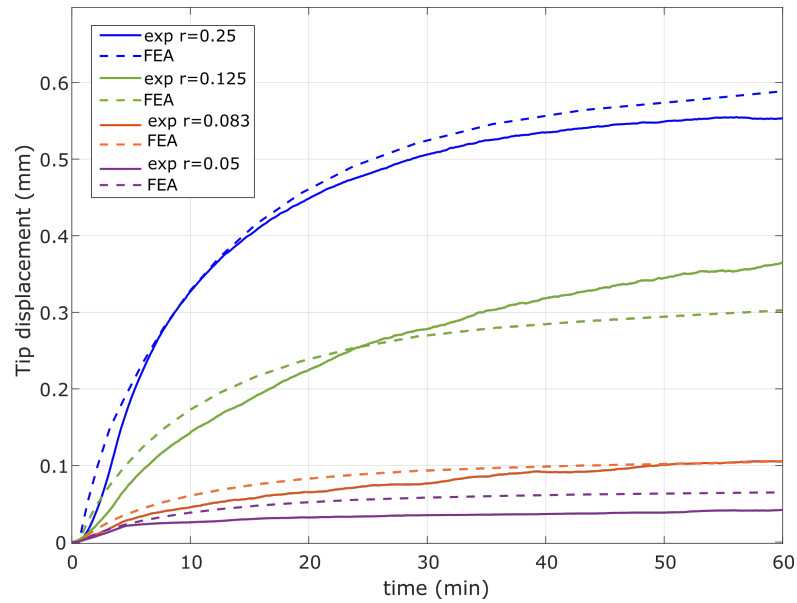
Figure 5.30: Tip displacement during UV irradiation varying DTE mass fraction (r). Experimental (solid line) v. FEA results (dashed line).

validated using experimental data. Finally, we introduced an important photomechanical parameter denoted as a^{ph}, which determines the degree of light-induced expansion in the axial direction as a function of the photoactive molecule concentration present in the thin film.

General conclusion and Future work

The development of light-responsive materials is a rapidly growing area of research with numerous applications in a range of fields. In this thesis, we have explored the mechanical and photochemical properties of supramolecular DTE-UPY-PEB thin films and investigated how they respond to light exposure.

One of the key insights gained from our research is the importance of understanding the interplay between the mechanical and photochemical properties of these films. By taking a multidisciplinary approach that combines knowledge of mechanics, materials science, and photochemistry, we have been able to gain a deeper understanding of the underlying physics behind the behavior of these films. Both the photochemical and mechanical properties of DTE-UPY-PEB thin films have been defined by experimental and numerical methods. The FEM allowed us to predict the behavior of theses films under different scenarios and we could validate the model with experimental results. This new tool could be used in future work to define optimization algorithms to design a more efficient smart material.

Our results have numerous practical implications for a range of applications, including the development of responsive surfaces for actuation and sensing. By leveraging the unique properties of light-responsive thin films, we can develop new technologies that are more efficient, cost-effective, and environmentally friendly.

Additionally, our work has contributed to the broader field of smart materials mechanics, which encompasses a wide range of systems that are characterized by their flexibility and responsiveness. By studying the mechanical behavior of light-responsive thin films, we have been able to gain insights into the fundamental principles that govern the

mechanics of supramolecular organic thin films.

Although our research has made significant progress in understanding the behavior of light-responsive thin films, still many unanswered questions need to be addressed. Future work in this area could focus on exploring the use of different elaboration methods, investigating the behavior of these films under different environmental conditions, and developing new techniques for studying their mechanical properties.

Furthermore, the finite element model could be optimized using different FEA software and coding a single subroutine that comprises the photo-visco-elastic behavior of the photoresponsive thin films, in this way future finite element simulations could be focused on exploring different geometries and different elastomer matrices, for example, simulating the photomechanical behavior of textile fibers with a DTE-based coating.

In conclusion, our research has contributed to a deeper understanding of the photomechanical properties of photoactive supramolecular organic thin films by proposing a first constitutive model that couples the photokinetics of DTE with the viscoelastic behavior of the elastomer PEB. This work has opened up new paths for developing innovative technologies. As we continue to explore the behavior of these materials, we can expect to see even more exciting discoveries and applications emerge in the years to come.

Bibliography

[1]   K. Uchino. "Photostrictive Actuator". In: *IEEE Symposium on Ultrasonics*. IEEE Symposium on Ultrasonics. Dec. 1990, 721–723 vol.2. DOI: 10.1109/ULTSYM.1990.171457.

[2]   Jianbo De et al. "Remotely Photocontrolled Microrobots Based on Photomechanical Molecular Crystals". In: *ACS Applied Materials & Interfaces* 12.24 (June 17, 2020), pp. 27493–27498. ISSN: 1944-8244, 1944-8252. DOI: 10.1021/acsami.0c03686.

[3]   P. G Datskos et al. "Photomechanical Chemical Microsensors". In: *Sensors and Actuators B: Chemical*. Proceeding of the Eighth International Meeting on Chemical Sensors IMCS-8 - Part 1 76.1 (June 1, 2001), pp. 393–402. ISSN: 0925-4005. DOI: 10.1016/S0925-4005(01)00647-5.

[4]   Il-Shin Song et al. "Sensitivity Enhancement of a UV Photo-Sensor Based on a Fiber Bragg Grating Coated by a Photomechanical Functional Polymer". In: *Sensors and Actuators A: Physical* 232 (Aug. 1, 2015), pp. 223–228. ISSN: 0924-4247. DOI: 10.1016/j.sna.2015.06.013.

[5]   Xiaoming Fan et al. "MoS $_2$ Actuators: Reversible Mechanical Responses of MoS $_2$ -Polymer Nanocomposites to Photons". In: *Nanotechnology* 26.26 (July 3, 2015), p. 261001. ISSN: 0957-4484, 1361-6528. DOI: 10.1088/0957-4484/26/26/261001.

[6]   M.-H. Li et al. "Light-Driven Side-On Nematic Elastomer Actuators". In: *Advanced Materials* 15.78 (Apr. 17, 2003), pp. 569–572. ISSN: 09359648, 15214095. DOI: 10.1002/adma.200304552.

[7]   Qi Yu et al. "Fabrication of Light-Triggered Soft Artificial Muscles via a Mixed-Matrix Membrane Strategy". In: *Angewandte Chemie International Edition* 57.32 (2018), pp. 10192–10196. ISSN: 1521-3773. DOI: 10.1002/anie.201805543.

[8] Xiaobo Zhang et al. "Photoactuators and Motors Based on Carbon Nanotubes with Selective Chirality Distributions". In: *Nature Communications* 5.1 (May 2014), p. 2983. ISSN: 2041-1723. DOI: 10.1038/ncomms3983.

[9] Klaudia Dradrach et al. "Traveling Wave Rotary Micromotor Based on a Photomechanical Response in Liquid Crystal Polymer Networks". In: *ACS Applied Materials & Interfaces* 12.7 (Feb. 19, 2020), pp. 8681–8686. ISSN: 1944-8244. DOI: 10.1021/acsami.9b20309.

[10] F. Agolini and F. P. Gay. "Synthesis and Properties of Azoaromatic Polymers". In: *Macromolecules* 3.3 (May 1970), pp. 349–351. ISSN: 0024-9297, 1520-5835. DOI: 10.1021/ma60015a015.

[11] Chong-Uk Bang, Atsushi Shishido, and Tomiki Ikeda. "Azobenzene Liquid-Crystalline Polymer for Optical Switching of Grating Waveguide Couplers with a Flat Surface". In: *Macromolecular Rapid Communications* 28 (May 2, 2007), pp. 1040–1044. DOI: 10.1002/marc.200700041.

[12] Wei Deng et al. "Light-Responsive Wires from Side-on Liquid Crystalline Azo Polymers". In: *Liquid Crystals* 36.10-11 (Oct. 1, 2009), pp. 1023–1029. ISSN: 0267-8292. DOI: 10.1080/02678290902759251.

[13] J. Konieczkowska, K. Bujak, and E. Schab-Balcerzak. "A Short Review of the Photomechanical Effect in Azo-Containing Amorphous (Glassy) Polymers". In: *Express Polymer Letters* 15 (2021), pp. 459–472. DOI: 10.3144/expresspolymlett.2021.39.

[14] Munenori Yamada et al. "Photomobile Polymer Materials: Towards Light-Driven Plastic Motors". In: *Angewandte Chemie International Edition* 47.27 (2008), pp. 4986–4988. ISSN: 1521-3773. DOI: 10.1002/anie.200800760.

[15] Masahiro Irie. "Diarylethenes for Memories and Switches". In: *Chemical Reviews* 100.5 (June 15, 2000), 1685−1716.

[16] I. Colombier et al. "Diarylethene Microcrystals Make Directional Jumps upon Ultraviolet Irradiation". In: *The Journal of Chemical Physics* 126.1 (Jan. 3, 2007), p. 011101. ISSN: 0021-9606. DOI: 10.1063/1.2429061.

[17] Kazuhiko Seki and M. Tachiya. "Theoretical Model Based on the Memory Effect for the Strange Photoisomerization Kinetics of Diarylethene Derivatives Dispersed on Polymer Films". In: *The Journal of Chemical Physics* 126.4 (Jan. 28, 2007), p. 044904. ISSN: 0021-9606, 1089-7690. DOI: 10.1063/1.2430527.

[18] Eun-Kyoung Kim, Mi-Young Kim, and Kyong-Tae Kim. "A New Diarylethene with Donor-acceptor Group for Reversible Photo-induced Electrochemical Switching". In: *Bulletin of the Korean Chemical Society* 29.4 (2008), pp. 827–832. ISSN: 0253-2964. DOI: 10.5012/bkcs.2008.29.4.827.

[19] André Ribeiro Santos et al. "Photochemical Investigation of a Photochromic Diarylethene Compound That Can Be Used as a Wide Range Actinometer". In: *Photochemical & Photobiological Sciences* 8.12 (2009), p. 1734. ISSN: 1474-905X, 1474-9092. DOI: 10.1039/b9pp00037b.

[20] Michinori Takeshita et al. "Photoreversible Supramolecular Polymer Formation". In: *Chemical Communications* 6 (2005), p. 761. ISSN: 1359-7345, 1364-548X. DOI: 10.1039/b415114c.

[21] Michinori Takeshita, Miyuki Hayashi, and Takashi Miyazaki. "A Fully Photoreversible Supramolecular Polymer Having a Diarylethene Photoswitch". In: *Chemistry Letters* 39.2 (Feb. 5, 2010), pp. 82–83. ISSN: 0366-7022, 1348-0715. DOI: 10.1246/cl.2010.82.

[22] B. J. B. Folmer et al. "Supramolecular Polymer Materials: Chain Extension of Telechelic Polymers Using a Reactive Hydrogen-Bonding Synthon". In: *Advanced Materials* 12.12 (2000), pp. 874–878. ISSN: 1521-4095. DOI: 10.1002/1521-4095(200006)12:12<874::AID-ADMA874>3.0.CO;2-C.

[23] L. Brunsveld et al. "Supramolecular Polymers". In: *Chemical Reviews* 101.12 (Dec. 1, 2001), pp. 4071–4098. ISSN: 0009-2665, 1520-6890. DOI: 10.1021/cr990125q.

[24] Maroua Louati. "Multiscale Approach of Photomechanical Thin Films Based on the Supramolecular Assembly of Bistable Photoswitch and Thermoplastic Elastomer". PhD thesis. France: Univeristé de Lille, 2019. 241 pp.

[25] michi_Saga Univ, director. *Supramolecularpolymer Vis*. Oct. 7, 2013. URL: https://www.youtube.com/watch?v=IVrt9k7rLOQ.

[26] Masakazu Morimoto and Masahiro Irie. "A Diarylethene Cocrystal That Converts Light into Mechanical Work". In: *Journal of the American Chemical Society* 132.40 (Oct. 13, 2010), pp. 14172–14178. ISSN: 0002-7863, 1520-5126. DOI: 10.1021/ja105356w.

[27] Daichi Kitagawa and Seiya Kobatake. "Crystal Thickness Dependence of the Photoinduced Crystal Bending of 1-(5-Methyl-2-(4-(p-Vinylbenzoyloxymethyl)Phenyl)-4-Thiazolyl)-2-(5-Methyl-2-Phenyl-4-Thiazolyl)Perfluorocyclopentene". In: *Photochemical & Photobiological Sciences* 13.5 (2014), p. 764. ISSN: 1474-905X, 1474-9092. DOI: 10.1039/c3pp50417d.

[28] Daichi Kitagawa, Rika Tanaka, and Seiya Kobatake. "Dependence of Photoinduced Bending Behavior of Diarylethene Crystals on Irradiation Wavelength of Ultraviolet Light". In: *Physical Chemistry Chemical Physics* 17.41 (2015), pp. 27300–27305. ISSN: 1463-9076, 1463-9084. DOI: 10.1039/C5CP03073K.

[29] Seiya Kobatake and Daichi Kitagawa. "Photomechanical Behavior of Photochromic Diarylethene Crystals". In: *Mechanically Responsive Materials for Soft Robotics*. Ed. by Hideko Koshima. 1st ed. Wiley, Jan. 7, 2020, pp. 1–28. ISBN: 978-3-527-34620-2 978-3-527-82220-1. DOI: 10.1002/9783527822201.ch1.

[30]   Ayako Fujimoto et al. "Photoinduced Swing of a Diarylethene Thin Broad Sword Shaped Crystal: A Study on the Detailed Mechanism". In: *Chemical Science* 11.45 (Nov. 25, 2020), pp. 12307–12315. ISSN: 2041-6539. DOI: 10.1039/D0SC05388K.

[31]   Kevin N. Long et al. "Photomechanics of Light-Activated Polymers". In: *Journal of the Mechanics and Physics of Solids* 57.7 (July 2009), pp. 1103–1121. ISSN: 00225096. DOI: 10.1016/j.jmps.2009.03.003.

[32]   Martin L. Dunn. "Photomechanics of Mono- and Polydomain Liquid Crystal Elastomer Films". In: *Journal of Applied Physics* 102.1 (July 2007), p. 013506. ISSN: 0021-8979, 1089-7550. DOI: 10.1063/1.2745063.

[33]   Craig M. Hamel, Fangda Cui, and Shawn A. Chester. "A Finite Element Method for Light Activated Shape-Memory Polymers: A FINITE ELEMENT METHOD FOR LIGHT ACTIVATED SHAPE-MEMORY POLYMERS". In: *International Journal for Numerical Methods in Engineering* 111.5 (Aug. 3, 2017), pp. 447–473. ISSN: 00295981. DOI: 10.1002/nme.5475.

[34]   Jing Ma et al. "A Photoviscoplastic Model for Photoactivated Covalent Adaptive Networks". In: *Journal of the Mechanics and Physics of Solids* 70 (Oct. 2014), pp. 84–103. ISSN: 00225096. DOI: 10.1016/j.jmps.2014.05.008.

[35]   Liang Cheng et al. "Photomechanical Bending Mechanics of Polydomain Azobenzene Liquid Crystal Polymer Network Films". In: *Journal of Applied Physics* 112.1 (July 2012), p. 013513. ISSN: 0021-8979, 1089-7550. DOI: 10.1063/1.4729771.

[36]   Jonghoon Bin and William S. Oates. "Unifying Relations in Polymer Photomechanics". In: SPIE Smart Structures and Materials + Nondestructive Evaluation and Health Monitoring. Ed. by Nakhiah C. Goulbourne. San Diego, California, United States, Apr. 1, 2015, p. 943202. DOI: 10.1117/12.2084344.

[37]   Dennice Roberts et al. "Photomechanically Coupled Viscoelasticity of Azobenzene Polyimide Polymer Networks". In: *Modelling and Simulation in Materials Science and Engineering* 25.5 (July 1, 2017), p. 055009. ISSN: 0965-0393, 1361-651X. DOI: 10.1088/1361-651X/aa7191.

[38]   Jisoo Jeon et al. "Continuous and Programmable Photomechanical Jumping of Polymer Monoliths". In: *Materials Today* 49 (Oct. 2021), pp. 97–106. ISSN: 13697021. DOI: 10.1016/j.mattod.2021.04.014.

[39]   Giorgio Pariani et al. "Kinetics of Photochromic Conversion at the Solid State: Quantum Yield of Dithienylethene-Based Films". In: *The Journal of Physical Chemistry A* 115.44 (Nov. 10, 2011), pp. 12184–12193. ISSN: 1089-5639, 1520-5215. DOI: 10.1021/jp207210p.

[40]   J. Lagowski and H. C. Gatos. "Photomechanical Effect in Noncentrosymmetric Semiconductors-CdS". In: *Applied Physics Letters* 20.1 (Jan. 1972), pp. 14–16. ISSN: 0003-6951, 1077-3118. DOI: 10.1063/1.1653958.

[41]   G Smets, J Braeken, and M Irie. "PHOTOMECHANICAL EFFECTS IN PHOTOCHROMIC SYSTEMS". In: *Pure & App. Chem* 50 (1978), pp. 845–856.

[42]   Seiya Kobatake, Hiroki Hasegawa, and Kentaro Miyamura. "High-Convertible Photochromism of a Diarylethene Single Crystal Accompanying the Crystal Shape Deformation". In: *Crystal Growth & Design* 11.4 (Apr. 6, 2011), pp. 1223–1229. ISSN: 1528-7483, 1528-7505. DOI: 10.1021/cg101448m.

[43]   Masahiro Irie, Seiya Kobatake, and Masashi Horichi. "Reversible Surface Morphology Changes of a Photochromic Diarylethene Single Crystal by Photoirradiation". In: *Science* 291.5509 (Mar. 2, 2001), pp. 1769–1772. ISSN: 0036-8075, 1095-9203. DOI: 10.1126/science.291.5509.1769.

[44]   Seiya Kobatake et al. "Rapid and Reversible Shape Changes of Molecular Crystals on Photoirradiation". In: *Nature* 446.7137 (Apr. 2007), pp. 778–781. ISSN: 0028-0836, 1476-4687. DOI: 10.1038/nature05669.

[45]   Akira Hirano et al. "Dependence of Photoinduced Bending Behavior of Diarylethene Crystals on Ultraviolet Irradiation Power". In: *Crystal Growth & Design* 17.9 (Sept. 6, 2017), pp. 4819–4825. ISSN: 1528-7483, 1528-7505. DOI: 10.1021/acs.cgd.7b00755.

[46]   Akira Hirano, Daichi Kitagawa, and Seiya Kobatake. "Photomechanical Bending Behavior of Photochromic Diarylethene Crystals Induced under Polarized Light". In: *CrystEngComm* 21.15 (2019), pp. 2495–2501. ISSN: 1466-8033. DOI: 10.1039/C9CE00175A.

[47]   Arri Priimagi et al. "Location of the Azobenzene Moieties within the Cross-Linked Liquid-Crystalline Polymers Can Dictate the Direction of Photoinduced Bending". In: *ACS Macro Letters* 1.1 (Jan. 17, 2012), pp. 96–99. ISSN: 2161-1653, 2161-1653. DOI: 10.1021/mz200056w.

[48]   Lingyan Zhu et al. "Photomechanical Effects in Photochromic Crystals". In: *Photomechanical Materials, Composites, and Systems*. Ed. by Timothy J. White. Chichester, UK: John Wiley & Sons, Ltd, June 2, 2017, pp. 233–274. ISBN: 978-1-119-12327-9 978-1-119-12330-9. DOI: 10.1002/9781119123279.ch7.

[49]   Lingyan Zhu, Rabih O. Al-Kaysi, and Christopher J. Bardeen. "Reversible Photoinduced Twisting of Molecular Crystal Microribbons". In: *Journal of the American Chemical Society* 133.32 (Aug. 17, 2011), pp. 12569–12575. ISSN: 0002-7863, 1520-5126. DOI: 10.1021/ja201925p.

[50]   Rabih O. Al-Kaysi. "Photomechanical Actuation in Organic Crystals: Expansion, Bending, Coiling, Twisting and Peeling". In: *Acta Crystallographica Section A Foundations and Advances* 71.a1 (Aug. 23, 2015), s125–s125. ISSN: 2053-2733. DOI: 10.1107/S2053273315098198.

[51]   Daichi Kitagawa, Hiroyasu Nishi, and Seiya Kobatake. "Photoinduced Twisting of a Photochromic Diarylethene Crystal". In: *Angewandte Chemie International Edition* 52.35 (Aug. 26, 2013), pp. 9320–9322. ISSN: 14337851. DOI: 10.1002/anie.201304670.

[52]   Daichi Kitagawa et al. "Control of Photomechanical Crystal Twisting by Illumination Direction". In: *Journal of the American Chemical Society* (), p. 7.

[53]   Panče Naumov et al. "Mechanically Responsive Molecular Crystals". In: *Chemical Reviews* 115.22 (Nov. 25, 2015), pp. 12440–12490. ISSN: 0009-2665, 1520-6890. DOI: 10.1021/acs.chemrev.5b00398.

[54]   Panče Naumov et al. "Dynamic Single Crystals: Kinematic Analysis of Photoinduced Crystal Jumping (The Photosalient Effect)". In: *Angewandte Chemie International Edition* 52.38 (2013), pp. 9990–9995. ISSN: 1521-3773. DOI: 10.1002/anie.201303757.

[55]   Peng-Fei Luo et al. "Photomechanical Polymer Hydrogels Based on Molecular Photoswitches". In: *Journal of Polymer Science* 59.20 (Oct. 15, 2021), pp. 2246–2264. ISSN: 2642-4150, 2642-4169. DOI: 10.1002/pol.20210567.

[56]   C. L. van Oosten et al. "Glassy Photomechanical Liquid-Crystal Network Actuators for Microscale Devices". In: *The European Physical Journal E* 23.3 (July 2007), pp. 329–336. ISSN: 1292-8941, 1292-895X. DOI: 10.1140/epje/i2007-10196-1.

[57]   A. Athanassiou et al. "All-Optical Reversible Actuation of Photochromic-Polymer Microsystems". In: *Advanced Materials* 17.8 (Apr. 18, 2005), pp. 988–992. ISSN: 0935-9648, 1521-4095. DOI: 10.1002/adma.200401078.

[58]   Alexis Perrot, Emilie Moulin, and Nicolas Giuseppone. "Extraction of Mechanical Work from Stimuli-Responsive Molecular Systems and Materials". In: *Trends in Chemistry* 3.11 (Nov. 2021), pp. 926–942. ISSN: 25895974. DOI: 10.1016/j.trechm.2021.08.007.

[59]   Shaodong Sun et al. "Photoresponsive Polymers with Multi-Azobenzene Groups". In: *Polymer Chemistry* (2019), p. 13.

[60]   H. Finkelmann et al. "A New Opto-Mechanical Effect in Solids". In: *Physical Review Letters* 87.1 (June 15, 2001), p. 015501. ISSN: 0031-9007, 1079-7114. DOI: 10.1103/PhysRevLett.87.015501.

[61]   Rob C. P. Verpaalen et al. "Liquid Crystal Networks on Thermoplastics: Reprogrammable Photo-Responsive Actuators". In: *Angewandte Chemie International Edition* 59.11 (2020), pp. 4532–4536. ISSN: 1521-3773. DOI: 10.1002/anie.201915147.

[62]   Ruoyuan Yin et al. "Can Sunlight Drive the Photoinduced Bending of Polymer Films?" In: *Journal of Materials Chemistry* 19.20 (May 12, 2009), pp. 3141–3143. ISSN: 1364-5501. DOI: 10.1039/B904973H.

[63]   Domenico Pirone et al. "Molecular Design of Microcapsule Shells for Visible Light-Triggered Release". In: *Polymers* 11.5 (5 May 2019), p. 904. ISSN: 2073-4360. DOI: 10.3390/polym11050904.

[64]   Rita Del Pezzo et al. "Ortho-Substituted Azobenzene: Shedding Light on New Benefits". In: *Pure and Applied Chemistry* 91.9 (Sept. 1, 2019), pp. 1533–1546. ISSN: 1365-3075. DOI: 10.1515/pac-2018-0719.

[65] Bartosz Tylkowski et al. "Light-Induced Switching of the Wettability of Novel Asymmetrical Poly(Vinyl Alcohol)-Co-Ethylene Membranes Blended with Azobenzene Polymers". In: *Langmuir* 26.18 (Sept. 21, 2010), pp. 14821–14829. ISSN: 0743-7463. DOI: 10.1021/la101809r.

[66] Bartosz Tylkowski et al. "Photo-Triggered Microcapsules". In: *Macromolecular Symposia* 360.1 (2016), pp. 192–198. ISSN: 1521-3900. DOI: 10.1002/masy.201500093.

[67] Chuang Li et al. "Light-Driven Expansion of Spiropyran Hydrogels". In: *Journal of the American Chemical Society* 142.18 (May 6, 2020), pp. 8447–8453. ISSN: 0002-7863, 1520-5126. DOI: 10.1021/jacs.0c02201.

[68] B. S. Lukyanov and M. B. Lukyanova. "Spiropyrans: Synthesis, Properties, and Application. (Review)". In: *Chemistry of Heterocyclic Compounds* 41.3 (Mar. 2005), pp. 281–311. ISSN: 0009-3122, 1573-8353. DOI: 10.1007/s10593-005-0148-x.

[69] Colin P. McCoy et al. "Synthesis and Characterisation of Polymerisable Photochromic Spiropyrans: Towards Photomechanical Biomaterials". In: *Tetrahedron Letters* 48.4 (Jan. 2007), pp. 657–661. ISSN: 00404039. DOI: 10.1016/j.tetlet.2006.11.110.

[70] Shinichiro Nakamura et al. "Photochromism of Diarylethene: Effect of Polymer Environment and Effects on Surfaces". In: *Journal of Photochemistry and Photobiology C: Photochemistry Reviews*. Special Issue on Photochromism 1 12.2 (Sept. 1, 2011), pp. 138–150. ISSN: 1389-5567. DOI: 10.1016/j.jphotochemrev.2011.07.002.

[71] Takuya Fukushima et al. "Diarylethene-Powered Light-Induced Folding of Supramolecular Polymers". In: *Journal of the American Chemical Society* 143.15 (Apr. 21, 2021), pp. 5845–5854. ISSN: 0002-7863, 1520-5126. DOI: 10.1021/jacs.1c00592.

[72] Bimalendu Adhikari et al. "Photoresponsive Supramolecular Copolymers from Diarylethene–Perylene Bisimide Hydrogen Bonded Complexes". In: *Polymer* 128 (Oct. 2017), pp. 356–362. ISSN: 00323861. DOI: 10.1016/j.polymer.2017.01.025.

[73] Qiu-Ting Fu et al. "Diarylethene-Based Conjugated Polymer Networks for Ultrafast Photochromic Films". In: *New Journal of Chemistry* 43.39 (2019), pp. 15797–15803. ISSN: 1144-0546, 1369-9261. DOI: 10.1039/C9NJ02596K.

[74] Kevin N. Long et al. "Constitutive Model for Photo-Mechanical Behaviors of Photo-Induced Shape Memory Polymers". In: SPIE Smart Structures and Materials + Nondestructive Evaluation and Health Monitoring. Ed. by Benjamin K. Henderson and M. Brett McMickell. San Diego, California, USA, Mar. 26, 2009, 72900N. DOI: 10.1117/12.817612.

[75] D. Corbett, C. L. van Oosten, and M. Warner. "Nonlinear Dynamics of Optical Absorption of Intense Beams". In: *Physical Review A* 78.1 (July 15, 2008), p. 013823. ISSN: 1050-2947, 1094-1622. DOI: 10.1103/PhysRevA.78.013823.

[76] Antoni Sánchez-Ferrer and Heino Finkelmann. "Opto-Mechanical Effect in Photoactive Nematic Main-Chain Liquid-Crystalline Elastomers". In: *Soft Matter* 9.18 (2013), p. 4621. ISSN: 1744-683X, 1744-6848. DOI: 10.1039/c3sm27341e.

[77] Naba K. Nath et al. "Model for Photoinduced Bending of Slender Molecular Crystals". In: *Journal of the American Chemical Society* 136.7 (Feb. 19, 2014), pp. 2757–2766. ISSN: 0002-7863, 1520-5126. DOI: 10.1021/ja4101497.

[78] Junghwan Moon et al. "Multiscale Study of the Relationship between Photoisomerization and Mechanical Behavior of Azo-Polymer Based on the Coarse-Grained Molecular Dynamics Simulation". In: *Macromolecules* 52.5 (Mar. 12, 2019), pp. 2033–2049. ISSN: 0024-9297, 1520-5835. DOI: 10.1021/acs.macromol.8b02535.

[79] Vladimir Toshchevikov, Jaroslav Ilnytskyi, and Marina Saphiannikova. "Photoisomerization Kinetics and Mechanical Stress in Azobenzene-Containing Materials". In: *The Journal of Physical Chemistry Letters* 8.5 (Mar. 2, 2017), pp. 1094–1098. ISSN: 1948-7185. DOI: 10.1021/acs.jpclett.7b00173.

[80] L. Jin, Y. Yan, and Y. Huo. "A Gradient Model of Light-Induced Bending in Photochromic Liquid Crystal Elastomer and Its Nonlinear Behaviors". In: *International Journal of Non-Linear Mechanics* 45.4 (May 2010), pp. 370–381. ISSN: 00207462. DOI: 10.1016/j.ijnonlinmec.2009.12.010.

[81] Muyoung Kim, Jung-Hoon Yun, and Maenghyo Cho. "Light Penetration-Coupled Photoisomerization Modeling for Photodeformation of Diarylethene Single Crystal: Upscaling Isomerization to Macroscopic Deformation". In: *Scientific Reports* 7.1 (Dec. 2017), p. 967. ISSN: 2045-2322. DOI: 10.1038/s41598-017-00910-5.

[82] W. J. Tomlinson. "Phase Holograms in Photochromic Materials". In: *Applied Optics* 11.4 (Apr. 1, 1972), p. 823. ISSN: 0003-6935, 1539-4522. DOI: 10.1364/AO.11.000823.

[83] S. Timoshenko. "Analysis of Bi-Metal Thermostats". In: *Journal of the Optical Society of America* 11.3 (Sept. 1, 1925), p. 233. ISSN: 0030-3941. DOI: 10.1364/JOSA.11.000233.

[84] Daichi Kitagawa et al. "Quantitative Evaluation of Photoinduced Bending Speed of Diarylethene Crystals". In: *Crystals* 5.4 (Nov. 6, 2015), pp. 551–561. ISSN: 2073-4352. DOI: 10.3390/cryst5040551.

[85] D. Corbett and M. Warner. "Linear and Nonlinear Photoinduced Deformations of Cantilevers". In: *Physical Review Letters* 99.17 (Oct. 25, 2007), p. 174302. ISSN: 0031-9007, 1079-7114. DOI: 10.1103/PhysRevLett.99.174302.

[86] Daniel Corbett, Chen Xuan, and Mark Warner. "Deep Optical Penetration Dynamics in Photobending". In: *Physical Review E* 92.1 (July 31, 2015), p. 013206. ISSN: 1539-3755, 1550-2376. DOI: 10.1103/PhysRevE.92.013206.

[87]   D. Corbett and M. Warner. "Nonlinear Photoresponse of Disordered Elastomers".
        In: *Physical Review Letters* 96.23 (June 12, 2006), p. 237802. ISSN: 0031-9007,
        1079-7114. DOI: 10.1103/PhysRevLett.96.237802.

[88]   D. Corbett and M. Warner. "Bleaching and Stimulated Recovery of Dyes and of
        Photocantilevers". In: *Physical Review E* 77.5 (May 30, 2008), p. 051710. ISSN:
        1539-3755, 1550-2376. DOI: 10.1103/PhysRevE.77.051710.

[89]   M. Warner, C. D. Modes, and D. Corbett. "Curvature in Nematic Elastica Re-
        sponding to Light and Heat". In: *Proceedings of the Royal Society A: Mathematical,
        Physical and Engineering Sciences* 466.2122 (Oct. 8, 2010), pp. 2975–2989. ISSN:
        1364-5021, 1471-2946. DOI: 10.1098/rspa.2010.0135.

[90]   J. S. Biggins, M. Warner, and K. Bhattacharya. "Elasticity of Polydomain Liquid
        Crystal Elastomers". In: *Journal of the Mechanics and Physics of Solids* 60.4 (Apr.
        2012), pp. 573–590. ISSN: 00225096. DOI: 10.1016/j.jmps.2012.01.008. arXiv:
        0911.3513.

[91]   Hongbo Wang and William S. Oates. "Light Induced Stress Rate Effects in
        Azobenzene Liquid Crystal Polymer Networks". In: SPIE Smart Structures and
        Materials + Nondestructive Evaluation and Health Monitoring. Ed. by Zoubeida
        Ounaies and Stefan S. Seelecke. San Diego, California, USA, Mar. 24, 2011,
        79780F. DOI: 10.1117/12.883154.

[92]   Jad Mahmoud Halabi et al. "Performance of Molecular Crystals in Conversion of
        Light to Mechanical Work". In: *Proceedings of the National Academy of Sciences*
        118.5 (Feb. 2, 2021), e2020604118. ISSN: 0027-8424, 1091-6490. DOI: 10.1073/
        pnas.2020604118.

[93]   Chi Chen et al. "Multiresponse Shape-Memory Nanocomposite with a Reversible
        Cycle for Powerful Artificial Muscles". In: *Chemistry of Materials* 33.3 (Feb. 9,
        2021), pp. 987–997. ISSN: 0897-4756, 1520-5002. DOI: 10.1021/acs.chemmater.
        0c04170.

[94]   Françisco M. Raymo et al. "Memory Effects Based on Intermolecular Photoin-
        duced Proton Transfer". In: *Journal of the American Chemical Society* 125.8 (Feb. 1,
        2003), pp. 2361–2364. ISSN: 0002-7863. DOI: 10.1021/ja027977j.

[95]   *Solid Mechanics Part I*. URL: https://pkel015.connect.amazon.auckland.ac.
        nz/SolidMechanicsBooks/Part_I/index.html.

[96]   T. Q. Nguyen and H. H. Kausch. "Molecular Weight Distribution and Mechanical
        Properties". In: *Mechanical Properties and Testing of Polymers: An A–Z Reference*.
        Ed. by G. M. Swallowe. Polymer Science and Technology Series. Dordrecht:
        Springer Netherlands, 1999, pp. 143–150. ISBN: 978-94-015-9231-4. DOI: 10.
        1007/978-94-015-9231-4_32.

[97]   David R. T. Roberts and Simon J. Holder. "Mechanochromic Systems for the
        Detection of Stress, Strain and Deformation in Polymeric Materials". In: *Journal
        of Materials Chemistry* 21.23 (2011), p. 8256. ISSN: 0959-9428, 1364-5501. DOI:
        10.1039/c0jm04237d.

[98]   Roderic Lakes. *Viscoelastic Materials*. First Edition. New York: Cambridge University Press, 2009. ISBN: ISBN-13 978-0-511-57995-0.

[99]   *Practical Maintenance » Blog Archive » Fatigue Test and Creep Test*. URL: https://practicalmaintenance.net/?p=989.

[100]   Kevin P Menard. *Dynamic Mechanical Analysis: Apractical Introduction*. Second Edition. Boca Raton, FL: Taylor & Francis Group, LLC, 2008. ISBN: 978-1-4200-5312-8.

[101]   R. S. RIVLIN. "Solution of Some Problems in the Exact Theory of Visco-Elasticity". In: *Journal of Rational Mechanics and Analysis* 5.1 (1956), pp. 179–188. ISSN: 1943-5282. JSTOR: 24900247. URL: https://www.jstor.org/stable/24900247.

[102]   M. Mooney. "A Theory of Large Elastic Deformation". In: *Journal of Applied Physics* 11.9 (Sept. 1940), pp. 582–592. ISSN: 0021-8979. DOI: 10.1063/1.1712836.

[103]   R. W. Ogden. "Large Deformation Isotropic Elasticity – on the Correlation of Theory and Experiment for Incompressible Rubberlike Solids". In: *Proceedings of the Royal Society of London. A. Mathematical and Physical Sciences* 326.1567 (Feb. 1972), pp. 565–584. ISSN: 0080-4630. DOI: 10.1098/rspa.1972.0026.

[104]   Cornelius O. Horgan. "The Remarkable Gent Constitutive Model for Hyperelastic Materials". In: *International Journal of Non-Linear Mechanics* 68 (Jan. 2015), pp. 9–16. ISSN: 00207462. DOI: 10.1016/j.ijnonlinmec.2014.05.010.

[105]   A. N. Gent. "A New Constitutive Relation for Rubber". In: *Rubber Chemistry and Technology* 69.1 (Mar. 1, 1996), pp. 59–61. ISSN: 0035-9475. DOI: 10.5254/1.3538357.

[106]   L.R.G. Treloar. *The Physics of Rubber Elasticity*. Third edition. Great Britain: Oxford University Press, 1975. ISBN: 0-19-851355-0.

[107]   Eugen Guth and Hermann Mark. "Zur innermolekularen, Statistik, insbesondere bei Kettenmolekiilen I". In: *Monatshefte für Chemie und verwandte Teile anderer Wissenschaften* 65.1 (Dec. 1, 1934), pp. 93–121. ISSN: 1434-4475. DOI: 10.1007/BF01522052.

[108]   Werner Kuhn and Franz Grün. "Statistical Behavior of the Single Chain Molecule and Its Relation to the Statistical Behavior of Assemblies Consisting of Many Chain Molecules". In: *Journal of Polymer Science* 1.3 (1946), pp. 183–199. ISSN: 1542-6238. DOI: 10.1002/pol.1946.120010306.

[109]   Stephen K. Melly et al. "A Review on Material Models for Isotropic Hyperelasticity". In: *International Journal of Mechanical System Dynamics* 1.1 (Sept. 2021), pp. 71–88. ISSN: 2767-1402, 2767-1402. DOI: 10.1002/msd2.12013.

[110]   Robert M. Hackett. *Hyperelasticity Primer*. Cham: Springer International Publishing, 2018. ISBN: 978-3-319-73200-8 978-3-319-73201-5. DOI: 10.1007/978-3-319-73201-5.

[111]   Ellen M. Arruda and Mary C. Boyce. "A Three-Dimensional Constitutive Model for the Large Stretch Behavior of Rubber Elastic Materials". In: *Journal of the Mechanics and Physics of Solids* 41.2 (Feb. 1993), pp. 389–412. ISSN: 00225096. DOI: 10.1016/0022-5096(93)90013-6.

[112]   G. Chagnon, G. Marckmann, and E. Verron. "A Comparison of the Hart-Smith Model with Arruda-Boyce and Gent Formulations for Rubber Elasticity". In: *Rubber Chemistry and Technology* 77.4 (Sept. 1, 2004), pp. 724–735. ISSN: 1943-4804, 0035-9475. DOI: 10.5254/1.3547847.

[113]   Christine Renaud et al. "The Yeoh Model Applied to the Modeling of Large Deformation Contact/Impact Problems". In: *International Journal of Impact Engineering* 36.5 (Feb. 2009), p. 659. DOI: 10.1016/j.ijimpeng.2008.09.008.

[114]   *Arruda–Boyce Model*. In: *Wikipedia*. Oct. 11, 2020. URL: https://en.wikipedia.org/w/index.php?title=Arruda%E2%80%93Boyce_model&oldid=982887573.

[115]   J Bergstrom. "Constitutive Modeling of the Large Strain Time-Dependent Behavior of Elastomers". In: *Journal of the Mechanics and Physics of Solids* 46.5 (May 1998), pp. 931–954. ISSN: 00225096. DOI: 10.1016/S0022-5096(97)00075-6.

[116]   Rongliang Wu, Ting Li, and Erik Nies. "Langevin Dynamics Simulation of Chain Crosslinking into Polymer Networks". In: *Macromolecular Theory and Simulations* 21.4 (May 2012), pp. 250–265. ISSN: 10221344. DOI: 10.1002/mats.201100088.

[117]   Masao Doi and Samuel Frederick Edwards. *The Theory of Polymer Dynamics*. International Series of Monographs on Physics. Oxford: Clarendon press, 1986. ISBN: 978-0-19-852033-7.

[118]   Ismael Arroyo. "A Novel Photomechanical Material Understanding Photochemical and Morphology". France: Universite de Lille, 2023.

[119]   *Thin Film*. In: *Wikipedia*. Apr. 3, 2022. URL: https://en.wikipedia.org/w/index.php?title=Thin_film&oldid=1080830921.

[120]   Alexa S. Kuenstler and Ryan C. Hayward. "Light-Induced Shape Morphing of Thin Films". In: *Current Opinion in Colloid & Interface Science* 40 (Apr. 2019), pp. 70–86. ISSN: 13590294. DOI: 10.1016/j.cocis.2019.01.009.

[121]   Edwin Acosta. "Thin Films/Properties and Applications". In: *Thin Films*. Ed. by Alicia Esther Ares. IntechOpen, Nov. 17, 2021. ISBN: 978-1-83881-986-6 978-1-83881-993-4. DOI: 10.5772/intechopen.95527.

[122]   Yan Liu et al. "Controllable Fabrication of Oriented Micro/Nanowire Arrays of Dibenzo-Tetrathiafulvalene by a Multiple Drop-Casting Method". In: *Nanoscale* 6.3 (2014), pp. 1323–1328. ISSN: 2040-3364, 2040-3372. DOI: 10.1039/C3NR05680E.

[123]   Morteza Eslamian and Fatemeh Zabihi. "Ultrasonic Substrate Vibration-Assisted Drop Casting (SVADC) for the Fabrication of Photovoltaic Solar Cell Arrays and Thin-Film Devices". In: *Nanoscale Research Letters* 10.1 (Dec. 1, 2015), p. 462. ISSN: 1556-276X. DOI: 10.1186/s11671-015-1168-9.

[124]   Karel Lambert et al. "Langmuir–Schaefer Deposition of Quantum Dot Mul-
        tilayers". In: *Langmuir* 26.11 (June 1, 2010), pp. 7732–7736. ISSN: 0743-7463,
        1520-5827. DOI: 10.1021/la904474h.

[125]   Kohei Miyamae et al. "Self-Healing, Expansion–Contraction, and Shape-Memory
        Properties of a Preorganized Supramolecular Hydrogel through Host–Guest In-
        teractions". In: *Angewandte Chemie International Edition* 54.31 (2015), pp. 8984–
        8987. ISSN: 1521-3773. DOI: 10.1002/anie.201502957.

[126]   *Ureidopyrimidinone.* ureidopyrimidinone (C5H6N4O2) ChemSpider. URL: http:
        //www.chemspider.com/Chemical-Structure.10606029.html.

[127]   Holger Kautz et al. "Cooperative End-to-End and Lateral Hydrogen-Bonding
        Motifs in Supramolecular Thermoplastic Elastomers". In: *Macromolecules* 39.13
        (June 2006), pp. 4265–4267. ISSN: 0024-9297, 1520-5835. DOI: 10.1021/ma060706z.

[128]   Souleymane Coulibaly et al. "Supramolecular Polymers with Orthogonal Func-
        tionality". In: *Macromolecules* 47.24 (Dec. 23, 2014), pp. 8487–8496. ISSN: 0024-
        9297, 1520-5835. DOI: 10.1021/ma501492u.

[129]   Martin S. Vollmer et al. "Photoswitchable Hydrogen-Bonding in Self-Organized
        Cylindrical Peptide Systems". In: *Angewandte Chemie International Edition* 38.11
        (June 1, 1999), pp. 1598–1601. ISSN: 1433-7851, 1521-3773. DOI: 10.1002/(SICI)
        1521-3773(19990601)38:11<1598::AID-ANIE1598>3.0.CO;2-J.

[130]   Cheng-Wei Huang et al. "Stimuli-Responsive Supramolecular Materials: Photo-
        Tunable Properties and Molecular Recognition Behavior". In: *Polymer Chemistry*
        7.4 (Jan. 19, 2016), pp. 795–806. ISSN: 1759-9962. DOI: 10.1039/C5PY01852H.

[131]   *Track Points in Video Using Kanade-Lucas-Tomasi (KLT) Algorithm - MATLAB.*
        URL: https://www.mathworks.com/help/vision/ref/vision.pointtracker-
        system-object.html#d123e90395.

[132]   Kevin N. Long et al. "Light-Induced Stress Relief to Improve Flaw Tolerance in
        Network Polymers". In: *Journal of Applied Physics* 107.5 (Mar. 2010), p. 053519.
        ISSN: 0021-8979, 1089-7550. DOI: 10.1063/1.3311553.

[133]   Xiaoming Mu et al. "Photo-Induced Bending in a Light-Activated Polymer Lami-
        nated Composite". In: *Soft Matter* 11.13 (2015), pp. 2673–2682. ISSN: 1744-683X,
        1744-6848. DOI: 10.1039/C4SM02592J.

[134]   Nancy Sowan et al. "Light-Activated Stress Relaxation, Toughness Improvement,
        and Photoinduced Reversal of Physical Aging in Glassy Polymer Networks". In:
        Advanced Materials 33.5 (Feb. 2021), p. 2007221. ISSN: 0935-9648, 1521-4095.
        DOI: 10.1002/adma.202007221.

[135]   Hideo Koseki and Akira Odajima. "Photo-Induced Stress Relaxation in Amor-
        phous Selenium Films". In: *Japanese Journal of Applied Physics* 21 (Part 1, No. 3
        Mar. 5, 1982), pp. 424–428. ISSN: 0021-4922, 1347-4065. DOI: 10.1143/JJAP.21.
        424.

[136] Heitor L. Ornaghi et al. "Stress Relaxation, Creep, and Recovery of Carbon Fiber Non-Crimp Fabric Composites". In: *Composites Part C: Open Access* 3 (Nov. 2020), p. 100051. ISSN: 26666820. DOI: 10.1016/j.jcomc.2020.100051.

[137] Malvern. *A Basic Introduction to Rheology*. Whitepaper. Malvern Instruments Worldwide, 2016, p. 20. URL: https://cdn.technologynetworks.com/TN/Resources/PDF/WP160620BasicIntroRheology.pdf.

[138] TA Intruments. *TA Instruments Q Series Thermal Analyzers*. 2006. URL: http://www.tainstruments.com/pdf/DMA_old.pdf.

[139] Xudong Liang et al. "Light Induced Reversible and Irreversible Mechanical Responses in Nanotube-Polymer Composites". In: *Composites Part B: Engineering* 134 (Feb. 2018), pp. 39–45. ISSN: 13598368. DOI: 10.1016/j.compositesb.2017.09.036.

[140] Kevin N Long et al. "Photo-Induced Creep of Network Polymers". In: (2010), p. 12.

[141] Apratim Majumder et al. "A Comprehensive Simulation Model of the Performance of Photochromic Films in Absorbance-Modulation-Optical-Lithography". In: *AIP Advances* 6.3 (Mar. 2016), p. 035210. ISSN: 2158-3226. DOI: 10.1063/1.4944489.

[142] Christian Schörner et al. "Nondestructive Probing of a Photoswitchable Dithienylethene Coupled to Plasmonic Nanostructures". In: *The Journal of Physical Chemistry C* 121.30 (Aug. 3, 2017), pp. 16528–16532. ISSN: 1932-7447, 1932-7455. DOI: 10.1021/acs.jpcc.7b05558.

[143] Lihua Jin, Yin Lin, and Yongzhong Huo. "A Large Deflection Light-Induced Bending Model for Liquid Crystal Elastomers under Uniform or Non-Uniform Illumination". In: *International Journal of Solids and Structures* 48.22-23 (Nov. 2011), pp. 3232–3242. ISSN: 00207683. DOI: 10.1016/j.ijsolstr.2011.07.015.

[144] Stanislav Chizhik et al. "Reversal of Photoinduced Bending of Crystals Due to Internal Refraction of Light". In: *Applied Sciences* 12.23 (Nov. 24, 2022), p. 12007. ISSN: 2076-3417. DOI: 10.3390/app122312007.

[145] Stanislav Chizhik et al. "Quantification of Photoinduced Bending of Dynamic Molecular Crystals: From Macroscopic Strain to Kinetic Constants and Activation Energies". In: *Chemical Science* 9.8 (2018), pp. 2319–2335. ISSN: 2041-6520, 2041-6539. DOI: 10.1039/C7SC04863G.

[146] J.M. Gere and Timoshenko S.P. *Mechanics of Materials*. Boston, MA PWS-KENT, 1990, pp. 301–8.

[147] MSC. Software. *Volume D: User Subroutines and Special Routines*. English. Version MARC 2015. MSC. Software. 2015. 625 pp. 2015.

[148] Hüsnü Dal and Michael Kaliske. "Bergström–Boyce Model for Nonlinear Finite Rubber Viscoelasticity: Theoretical Aspects and Algorithmic Treatment for the FE Method". In: *Computational Mechanics* 44.6 (Nov. 2009), pp. 809–823. ISSN: 0178-7675, 1432-0924. DOI: 10.1007/s00466-009-0407-2.

[149] C. Ovalle Rodas et al. "A Thermo-Visco-Hyperelastic Model for the Heat Build-up during Low-Cycle Fatigue of Filled Rubbers: Formulation, Implementation and Experimental Verification". In: *International Journal of Plasticity* 79 (Apr. 2016), pp. 217–236. ISSN: 07496419. DOI: 10.1016/j.ijplas.2015.01.001.

A Absorbance

T Transmittance

ϵ Molar absorptivity

I light intensity

I_0 incident light intensity

n total number density of photoisomerizable groups

τ_{uv} UV intensity rate

τ_{ct} thermal rate of the reverse reaction

τ_{tc} relaxation time

T_{ni} critical transition temperature

$T_{ni}^{(0)}$ transition temperature in pure material

χ_{OF} Molecular fraction of OF configuration

χ_{CF} Molecular fraction of CF configuration

ϵ_{OF} absorption cross section of species of the OF configuration

ϵ_{CF} absorption cross section of species of the CF configuration

$\sigma_{OF}(\lambda)$ interaction cross section for molecules in OF configuration

$\sigma_{CF}(\lambda)$ interaction cross section for molecules in CF configuration

λ light wavelength

$\Phi_{(OF-CF)}$ quantum yield of the cyclization photoreaction

$\Phi_{(CF-OF)}$ quantum yield of the cycloreversion photoreaction

C Concentration of active molecules by meter cubic

$g\%$ weight percentage of photoactive molecules

ρ thin film's density

M_{ph} molar mas of photoactive molecules

α_{OF} absorption coefficient of the OF configuration during UV irradiation

α_{CF} absorption coefficient of the CF configuration during VIS irradiation

α_{matrix} absorption coefficient of the polymer matrix

k_{vis} CF to OF conversion rate

k_{uv} OF to CF conversion rate

R radius of curvature

ε_{ph} photo-induced strain

w thin film's thickness

$\mathbf{F}$ deformation gradient tensor

$\mathbf{F}^{T}$ transpose of the deformation gradient tensor

B left Cauchy-Green tensor

T Cauchy stress tensor

$\mathscr{L}^{-1}$ inverse Langevin function

$\mathscr{L}$ Langevin function

$\lambda_{chain}^{(i)}$ principal stretches of the network chains

$I_1^{(i)}$ first invariant of the left Cauchy-Green Tensor

v^{ph} photo-viscous element for a PNR material

σ_s spring element stress

σ_v viscous element stress

E Young Modulus

ε_s spring strain

$\dot{\varepsilon}_v$ viscous strain rate

η viscosity

σ normal stress

σ_y yield strength

σ_b tensile strength

ε normal strain

ε_b ultimate elongation

$\mathcal{H}(t)$ Heaviside step

δ Shift angle between applied stress and strain response in DMA (damping factor)

ω Angular frequency of the applied stress in DMA

E' Storage modulus

E'' Loss or viscous modulus

T_g glass-transition temperature

ν Poisson's ratio

Ψ strain energy density function

$\mathbf{C}$ right Cauchy-Green deformation tensor

C_{ijk} material parameters in theMooney-Rivlin model

G Rubbery modulus

$P(r)$ Probability function

Θ temperature

k Boltzmann's constant

N number of total chains contained in one unit volume (crosslink density)

λ_{lock} chain limit extensibility

λ_i principal stretch ratio in the ith direction

r_0 network chain length

r_{chain} stretch vector length

λ_{chain} network chain stretch

$\mathbf{F}_A$ time-independent gradient deformation tensor

$\mathbf{F}_B$ time-dependent gradient deformation tensor

$\bar{\mathbf{F}}$ isochoric part of the deformation gradient tensor

$\mathbf{F}_B^e$ elastic part of the deformation gradient tensor

$\mathbf{F}_B^v$ viscous or inelastic part of the deformation gradient tensor

$\mathbf{B}^*$ isochoric left Cauchy-Green deformation gradient tensor

κ_B bulk modulus

$\bar{\lambda}^*$ elastic stretch

$\mathbf{L}_B$ The total velocity gradient (strain-rate tensor)

$\mathbf{D}$ deformation rate tensor

$\mathbf{W}$ spin tensor

$\mathbf{T}_B^{*'}$ deviatoric of the Cauchy stress tensor of the time-dependent branch

$\mathbf{N}_B$ driving stress

τ_B effective shear stress acting on the time-dependent branch

$\dot{\gamma}$ creep rate function

a^{ph} photo-expansion coefficient

Acronyms

DAE diarylethene

DTE dithienylethene

PEB poly(ethylene-co-butylene)

VIS visible

UV ultaviolet

OF open form

CF closed form

FEA finite element analysis

FEM finite element model

LEDs light-emitting diodes

CdS cadmium sulfide

PNR Photo-Induced Network Rearrangement

PMC Photo-tunable molecular crosslink

LCE liquid crystal elastomer

LCP liquid crystal polymer

LCNs liquid-crystalline networks

PET poly(ethyleneterephthalate)

UEL user element

DMA Dynamic Mechanical Analysis

DMTA Dynamic Mechanical Thermal Analysis

SLS Standard Linear Solid

PDM physical deposition methods

CDM chemical deposition methods

LBS Langmuir-Blodgett-Shaefer

UPy ureidopyrimidinone

KLT Kanade-Lucas-Tomasi algorithm

TGA thermogravimetric analysis

DFS Dynamic Frequency Sweep

LVER Linear viscoelastic region